Doctoral Dissertation
Doctoral Program in Chemical Engineering (36th Cycle)

Synthesis and In-Depth Characterization of Fe-Based Catalysts and Zeolites for Efficient CO_2 Hydrogenation to Hydrocarbons

Elena Corrao

* * * * * *

Supervisors
Prof. Supervisor Samir Bensaid (PoliTo)
Prof. Co-Supervisor Raffaele Pirone (PoliTo)
Prof. Co-Supervisor Agustín Martínez Feliu (ITQ-UPV)

Politecnico di Torino
July, 2024

This thesis is licensed under a Creative Commons License, Attribution - Noncommercial - NoDerivative Works 4.0 International: see www.creativecommons.org. The text may be reproduced for non-commercial purposes, provided that credit is given to the original author.

I hereby declare that the contents and organization of this dissertation constitute my own original work and does not compromise in any way the rights of third parties, including those relating to the security of personal data.

…….....

Elena Corrao

Turin, July, 2024

Summary

Nowadays, global warming caused by CO_2 emissions has a wide range of negative impacts, both environmentally and socially. To address this issue, this doctoral work focuses on the conversion of CO_2 into liquid hydrocarbons through the hydrogenation process.

The main investigation took place at the Polytechnic University of Turin. In this initial stage, the $NaFe_3O_4$_CP catalyst was tested in physical mixture with both a commercial MFI zeolite (labelled HZSM5) and a homemade hierarchical MFI zeolite (labelled HZ). These configurations showed higher catalytic activity than the corresponding core-shell samples having the same active phase and zeolite. In particular, the catalyst labeled $NaFe_3O_4$_CP+HZ (physical mixture) demonstrated the best catalytic performance. The superior catalytic performance of the hierarchical zeolite can be attributed to the presence of mesopores, which facilitate the desorption of aromatic and/or long-chain products due to the larger pore size of the zeolite. In an attempt to introduce innovation, the exploration continued with the creation of core-shell structures. However, from this inaugural study emerged the central role of sodium as a promoter and, in particular, the effects of its migration. In fact, it was significant to confirm that sodium migration from bulk iron to the acidic sites of the zeolite compromises the selectivity for desired hydrocarbon products, especially gasoline [1].

These preliminary conclusions prompted an extension of the research at the Instituto de Tecnología Química (ITQ) in Valencia, , where the focus remained on sodium-promoted iron catalysts but was supported by a hydrophobic material to limit the migration of the alkaline metal. Specifically, the decision was made to support sodium-promoted iron catalysts externally and internally on carbon nanotubes (CNTs) with various external diameters in order to evaluate if the

confinement of sodium and iron inside materials with an inherently hydrophobic nature could effectively achieve the goal. In addition to diameter variations, impregnated CNTs were synthesized with different percentages of iron while keeping the iron-sodium ratio constant. These CNTs underwent individual tests and were also examined together with an MFI-type zeolite in two different contact modes: a granular mixture and a powder mixture, specifically using a commercial HZSM-5 zeolite. In particular, for the CNT-S-O10FeNa catalyst, it was found that confining iron inside the nanotube greatly limits sodium migration. Consequently, no substantial difference in terms of CO_2 conversion and selectivity to CO and CH_4 was noted when testing this catalyst in the two above-mentioned contacts with acid sites of the zeolite. All fresh, used, and reduced catalysts were extensively characterized to ascertain the position of iron rather than the CNT, especially through TEM analysis, examining the nanoparticles of iron in each sample in different grid regions in order to establish their position (in or out of the CNT) and to calculate the particle diameter distribution as accurately as possible. To support the catalytic results obtained, other advanced characterizations like Raman investigation and XPS analysis were carried out.

Based on the results of this comprehensive experimental campaign, attention shifted to a particular iron- and sodium-impregnated CNT named CNT-M-O15FeNa, which showed sodium migration from iron sites to the acidic sites of the zeolite. This subsequent experimental phase explored the surface properties, Si/Al ratio, grain sizes, and pore sizes of MFI-type structure zeolites. Most of these zeolites were synthesized and/or modified at the ITQ laboratories, which highlighted how reducing the number of surface acid sites can be a valid alternative to counteract sodium migration. In particular, among all tested zeolites, μMFI35, characterized by a very low external surface area, proved to be the best zeolite at achieving this goal.

Finally, the last work carried out had a slightly diversified goal. Recognizing the migratory capacity of sodium and identifying alternatives, the choice was made to focus on examining zeolites with different frameworks (FAU, MFI, BEA, MWW, TON and and ITQ-2), Si/Al ratios, and the impact of mesoporosity on their ability to modulate selectivity across different ranges of liquid hydrocarbon products. To eliminate potential distortions of selectivity results due to sodium migration, this study was conducted in a double-bed mode. However, despite the intention to use different zeolite structures to modulate hydrocarbon selectivity, the obtained cutting was predominantly gasoline-like, and the MFI zeolite was reaffirmed as the most effective material for this purpose.

However, it is important to emphasize that numerous challenges have been faced, and much effort is still needed to address issues related to energy input, catalytic challenges, raw material availability, operating costs, and environmental impact to maximize their potential and effectiveness.

Acknowledgment

The investigation presented in this Ph.D. dissertation was conducted as part of the Chemical Engineering Ph.D. program, XXXVI° cycle, at Politecnico di Torino.

Special recognition is given for the financial support received from the Italian Ministero dell'Università e della Ricerca (MUR) under the PON Ricerca e Innovazione project "REACT-EU" (DM 1062/21).

Gratitude is expressed for the substantial resources provided by the Instituto de Tecnología Química-Universitat Politècnica de València (ITQ-UPV), with particular appreciation for Prof. Agustín Martínez Feliu 's guidance during the research abroad phase of the Ph.D. program.

I would like to dedicate this thesis to all those who have been by my side during these three intense years, marked by few positive moments and numerous obstacles. A special thanks goes to my family for understanding the challenging days and for always standing by me. In particular, I dedicate this work to Daniele, my anchor and safe haven. If I started and completed this journey, it is primarily thanks to his patience and words in the many moments of discouragement.

Contents

1. General Introduction and Aim of the Work 1

1.1 Climate change, Fossil Fuels Demand and Urgency for Sustainable Alternatives 1

1.2 CO_2 Capture, Storage and Utilization Technologies 6

1.2.1 CO_2 Capture..... 8

1.2.2 CO_2 Storage 13

1.2.3 CO_2 Utilisation 13

1.3 Green H_2 Production..... 15

1.4 Efforts to reduce CO_2 Emissions through the Production of Liquid Hydrocarbons: Potentials and Limitations 20

1.4.1 Catalysts for Fischer Tropsch Synthesis from CO_2..... 24

1.4.1.1 Promoter Effects on Fischer Tropsch synthesis 27

1.4.1.2 Effects in CO_2-FTS of metal-oxide catalyst supported on inorganic substrates..... 28

1.4.1.3 Zeolite support effects on CO_2-FTS..... 29

1.4.1.4 Migration of alkali promoters from oxide-phase to acid sites of Zeolite 31

1.5 Structure and Aim of the Work of the Doctoral Thesis..... 32

2. Experimental methods 35

2.1 Synthesis of bulk iron catalysts combined with zeolite..... 35

2.1.1 Preparation of the bulk Na/Fe_3O_4 catalyst..... 36

2.1.2 $NaFe_3O_4$ Obtained by Coprecipitation with NaOH..... 37

2.1.3 Synthesis of Hierarchical Zeolite HZSM-5: HZ 37

2.1.4 Core-shell catalysts: $NaFe_3O_4$@HZSM5 and $NaFe_3O_4$@HZ 38

2.2 Iron catalysts supported on Carbon Nanotubes (CNTs) 38

2.2.1 Carbon nanotubes pretreatment and impregnation with Iron 39

2.3 Synthesis, desilication, ion-exchange and passivation of MFI-type zeolites 41

2.3.1 Synthesis of extra-large crystal size zeolite: µMFI35 42

2.3.2 Desilication of microcrystalline zeolite, µMFI35 43

2.3.3 Nanocrystalline ZSM-5 zeolite, MFI46-nano 43

2.3.4 Partial Na ion-exchange on CBV5524G (H^+ form) 44

2.3.5 Surface sylilation treatment.....44

2.4 Different types of zeolites used in dual bed mode tests with 1 NaFe 45

2.4.1 Bulk iron synthesis: 1NaFe 46

2.4.2 Desilication of commercial CBV760 46

2.4.3 Desilication of commercial CP814C.....47

2.4.4 Synthesis of MCM-22 and ITQ-2 47

2.5 Characterization Techniques 48

2.5.1 Inductively coupled plasma-Optical Emission Spectroscopy (ICP-OES) 49

2.5.2 Energy-Dispersive X-Ray Fluorescence Analysis (XRF).....49

2.5.3 N_2 Adsorption.....50

2.5.4 X-Ray Diffraction (XRD) 51

2.5.5 Temperature programmed techniques.....57

2.5.6 Transmission Electron Microscopy (TEM) 59

2.5.7 Scanning Electron Microscopy (SEM) 62

2.5.8 Energy-Dispersive X-Ray Spectroscopy.....63

2.5.9 X-Ray Photoelectron Spectroscopy (XPS) 63

2.6 Catalytic tests conducted in Italy.....65

2.6.1 Data processing 73

2.7 Catalytic tests conducted in Spain.....78

2.7.1 Experimental procedure in catalytic tests 80

2.7.2 Reactor loading protocols 81

2.7.3 Activation and Start-up of the Catalytic Experiment 84
2.7.4 Catalytic Tests 84
2.7.5 Identification and Analysis of Products 85
2.7.6 Data processing 86
2.8 Comparison of Test Benches Used in This Thesis: Advantages and Limitations of Each 89
3 CO_2 conversion into hydrocarbons via modified Fischer-Tropsch synthesis by using bulk iron catalysts combined with zeolites. 91
3.1 Introduction 91
3.2 Results and discussion 96
3.2.1. Characterization of the catalysts 96
3.2.2. Catalytic tests 115
3.3 In closing 124
4. Strategies to inhibiting alkali migration 126
4.1. Introduction 126
4.2. Results and discussions 129
4.2.1 Catalysts characterization 129
4.2.2 Catalytic tests 141
4.2.3 Reduced/Passivated and Spent Catalysts characterization 149
4.3. Conclusion 150
5. Examining Alkali Migration in Na-promoted Fe-CNT/Zeolite Systems with a Focus on Various MFI Zeolite Properties 152
5.1. Introduction 153
5.2. Results and discussions 156
5.2.1 Catalysts characterization 156
5.2.2 Catalytic tests 166
5.3. Conclusion 174
6. Impact of Different Zeolite Structures on the Catalytic Performances of NaFe-Zeolite Systems Tested in Dual-Bed Mode 176

6.1. Introduction 177
6.2. Results and discussions 182
6.2.1 Catalysts characterization 182
6.3. Catalytic tests 190
6.3.1 Influence of catalytic bed configuration: granule mixing versus dual bed 190
6.3.2 Characterization of spent zeolites 207
6.4. Conclusion 211
7. Conclusion 212
References 215
Appendix 1 241
Appendix 2 248

List of Tables

Table 2. 1. Synthesis and Summary Characteristics of Catalytic Samples Used in Chapter 3. 35

Table 2. 2. Synthesis and Summary Characteristics of Catalytic Samples Used in Chapter 4. 39

Table 2. 3. Synthesis and Summary Characteristics of Catalytic Samples Used in Chapter 5. 42

Table 3. 1. Chemical composition and textural properties of fresh catalysts. 96

Table 3. 2. Crystalline size fresh iron phase calculated with Scherrer equation, based on the broadening of the most intense peak (311) at 2 Theta: 35.52 °. .. 100

Table 3. 3. Quantitative analysis of the H_2-TPR measurements. 107

Table 3. 4. Quantitative analysis of the NH_3-TPD measurements. 109

Table 3. 5. CO_2-TPD fresh and spent iron-oxide phases. 112

Table 3. 6. XPS relative atomic concentration (at.%) for all the samples, fresh and spent ones. 113

Table 3. 7. Results catalytic tests. 118

Table 3. 8. Results derived from TOC and HPLC. 119

Table 3. 9. TPC results. 124

Table 4. 1. Principal samples details involved in this study. 129

Table 4. 2 Textural properties of carbon nanotubes catalyst impregnated with Fe and Na measured by N_2 physisorption and chemical analysis of carbon nanotubes impregnated with Fe and Na catalyst. 130

Table 4. 3. Fe_3O_4 particle sizes of catalysts supported on carbon nanotubes (CNTs). 136

Table 4. 4. Results H_2-TPR. 140

Table 4. 5. Hydrocarbons distribution for CO_2 hydrogenation at 340 °C, 20 bar, GHSV = 3.1 $L_{CO2+H2}/(g_{cat} \cdot h)$, H_2/CO_2 = 3.1 mol/mol. Data averaged for TOS = 21 – 27 h. 141

Table 5. 1. Principal samples details involved in this study. 155

Table 5. 2. Bulk chemical composition determined by ICP-OES, Si/Al atomic ratio in the near-surface region measured by XPS, and percentage of framework (FAL) and extra-framework (EFAL Al species derived from ^{27}Al MAS NMR for MFI samples. 156

Table 5. 3. Textural properties of MFI zeolites determined by N_2 adsorption measurements. 159

Table 5. 4. Density of acid sites of MFI samples determined by NH_3-TPD. 164

Table 5. 5. Acidity of MFI zeolites determined by FTIR of adsorbed pyridine. 165

Table 5. 6. Overall product selectivity. 168

Table 6. 1. Name used in this chapter and additional information of each zeolite. 181

Table 6. 2. Chemical analysis of bulk iron catalyst impregnated with Na. 183

Table 6. 3. Textural properties of bulk iron impregnated with Na measured by N_2 physisorption. 183

Table 6. 4. Fe_3O_4 crystallite size of bulk iron catalysts. 184

Table 6. 5. Chemical analysis and textural properties of zeolites. 186

Table 6. 6. Loss of crystallinity of mesoporous zeolites. 187

Table 6. 7. Zeolite Acidity Determined by TPD-NH_3. 188

Table 6. 8. Acidity of zeolites determined by IR-pyridine (μmol py$\cdot g^{-1}$), at different pyridine desorption temperatures. 188

Table 6. 9. Percentage of extraframework and framework Al estimated from ^{27}Al MAS NMR (FAL = framework Al, EFAL = extraframework Al). 189

Table 6. 10. XRD-based framework and extraframework composition of USY-type zeolites. 190

Table 6.11. Hydrocarbons distribution at 1.5 h. 206

Table 6.12. Chemical composition (ICP) and coke content (elemental analysis, TG analysis) of spent zeolites. 208

Table 6.13. Type of coke deposits in spent zeolites determined by temperature-programmed oxidation (TPO). 210

List of Figures

Figure 1. 1. Representation of the Earth's average global energy budget, adapted by [6], [7], [8]. 3

Figure 1. 2. Illustration of the capture, use, and storage of carbon. 8

Figure 1. 3. Methods for capturing CO_2 from a gas stream, adapted by [34], [35]. 9

Figure 1. 4. Schematic production of fuels from CO_2 hydrogenation. 21

Figure 1. 5. Different ways to hydrogenate CO_2 to hydrocarbon final products [1]. 23

Figure 1. 6. Catalysts used for CO_2-FTS, adapted by [70], [77], [78]. 24

Figure 1. 7. Illustration of how an iron-based catalyst behaves during reduction and carburization treatment. 26

Figure 1. 8. Hydrogenation of CO_2 to olefin on Fe-based catalysts. 27

Figure 1. 9. Simplified conversion mechanism of olefins over acid sites of zeolites. 29

Figure 1. 10. Mechanism of Na migration. 31

Figure 2.1. Schematic representation of Bragg's Equation (2. 1). 52

Figure 2.2. a) Processes that result from X-ray bombardment of a surface include emission of a photoelectron on the left and emission of an Auger electron on the right; b) Energy level diagram illustrates the basic XPS equation (2. 14) schematically. 64

Figure 2.3. Italy test bench plant. 66

Figure 2.4. Italy Reactor Configuration. 67

Figure 2.5. Details of the analysis program, outlining temperature ramps and isothermal intervals employed to achieve an effective separation of mixture components. 69

Figure 2.6. System for the Analysis of Liquid Reaction Products. 70

Figure 2.7. Details of the analysis program, outlining temperature ramps employed to achieve an effective separation of mixture components. 72

Figure 2.8. Valencia test bench plant. 80

Figure 2.9. Carbon nanotubes configurations. 82

Figure 2.10. Bulk iron configurations. 83

Figure 2.11. Details of the analysis program, outlining any temperature ramps or isothermal intervals employed to achieve an effective separation of mixture components. This on-line analysis detects hydrocarbons in the C_1-C_{20} range. ... 86

Figure 3. 1. N_2 adsorption-desorption isotherms of the calcined: a) 1%$NaFe_3O_4$_WI, b) 5%$NaFe_3O_4$_WI and c) $NaFe_3O_4$_CP. 97

Figure 3. 2. N_2 adsorption-desorption isotherms of the calcined: a) HZSM5 and b) HZ. 98

Figure 3. 3. N_2 adsorption-desorption isotherms of the calcined: a) $NaFe_3O_4$_CP@HZSM5, b) $NaFe_3O_4$_CP@HZ. 98

Figure 3. 4. Pore size distribution. 99

Figure 3. 5. XRD patterns of the a) fresh and b) spent Fe_3O_4-based catalysts: 1%$NaFe_3O_4$_WI, 5%$NaFe_3O_4$_WI and Na-Fe_3O_4_CP 100

Figure 3. 6. XRD patterns of a) fresh zeolites and core-shell structures and b) spent granule mixed catalysts and core-shell structures. 101

Figure 3. 7. In situ XRD patterns of fresh $NaFe_3O_4$_CP catalytic powder under reducing atmosphere H_2/Ar from 25 °C to 900 °C. 102

Figure 3. 8. In situ XRD patterns of fresh $NaFe_3O_4$_CP catalytic powder under reducing atmosphere a) H_2/Ar from 25° to 450 °C, black profiles; b) H_2/Ar at 450 °C for 14 h, black profile and H_2/CO/N_2 at 330 °C for 18 h, blue profiles. 103

Figure 3. 9. HR-TEM images of a) fresh and b) spent 1%$NaFe_3O_4$_WI. 103

Figure 3. 10. HR-TEM images of (a) fresh and (b) spent $NaFe_3O_4$_CP. 104

Figure 3. 11. HR-TEM images of spent $NaFe_3O_4$_CP. 105

Figure 3. 12. TEM images of the homemade HZ sample. 105

Figure 3. 13. SEM images of the homemade HZ sample. 106

Figure 3. 14. H_2-TPR profiles of fresh catalysts: (a) 1%Na-Fe_3O_4_WI, 5%Na-Fe_3O_4_WI 5%Na-Fe_3O_4_CP; (b) $NaFe_3O_4$_CP@HZSM5 and $NaFe_3O_4$_CP@HZ. 108

Figure 3. 15. NH_3-TPD fresh catalysts profiles. 110

Figure 3. 16. FESEM-EDS images of the sample: $NaFe_3O_4$_CP@HZSM5. ... 110

Figure 3. 17. CO_2-TPD profiles a) fresh iron-oxide and b) spent iron-oxide samples..... 112

Figure 3. 18. CO_2-TPD profiles a) fresh core-shell catalyst; b) spent core-shell structures and physical mixture. 112

Figure 3. 19. XPS spectra related to survey regions for fresh a) and spent b) samples. C) HR N1s region deconvoluted to show the chemical shift of N due to $NaNO_3$ bond in 5%$NaFe_3O_4$_WI_f sample. 113

Figure 3. 20. XPS HR spectra: Fe2p doublet (a, d), C1s region (b, e) and Na1s region (c, f) for fresh (upper row) and spent (lower row) samples. 115

Figure 3. 21. Time-on-stream (TOS) tests up to ≈ 14 hours, temperature: 330 °C, pressure: 2.3 MPa, and flow rate: 22 $NL \cdot g^{-1}_{Fe3O4} \cdot h^{-1}$ with an inlet $H_2/CO_2/N_2$ molar ratio equal to 15/5/3: a) 1%$NaFe_3O_4$_WI; b) 5%$NaFe_3O_4$_WI; c) $NaFe_3O_4$_CP. 117

Figure 3. 22. Comparison catalytic performance of 1%$NaFe_3O_4$_WI, 5%$NaFe_3O_4$_WI and $NaFe_3O_4$_CP catalysts at 330 °C. Reaction conditions: 2.0 MPa, 21.96 $NL \cdot gFe_3O_4 \cdot h^{-1}$, TOS = 14 h..... 117

Figure 3. 23. Mass chromatogram $NaFe_3O_4$ _CP. 118

Figure 3. 24. Time-on-stream (TOS) tests up to ≈ 14 hours, temperature: 330 °C, pressure: 2.3 MPa, and flow rate: 22 $NL \cdot g^{-1}_{Fe3O4} \cdot h^{-1}$ with an inlet $H_2/CO_2/N_2$ molar ratio equal to 15/5/3: a) $NaFe_3O_4$_CP+HZSM5; b) $NaFe_3O_4$_CP+HZ. 120

Figure 3. 25. Time-on-stream (TOS) tests up to ≈ 14 hours, temperature: 330 °C, pressure: 2.3 MPa, and flow rate: 22 $NL \cdot g^{-1}_{Fe3O4} \cdot h^{-1}$ with an inlet $H_2/CO_2/N_2$ molar ratio equal to 15/5/3: a) $NaFe_3O_4$_ CP@HZSM5; b) $NaFe_3O_4$_CP@HZ. 121

Figure 3. 26. Comparison of catalytic performance among physical mixture and core-shell of $NaFe_3O_4$_CP with commercial and homemade hierarchical zeolite. Reaction conditions: 330°C, 2.3 MPa, and a flow rate of 21.96 $NL \cdot g_{Fe3O4} \cdot h^{-1}$ TOS=14 h..... 121

Figure 3. 27. Mass chromatogram $NaFe_3O_4$ _CP+HZSM-5. 122

Figure 3. 28. Mass chromatogram $NaFe_3O_4$ _CP+HZ..... 123

Figure 4. 1 TEM images and nanoparticles distributions for the fresh CNT samples: a) CNT-S-C10FeNa_fresh, b) CNT-S-O10FeNa_fresh, c) CNT-S-O15FeNa_fresh, d) CNT-M-O15FeNa_fresh and e) CNT-L-O15FeNa_fresh. 134

Figure 4. 2. XRD profiles of fresh carbon nanotubes.....135

Figure 4. 3. XRD profile of CNT samples alone a) and in powder mixing with the commercial zeolite MFI27 b), both after reduction in H_2 at 400 °C for 10 h. ..137

Figure 4. 4. XRD pattern spent catalysts a) without zeolite and b) with zeolite. 138

Figure 4. 5. H_2-TPR profiles.....139

Figure 4. 6. TOS monitoring of CO_2 hydrogenation at 340 °C, 20 bar, GHSV = 3.1 $L_{CO2+H2}/(g_{CNT}\cdot h)$, H_2/CO_2 = 3.1 mol/mol for: a) CNT-S-C10FeNa, b) CNT-S-C10FeNa+MFI27 (GM), c) CNT-S-C10FeNa+MFI27 (PM), d) CNT-S-O10FeNa, e) CNT-S-O10FeNa+MFI27 (GM) f) CNT-S-O10FeNa+MFI27 (PM). To specify: (a, b, c) Na promoted Fe outside CNT and (d, e, f) Na promoted Fe inside CNT.....142

Figure 4. 7. Comparison of CO_2 conversion, CO selectivity and metal selectivity for the CNT-S-C-10FeNa sample with “close caps” (first line) and the CNT-S-O-10FeNa sample with “open caps” (second line). In particular each graph is compared the single Na-Fe/CNT (full symbol), the granule mixture Na-Fe/CNT+zeolite (empty symbol) and the powder mixture Na-Fe/CNT+zeolite (half-full symbol).....143

Figure 4. 8. Comparison of total C_2-C_4 (paraffins+ olefins) and total C_{5+} selectivity for the CNT-S-C-10FeNa sample with “close caps” (first line) and the CNT-S-O-10FeNa sample with “open caps” (second line). In particular each graph is compared the single Na-Fe/CNT (full symbol), the granule mixture Na-Fe/CNT+zeolite (empty symbol) and the powder mixture Na-Fe/CNT+zeolite (half-full symbol).....144

Figure 4. 9. TOS monitoring of CO_2 hydrogenation at 340 °C, 20 bar, GHSV = 3.1 $L_{CO2+H2}/(g_{CNT}\cdot h)$, H_2/CO_2 = 3.1 mol/mol for: a) CNT-S-O15FeNa, b) CNT-S-O15FeNa+MFI27 (GM), c) CNT-S-O15FeNa+MFI27 (PM), d) CNT-M-O15FeNa, e) CNT-M-O15FeNa+MFI27 (GM), f) CNT-M-O15FeNa+MFI27 (PM), g) CNT-L-O15FeNa, h) CNT-L-O15FeNa+MFI27 (GM) and i) CNT-L-O15FeNa+MFI27 (PM).....145

Figure 4. 10. Comparison CO_2 conversion, CO selectivity and CH_4 selectivity for the samples: CNT-S-O15FeNa (a-c); CNT-M-O15FeNa (d-f); CNT-L-O15FeNa (g-i), tested without and with zeolite in the two different mode: GM and PM. 147

Figure 4. 11. TOS monitoring of aromatics product calculated inside C_{5+} products. 148

Figure 4. 12. TEM images of *Reduced/Passivated (R/P) catalysts (Group 1, blue color)*: a) CNT-S-C10FeNa_R/P, c) CNT-S-O10FeNa_R/P, e) CNT-S-O15FeNa_R/P, g) CNT-M-O15FeNa_R/P and i) CNT-L-O15FeNa_R/P; *Spent (S) catalysts (Group 2, red color)*: b) CNT-S-C10FeNa_S, d) CNT-S-O10FeNa_S, f) CNT-S-O15FeNa_S, h) CNT-M-O15FeNa_ S and j) CNT-L-O15FeNa_S..... 150

Figure 5. 1. XRD patterns obtained for commercial MFI samples, namely MFI27 and MFI112; alongside other samples home-prepared. 157

Figure 5. 2. Normalized ^{27}Al MAS NMR spectra of hydrated MFI zeolites.... 158

Figure 5. 3. N_2 adsorption isotherms measured at -196 °C for MFI zeolites. For the sake of clarity, the isotherms have been upshifted by 30, 40, 60, 70, and 100 $cm^3 \cdot g^{-1}$ for MFI34@Sil3, MFI112, MFI46-nano, μMFI35, and μMFI27-meso, respectively. 160

Figure 5. 4. Representative FESEM images of (a) MFI27, (b) MFI46-nano, (c, d) μMFI35 and (e) μMFI27-meso zeolites. 161

Figure 5. 5. Representative TEM images of MFI46-nano (a) and μMFI27-meso (b) zeolites..... 162

Figure 5. 6. NH_3-TPD profiles of MFI zeolites. 163

Figure 5. 7. FTIR-DTBPy spectra of MFI zeolites. Spectra normalized to sample weight..... 165

Figure 5. 8. TOS monitoring CNT-M-O15FeNa+different MFI zeolite, weight ratio 1:1, granular mixture mode: a) CNT-M-O15FeNa+0.4NaMFI27, b) CNT-M-O15FeNa+MFI34@Sil3, c) CNT-M-O15FeNa+MFI112, d) CNT-M-O15FeNa+MFI46-nano, e) CNT-M-O15FeNa+μMFI35, f) CNT-M-O15FeNa+ μMFI27-meso. 168

Figure 5. 9. Comparison conversion and overall selectivity..... 171

Figure 5. 10. Influence of different MFI in CNT-M-O15FeNa, to specify relative value related to itself conversion and to itself selectivity. 172

Figure 5. 11. Effect of CNT and site distance (GM) on aromatics formation...173

Figure 6. 1. Main characteristics of the zeolites studied in this thesis work, (framework created by 3D Drawing tool in the Database of Zeolite Structures, accessed 11 December 2023). 179

Figure 6. 2. XRD pattern of a) fresh of Fe_3O_4 and 1NaFe catalysts and b) spent of 1NaFe catalyst. 184

Figure 6. 3. XRD profiles of a) zeolites with 12-ring channels and b) zeolites with 10-ring channels. 186

Figure 6. 4. NH_3-TPD profiles of a) zeolites with 12-ring channels and b) zeolites with 10-ring channels. 188

Figure 6. 5. ^{27}Al MAS NMR spectra of fully hydrated zeolites: a) zeolites with 12-ring channels and b) zeolites with 10-ring channels. 189

Figure 6. 6. TOS monitoring of 1NaFe tested in two different configurations: dual bed (DB, full symbols) and granule mixture (GM, empty symbols).....192

Figure 6. 7. Product distribution calculated after 1.5 h (a), 9 h (b) and 27 h (c) over time on stream, for carbon number of standalone 1NaFe and 1NaFe combined in dual bed mode with 12 MR zeolites: USY24, USY15M, USY13, USY5, BEA17 and BEA17M. 193

Figure 6. 8. a), c) and d) A comparison of catalytic data obtained with various zeolites; b), d) and e) explanation in detail of the (net) increase (or decrease) in selectivity of specific hydrocarbon groups when zeolites are introduced in comparison to the 1NaFe catalyst used alone. Reaction parameters include 2.0 bar, 340 °C, H_2/CO_2 = 3, and 19.2 $L \cdot g^{-1} \cdot h^{-1}$, with a time on stream of 27 h. 194

Figure 6. 9. Product selectivity to gasoline product (C_5-C_{12}) over zeolite with large-pore-size. Reaction parameters include 2.0 bar, 340 °C, H_2/CO_2 = 3, and 19.2 $L \cdot g^{-1} \cdot h^{-1}$, with a time on stream of 27 h. 195

Figure 6. 10. Effect of zeolite topology over aromatics selectivity calculated in the C_{5+} fraction. Results reported: a) beginning of TOS (1.5 h), b) middle of the TOS (9 h), c) end of the TOS (27 h). Reaction parameters include 2.0 bar, 340 °C, H_2/CO_2 = 3, and 19.2 $L \cdot g^{-1} \cdot h^{-1}$, with a time on stream of 27 h. 196

Figure 6. 11. Effect of different zeolite frameworks with 12-ring on the isomerization of C_5 compounds. Reaction parameters include 2.0 bar, 340 °C, H_2/CO_2 = 3, and 19.2 $L \cdot g^{-1} \cdot h^{-1}$, with a time on stream of 27 h. 198

Figure 6. 12. Catalysts activity and products distribution over 1NaFe tested in dual bed mode with large-pore size zeolite: a) USY24, b) USY15M, c) USY13, d)USY5, e) BEA17 and f) BEA17M. Reaction parameters include 2.0 bar, 340 °C, H_2/CO_2 = 3, and 19.2 $L \cdot g^{-1} \cdot h^{-1}$, with a time on stream of 27 h. 199

Figure 6. 13. Product selectivity to gasoline product (C_5-C_{12}) over zeolite with medium-pore-size. Reaction parameters include 2.0 bar, 340 °C, H_2/CO_2 = 3, and 19.2 $L \cdot g^{-1} \cdot h^{-1}$, with a time on stream of 27 h..... 201

Figure 6. 14. Effect of zeolite topology over aromatics selectivity calculated in the C_{5+} fraction. Results reported: a) beginning of TOS (1.5 h), b) middle of the TOS (9 h), c) end of the TOS (27 h). Reaction parameters include 2.0 bar, 340 °C, H_2/CO_2 = 3, and 19.2 $L \cdot g^{-1} \cdot h^{-1}$, with a time on stream of 27 h. 202

Figure 6. 15. Effect of different zeolite frameworks with 10-ring on the isomerization of C_5 compounds. Reaction parameters include 2.0 bar, 340 °C, H_2/CO_2 = 3, and 19.2 $L \cdot g^{-1} \cdot h^{-1}$, with a time on stream of 27 h. 203

Figure 6. 16. a) A comparison of catalytic data obtained with various zeolites; b) explanation in detail of the (net) increase (or decrease) in selectivity of specific hydrocarbon groups when zeolites are introduced in comparison to the 1NaFe catalyst used alone. Reaction parameters include 2.0 bar, 340 °C, H_2/CO_2 = 3, and 19.2 $L \cdot g^{-1} \cdot h^{-1}$, with a time on stream of 27 h..... 204

Figure 6. 17. Catalysts activity and products distribution over 1NaFe tested in dual bed mode with large-pore size zeolite: a) MFI27, b) MFI17M, c) Z22-32, d) M22-20 and e) ITQ2-18. Reaction parameters include 2.0 bar, 340 °C, H_2/CO_2 = 3, and 19.2 $L \cdot g^{-1} \cdot h^{-1}$, with a time on stream of 27 h..... 206

Figure 6. 18. TG profiles for a) spent large pore (12-ring) and b) medium pore (10-ring) zeolites..... 208

Figure 6. 19. TPO-MS profiles (CO_2 signal, m/z=44) for a) spent large pore (12-ring) and b) medium pore (10-ring) zeolites..... 210

Figure A1. 1. N_2 adsorption of original CNT, without any treatment. 241

Figure A1. 2. N_2 adsorption of small CNT (CNT-S-original), subjected to mild acid treatment (MAT) and strong acid treatment (SAT). 242

Figure A1. 3. N_2 adsorption of CNTs with Fe and Na inside and/or outside the CNT. 243

Figure A1. 4. Temperature-resolved X-ray diffractograms were obtained for the following catalysts: a) CNT-S-C10FeNa, b) CNT-S-C10FeNa+MFI27 (PM),

during in situ reduction treatment in a flowing 10% H2/N2 atmosphere. Additionally, the corresponding temperature-resolved evolution of the normalized area for the most intense diffraction line of detected crystalline species was examined. These species include: Fe2O3 (1 0 4), JCPDS24-0072; Fe3O4 (3 1 1), JCPDS 88-0315; FeO (2 0 0), JCPDS 74-1886 and Fe0 (1 1 0), JCPDS 87-0722. 244

Figure A1. 5. Temperature-resolved X-ray diffractograms were obtained for the following catalysts: a) CNT-S-O10FeNa, b) CNT-S-O10FeNa+MFI27 (PM), during in situ reduction treatment in a flowing 10% H2/N2 atmosphere. Additionally, the corresponding temperature-resolved evolution of the normalized area for the most intense diffraction line of detected crystalline species was examined. These species include: Fe2O3 (1 0 4), JCPDS24-0072; Fe3O4 (3 1 1), JCPDS 88-0315; FeO (2 0 0), JCPDS 74-1886 and Fe0 (1 1 0), JCPDS 87-0722. 246

Figure A1. 6. Temperature-resolved X-ray diffractograms were obtained for the following catalysts: a) CNT-M-O15FeNa, b) CNT-M-O15FeNa+MFI27 (PM), during in situ reduction treatment in a flowing 10% H2/N2 atmosphere. Additionally, the corresponding temperature-resolved evolution of the normalized area for the most intense diffraction line of detected crystalline species was examined. These species include: Fe2O3 (1 0 4), JCPDS24-0072; Fe3O4 (3 1 1), JCPDS 88-0315; FeO (2 0 0), JCPDS 74-1886 and Fe0 (1 1 0), JCPDS 87-0722. 247

Figure A2. 1. Nitrogen adsorption-desorption isotherms and pore distribution of commercial USY24 and mesoporous USY15M.....248

Figure A2. 2. Nitrogen adsorption-desorption isotherms and pore distribution of MFI27 and mesoporous MFI17M. 248

Figure A2. 3. Nitrogen adsorption-desorption isotherms and pore distribution of BEA17 and mesoporous BEA17M. 249

Figure A2. 4. Nitrogen adsorption-desorption isotherms and pore distribution of M22-20 and delaminated ITQ2-18 zeolites.....249

Figure A2. 5. Nitrogen adsorption-desorption isotherms and pore distribution of Z22-32 zeolite.....250

Figure A2. 6. Deconvoluted NH_3-TPD profiles of commercial BEA, USY, and MFI zeolites and their mesoporous counterparts.....253

Figure A2. 7. Infrared spectra of USY24 zeolite in hydroxyl region, recorded after a) overnight activation at 400 °C under dynamic vacuum and after adsorption and desorption of pyridine at 250 °C; b) adsorption and desorption of pyridine at 250 °C, 350 °C and 400 °C. 253

Figure A2. 8. spectra of USY15M zeolite in hydroxyl region, recorded after a) overnight activation at 400 °C under dynamic vacuum and after adsorption and desorption of pyridine at 250 °C; b) adsorption and desorption of pyridine at 250 °C, 350 °C and 400 °C. 254

Figure A2. 9. Infrared spectra of USY13 zeolite in hydroxyl region, recorded after a) overnight activation at 400 °C under dynamic vacuum and after adsorption and desorption of pyridine at 250 °C; b) adsorption and desorption of pyridine at 250 °C, 350 °C and 400 °C. 254

Figure A2. 10. Infrared spectra of USY5 zeolite in hydroxyl region, recorded after a) overnight activation at 400 °C under dynamic vacuum and after adsorption and desorption of pyridine at 250 °C; b) adsorption and desorption of pyridine at 250 °C, 350 °C and 400 °C. 255

Figure A2. 11. Infrared spectra of BEA17 zeolite in hydroxyl region, recorded after a) overnight activation at 400 °C under dynamic vacuum and after adsorption and desorption of pyridine at 250 °C; b) adsorption and desorption of pyridine at 250 °C, 350 °C and 400 °C. 255

Figure A2. 12. Infrared spectra of BEA17M zeolite in hydroxyl region, recorded after a) overnight activation at 400 °C under dynamic vacuum and after adsorption and desorption of pyridine at 250 °C; b) adsorption and desorption of pyridine at 250 °C, 350 °C and 400 °C. 256

Figure A2. 13. Infrared spectra of MFI27 zeolite in hydroxyl region, recorded after a) overnight activation at 400 °C under dynamic vacuum and after adsorption and desorption of pyridine at 250 °C; b) adsorption and desorption of pyridine at 250 °C, 350 °C and 400 °C. 256

Figure A2. 14. Infrared spectra of MFI17M zeolite in hydroxyl region, recorded after a) overnight activation at 400 °C under dynamic vacuum and after adsorption and desorption of pyridine at 250 °C; b) adsorption and desorption of pyridine at 250 °C, 350 °C and 400 °C. 257

Figure A2. 15. Infrared spectra of Z22-32 zeolite in hydroxyl region, recorded after a) overnight activation at 400 °C under dynamic vacuum and after adsorption

and desorption of pyridine at 250 °C; b) adsorption and desorption of pyridine at 250 °C, 350 °C and 400 °C.....257

Figure A2. 16. Infrared spectra of M22-20 zeolite in hydroxyl region, recorded after a) overnight activation at 400 °C under dynamic vacuum and after adsorption and desorption of pyridine at 250 °C; b) adsorption and desorption of pyridine at 250 °C, 350 °C and 400 °C.....258

Figure A2. 17. Infrared spectra of ITQ2-18 zeolite in hydroxyl region, recorded after a) overnight activation at 400 °C under dynamic vacuum and after adsorption and desorption of pyridine at 250 °C; b) adsorption and desorption of pyridine at 250 °C, 350 °C and 400 °C.....258

Figure A2. 18. Catalysts activity and products distribution over 1NaFe tested in dual bed mode without zeolite.....259

Chapter 1

1. General Introduction and Aim of the Work

It is known that fighting climate change is becoming an increasingly urgent challenge for all of the world. For this reason, it is essential to consider innovative solutions that not only address greenhouse gas emissions, but also contemplate sustainable alternatives to conventional fossil fuels.

Within this framework, the first chapter of this thesis focuses on exploring strategies for the hydrogenation of carbon dioxide (CO_2) into liquid hydrocarbons through the analysis of thermocatalytic approaches. In particular, the idea is to promote a deeper understanding of environmental issues and potential solutions to address them.

1.1 Climate change, Fossil Fuels Demand and Urgency for Sustainable Alternatives

In the beginning, it is important to emphasize the importance of the complex layer of gases that surround the Earth. In fact, the atmosphere has a central role in maintaining climate balance on earth. This gaseous coat naturally contains greenhouse gases (GHG) like carbon dioxide (CO_2), methane (CH_4) and nitrous oxide (N_2O), working harmoniously to trap essential solar heat and provide the ideal conditions for life on Earth. Nevertheless, these emissions or GHGs from

human beings have disrupted this delicate atmospheric equilibrium. Basically, wide spread use of fossil fuels including coal, oil and natural gas for energy needs, industrial processes intensive agriculture and deforestation has boosted an alarming rise in green house effect. Consequently, global warming which is at the heart of climate change has occurred [2].

Climate change is a widespread phenomenon marked by long-term variations in weather patterns. These shifts include increased average global temperatures, humidity variations, and extended periods of drought, indicating a continuous climate trend separate from natural weather variability [3]. The key role of the natural greenhouse effect, which maintains a surface temperature conducive to life, becomes evident when it is considered the alternative scenario; without this effect, the Earth's surface would be significantly colder, making it an extremely inhospitable place for life. How it is known, the underlying reasons of these shifts are found in the complex mechanics of the Earth's climate system, with a particular emphasis on radiative balance. In fact, the climate system acts as a regulator, with incoming solar energy that is either reflected back into space by the Earth or emitted as infrared radiation from the atmosphere being essential for maintaining terrestrial temperatures [4]. In particular, the greenhouse effect comes into play when incoming solar radiation, in the form of shortwaves, penetrates the Earth's atmosphere, reaches the planet's surface, and gets absorbed. When this energy is reemitted as infrared radiation back to Earth, the resulting longwave radiation encounters obstacles as it travels through the atmosphere [5]. Furthermore, greenhouse gases, particularly CO_2, CH_4, and water vapor, absorb infrared radiation, causing atmospheric warming.

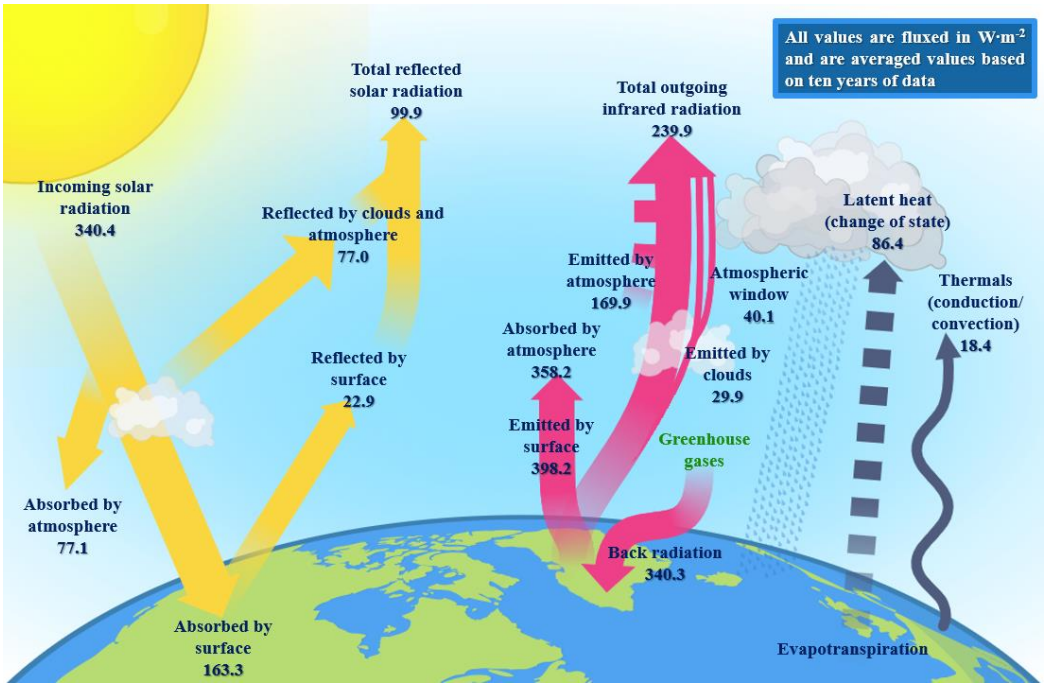


Figure 1. 1. Representation of the Earth's average global energy budget, adapted by [6], [7], [8].

In this context, Figure 1. 1 illustrates the mechanisms of energy transfer, clearly depicting the upper atmosphere, the Earth's surface, and the intermediate atmosphere. Solar and terrestrial radiation are distinct, representing the best estimates of the variables involved in the global energy balance, offering an overview of the climatic conditions in the early 21st century. Within this visual representation, there are globally averaged values for each component, measured in Watts per square meter ($W \cdot m^{-2}$). Additionally, the image includes indications of the associated ranges of uncertainty or variability, which are conveyed through numerical values within parentheses, typically represented as 5-95% confidence intervals. Conversely, the lower part of the diagram offers an insight into the energy budget when there is an absence of cloud cover, with all other atmospheric and surface properties kept constant. In this cloud-free scenario, there is a conspicuous decrease in the global-scale reflection of solar radiation (53 ± 2 $W \cdot m^{-2}$), contrasting with the standard condition featuring cloud cover (100 ± 2 $W \cdot m^{-2}$). Simultaneously, there is a noticeable escalation in the emission of thermal radiation from both the Earth's surface and its atmosphere into space. This pronounced variation in the volume of incoming solar radiation reaching the Earth's surface implies that the planet would undergo a substantial warming effect in the absence of cloud cover [6].

As anticipate before, the Earth's atmosphere contains a wide range of GHGs, some of which have been increasing since pre-industrial periods. These include nitrous oxide (N_2O), water vapor (H_2O), methane (CH_4), ozone (O_3), and carbon dioxide (CO_2) [9]. As a confirmation of this hypothesis, the Intergovernmental Panel on Climate Change (IPPC) published a report in 2007 in which it was highlighted that global greenhouse gas emissions have steadily increased over time, with a notable 70% increase noted between 1970 and 2004. The IPCC concluded with high confidence that human activities are the primary driver of climate change [9].

The demand for fossil fuels, such as coal, oil, and natural gas, has been steadily rising. These fuels have been essential to technological, social, and economic advancement, but they also inevitably result in a rise in GHG emissions, which is what causes human influence on climate change [10], [11]. Presently, over 80% of the global primary energy demand relies on fossil fuels, with oil being the primary source, followed by coal and natural gas. This situation is, in part, due to the continuous growth of the global population and the increasing energy demand, directly impacting atmospheric carbon dioxide (CO_2) levels and led to the signing of the Paris Agreement in December 2015, providing a binding framework for addressing climate change, with the goal of limiting the increase in the global average temperature to below 2 °C and achieving carbon neutrality by the second half of the century [12], [13].

One of the main causes of the current climate change is the widespread existence of long-lived greenhouse gases in the atmosphere. For many decades, scientists have consistently cautioned that a future characterized by extreme climate conditions was imminent due to the rising global temperatures resulting from human activities, particularly the release of CO_2 from the combustion of fossil fuels. Unfortunately, time has elapsed, and we are presently observing the realization of these predictions, marked by a distressing and unprecedented series of climate records being broken, leading to profoundly distressing scenes of suffering [14].

In May 2021, the IEA published a report that charted a practical path for the global energy sector to contribute to achieving the goal of the Paris Agreement by 2050 [15]. The Net Zero Roadmap quickly became a significant reference point for policymakers, industry, finance, and civil society. Ever since, significant modifications have actually taken place consisting of the international power situation triggered by Russia's intrusion of Ukraine in February 2022 along with

a rise in CO_2 exhausts in the power field in 2022 [16]. Nevertheless, there are also reasons for optimism due to advancements in clean energy technologies.

As support for the imminent problem, the IPCC report, published in 2022, unequivocally confirms that human-induced climate change represents a widespread and perilous disruption to the Earth's ecosystem, significantly impacting the lives and livelihoods of billions of people, despite mitigation efforts [17]. The International Energy Agency (IEA) estimates that CO_2 emissions have increased from pre-industrial levels (280 ppm) to amounts exceeding 400 ppm by more than 40% [18], [19]. Alongside the National Oceanic and Atmospheric Administration (NOAA) report, released in January 2023, provides credence for these findings by showing a startling 50% increase from pre-industrial levels, with the present concentration reaching 419 ppm [20]. Considering these alarming findings, it is clear that prompt action is required.

Current policies aimed at limiting the growth of CO_2 and other greenhouse gas emissions, if consistently followed, can positively impact future global warming. Key areas of focus include energy, encompassing electricity, heating, transportation, and industrial activities, as well as food and agriculture, including changes in land use. The transition to low-carbon alternatives is essential to address these challenges and create a more sustainable energy future. Primary strategies to reduce dependence on fossil fuels and mitigate emissions include improving energy efficiency, replacing fossil fuels with renewable energy sources, and capturing and storing CO_2 emissions. The growing awareness of climate change and the scarcity of fossil resources have prompted many nations, companies, and individuals to explore alternative and renewable energy sources, such as solar, wind, and hydropower. These energy sources are becoming increasingly economically competitive and play a significant role in reducing dependence on fossil fuels and mitigating climate change.

In 1990, Finland set a pioneering example by implementing a carbon tax, which later found adoption in 47 other countries [21]. Notably, the United States Congress passed the “Inflation Reduction Act of 2022” in August 2022, significantly increasing federal tax credits for carbon capture and long-term sequestration (CCS) using direct air capture (DAC) technology, with the credit reaching up to \$180 per metric ton of CO_2 for the first five years of operation [22].

This transition from carbon capture and storage (CCS), often reliant on policy support, to the conversion of CO_2 into synthetic fuels and petrochemicals

represents a crucial step towards achieving profitable carbon neutrality[13], [23]. It entails a gradual reduction in the use of fossil fuels as the primary carbon feedstock. For example, petrochemicals like light olefins (C_2-C_4), with a global market worth approximately $240 billion in 2021 [24], demonstrate significant potential. Furthermore, the market for renewable aviation fuels is poised for substantial growth, anticipated to leap from $1.1 billion in 2023 to $16.8 billion in 2030 [25], indicating a multi-billion-dollar market for CO_2-derived commodities.

Particularly, renewable energy sources like solar, wind, and hydropower are central to reducing CO_2 emissions in the energy sector. However, the variability of these resources can limit their ability to provide a consistent and reliable energy supply. The conversion of CO_2 into fuels is an option to capture CO_2 emissions and use them to synthesize new renewable fuels, thereby contributing to the reduction of net CO_2 emissions in the atmosphere.

While renewable sources hold promise, it is likely that fossil fuels will continue to play a significant role in the transition to a net-zero energy future. Carbon capture and utilization (CCU) represent an option to contribute to the defossilization of the energy sector.

1.2 CO_2 Capture, Storage and Utilization Technologies

A sustainable balance of greenhouse gases can be maintained by reducing CO_2 emissions. In fact, the concentration of CO_2 in the atmosphere has been steadily rising every year since the 1950s, coinciding with the onset of industrial growth, and it now exceeds 410 parts per million (ppm). Projections indicate that this concentration may increase to 800-1000 ppm by the end of the 21st century [26].

To delve deeper, approximately half of anthropogenic CO_2 emissions arise from decentralized sources like transportation and residential/commercial heating, while the remaining half is attributed to concentrated sources such as power plants, refineries, and the cement and steel industries. Specifically addressing emissions from non-renewable sources, currently developed technologies primarily focus on diminishing emissions from the latter category of sources.

This scenario highlights the need for a reliable approach to address the significant presence of CO_2 in the atmosphere. The goal is to integrate CO_2 as a

raw material into a circular economy framework for the synthesis of high-value products while simultaneously addressing the continuous growth in global fuel demand. This strategy involves using CO_2 to sustainably produce fuels and chemicals, thereby replacing traditional fossil fuels. There are several ways to valorise CO_2 [27]:

Carbon capture and storage technology (CCS) is the process of extracting CO_2 from significant emission sources, transporting it to a storage facility, and then permanently removing it from the atmosphere. Although this method can remove CO_2 on a large scale and reduce emissions at the source, it presents some challenges. These include the high cost of carbon capture due to the energy required for separation and pumping, the increased use of fossil fuels (20% to 60%) during the process, and the potential for CO_2 leakage from the geological storage [28]. Another alternative to remove CO_2 is the Carbon Capture and Utilization (CCU) technology, where "U" indicates utilization, in fact employing captured CO_2 for oil flooding serves as both a resource reuse technique and a method for lowering CO_2 emissions [29]. This process represents a novel economic opportunity that allows stakeholders to use captured CO_2 as a raw material for the production of fuels and value-added products through various processes. CO_2 has garnered attention as a promising and renewable carbon source due to its economic and readily available nature. It can serve as a fundamental building block (C1) for creating various organic chemicals, materials, and carbohydrates, making it an attractive feedstock for different industries [30], [31]. Utilizing CO_2 as a feedstock not only aids in mitigating the effects of global climate change resulting from rising CO_2 emissions, but also offers exciting prospects for catalytic and industrial development, thereby opening new avenues for research and application [32].

In recent decades, scientists have dedicated significant attention to CCSU technologies [33], which integrate elements from both CCS and CCU.

These technologies adhere to three fundamental steps: capture, transportation, and utilization or storage of CO_2, Figure 1. 2. The following summarizes the methodologies of capturing, utilizing and storing carbon dioxide and described in detail in the following sub-sections 1, 1.1.1 and 1.2.3.

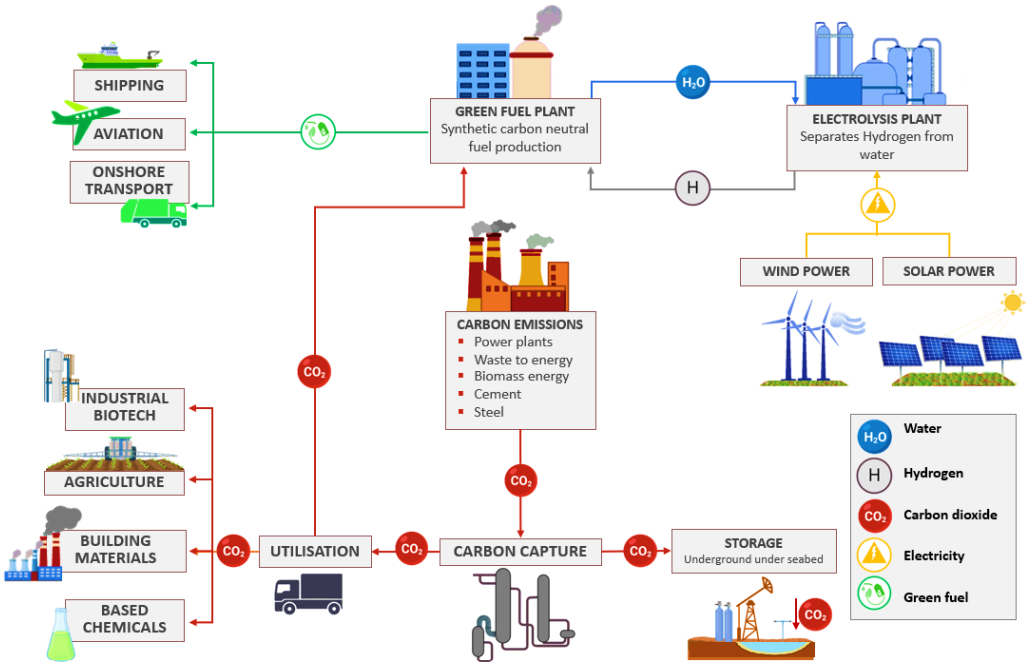


Figure 1. 2. Illustration of the capture, use, and storage of carbon.

1.2.1 CO_2 Capture

Carbon capture methodologies for capturing CO_2 are often categorized into pre-combustion, post-combustion, oxy-combustion, and direct air capture, as depicted in Figure 1. 3.

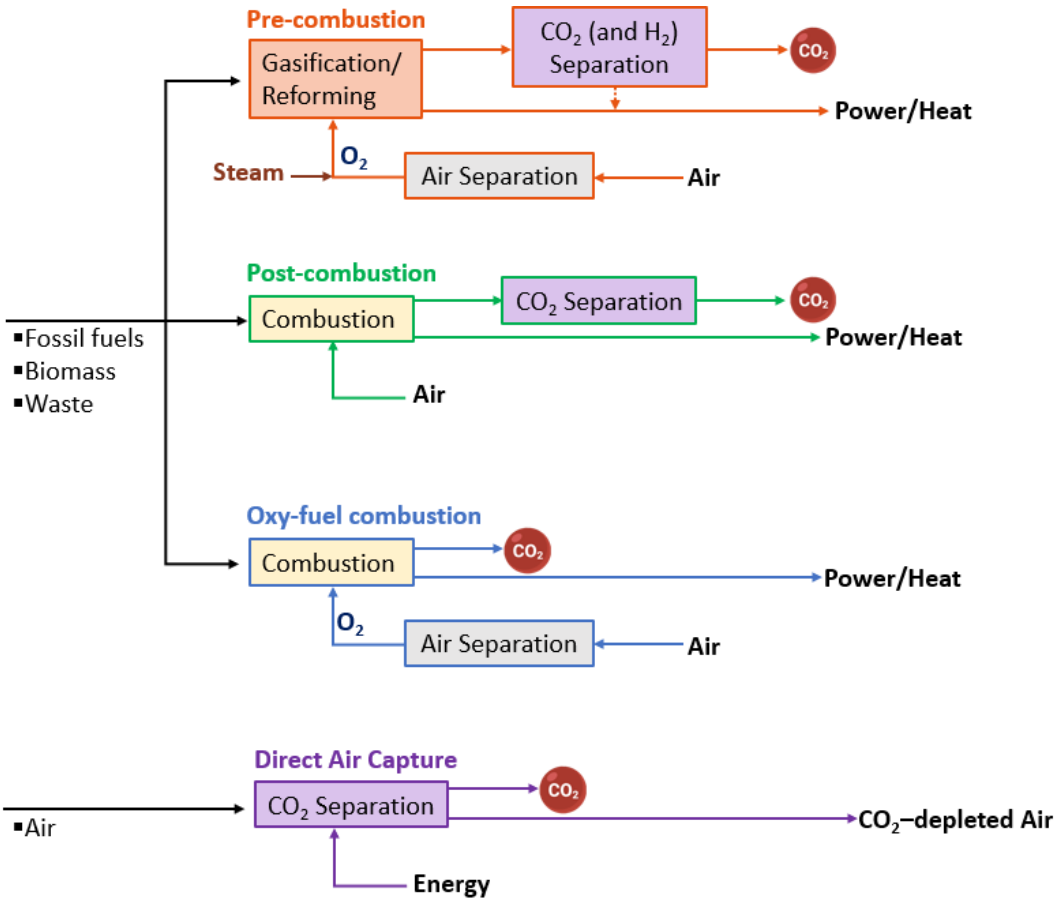


Figure 1. 3. Methods for capturing CO_2 from a gas stream, adapted by [34], [35].

Oxy-fuel combustion capture: it involves a flow of pure or enriched oxygen, often obtained from an air separation unit. This leads to extremely high temperatures (up to 2500 °C) in the combustion chamber, which require the use of durable and expensive materials. To partially solve this problem, part of the output flow is sent back to the input to dilute the supply and reduce the temperature inside the boiler. However, this method leads to a highly concentrated CO_2 exhaust flow that does not require further separation processes. The exclusion of nitrogen from the system also reduces the volume of exhaust gases by 75% and the production of NO_x by 66%. However, this method increases the concentration of fly ash, SO_2 and HCl, which could lead to corrosion in the combustion chamber [35].

In addition, concerning air separation unit, cryogenic air separation is typically favoured for producing highly enriched oxygen (around 95%) for oxy-combustion. However, alternative methods of oxygen production, including the use of polymeric, ceramic, or composite membranes, have also been explored [35].

Pre-combustion capture: it requires the gasification of the fuel into syngas, a mixture of CO and H_2 with variable concentrations, obtained through the reaction of the fuel with steam and oxygen [36]. The nearly pure oxygen required is produced through an air separation process, which may include cryogenic distillation, membrane separation, or adsorption on activated carbons or zeolites [35], [37]. Subsequently, gasification is typically followed by the water gas shift reaction of syngas, catalytically converting the produced CO into CO_2 and hydrogen. At the end of this stage, the CO_2 involves undergoing a physical or chemical absorption process, leading to the production of hydrogen-rich fuel applicable in various uses, including boilers, furnaces, gas turbines, engines, and fuel cells to generate electrical energy. Typical examples of this process include integrated gasification combined cycle plants (IGCC), where coal is transformed into syngas before combustion [36], and integrated gasification fuel cell plants (IGFC), where the synthesis gas, purified from contaminants, is fed into a solid oxide fuel cell (SOFC) for electricity generation [34], [35]

Direct Air Capture (DAC): eliminates the necessity of capturing CO_2 exclusively from point sources, contributing directly to reducing atmospheric CO_2 levels. To achieve this, the technologies used for the direct separation of CO_2 from the air are the same as those employed in post-combustion processes, described in more detail below. Because of the extremely low CO_2 concentration in the atmosphere, effective materials with high affinity and selectivity for carbon dioxide, as well as a significant energy input, are required [35]. As a result, the technology comes at a high cost, estimated to be between \$125 and \$335 per ton of CO_2. According to the International Energy Agency (IEA), Direct Air Capture (DAC) technology will be critical in achieving Net Zero Emissions (NZE) by 2050. This assumes capturing 85 $MtCO_2$ by 2030 and 980 $MtCO_2$ by 2050, a significant increase from the current 0.01 $MtCO_2$. According to IEA projections, the potential for lowering separation costs to less than \$100/tCO_2 due to technological advancements and increased interest from both public and private investors could ease this transition [38].

Post-combustion capture: in contrast to previous examples, removes carbon dioxide from the nitrogen-rich exhaust gases only after the combustion process is complete and before the gases are released into the atmosphere. Many technological options are available depending on the composition and volume of the exhaust gas stream. These options are detailed below [35].

Absorption: Among the separation technologies that can be implemented, one possibility is certainly absorption. It can be distinguished into:

Chemical Absorption: a neutralization reaction occurs between the CO_2 molecule in the gas stream and the molecule of the absorbing agent; in this case the choice of solvent is crucial and must possess some essential properties: high absorption capacity, high reactivity towards CO_2 to reduce the solvent flow rate sent to the column for separation; thermal and chemical stability to limit solvent consumption; low environmental impact and low cost. Given the slightly acidic nature of the CO_2 molecule, typical solvents used are strong alkaline solutions (KOH, NaOH) or weak ones (alcoholic amines such as MEA, DEA, TEA, or $NH_3 \cdot H_2O$), each with advantages and disadvantages. For example, strong alkaline solutions are rarely used due to corrosion issues, while ethanolamines, despite their excellent absorption capacity, require high regeneration energies due to their volatility and are easily degraded by O_2 and SO_2, typically present in exhaust gases. Additionally, amine solvents are not very stable and tend to form compounds, such as nitrosamines, carcinogenic and harmful to humans even at low concentrations. An alternative to these solvents, still under study and investigation, could be ionic liquids, characterized by almost negligible vapor pressures at room temperature (on the order of 9-10 bar) [39], making them non-volatile. This implies a low tendency to vaporize, reducing solvent losses and eliminating atmospheric contamination. Moreover, they are characterized by high thermal and chemical stability, allowing degradation at temperatures above 300 °C, and the absence of corrosive phenomena. However, conventional ionic liquids are not yet a promising alternative to amine solutions, as they possess significantly lower absorption capacities. To overcome these issues, attention is being paid to new "functionalized" ionic liquids, equipped with specific functional groups, such as amino groups, that show affinity for CO_2 and are capable of chemisorbing it. Initial experimental results have shown that the reaction mechanism between these molecules and CO_2 is the same as with organic amines and that these systems are able to reduce the energy consumption of the separation process compared to the conventional process with MEA [39]. However, this is still a relatively immature technology that requires further study.

Physical Absorption: the process is related to the solvent's ability to promote gas solubilization. It requires high partial pressures of CO_2 in the gas stream, to the point that the process becomes economically unsustainable when it is at values below 15% of the total pressure. Since this process is linked to the gas solubility in the liquid solvent, governed by Henry's law, the phenomenon is indeed influenced by the partial pressure of the gas to be removed and the temperature at which the process takes place: regulating the partial pressure to higher levels and lowering the temperature, both contribute to an increase in the solubility of CO_2 in the sorbent. Typical examples of physical absorption processes are Rectisol, which uses a cold stream of methanol, and Purisol, which instead uses N-methyl-2-pyrrolidone as a solvent: both are processes that achieve good results, but use toxic and irritating solvents [35].

Adsorption: is a selective process in which molecules in a liquid or gaseous stream adhere to the surface of a solid, known as an adsorbent, such as zeolites. The adsorption capacity strongly depends on the structure and composition of zeolites, including pore size and deposited cations. However, it also depends on the size, shape, and polarity of the gas molecule to be separated. For instance, as CO_2 is weakly acidic, zeolites with alkaline cationic sites can be employed for separation [35].

To regenerate the material, the temperature of the system can be increased, as the adsorption process is exothermic. Industrially, the process is conducted cyclically, alternating between adsorption and regeneration phases. This necessitates at least two columns operating in parallel. These processes can be categorized into two groups based on how the adsorbent is exchanged between adsorption and desorption steps: pressure swing adsorption (PSA), occurring due to pressure variation (typically at pressures higher than atmospheric for adsorption and at atmospheric pressure or under vacuum for desorption); temperature swing adsorption (TSA), occurring due to temperature variation [35].

Membrane Separation: membranes enable the selective permeation of a specific gas, such as CO_2, from a gas stream due to the size of its molecules or its chemical affinity with membrane materials (polymeric, metallic, ceramic). In the latter case, this is made possible, for example, by impregnating the membrane with a scrubbing solution or equipping it with functional chemical groups (e.g., amines) selective towards carbon dioxide. The driving force of the process is the pressure difference of the gaseous species on either side of the membrane wall; the greater the difference, the smaller the area required for separation, and consequently, the

lower the investment cost. These systems certainly have advantages: no regeneration energy is required, no waste streams are generated, high packing density minimizes the installation volume [35].

Cryogenic Distillation: is a process of fractional distillation at low temperatures (below -73.3 °C to facilitate the liquefaction and separation of CO_2) of a gas stream, with the potential to recover 90-95% of the CO_2 in the feed [35]. Such temperatures can be achieved by operating a closed-cycle refrigeration system, typically consisting of a compressor, an isoenthalpic valve (or Joule-Thompson valve, JTV), and a system of heat exchangers [40]. Once the gas stream is liquefied, it can be sent to a distillation column to separate the different components based on their boiling temperature.

1.2.2 CO_2 Storage

One of the early mitigation strategies that the scientific community has explored in past years is storage, although issues related to feasibility and long-term consequences were highlighted from the outset. Some possibilities include storing CO_2 in underground geological formations (depleted gas and oil reservoirs, saline aquifers), injection into the seafloor, or chemical conversion into thermodynamically stable minerals. However, the first two options, due to the potential for leaks from reservoirs (either sudden during injection or gradual due to fractures that may occur in the well) or ocean acidification leading to an imbalance in the marine ecosystem, have seen limited adoption by the scientific community. Another method for storing CO_2 could involve its mineralization (or non-geological storage): the production of stable mineral carbonates obtained by treating carbon dioxide with metallic oxides of calcium and magnesium. It is a process that naturally occurs, but is thermodynamically favorable yet kinetically slow. This limitation can be partially overcomed by using concentrated CO_2 and operating at high temperatures, but it makes the process energetically intensive. This method allows for the capture and permanent storage of CO_2, but unlike other CCS systems, the final product is stable and secure [41].

1.2.3 CO_2 Utilisation

Concerning CO_2 utilisation processes, there are four different strategies [41].

1. **Mineralization**: CO_2 mineralization involves the production of stable carbonates by treating carbon dioxide with metal oxides such as calcium and magnesium oxides, which are abundantly present in the form of mineral silicates. The carbonation of magnesium and calcium silicates through spontaneous reaction with atmospheric CO_2 at ambient pressure and temperature is thermodynamically favoured, although kinetically limited. Injection of fluids with high CO_2 concentrations and an increase in temperature can accelerate the kinetics [41].

2. **Desalination**: Carbon dioxide can be used for the removal of total dissolved solids (TDS) and to transform brine into potable water. When seawater, mixed with ammonia, is exposed to CO_2, the formation of Na_2CO_3 and NH_4Cl occurs, which precipitate to the bottom and can be easily separated. NH_4Cl can be recycled through thermal treatments with calcium oxide or can be directly used as a raw material for ammonia and chlorine synthesis [41].

3. **Enhanced oil/gas recovery (EOR/EGR):** refers to a procedure where a substance (in this case, carbon dioxide) is injected into a reservoir to push the oil to the surface and reduce its viscosity [41]. It is estimated that EOR allows the recovery of about 10-20% of the originally present oil from a depleting well. This is possible because the injected CO_2, at well pressures, reaches a supercritical state, becoming highly miscible with crude oil. As a result, viscosity and surface tension with the rocks containing the crude oil are reduced. At the end of the process, approximately 50-75% of the injected CO_2 is recovered from the extracted crude oil and returned to the reservoir where it remains trapped [42].

4. **Chemical conversion:** the conversion of CO_2 into fuels and other valuable products is considered the best utilization strategy. Methane, methanol, syngas, and higher (C_{2+}) hydrocarbons, including alkanes, alkenes and aromatics are some of the compounds that can be produced using captured CO_2 as a feedstock. Since CO_2 is a thermodynamically stable molecule, its utilization requires a significant energy expenditure and the use of an efficient catalyst to achieve high yields. In this context, the thermocatalytic hydrogenation of CO_2 is very promising, mainly because this chemical process involves the transformation of CO_2 into valuable compounds such as synthetic fuels and chemicals [43]. This approach holds promise due to its rapid reaction rates, enabling large-scale production [44]. In spite of this process requires a

significant amount of energy, it offers the opportunity to recycle carbon dioxide, produce synthetic fuels, and address the issue of renewable electricity storage. Furthermore, this predominantly involves hydrogenation reactions that can yield products such as CO, CH_4, and CH_3OH, Eq. (1. 1), (1. 2) and (1. 3).

$$CO_{2(g)} + H_{2(g)} \rightleftharpoons CO_{(g)} + H_2O_{(g)}, \qquad \Delta H^{\circ}_{298} = 42.1\ \text{kJ·mol}^{-1} \quad (1.\ 1)$$

$$CO_{2(g)} + 3H_{2(g)} \rightleftharpoons CH_3OH_{(g)} + H_2O_{(g)}, \qquad \Delta H^{\circ}_{298} = -49.9\ \text{kJ·mol}^{-1} \quad (1.\ 2)$$

$$CO_{2(g)} + 4H_{2(g)} \rightleftharpoons CH_{4(g)} + 2H_2O_{(g)}, \qquad \Delta H^{\circ}_{298} = -113\ \text{kJ·mol}^{-1} \quad (1.\ 3)$$

Each of these equilibrium reactions is of interest to the petrochemical industry. However, these reactions at a given temperature can be further complicated by other equilibria that occur in parallel. Another alternative is to use CO_2 as a feedstock for the production of a wide range of chemicals. Key applications include urea production, inorganic carbonates, formic acid, polyurethanes, acrylic acid and acrylates, and polycarbonates [41]. Anyway, since the focus of this doctoral thesis is on the chemical conversion of CO_2 into fuels, the overall reaction will be thoroughly examined in the following section 1.4. To ensure the sustainability of this process, the hydrogen used as a reactant should be green hydrogen (Paragraph 1.3), meaning it is produced, for example, through water electrolysis using renewable energy sources such as solar and/or wind energy. Additionally, in thermocatalytic processes, effectively managing heat, depending on the endothermic/exothermic nature of each reaction, and addressing catalyst deactivation are challenges that require innovative designs of reactors and nanostructured heterogeneous catalysts that are highly active, stable, and cost-effective [45], [46].

1.3 Green H_2 Production

The utilization of renewable energy sources for hydrogen production is crucial in the effort to decrease CO_2 emissions, yielding high-value fuels and chemicals. First on the periodic table and most prevalent element on Earth, hydrogen makes up between 70-80 % of the observable universe. Even though it is widely distributed, hydrogen only makes up 0.88 wt. % of the elements in the Earth's crust, making it ninth among them [47], [48]. Under normal circumstances, it

exists as a diatomic gas that is highly flammable, colorless, and odorless. The energy content of hydrogen is high (120 $MJ \cdot kg^{-1}$), making it a very reactive molecule [48].

$$H_{2(g)} + \frac{1}{2}O_{2(g)} \rightarrow H_2O_{(g)}, \qquad \Delta H^{\circ}_{298} = -286\ kJ \cdot mol^{-1} \quad (1.4)$$

As demonstrated by the reaction and its standard enthalpy Eq. (1. 4), hydrogen combustion is an extremely exothermic process that releases a significant amount of energy. The only substance released into the atmosphere by this reaction is water vapor, making hydrogen an outstanding clean fuel. Unfortunately, the high flammability of hydrogen presents problems for transportation, storage, and safety. It also increases the risk of tank leaks due to the high cost of compressing hydrogen at extremely high pressures.

The technologies and processes used in the production of hydrogen must be carefully evaluated if the intention is to use it to help reduce CO_2 emissions. According to the International Energy Agency (IEA), until 2019, 76% of the hydrogen produced globally came from natural gas steam reforming, 23% from coal gasification, and 2% from water electrolysis. This strategy has resulted in an increase in emissions of 830 $MtCO_2$/year [49].

It is evident that using grey hydrogen, made from fossil fuels through processes like natural gas reforming or coal gasification (which produce CO_2), only covers up the problem without solving it. In fact the *Steam Reforming of Methane* is an endothermic process that requires the use of steam and external energy. Since hydrocarbons use less energy than water electrolysis, which requires 242 MJ/kmol H_2 for electrolysis against 41.28 MJ/kmol H_2 for methane steam reforming, hydrocarbons are the main source of hydrogen on an industrial scale [47]. In addition, when hydrogen is produced, also synthesis gas (syngas) is generated, Eq. (1. 5). It is a mixture of CO and H_2 that can be processed further to produce a hydrogen-rich stream. Natural gas Steam Reforming (SR) is the method most frequently employed. Prior to being used in any further processing, natural gas is treated to remove sulfur compounds, which include pollutants and catalyst poisons. This is done by either hydrodesulfurization, which involves hydrogen and a molybdenum oxide-based catalyst, if the sulfur-containing load is organic in nature, or desulfurization, which involves zinc oxide if only H_2S is present. Methane and water vapor are mixed and preheated in the convective section of the reforming reactor. At this point, they enter the radiant section, inside tubes, where

they react at high temperatures (800-900 °C) in the presence of a nickel oxide catalyst on alumina. The overall *Steam Reforming reaction* is:

$$CH_{4(g)} + H_2O \rightarrow 3H_{2(g)} + CO_{(g)}, \qquad \Delta H^{\circ}_{298} = 205.8 \ \text{kJ·mol}^{-1} \qquad (1.\ 5)$$

When the reactor is operating with excess steam and short residence times below 700 °C, the ratio of the amount of hydrocarbons fed to the amount of water is crucial for suppressing carbon-forming reactions, like the *Boudouard reaction,* Eq. (1. 6), resulting in the deposition of coke on the catalyst surface:

$$2CO_{(g)} \rightarrow CO_{2(g)} + C_{(s)}, \qquad \Delta H^{\circ}_{298} = -172.54 \ \text{kJ·mol}^{-1} \qquad (1.\ 6)$$

However, the *Water Gas Shift (WGS) reaction,* Eq. (1. 7) also takes place consecutive to the reforming reaction:

$$CO_{(g)} + H_2O_{(g)} \rightarrow CO_{2(g)} + H_{2(g)}, \qquad \Delta H^{\circ}_{298} = -42.1 \ \text{kJ·mol}^{-1} \qquad (1.\ 7)$$

It is an exothermic reaction that leads to the production of carbon dioxide and hydrogen and can be catalyzed by many metal oxides. To ensure that the reaction between carbon monoxide and steam is complete, the shift reaction is conducted in two steps, the first at high temperature within a range of 300 to 500 °C, and the second at 200 °C. The output from the low-temperature WGS reactor is fed to the purification section to remove residual carbon monoxide (<10 ppm), methane, and nitrogen, resulting in a hydrogen stream with a purity exceeding 99% [50].

However, as anticipated before (Paragraph 1.2.3), it is important to highlight that the aim should be to use green hydrogen, produced by water splitting using renewable electricity, according to the reactions shown in Eq. (1. 8), (1. 9) and (1. 10).

Anode: $$H_2O \rightarrow \frac{1}{2}O_2 + 2H^+ + 2e^- \qquad (1.\ 8)$$

Cathode: $$2H^+ + 2e^- \rightarrow H_2 \qquad (1.\ 9)$$

$$\text{Overall reaction: } H_2O_{(l)} \rightarrow H_{2(g)} + \frac{1}{2}O_{2(g)},\ \Delta H^{\circ}_{298} = +285.83\ \text{kJ·mol}^{-1} \quad (1.\ 10)$$

According to the IEA, in order to handle future production peaks, it is imperative that numerous sectors be electrified and that storage systems be installed [49].

Throughout the years, several electrochemical systems have been engineered to facilitate water electrolysis, including alkaline electrolyzers (AEL), proton exchange membrane (PEM) technologies, and solid oxide electrolyzers (SOE):

Alkaline Electrolyzers (AEL): operating at low temperatures (60-80 °C), these systems utilize an aqueous solution of KOH and/or NaOH as an electrolyte, along with nickel electrodes. The electrodes are submerged in the electrolytic solution and separated by a semi-permeable membrane that permits the transport of ions. Furthermore, to eliminate the generated gas bubbles and disperse heat, the solution undergoes constant recirculation. Eq. (1. 11) and (1. 12) show the reactions taking place in each cell:

$$\text{Anode: } 2OH^- \rightarrow \frac{1}{2}O_2 + H_2O + 2e^- \quad (1.\ 11)$$

$$\text{Cathode: } 2H_2O + 2e^- \rightarrow H_2 + 2OH^- \quad (1.\ 12)$$

As seen in these reactions, water is utilized at the cathode and generated at the anode. Consequently, it becomes necessary to blend the hydroxide currents from both semi-cells to prevent electrolyte concentration at the cathode and dilution at the anode. This mixing process may lead to electrolyte stream contamination with dissolved gases, potentially resulting in the creation of flammable mixtures.

Regarding performance, this technology allows for the production of highly pure hydrogen and oxygen streams, reaching approximately 99.5-99.9 % and 99-99.8 %, respectively. The associated electrical consumption ranges from 4.5-5.5 kWh/Nm^3 of hydrogen produced, with an efficiency of around 60-70 % [51].

Proton Exchange Membrane (PEM): in PEM electrolyzers, a membrane (such as Nafion®) is employed to separate the two half-cells, and the electrodes are directly affixed to it. Given the acidic operating environment, it is imperative to utilize noble metals for the electrodes, generally iridium for the anode and

platinum for the cathode. Water is fed to the anode, comes into contact with the electrode surface, and splits, producing protons and electrons while releasing molecular oxygen. Electrons travel through an external circuit, which typically includes a renewable electric power source, providing the potential difference required between the anode and cathode to drive electrolysis. Protons, on the other hand, traverse the polymeric membrane and reach the cathode, where they recombine with electrons to produce molecular hydrogen [50]. The key benefit of these systems is attributed to the polymeric electrolyte membrane employed. Its permeability guarantees a hydrogen current purity exceeding 99.99 % post-drying. Additionally, the physical characteristics of the membrane enable the development of compact modules capable of operating at high current densities. Performance-wise, these systems achieve levels akin to alkaline electrolyzers, with an electrical consumption ranging 4.4-5 kWh/Nm^3 of hydrogen produced and an efficiency of 60-68% [52].

Solid Oxide Electrolyzers (SOE): unlike alkaline electrolyzers, solid oxide electrolyzers function at elevated temperatures (700-900 °C). While this enables higher efficiencies, it introduces considerable challenges in selecting suitable materials for construction. Water or steam is preheated using the hot products exiting the cell and is then directed to the cathode, where it undergoes partial conversion into hydrogen. This system functions by generating the O^{2-} ion at the cathode, which can then be transferred to the anode through the use of a ceramic membrane serving as an electrolyte. This leads to the reactions sequence given on Eq. (1. 13) and (1. 14):

$$\text{Anode: } 2O^{2-} \rightarrow O_2 + 4e^- \quad (1.\ 13)$$

$$\text{Cathode: } H_2O + 2e^- \rightarrow H_2 + O^{2-} \quad (1.\ 14)$$

Notable advantages of this approach include increased reaction rates and the capacity to integrate heat, utilizing the energy released from subsequent exothermic processes following electrolysis. Examples of such processes include the synthesis of methanol, DME, Fischer Tropsch Synthesis (FTS), or even the co-electrolysis of steam and CO_2 to produce syngas for producing synthetic fuels. This leads to a noteworthy 20-30% reduction in the voltage required for water molecule dissociation compared to the previously discussed technologies, resulting in decreased operational costs [53].

1.4 Efforts to reduce CO_2 Emissions through the Production of Liquid Hydrocarbons: Potentials and Limitations

As previously mentioned in Paragraph 1.1, the thermocatalytic conversion of CO_2 into hydrocarbons is a promising technology for producing hydrocarbons, aromatics, and olefins, providing an attractive route to generate fuels (C_{2+}) and an intriguing perspective in the battle against CO_2 emissions and CO_2 circularity. Lightweight olefins such as ethylene, propylene and butylene are essential ingredients used in the chemical industry, in the production of plastics, textiles and other chemicals. Indeed, aromatics serve as crucial starting points for the synthesis of polymers, medicines and petrochemicals. It is clear that this strategy not only fosters the development of sustainable pathways for value-added chemical production, but also helps reduce dependence on fossil sources, aligning with environmental and economic sustainability objectives [54].

Nevertheless, it is important to thoroughly examine both the positive aspects and limitations of converting CO_2 into value-added products. Achieving continuous scientific advancements is crucial to optimize the potential of this technology and navigate the challenges encountered during its implementation.

On one side, the potential benefits of this approach are substantial. One of the primary potentials of liquid hydrocarbon production from CO_2 is carbon recycling. It involves the capture and utilization of CO_2 from different sources to decrease its overall impact on atmospheric CO_2 levels. This approach contributes to mitigating the effects of climate change. Additionally, the industrial-scale adoption of the CO_2 hydrogenation process, producing various products like MeOH, CO, DME (dimethyl ether), is widespread across many countries. Carbon Recycling International initiated the first industrial plant in Iceland, utilizing geothermal energy to produce methanol from CO_2 [55]. This connection is closely related to the energy storage potential. In fact, liquid hydrocarbons derived from CO_2 represent an effective means of energy storage, particularly advantageous for managing the surplus of renewable energy from sources such as solar and wind [56], [57], [58], **Figure 1. 4**.

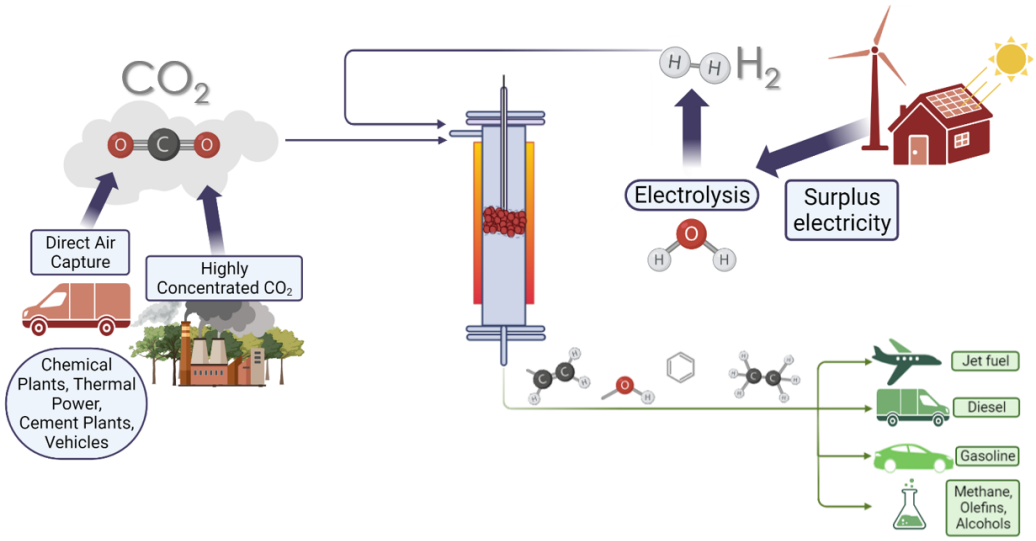


Figure 1. 4. Schematic production of fuels from CO_2 hydrogenation.

In this process, excess energy is utilized for hydrogen production through water electrolysis, which, when reacted with CO_2, is subsequently converted into synthetic fuels like methane (Power-to-Gas) [56], [59], [60], methanol [61], [62], [63], dimethyl-ether [64], [65] and hydrocarbons (Power-to-Liquid) [1], [66], [67], [68], [69], [70], [71], demonstrating how the hydrogenation of CO_2 is highly versatile. In particular Power-to-Liquid is one viable option for medium-term energy storage. In contrast to gaseous goods, which need to be compressed or liquefied, liquid products are easier to carry and store, having a higher energy density per unit volume and losing less material over time in storage [1]. In addition, liquid fuels can be integrated into an industrial sector without significant investments or technical revolutions because they are compatible with the existing infrastructure [1], presenting a promising solution to energy shortages and global environmental pollution [72]. Lastly, fuels obtained from CO_2 often contain lower sulfur and aromatic compound content, making them cleaner and more environmentally friendly.

To sum up the potentials, the conversion of CO_2 into liquid hydrocarbons can yield high-value products, including synthetic fuels and chemicals. This form of storage proves more practical for conservation and transportation compared to electricity. Moreover, these hydrocarbons can be used to generate energy, thus contributing to reducing dependence on fossil fuels [55], creating economic opportunities and diversify industries while simultaneously addressing environmental concerns.

Conversely, it is vital to recognize the limitations associated with this technology. First of all the thermodynamic stability of CO_2 poses significant catalytic challenges. It has a high Gibbs energy (ΔG^0 = -396 kJ/mol), meaning that substantial energy is needed to overcome the conversion barriers [73], [74], [75], [76]. Developing efficient and cost-effective catalysts for this process is a significant challenge. In this scenario, researchers have explored traditional Fischer-Tropsch synthesis (FTS) catalysts based on Fe, Co, Ni, and Ru [65], [70], [77], [78] or the purpose of CO_2 hydrogenation into hydrocarbons. Notably, Ni- and Ru-based catalysts exhibit notable efficiency in CH_4 production [79], [80], although generating only limited quantities of C_{2+} hydrocarbons [1]. Furthermore, CO_2 is the most oxidized state of carbon, with an oxidation number of +4. This implies that for its conversion into more energetic chemicals, electron transfers are necessary to reduce its oxidation state [76]. Other challenges include high energy demands for driving endothermic reactions. This can be a limitation, especially if the energy used is derived from non-renewable sources. For the process to be environmentally sustainable, it is essential to use renewable and low-carbon energy sources [28]. Another factor to take into account is the deactivation and regeneration of catalysts, which continue to be a problem in terms of industrial implementation [81]. In addition, the energy-intensive nature of CO_2 conversion and the need for high-quality catalysts can result in significant operating costs. These costs must be managed effectively to ensure the economic viability of the process [28]. Furthermore, it is crucial to thoroughly evaluate the environmental impact of the entire production process with the goal of reducing CO_2 emissions, while avoiding the introduction of further environmental issues [28].

In the process of transforming CO_2 into hydrocarbons through hydrogenation, it is crucial to recognize the existence of two distinct pathways: a direct route and an indirect one. The hydrogenation of CO_2 into liquid fuels can be achieved through either of these pathways, as illustrated in Figure 1. 4. The indirect approach necessitates the use of two separate reactors. In the initial reactor, CO_2 and H_2 can be initially converted into CH_3OH or CO (depending on the catalyst), which are subsequently transformed into hydrocarbons in a second step or reactor [1], [82]. On the contrary, the direct pathway may offer economic advantages compared to the indirect one, owing to the utilization of a single reactor. The direct conversion process involves the coupling of the endothermic reverse water gas shift (RWGS) reaction and the exothermic Fischer-Tropsch synthesis (FTS) within the same catalytic particles. In addition, in the direct pathways, CO_2 undergoes conversion into CO through the endothermic RWGS reaction (equation 1.15), followed by its hydrogenation into hydrocarbons via

exothermic Fischer-Tropsch synthesis (FTS) as outlined in equations (1.16), (1.17) and (1.18) [54], [78], [83], [84].

$$CO_2 + H_2 \rightleftharpoons CO + H_2O \qquad \Delta\tilde{H}^0_{298K} = +41\ kJ\ mol^{-1} \qquad (1.15)$$

$$2CO + 4H_2 \rightleftharpoons C_2H_4 + 2H_2O \qquad \Delta\tilde{H}^0_{298K} = -210\ kJ\ mol^{-1} \qquad (1.16)$$

$$n\ CO + 2n\ H_2 \rightarrow C_nH_{2n} + n\ H_2O \qquad (1.17)$$

$$n\ CO + (2n+1)\ H_2 \rightarrow C_nH_{2n+2} + n\ H_2O \qquad (1.18)$$

Therefore, the equilibrium of the RWGS reaction can be influenced by the utilization of CO in the FTS for the production of hydrocarbons [54]. This process is commonly referred to CO_2-FTS, that is an extension of the traditional Fischer-Tropsch process, where CO_2 is used as a feedstock alongside syngas (a mixture of CO and H_2) for the production of liquid hydrocarbons and generally known as modified Fischer-Tropsch synthesis (Figure 1. 5) [70], [75]. The primary products obtained from CO_2-FTS include olefins, paraffins, and naphthenes, while some oxygenates such as alcohols, carboxylic acids, and aldehydes serve as by-products [1].

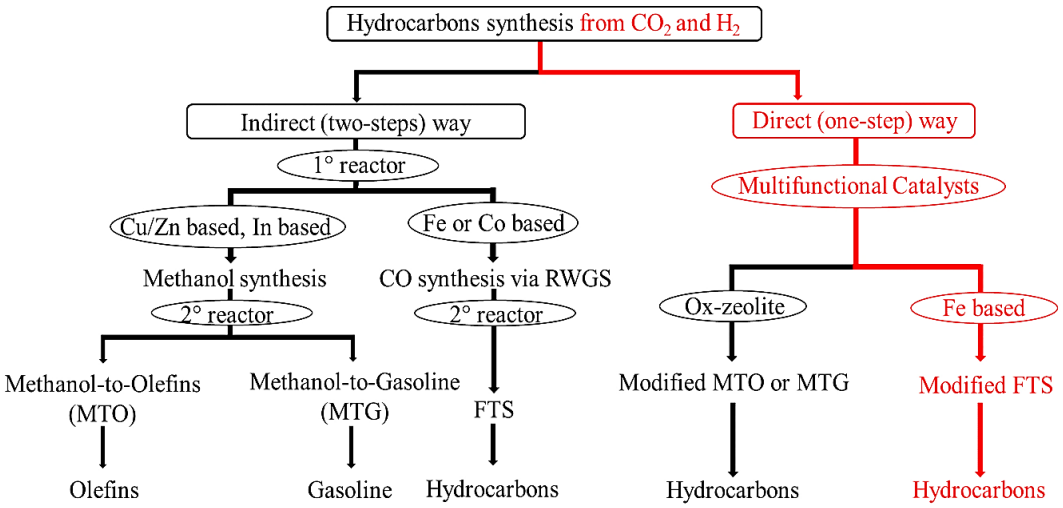


Figure 1. 5. Different ways to hydrogenate CO_2 to hydrocarbon final products [1].

Among all the catalysts investigated for CO_2-FTS, Fe-based catalysts have been studied extensively for their high activity and stability in hydrocarbons production have shown the most potential [85]. They are particularly attractive due to their capability in directly converting CO_2 into fuels. Therefore, efforts are still underway to improve the catalytic performance of Fe-based catalysts by

incorporating promoters. In the following sub-paragraphs, all these aspects will be thoroughly examined and analyzed.

1.4.1 Catalysts for Fischer Tropsch Synthesis from CO_2

Catalysts for CO_2-FTS are crucial components in the production of liquid hydrocarbons and are responsible for facilitating the chemical reactions involved. These catalysts are essential for controlling reaction rates, product selectivity, and overall process efficiency. The FTS from CO_2 typically employs heterogeneous catalysts, which are solid materials that facilitate the reaction without being consumed, lowering the activation energy. As anticipated before in paragraph 1.4, common catalysts for FTS include iron (Fe), cobalt (Co), and ruthenium (Ru). However, Cobalt-based catalysts are widely used and have good activity and selectivity for hydrocarbon production in traditional FTS. Below, an overview of the catalysts used in the process (**Figure 1. 6**):

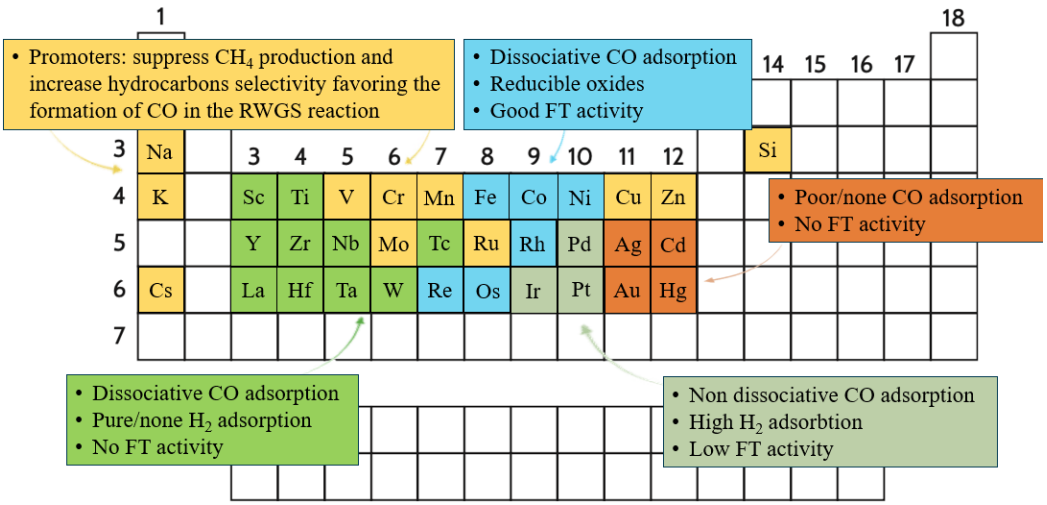


Figure 1. 6. Catalysts used for CO_2-FTS, adapted by [70], [77], [78].

Researchers are continually exploring new catalyst formulations and support materials to improve the conversion of CO_2 and H_2 into valuable hydrocarbons. The selection of catalysts and their properties significantly impact the success and commercial feasibility of these technologies. The choice of catalyst and reaction conditions can influence the product distribution, determining the mix of

hydrocarbons, from light gases to waxes and liquid fuels. Catalysts should be designed to promote the selective formation of hydrocarbons, particularly higher-value liquid hydrocarbons, while minimizing undesirable by-products. Additionally, the challenge of finding an efficient catalyst for CO_2 hydrogenation stems from the necessity for it to be active in both the RWGS and FTS reactions. This is the primary reason why iron-based catalysts are preferred over their counterparts Co, Ni, and Ru. Iron catalysts exhibit superior RWGS activity and slightly higher selectivity for C_{2+} hydrocarbons in the FTS reaction compared to when other transition metals are used. Indeed, some iron-based catalysts have demonstrated exceptional capability in CO_2 hydrogenation, resulting in lower selectivity towards methane. The predominant products are olefins, especially light olefins (C_2-C_4), followed by paraffins. Additionally, smaller quantities of oxygenated products, mainly alcohols, have also been observed. However, there are challenges that need to be addressed for potential industrial applications, including catalyst formation, the need for binders, and the inhibitory effect of water. It's worth noting that iron-based catalysts typically operate at higher temperatures, ranging between 260 and 320 °C, compared to, for example, cobalt-based catalysts that operate in the range of 220-260 °C. However, it should be added that cobalt-based catalysts, commonly used in FT applications with syngas, are less suitable for reactions with CO_2. In fact, they exhibit significant inactivity in the WGS and RWGS reactions, acting as methanation catalysts. Consequently, cobalt-based catalysts in CO_2 hydrogenation show increased selectivity towards methane and short-chain hydrocarbons compared to CO hydrogenation. On the other hand, Ni and Ru are well-suited for methane production [70], [77], [78].

It is widely acknowledged that the hydrogenation of CO_2 involves a two-step process to generate olefins, with Fe_3O_4 and χ-Fe_5C_2 (known as Hägg carbide) serving as active phases for the RWGS and FTS reactions, respectively. Typically, iron-based catalysts employed need to be activated before use, often through reduction in a controlled environment with hydrogen gas at higher temperature, generally higher than the reaction temperature. This process prepares the catalyst surface for the FTS reaction. In fact, the precursors of Fe-based catalysts consist of iron oxides like α-Fe_2O_3 or γ-Fe_2O_3, which undergo reduction by H_2 to form Fe_3O_4 or a combination of Fe_3O_4 and FeO during the reaction [86], **Figure 1. 7**.

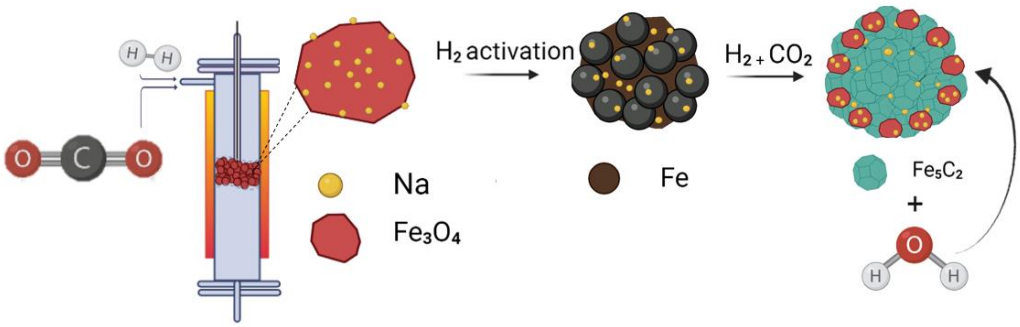


Figure 1. 7. Illustration of how an iron-based catalyst behaves during reduction and carburization treatment.

At this point, CO_2 undergoes conversion to CO through the RWGS reaction on Fe_3O_4 as reported in equation (1.15). Subsequently, CO transforms into -CH_2- groups as chain initiators and monomer units for the chain growth (FTS), as reported in equations (1.17) and (1.18) [87] on Fe_5C_2. The initial step involves the adsorption and activation of CO_2 on Fe_3O_4, leading to the formation of *CO_2. This *CO_2 then reacts with *H to create a *HOCO intermediate, which further dissociates into *OH and *CO. The *OH reacts with hydrogen to produce *H_2O, while *CO either desorbs or reacts with hydrogen via the FTS reaction to yield hydrocarbons. Additionally, *CO can dissociate into *C and *O, and a portion of the *C diffuses into the crystal lattices of Fe metal, resulting in the formation of iron carbides (FeC_x) phases under various reaction conditions, such as Fe_7C_3, χ-Fe_5C_2, θ-Fe_3C, etc. Furthermore, some of the *CO undergoes hydrogenation to form *HCO. This is followed by subsequent hydrogenation, dissociation, and dehydration to generate *CH_2. Ultimately, these processes contribute to the production of hydrocarbons through chain growth [86]. Of course, to achieve high selectivity of light olefins, the carbon chain growth reaction needs to be effectively controlled [83]. A simplified scheme of the process is illustrated in Figure 1. 8.

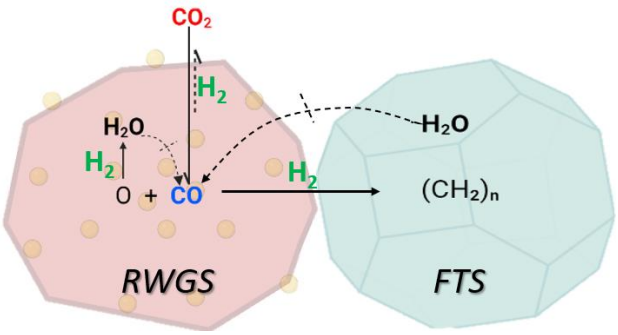


Figure 1. 8. Hydrogenation of CO_2 to olefin on Fe-based catalysts.

1.4.1.1 Promoter Effects on Fischer Tropsch synthesis

Promoter effects on Fischer-Tropsch synthesis (FTS) refer to the influence of certain additives, known as promoters, on the activity, selectivity, and overall performance of FTS catalysts. Promoters are generally introduced into the catalyst formulation to enhance specific aspects of the FTS process. Their role is to improve the efficiency of the catalyst in producing desired hydrocarbon products and controlling the reaction. The introduction of promoters not only boosts the activity of CO_2 hydrogenation but also facilitates the formation of olefins, resulting in a modification of the product distribution. These promoters predominantly include alkali metals Na, K, and transition metals Zn, Mn, Cu, and Al. Specifically, alkali metals function as electron promoters, regulating the electron density on the Fe surface to adapt to the adsorption, dissociation, and desorption of reactants and intermediates [86]. In a broader context, they enhance the chemisorption of electron acceptors (CO_2 and CO) and hindering the adsorption of electron donors (H_2 and olefins). These modifications decrease hydrogenation activity, strengthen the Fe-C bond, increase chain growth, and inhibit the formation of CH_4 [88]. However, the roles of alkali metal promoters differ in terms of their ability to promote carbonization, diffusivity in the catalyst matrix, olefin selectivity, and hydrogenation capacity. Specifically, with an increase in atomic number, a decrease in selectivity for lower hydrocarbons and an increase for longer-chain hydrocarbons are observed. Concurrently, the ability to adsorb H_2 decreases with the higher atomic number, resulting in reduced hydrogenation capability and an increase in the O/P value [89], [90]. In addition, Na has been shown to reduce the particle size of Fe_2O_3 and Fe_3O_4, contributing to

a reduction in Fe_5C_2 particle size during CO reduction, which can enhance catalytic activity [91]. Another important advantage of Na is its lower hydrophilicity compared to potassium. This reduces the physical adsorption of H_2O on Na_2O, minimizing interference with CO adsorption on iron carbides, thereby improving the conversion rate [92]. In contrast, K, while promoting carbide formation and increasing the linear/branched hydrocarbon ratio, exhibits strong hydrophilicity that can hinder the effectiveness of the catalytic process [92]. Finally, the excessive use of both promoters can lead to issues such as reduced catalyst activity and increased surface alkalinity, which hampers olefin adsorption [92], [93], [94]. However, Na tends to have a less negative impact in this regard, making it a more balanced and stable choice compared to K for applications where long-term catalyst stability and efficiency are priorities. In contrast, Cu and Al serve as structure promoters, enhancing the dispersion of active metals. Meanwhile, Zn and Mn act as both electron and structure promoters, contributing to an enhanced catalytic stability [86].

1.4.1.2 Effects in CO_2-FTS of metal-oxide catalyst supported on inorganic substrates

The primary role of supports includes enhancing the dispersion of active metals and the stability of the catalyst, facilitating the adsorption of CO_2 and CO while impeding the adsorption of H_2. Additionally, supports play a crucial role in preventing the secondary hydrogenation of olefins, increasing the selectivity of olefins, and regulating the ratio of FeO_x to FeCx as well as the composition of FeC_x in Fe-based catalysts. Furthermore, supports contribute to the promotion and stabilization of active phases of FeC_x [95]. It is noteworthy that the structure and properties of supports exert a significant influence on catalyst activity, selectivity, and stability [86], [96].

The metal oxide catalysts chosen to catalyse the CO_2-FTS reaction could be supported on various inorganic substrates like alumina (Al_2O_3), silica (SiO_2), or titania (TiO_2), which provide a high surface area or catalytic activity. Another support that has found recent application is based on carbon nanotubes (CNT), which, thanks to their hydrophobicity, can avoid the migration of promoters, like sodium, when a zeolite is involved. The migration aspect will be fully discussed in chapters 3, 4, and 5, with experimental examples conducted during the PhD work and supported by the open literature.

1.4.1.3 Zeolite support effects on CO_2-FTS

Zeolites are crystalline microporous substances, known for their versatility, are also employed as adsorbents, ion exchangers, and catalysts in various chemical processes. They play a crucial role in the petroleum refining and petrochemical industries, serving as essential catalysts. It is important to highlight that zeolites are a crucial components of tandem catalysts in both discussed routes for CO_2 hydrogenation (Figure 1. 5), as they possess unique shape selectivity and acidity, enabling hydrocarbons oligomerization, isomerization, and aromatization. Figure 1. 9 illustrates the outcomes when a zeolite, specifically HZSM-5 with an MFI-type framework, is involved.

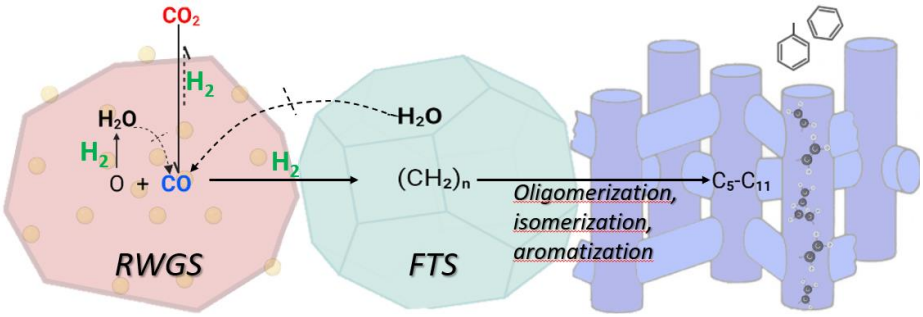


Figure 1. 9. Simplified conversion mechanism of olefins over acid sites of zeolites.

If a MFI zeolite is involved, lower olefins may undergo oligomerization (according to the hydrogen transfer mechanism) to produce olefins in the C_6-C_{10} range. Subsequently, the longer olefins can transfer their hydrogen to another olefin molecule, leading to the generation of dienes and paraffins. The dienes then form cyclic olefins via cyclization and undergo two hydrogen transfer steps, producing cyclic dienes and aromatics, as reported in the simplified equation (1.19). The occurrence of each hydrogen transfer step results in the formation of one paraffin molecule, which reduces the carbon utilization in terms of producing the desired chemicals (C_2-C_4 olefins and aromatics) [36], [97], [98], [99], [100]. Organic oxygen compounds obtained on the Fe-based catalyst, especially alcohols and ethers, can react on the acid sites of the zeolite, following the reaction pathway reported in the equations (1.20) and (1.21). To specify, equations (1.20) and (1.21) can lead to the formation of paraffins and olefins, respectively [101]. The latter may undergo further conversion to aromatic products on the acidic sites of the zeolite as previously mentioned. The capability of zeolite to transform light olefins

and alcohols intermediate products depends on the strongness of acid sites of the zeolite.

$$C_nH_{2n} \rightarrow \frac{1}{m}C_6H_6 + \frac{3}{m}\,C_nH_{2n+2} \qquad \text{where: } m = \frac{6}{n} + 3 \qquad (1.19)$$

$$C_nH_{2n+2}O \;\rightarrow\; C_nH_{2n+2} \;+\; H_2O + \;C \qquad (1.20)$$

$$C_nH_{2n+2}O \;\rightarrow C_nH_{2n} \;+ H_2O \qquad (1.21)$$

MFI zeolites with low Si/Al atomic ratio (lower than 10) could cause the over-cracking of heavy hydrocarbons due to their high acidity, leading to a decrease in selectivity towards liquid hydrocarbons in FT synthesis. On the contrary, zeolites with a high Si/Al ratio (greater than 100) are characterized by a lower concentration of acid sites, which is not beneficial for the oligomerization, isomerization, and aromatization of primary CO_2-FT products. HZSM-5 with a medium number of acid sites gives the possibility to obtain a gasoline-like product [102].

Therefore, the Si/Al atomic ratio for zeolites used in FT synthesis ranges typically between 40 and 80, which provides a balance between activity, selectivity, and stability of the catalyst. However, the optimal Si/Al ratio depends on the specific reaction conditions and the type of syngas used in the process. Due to its larger average pore size, a hierarchical zeolite is able to enhance mass transport by enabling faster movement of reactant and product molecules through the catalyst, resulting in improved catalytic activity and selectivity. Additionally, the mesopores present in hierarchical zeolites offer better accessibility to active sites for intermediate products, thereby enhancing catalytic performance in reactions involving larger molecules. Moreover, the presence of mesopores helps to mitigate the diffusion limitations that can lead to catalyst deactivation in conventional zeolites [102], [103].

To sum up the choice of a specific zeolite can significantly impact the performance of FTS catalysts and the products distribution obtained. Researchers continue to investigate various zeolite materials and formulations to improve the production of liquid hydrocarbons and fine-tune catalysts for specific applications. Zeolite support effects on CO_2-FTS are not only part of ongoing research, but also of this PhD thesis and development efforts to enhance the efficiency and selectivity to specific target of product have to be made.

1.4.1.4 Migration of alkali promoters from oxide-phase to acid sites of Zeolite

The migration of alkali promoters can affect the reaction pathways and selectivity of the hydrogenation process. The presence of alkali species at acid sites can modify the surface properties of the catalyst, leading to changes in the adsorption, activation, and transformation of CO_2 and hydrogen. It is known that a short distance between the iron (-carbide) and the acid sites of a bifunctional catalyst system may facilitate migration of alkali metal ions from the iron (-carbide) catalyst towards the zeolite due to high mobility of alkali metal ions. This could not only lower the activity and selectivity of the FTO catalyst, but also neutralize the acid sites of the zeolite with alkali metal ions leading to a decreased selectivity to aromatization of olefins [104], Figure 1. 10. Understanding the migration of alkali promoters is important for optimizing catalyst stability. The redistribution of promoters during catalysis can impact the longevity and effectiveness of the catalyst over multiple reaction cycles. In the context of migration of alkali promoters like sodium (Na) from iron oxide to acid sites of zeolite during the hydrogenation of CO_2 to hydrocarbons, the process involves the dynamic movement of these promoters within the catalyst system. Under the reaction conditions, such as elevated temperatures and pressures typical in catalytic processes, sodium ions can migrate from the iron oxide phase to the acid sites on the zeolite catalyst. This migration is influenced by factors such as the affinity of sodium for acidic sites and the overall stability of the catalyst system. Sodium, being an alkali metal, can interact with the acid sites on the zeolite, modifying its acidic properties. The migration of sodium to acid sites can impact the catalytic activity and selectivity of the zeolite in hydrogenation reactions.

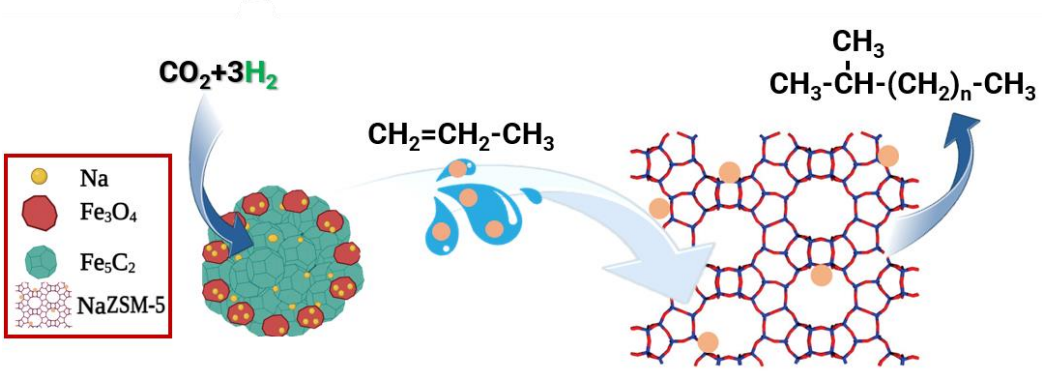


Figure 1. 10. Mechanism of Na migration.

The migration of sodium from iron oxide to acid sites can influence the selectivity of the catalyst. Depending on the specific reaction pathways involved in CO_2 hydrogenation, the presence of sodium on acid sites may favour or hinder certain reaction routes, affecting the distribution of hydrocarbon products. In fact, the problem associated with the migration of Na from iron oxide to acid sites of zeolite lies in finding a balance. While alkali promoters like sodium can enhance catalytic activity, their migration and accumulation on acid sites need to be controlled to prevent catalyst deactivation and maintain the desired product selectivity [105], [106], [107], [108].

In recent years, researchers have sought to address this issue by designing catalysts with optimal properties. In this thesis, the problem was approached by studying the effect of hydrophobic supports. The goal is to achieve better control over the migration and impact of alkali promoters during CO_2 hydrogenation. For this reason, Chapters 4 and 5 will present the results obtained using Carbon Nanotubes (CNTs) with the aim of mitigating the migration of sodium (Na) from iron to zeolite in catalytic systems. As demonstrated, the use of CNTs as a support offers several benefits that contribute to better stability and control over catalyst performance.

1.5 Structure and Aim of the Work of the Doctoral Thesis

As extensively discussed in this introduction, substantial efforts must be made to reduce CO_2 emissions in order to address climate change and address the energy crisis. These challenges can be tackled through the production of liquid hydrocarbons, which is the core idea behind this doctoral thesis or, rather, this project aiming to find viable alternatives to fossil fuels and contribute to a zero-emission CO_2 scenario.

Over the course of the three-year doctoral program, the research endeavors were shaped by an exhaustive literature review and insights gained during the initial experimental campaigns. The primary investigation along this research trajectory took place at the Politecnico di Torino. In this initial phase, bulk iron-based catalysts were tested, employing sodium as a promoter. This choice was

driven not only by the intention to reproduce existing literature data but also to underscore the merits and limitations of these catalysts.

In an effort to infuse innovation, the exploration commenced with the creation of core-shell structures, extensively expounded upon in Chapter 3. From this inaugural study, the pivotal role of sodium as a promoter became apparent. Equally noteworthy was the confirmation that sodium migration from bulk iron to the acidic sites of the zeolite compromises selectivity for desired hydrocarbon products, specifically gasoline. These preliminary findings provided the impetus to extend the research at the Instituto de Tecnología Química (ITQ) in Valencia, where the focus remained on iron-based catalysts promoted by sodium but with additional support.

Precisely, the decision was made to externally and internally support carbon-based nanotubes (CNTs) with varying external diameters, leveraging their inherent hydrophobic nature. Beyond the diameter variations, the impregnated CNTs were synthesized with different iron percentages, while maintaining a constant iron-sodium ratio. These CNTs were subjected to individual testing and were also scrutinized alongside an MFI-type zeolite in two different contact scenarios: a granular mixture and a powder mixture, specifically utilizing a commercial HZSM-5 zeolite. Further details regarding the preparation can be found in Chapter 2.

The outcomes of this comprehensive experimental campaign are meticulously presented and discussed in Chapter 4. Building upon these results, the focus of the study shifted to one particular CNT impregnated with iron and sodium, which exhibited sodium migration from iron to the acidic sites of the zeolite. This subsequent experimental phase delved into the surface properties, Si/Al ratio, grain size, and pore size of zeolites, all characterized by an MFI-type framework. The majority of these zeolites were synthesized and/or modified at the ITQ laboratories (Chapter 2 for major details). The findings from this phase are thoroughly expounded upon in Chapter 5 and offer substantial support to the conclusions drawn from the preliminary study in Chapter 4.

Chapter 6 introduces a study with a slightly nuanced objective. Recognizing the sodium's migratory capability and identifying alternatives, this chapter focuses on the examination of zeolites with diverse frameworks, Si/Al ratios, and the impact of mesoporosity on their ability to modulate selectivity across different ranges of liquid hydrocarbon products. To eliminate potential distortion of

selectivity results due to sodium migration, this study was conducted in dual-bed mode.

However, it is important to emphasize that numerous challenges have been addressed, and many more efforts need to be made to tackle issues related to energy input, catalytic challenges, feedstock availability, operating costs, and environmental impact to maximize their potential and effectiveness.

Chapter 2

2. Experimental methods

This chapter aims to provide a comprehensive overview of the experimental methods employed in the research outlined in this thesis. It focuses on documenting the catalyst synthesis process, providing a broad introduction to the operating conditions used for characterization techniques and catalytic tests. To enhance the readability of the thesis, the synthesis of catalysts has been organized into sub-sections, each correlated with a specific macro-chapter presented in the subsequent sections.

2.1 Synthesis of bulk iron catalysts combined with zeolite

Below, the synthesis procedures used to prepare bulk iron-based catalysts impregnated with sodium, H-ZSM-5 zeolite with a hierarchical structure, and core-shell structures employed in the initial work of this research thesis will be described. Table 2. 1 summarizes the main information about the names used for the catalysts, while further details about the choice of these materials will be provided in Chapter 3 [1].

Table 2. 1. Synthesis and Summary Characteristics of Catalytic Samples Used in Chapter 3.

Name used	Nominal Si/Al at. ratio (a.u.)	Nominal Na/Fe_3O_4 ratio (wt. %)	Preparation Method	Additional information
1%$NaFe_3O_4$_WI	-	1	Wet Impregnation (WI)	Sample obtained by subsequent impregnation with proper amount of $NaNO_3$ from homemade Fe_3O_4.
5%$NaFe_3O_4$_WI	-	5	Wet Impregnation (WI)	Sample obtained by subsequent impregnation with proper amount of $NaNO_3$ from homemade Fe_3O_4.

$NaFe_3O_4$_CP	-	Dependent on washing water	Coprecipitation (CP)	Sample obtained by direct coprecipitation of Fe_3O_4 with NaOH.
HZSM5	40	-	Commercial Zeolite	Purchased from Alfa Aesar.
HZ	40	-	Hydrothermal Synthesis	Homemade hierarchical zeolite, obtained directly in H^+ form.
$NaFe_3O_4$_CP@HZSM5	40	Dependent on washing water	Cladding Method	Core made with $NaFe_3O_4$_CP from coprecipitation, shell made with commercial HZSM5 using colloidal
$NaFe_3O_4$_CP@HZ	40	Dependent on washing water	Cladding Method	Core made with $NaFe_3O_4$_CP from coprecipitation, shell made with homemade HZ (hierarchical zeolite) using colloidal silica as glue.

More details about the synthesis will be provided in the following paragraphs: 2.1.1, 2.1.2, 2.1.3 and 2.1.4.

2.1.1 Preparation of the bulk Na/Fe_3O_4 catalyst

In the first step, a bulk Fe_3O_4 sample was prepared by adding the following reagents to a 250 mL three-neck round-bottom flask:

- 6 grams of $FeCl_2 \cdot 4\,H_2O$
- 8.6 grams of $FeCl_3$
- 125 mL of Milli-Q water

The mixture was vigorously stirred for 30 minutes under a nitrogen atmosphere at 90 °C. Subsequently, 45 mL of ammonium hydroxide solution (NH_4OH, 28 wt. %) were added rapidly. This resulted in the mixture turning black, and the reaction was maintained at 90 °C for 3 hours. At this point, the product was magnetically separated, washed with Milli-Q water until the pH was neutral, and then dried at 60 °C overnight [109]. Finally, the obtained Fe_3O_4 was impregnated with the desired amount of sodium using the wet impregnation method. Specifically, 185 mg of $NaNO_3$ were mixed with 5.0 mL of H_2O in a beaker, followed by adding 5.0 grams of Fe_3O_4. The suspension was sonicated, under agitation, for 30 minutes and left to stand for 4 hours at room temperature. This procedure was repeated three times. The solvent was evaporated, and the sample was dried at 60 °C overnight. Subsequently, the sample was calcined under

static air at 400 °C for 4 hours (heating rate: 5 °C·min^{-1}). This sample was named '1%$NaFe_3O_4$_WI'. A similar procedure was employed to prepare a second sample labeled '5%$NaFe_3O_4$_WI', by adjusting the amount of $NaNO_3$ [110] (The % Na nominal content is expressed as $g_{Na}/g_{Fe_3O_4}$).

2.1.2 $NaFe_3O_4$ Obtained by Coprecipitation with NaOH

A $NaFe_3O_4$ catalyst was synthesized using a one-pot synthesis method [97]. A suitable amount of iron chlorides (18.98 g of $FeCl_3$ and 12.54 g of $FeCl_2 \cdot 4H_2O$) was dissolved in 5.1 mL of HCl (12.1 mol·L^{-1}), and then 150 mL of water were added. NaOH (1.5 mol·L^{-1}) was added dropwise to the solution while stirring at 60 °C until the pH of the final solution was maintained at approximately 10. After continuous stirring for 1 hour, the black-brown product was separated using a magnet and washed with 800 mL of deionized water. The washed solid was dried overnight at 60 °C and referred to as '$NaFe_3O_4$_CP'.

2.1.3 Synthesis of Hierarchical Zeolite HZSM-5: HZ

A homemade hierarchical ZSM-5 zeolite with a theoretical Si/Al atomic ratio of 40 was prepared through hydrothermal synthesis [110] and labeled as 'HZ'. Specifically, an aqueous solution was prepared in a flask, containing 29.2 g of tetraethyl orthosilicate (TEOS), 0.75 g of aluminum isopropoxide (AIP), 13 g of tetrapropylammonium hydroxide (TPAOH, 40 wt. % in water), and 68 mL of water. The mixture was stirred at room temperature for 30 minutes. Then, the solution was left under reflux with stirring at 90 °C for 20 hours. Subsequently, 1.20 g of 3-aminopropyltrimethoxysilane (3-APTMS, 97 %) was added to the solution, and the mixture was stirred for another 6 hours at 90 °C. The ZSM-5 precursor solution was crystallized in a Teflon-lined stainless-steel autoclave at 170 °C for 5 days. Afterward, the precipitate was separated by centrifugation and washed with water. After being dried overnight at 60 °C, the sample was calcined in a muffle at 550 °C for 5 hours.

2.1.4 Core-shell catalysts: $NaFe_3O_4$@HZSM5 and $NaFe_3O_4$@HZ

The selection of the metallic phase derived from coprecipitation ($NaFe_3O_4$_CP) was made due to its potential for close interaction with the zeolite, particularly in terms of the diffusion of reactants, products, and the mobility of sodium. As a result, two core-shell catalysts, identified as '$NaFe_3O_4$_CP@HZSM5' and '$NaFe_3O_4$_CP@HZ', were fabricated using a physically adhesive method [100].

For the synthesis of $NaFe_3O_4$_CP@HZSM5, 2 g of $NaFe_3O_4$ pellets (sieved to a size range of 300–500 μm) were mixed with 0.5 g of LUDOX (an aqueous solution containing 30 wt. % SiO_2) that had been diluted with 2 mL of Milli-Q water. Subsequently, 2 g of commercial HZSM-5 powder (purchased by Alfa Aesar Si/Al theorical atomic ratio of 40) were manually added to the damp granules. The resulting pellets were transferred to a round-bottom flask and rotated for 2 hours to facilitate drying. Afterward, the core-shell pellets underwent a calcination process in static air at 400 °C for 3 hours, with a heating rate of 2.5 $°C \cdot min^{-1}$.

For $NaFe_3O_4$_CP@HZ, the same active phase as $NaFe_3O_4$_CP@HZSM5 was employed, but HZ zeolite was used in its 'as-made' state, with the pores still filled with the structure-directing agent, instead of using commercial HZSM-5. Once the core-shell structure was achieved (the sample showed white color, thanks to the good coating of $NaFe_3O_4$_CP with the zeolite), $NaFe_3O_4$_CP@HZ pellets were heated in a muffle to 550 °C at a rate of 2 $°C \cdot min^{-1}$ for 3 hours to decompose the organic template [1].

2.2 Iron catalysts supported on Carbon Nanotubes (CNTs)

In the following subsection, a detailed description of the method used to impregnate carbon nanotubes will be provided. In the initial phase of this description, the methods for cleaning the surface of the nanotubes will be outlined, both by keeping the caps at the ends of the carbonaceous materials and by removing them. Table 2. 2 summarizes the main information about the names used for the catalysts, while physicochemical properties of the CNT and derived iron

catalysts performance in the CO_2 hydrogenation reaction will be extensively discussed in Chapter 4.

Table 2. 2. Synthesis and Summary Characteristics of Catalytic Samples Used in Chapter 4.

Name used	Outer diameter (nm)	Synthesis procedure
CNT-S-original	10-20	Commercial CNTs
CNT-M-original	40-60	Commercial CNTs
CNT-L-original	60-100	Commercial CNTs
CNT-S-C-MAT[b]	10-20	Treated with HNO_3 35% at vol. %, for 20 h, at 140 °C
CNT-S-O-SAT[c]	10-20	Treated with HNO_3 68% at vol. %, for 20 h, at 140 °C
CNT-S-C10FeNa	10-20	Treated with HNO_3 35% at vol. %, for 20 h, at 140 °C, then impregnated with 10 % wt. of Fe and a Na/Fe ratio of 25
CNT-S-O10FeNa	10-20	Treated with HNO_3 68% at vol. %, for 20 h, at 140 °C, then impregnated with 10 % wt. of Fe and a Na/Fe ratio of 25
CNT-S-O15FeNa	10-20	Treated with HNO_3 68% at vol. %, for 20 h, at 140 °C, then impregnated with 15 % wt. of Fe and a Na/Fe ratio of 25
CNT-M-O15FeNa	40-60	Treated with HNO_3 68% at vol. %, for 20 h, at 140 °C, then impregnated with 15 % wt. of Fe and a Na/Fe ratio of 25
CNT-L-O15FeNa	60-100	Treated with HNO_3 68% at vol. %, for 20 h, at 140 °C, then impregnated with 15 % wt. of Fe and a Na/Fe ratio of 25

More details about the synthesis will be provided in the following paragraph: 2.2.1.

2.2.1 Carbon nanotubes pretreatment and impregnation with Iron

During the course of this research, a comprehensive analysis of the synthesis of carbon nanotubes (CNTs) impregnated with sodium (Na) and iron (Fe) was conducted, with a specific focus on exploring the effect of the location of Fe and Na (inside/outside the CNTs) on alkali migration. In addition, were varied different parameters, such as the percentages of impregnated Fe (constant Na/Fe atomic ratio), and the CNT diameters in order to assess their influence on Na-Fe location and their impact on alkali migration after mixing with the zeolite.

To carry out these experiments, commercial carbon nanotubes were categorized into three groups, according to their outer diameters (OD):

1. CNT-S (where 'S' indicates 'small') the CNT purchased by ACS Materials and with an outer diameter (OD) ranging from 10-20 nm.
2. CNT-M (where 'M' indicates 'medium') the CNT purchased by Iolitec with an OD ranging from 40-60 nm.
3. CNT-L (where 'L' indicates 'large') the CNT purchased by Iolitec with an OD ranging from 60-100 nm.

Initially, two distinct cleaning treatments were conducted on the CNTs [111]:

1. In the first set of experiments, the icone severe treatment with HNO_3 to open the CNTs also serves for cleaning, while preserving the closed caps at both ends of the nanotubes. To accomplish this, we used the same treatment conditions described above, with the exception that we employed a 37 wt. % concentrated HNO_3 solution. These samples were labeled with the "-C" designation (for "close") instead of "-O." In both cases, after the high-temperature acid treatment, the CNTs were thoroughly washed with deionized water until reaching a neutral pH and subsequently dried overnight at 100 °C.
2. In the second set of experiments, the CNTs underwent a treatment aimed at removing the "caps," which are the closed ends of the nanotubes, to make the nanotube walls accessible to the active phases (Na-Fe). To achieve this, we refluxed 3 grams of the commercial CNTs (CNT-S, CNT-M, and CNT-L) in a 150 mL solution of 69 wt. % nitric acid (HNO_3, Merck) at a temperature of 140°C for 20 hours. The samples treated in this manner were labeled with the suffix "-O" (for "open") in addition to the CNT nomenclature.
3. Regarding the percentages of Fe to be impregnated into the CNTs, we selected two values: 10 wt. % and 15 wt. % , while keeping the atomic ratio Na/Fe constant at 0.025. This variation allowed to obtain samples with different Fe loads, influencing the catalytic properties of the final materials. To impregnate CNTs with 10 wt. % Fe, we dissolved 2.5364 g of $Fe(NO_3)_3 \cdot 9H_2O$ and 0.0133 g of $NaNO_3$ (both purchased by Sigma Aldrich) in 30 mL of distilled water to prepare a solution, to which we added 3 g of carbon nanotubes (CNTs) that had been previously cleaned and/or opened and dried. To ensure a uniform distribution of Fe and Na and to facilitate effective impregnation of the CNTs, the solution underwent simultaneous ultrasonic treatment and stirring for 4 h [112]. Of course, the quantities of iron nitrate and sodium were rearranged to

maintain the Na/Fe atomic ratio at 0.025 and introduce 15% Fe into the nanotubes instead of 10%.

Subsequently, we proceeded with the slow evaporation of the solvent at room temperature, followed by drying in an oven at 100 °C overnight. The resulting product was then subjected to heat treatment at 350 °C for 3 h, using a N_2 flow at a rate of 300 $mL \cdot g^{-1} \cdot min^{-1}$ and with a temperature increase rate of 2 $°C \cdot min^{-1}$.

In parallel, were prepared CNTs with various outer diameters to assess the effect of pore size on the structure and performance of the impregnated nanotubes.

The synthesized samples were named as follows:

- CNT-S-C-10FeNa → CNT with OD: 10-20 nm, closed caps, and 10 wt. % of Fe.
- CNT-S-O-10FeNa → CNT with OD: 10-20 nm, open caps, and 10 wt. % of Fe.
- CNT-S-O-15FeNa → CNT with OD: 10-20 nm, open caps, and 15 wt. % of Fe.
- CNT-M-O-15FeNa → CNT with OD: 40-60 nm, open caps, and 15 wt. % of Fe.
- CNT-L-O-15FeNa → CNT with OD: 60-100 nm, open caps, and 15 wt. % of Fe.

Each sample was meticulously characterized by analyzing structural and catalytic properties. Furthermore, these materials underwent testing in both granular and powder forms, alongside a commercial MFI-type zeolite, namely the ZSM-5 zeolite acquired from Zeolyst (commercially known as CBV 5524G and labelled in this thesis as MFI27, where the number 27 is referred to the Si/Al ratio, determined by ICP-OES). For a detailed account of the preparation of granule mixing and powder mixing and a description of reactor loading, refer to Section 2.7 in this chapter.

2.3 Synthesis, desilication, ion-exchange and passivation of MFI-type zeolites

The purpose of this subsection is to describe the methodology for the preparation of MFI-type zeolites used in Chapter 5, in combination with the CNT-M-O-15FeNa sample (detailed in Section 2.2.1). These bifunctional catalysts, made with the CNT sample and the zeolite, were prepared by granule mixing.

Table 2. 3 summarizes the main information about the names used for the catalysts employed in Chapter 5.

Table 2. 3. Synthesis and Summary Characteristics of Catalytic Samples Used in Chapter 5.

Name Used	IZA	Synthesis procedure	Additional Information
CNT-M-O15FeNa	-	Wet impregnation	Commercial CNTs with outer diameter 40-60 nm, treated with HNO_3 68% at vol. %, for 20 h, at 140 °C, then impregnated with 15 % wt. of Fe and a Na/Fe ratio of 25
MFI27	MFI	Commercial zeolite	H-ZSM-5 zeolite purchased by Zeolyst International with the following code: CBV 5524G
04NaMFI27	MFI	Commercial zeolite partially ion-exchanged	Commercial zeolite CBV 5524G partially ion-exchanged with Na (40% of acid sites ion-exchanged)
MFI34@Sil3	MFI	Commercial zeolite sylilated with amourphous SiO_2	Commercial CBV 5524G silylated 3 times with SiO_2 in hexane
MFI112	MFI	Commercial zeolite	H-ZSM-5 zeolite purchased by Zeolyst International with the following code: CBV 28014
µMFI35	MFI	Hydrothermal synthesis	Zeolite with low external surface area and high crystal
µMFI27-meso	MFI	Desilication of homemade µMFI35	-
MFI46-nano	MFI	Hydrothermal synthesis	Nanocrystalline zeolite with crystal size of 10-20 nm

More details about the synthesis will be provided in the following paragraphs: 2.3.1, 2.3.2, 2.3.3 and 2.3.4, 2.3.5.

2.3.1 Synthesis of extra-large crystal size zeolite: µMFI35

The extra-large crystal size zeolite, labelled as µMFI35 with a theoretical Si/Al atomic ratio of 35 was prepared using the following procedure [113]: A solution was prepared by dissolving 2.17 g of tetrapropylammonium bromide (98%, Sigma-Aldrich) and 0.919 g of $Al(NO_3)_3 \cdot 9H_2O$ (98%, Thermo Scientific) in 17.2 g of demineralized water. Subsequently, 15.0 g of Ludox AS-40 (40 wt. % SiO_2 in H_2O, Sigma Aldrich) were added to this well-dispersed mixture. To this mixture, 16.08 g of ammonia solution (28 wt. % in water, Sigma Aldrich) were introduced. The molar composition of the resulting gel solution was as follows:

$$1SiO_2:0.0245(NO_3)_3Al:1.285\ NH_4OH:0.08TPABr:21H_2O$$

Crystallization took place under rotation, with continuous stirring, in stainless-steel autoclaves at 150 °C for 12 days. The crystalline product was then filtered, thoroughly washed with water, and dried overnight at 100 °C. Finally, the sample was calcined in air at 550 °C for 3 h to effectively eliminate any residual organic components.

2.3.2 Desilication of microcrystalline zeolite, µMFI35

The desilication process was carried out by treating calcined CBV 5524G with a basic solution containing 0.2 M NaOH (Sigma Aldrich) and TBAOH (Alpha Aesar, 40 % w/w aq. solution) in a molar ratio of TBAOH/(TBAOH+NaOH)=0.4. The basic solution was refluxed with 10 g of µMFI34 zeolite, prepared as described in 2.3.1, with a liquid-to-solid ratio of 25 $mL \cdot g^{-1}$ at 80 °C for 1 h under vigorous stirring. Subsequently, the mixture was cooled down, and the solid was recovered by centrifugation five times (at 15000 rpm for 30 minutes), with the addition of distilled water to adjust the pH. The solid was separated by filtration using a nylon filter (0.22 µm) and washed until the pH reached 7 [114].

In order to remove the Na located in the acid sites of the zeolite during the desilication treatment, the sample underwent ion exchange, before the heat treatment. Specifically, 5 g of µMFI35 were refluxed at 80 °C for 3 h in a flask containing 50 mL of a 2.5 M solution of $NH_4(NO_3)$ (Sigma Aldrich). After the ion exchange process, the sample was dried overnight at 60 °C and then subjected to calcination in a muffle furnace at 550 °C for 4 h, with a heating rate of 2 °C/min. The resulting sample was labeled as µMFI27M, where 'MFI' indicates the ZSM-5 zeolite, '27' represents the bulk Si/Al atomic ratio determined by ICP-OES, and 'M' signifies the mesoporous and ion exchanged structure.

2.3.3 Nanocrystalline ZSM-5 zeolite, MFI46-nano

The nanocrystalline MFI sample was synthesized via a hydrothermal method, utilizing tetraethoxysilane (TEOS, Sigma-Aldrich, ≥ 99%), aluminum isopropoxide (AIP, Sigma-Aldrich, ≥ 98%), and tetrapropylammonium hydroxide (TPAOH, 40 wt. % aqueous solution) as reagents, according to the procedure reported in [115]. The clear gel solution had the following molar composition:

1TEOS:0.01AIP:0.25TPAOH:20H_2O.

The solution underwent vigorous stirring at room temperature to facilitate the hydrolysis of TEOS and the removal of water until a H_2O/SiO_2 molar ratio of 5 was achieved. Subsequently, the resulting solution was introduced into Teflon-lined stainless steel autoclaves, where it was allowed to age statically at 80 °C for 20 hours and then subjected to hydrothermal treatment at 180 °C for 90 minutes with rotation. The solid product was recovered by repeated centrifugation-washing cycles, drying at 100 °C, and finally calcination in air at 550 °C for 3 hours to obtain the sample referred to here as 'MFI46-nano'.

2.3.4 Partial Na ion-exchange on CBV5524G (H^+ form)

The commercial zeolite CBV5524G, initially provided in the NH_4^+ form by Zeolyst International, was converted into the corresponding protonic (H^+) form by calcination in a muffle oven, under air atmosphere at 500 °C for 3 hours, with a heating rate of 2 °C·min^{-1}.

Specifically, 5 grams of the CBV5524G zeolite in the H^+ form were placed into a flask containing 125 mL of a 1 M solution of $NaNO_3$. The solution was allowed to stir for 7 hours under reflux conditions at a temperature of 80 °C. Subsequently, it underwent several rinses with distilled H_2O to eliminate any residual NO_3^- ions. The sample obtained from this process was labeled as 04NaMFI27, with '04' representing the Na/Al atomic ratio, which should ideally be 1 for a complete ion exchange, and '27' indicating the bulk Si/Al atomic ratio. Both of these atomic ratios were determined through ICP-OES analyses.

2.3.5 Surface sylilation treatment

The commercial zeolite CBV5524G sample underwent a surface silylation treatment utilizing the chemical liquid deposition (CLD) method. In this process, tetraethoxysilane (TEOS, Sigma-Aldrich, ≥ 99%) was used as the source of silica to passivate external acid sites. This method is chosen for its efficiency, simplicity, and adaptability for larger-scale applications [115], [116], [117], [118]

In brief, 6 g of CBV5524G were mixed with 150 mL of n-hexane and refluxed at 60 °C for 30 min with continuous stirring. Subsequently, 0.9 mL of TEOS (equivalent to a 4 wt. % SiO_2 loading) was added to the mixture, and it was stirred and refluxed for an additional hour. After removing the n-hexane solvent by evaporation, the solid was dried at 100 °C overnight. Finally, it underwent calcination under flowing air at 500 °C for 4 h, with a heating rate of 1 °C/min. This entire procedure was repeated three times to obtain the sample designated as MFI34@Sil3. Here, '34' signifies the bulk Si/Al atomic ratio, determined through ICP-OES analyses, and Sil3 indicates that the surface silylation treatment was repeated for three times.

2.4 Different types of zeolites used in dual bed mode tests with 1 NaFe

The purpose of this subsection is to summarize and provide details on the materials utilized in Chapter 6. Specifically, the objective is to describe the preparation of bulk iron (1NaFe) for use in dual-bed mode or granule mixing mode with the following zeolites:

- MFI, specifically H-ZSM-5 (CBV5524G, purchased from Zeolyst International and referred to as MFI27 in this work) and ZSM-22 (purchased from Zeolyst International and referred to as Z22-32).
- FAU, particularly USY zeolite purchased from Zeolyst International, identified as CBV760, CBV720, and CBV712, and labeled in this thesis as USY24, USY13, and USY5, respectively.
- BEA (purchased from Zeolyst International as CP814C, labeled as BEA17 in this work).
- MCM-22 and ITQ-2, both synthesized in the ITQ laboratory and labeled in this thesis as M22-20 and ITQ2-18. The procedure for synthesizing M22-20 and ITQ2-18 is detailed in paragraph 2.4.4.
- MFI17M obtained by desilication of MFI27

It is worth noting that the desilication process for the MFI27 zeolite is not described here since it is identical to the procedure outlined in Section 2.3.2. The resulting sample is named MFI17M because '17' represents the Si/Al ratio determined by ICP-OES, and the 'M' indicates that the zeolite has been

transformed into a mesoporous zeolite. Details regarding the reactor loading mode are provided in Section 2.7.2.

2.4.1 Bulk iron synthesis: 1NaFe

Fe_3O_4 was produced through the introduction of 15.82 g of $FeCl_3 \cdot 6H_2O$, 6.27 g of $FeCl_2 \cdot 4H_2O$, 2.55 mL of HCl (37 %), and 75 ml of H_2O into a beaker. The mixture was stirred at 60 °C until the salts completely dissolved. Subsequently, a 5% v/v solution of NH_4OH was carefully added dropwise until pH 10 was reached and kept stirring at 60 °C for an hour. At the end, the solution was filtered, and the resultant black solid was washed several times with H_2O until neutral pH. The catalyst was then dried overnight in an oven at 100 °C [119]. Then 5 g of Fe_3O_4 were impregnated with a previously prepared solution of 0.185 g of $NaNO_3$ and 2.5 g of H_2O. Gradually, this solution was added dropwise to the catalyst powder, ensuring thorough mixing after each drop addition. The catalyst was then left to dry in an oven overnight at 100 °C. On the subsequent day, it was subjected to calcination at 400 °C for a duration of 4 hours, following a ramping rate of 2 $°C \cdot min^{-1}$ and an airflow rate of 300 $mL \cdot min^{-1}$.

2.4.2 Desilication of commercial CBV760

A solution of 200 mL of 0.2 M NaOH was put in a flask with 10.8678 g of tetrapropylammoniumbromide (TPABr). The resulting mixture was kept under stirring at 500 rpm for 10 minutes. Next, 6.6 g of zeolite CBV760 (H^+ form), were added to the solution, stirring at 500 rpm and refluxing at 65 °C for 30 minutes. Then, the reaction was stopped with an ice-water bath and was kept under these conditions for 20 minutes. Finally, the resulting solid was washed, filtered (with 18 L of H_2O) and dried in an oven at 100 °C for 24 hours. The dry product obtained was calcined under air flow (GSHV = 100 $mL \cdot g^{-1} \cdot min^{-1}$) at 550 °C for 5 hours with a ramp of 5 $°C \cdot min^{-1}$ to remove the organic matter.

The resulting sample underwent an ion exchange process by refluxing at 80 °C for 3 h with 2.5 M $NH_4(NO_3)$ (Sigma Aldrich) (L/S ratio 20 $mL \cdot g^{-1}$). Then the solid was recovered by filtration until pH=7. Later the sample is dried overnight at 60 °C and calcinated in a muffle at 550 °C for 4 h with a ramp of 2 °C/min. The sample obtained was labeled as USY15M.

2.4.3 Desilication of commercial CP814C

In a beaker, 31.5 mL of deionized water (H_2O), 0.46 g of sodium hydroxide (NaOH), and 2.5 g of hexadecyltrimethylammonium bromide (CTABr) were continuously stirred until complete dissolution. Subsequently, 5 g of commercial zeolite CP814C, purchased to Zeolyst Intenational in NH_4^+ form, were introduced, and the solution was stirred for other 20 min at room temperature. The mixture was then transferred to an autoclave and placed in an oven at 80 °C for 6 h. Later, it was filtered, washed, and dried in an oven at 60 ºC overnight. The resulting dry product was subjected to calcination at 550 °C with a heating ramp of 3 $°C \cdot min^{-1}$. During the initial heating stage, and for the first hour after reaching 550 ºC, a stream of pure nitrogen (N_2) was used. Subsequently, the N_2 stream was replaced with air, and the temperature was maintained for an additional 6 h. A gas hourly space velocity (GSHV) of 100 $mL \cdot g^{-1} \cdot min^{-1}$ was maintained throughout the process.

Specifically, the resulting product, was placed in a flask along with 50 mL of a 2.5 M $NH_4(NO_3)$ solution. The mixture was refluxed at 80 °C for 3 hours for the ion exchange process. After completion, the mixture was dried overnight at 60 °C. The resulting dried product was then subjected to calcination in a muffle furnace at 550 °C for 4 hours, with a heating rate of 2 $°C \cdot min^{-1}$. This final sample was labeled as BEA17M, where 'BEA' denotes the Beta zeolite, '17' signifies the bulk Si/Al atomic ratio determined by ICP-OES and 'M' indicate that the sample underwent desilication.

2.4.4 Synthesis of MCM-22 and ITQ-2

ITQ-2 was made by first synthesizing MCM-22(P), a lamellar precursor for the MCM-22 zeolite (MWW-type structure), which consists of inorganic layers connected together by a layer of organic material (hexamethyleneimine, HMI).

Synthesis of the MCM-22(P) precursor

Typically, 0.365 g of sodium aluminate (56%Al_2O_3, 37%Na_2O, Carlo Erba) and 0.375 g of sodium hidroxide (98%, Prolabo) were dissolved in 80.71 g of distilled water, after which 4.96 g HMI, (98%, Aldrich) and 6.00 g silica (Aerosil 200, Degussa) were added consecutively. The mixture was stirred vigorously for 30 minutes at room temperature, producing a gel with silicon-to-aluminum (Si/Al)

atomic ratio of 25 (corresponding silica-to-alumina molar ratio of 50). The crystallization of the lamellar precursor was done at 150 °C during 7 days in a stirred PTFE-lined stainless-steel autoclave under autogenous pressure. The crystalline product was filtered, washed with distilled water until pH < 9, and dried at 60 °C during 12 hours to produce the MCM-22(P) precursor.

Synthesis of the MCM-22 zeolite

The MCM-22 zeolite was obtained by calcination of the dried lamellar MCM-22(P) precursor in a muffle oven at 580 °C during 8 h. The sample obtained was labeled M22-20, where '20' indicates the bulk Si/Al atomic ratio determined by ICP-OES.

Synthesis of the ITQ-2 zeolite

In order to prepare the ITQ-2, 10 g of the lamellar precursor were dispersed in 40 g of H_2O milliQ, and 200 g of a cetyltrimethylammonium hidroxide solution (25 wt%, 50% exchanged Br^-/OH^-) and 60 g of a solution of tetrapropylammonium hidroxide (40 wt%, 30% exchanged Br^-/OH^-) were added, being the final pH ≥ 12.5. At this point, the suspension was sonicated in an ultrasound bath (50W, 50Hz) during 1 hour to disperse the individual sheets. Then, the pH was decreased to 3.0 by adding HCl (6M) in order to facilitate the flocculation of the delaminated solid. This was recovered by centrifugation and washed with distilled water. After drying at 60 °C for 12 hours, the solid was calcined for 3 hours at 540 °C in flowing N_2 and then during 6 hours in air (flowrate 2.5 mL/s, heating rate 3 ºC/min). With this calcination treatment, all the organic was decomposed, yielding a material having the structural and textural characteristics of ITQ-2. The sample obtained was named as ITQ2-18, where '18' indicates the bulk Si/Al atomic ratio determined by ICP-OES.

2.5 Characterization Techniques

Below, a concise description will be provided for chemical, physical, and morphological characterizations, along with the specific operational parameters applied for each technique. This approach enables the acquisition of detailed information about material properties by integrating data related to chemical composition, crystalline structure, and material morphology.

2.5.1 Inductively coupled plasma-Optical Emission Spectroscopy (ICP-OES)

Inductively coupled plasma (ICP) is a type of plasma source frequently employed in the realm of analytical chemistry, particularly for atomic spectroscopy. It constitutes a high-temperature, electrically conductive gas formed by ionizing a gas through the application of high-frequency electromagnetic fields. Within an ICP system, the plasma is generated through an induction coil enveloping the plasma torch, a conduit through which the gas passes. The high-frequency electromagnetic fields induced by the coil result in the ionization of the gas, giving rise to the plasma [120]. One of the primary advantages of ICP lies in its capacity to produce high-temperature plasmas, reaching temperatures as high as 10,000 K, thereby enabling the atomization and ionization of a broad spectrum of elements. This feature renders it a valuable tool for the analysis of samples exhibiting diverse compositions. ICP is frequently employed in conjunction with other methodologies to examine samples for various applications such as environmental testing, food safety, and materials analysis.

Technical details: In Valencia, the chemical composition of selected materials was evaluated via Inductively Coupled Plasma-Optical Emission Spectroscopy (ICP-OES) using a Varian 715-ES instrument. Solid powder samples (approximately 20-30 mg) were dissolved in a mixture of HNO_3/HF/HCl with volumetric proportions of 1/1/3. In all cases, the calibration curve was adjusted to the approximate expected concentration of the analyte and determined using standard solutions (Aldrich).

2.5.2 Energy-Dispersive X-Ray Fluorescence Analysis (XRF)

X-ray fluorescence analysis is a precise, non-destructive analytical technique used to determine the chemical composition of a material. During an XRF study, the material is exposed to X-rays coming from a source, that is typically manifested as a tube emitting radiation, although alternatives include a synchrotron or a radioactive substance. The components of the sample release fluorescent radiation with distinct energy levels when they come into contact with

the X-rays. It is possible to perform a qualitative study by looking at the radiations that are released, which can help identify different components in the sample. Meanwhile, it is possible to do a quantitative evaluation by measuring the signal intensity to determine the amount of each component that is present. Basically, when X-rays come into contact with matter, three sorts of interactions take place: fluorescence, Compton scatter, and Rayleigh scatter. When an X-ray beam strikes a sample, some of it passes through, some of it is absorbed and emits fluorescent light simultaneously, and the remaining component scatters. There are two types of scattering events: Compton scattering, which happens when there is an energy loss, and Rayleigh scattering, which happens when there is no energy loss. The fluorescence and scattering phenomena rely on several factors such as the material composition, thickness (d), density (ρ), and energy of the incident X-rays on the sample [121].

Technical details: A wavelength dispersive X-ray fluorescence spectrometer (Rigaku Supermini 200) fitted with three standard crystals (LiF200, PET, and RX26) was used in Italy to evaluate the sodium concentration in Fe-based catalysts and the Si/Al ratio of the zeolite using XRF.

2.5.3 N_2 Adsorption

To learn more about the textural characteristics of the adsorbent, the gas adsorption approach is predicated on the investigation of gas-solid adsorption and desorption events. The specific surface area, pore diameter, and pore volume of the solid under study can be found by interpreting adsorption-desorption isotherms using the geometric properties of the adsorbate and mathematical modeling of surface phenomena that determine the thermodynamics of adsorption and desorption processes. The most often utilized adsorbate is nitrogen, which is employed at a temperature of -196 ºC.

The Brunauer, Emmett, Teller (BET) approach, which measures nitrogen adsorption on the surface and in micropores, is the most used technique for calculating surface area [122]. The BET measurement takes into consideration the possibility of numerous adsorbed layers and finds a balance between adsorption and desorption. The following assumptions define the BET model:

i. The rates of adsorption and desorption in every layer are identical;
ii. The heat of adsorption in the second layer stays constant and is comparable to the heat of vapor condensation;

iii. Vapor condenses into a liquid at the saturation point of pressure, producing an endless number of adsorbed layers.

Through the BET method, it becomes possible to determine the quantity of adsorbed material in the monolayer and calculate the corresponding surface area [122], [123]. On the other side, the statistical thickness of the Harkins-Jura adsorbate was used to determine the micropore volume from the t-plot graph [124]. Unless otherwise noted, the adsorption branch of the isotherm was employed to determine the mean pore diameter distribution, using the Barret-Joyner-Halenda (BJH) model [125].

Technical details: In Italy, the specific surface area (S_{BET}), the total pore volume (V_p), and the mean pore diameter (D_p) were measured by using N_2 physisorption at -196 °C utilizing a Micromeritics Tristar II 3020, v1.03. Prior to analysis, samples underwent a pre-treatment at 200 °C for 2 h (iron bulk samples), while for zeolites the pre-treatment was carried out at 400 °C for 2 h, under nitrogen flow in a Micromeritics FlowPrep 060 to remove adsorbed gases. Instead, in Valencia, the adsorption-desorption isotherms of N_2 were recorded at -196 °C using a Micromeritics ASAP 2000 instrument. The samples were vacuum-treated for 12 hours before the adsorption tests. The pre-treatment temperature was typically 400 °C for the zeolites, whereas for the iron-containing samples the treatment temperature was 250 °C.

2.5.4 X-Ray Diffraction (XRD)

One of the most important techniques for describing crystalline materials is X-ray diffraction (XRD), which allows one to look at atomic distances and crystal structures [126]. It provides a thorough explanation of a substance's structure, but when interpreting it, one must take into account the possibility of amorphous phases. The basis of X-ray diffraction is the constructive interference of monochromatic X-rays with a crystalline material. A cathode ray tube, mostly made of copper, produces monochromatic X-rays, which are filtered to produce collimated monochromatic radiation that is directed toward the sample (Figure 2.1). X-ray diffraction (XRD) stands as a crucial method for characterizing materials, enabling the examination of crystal structures.

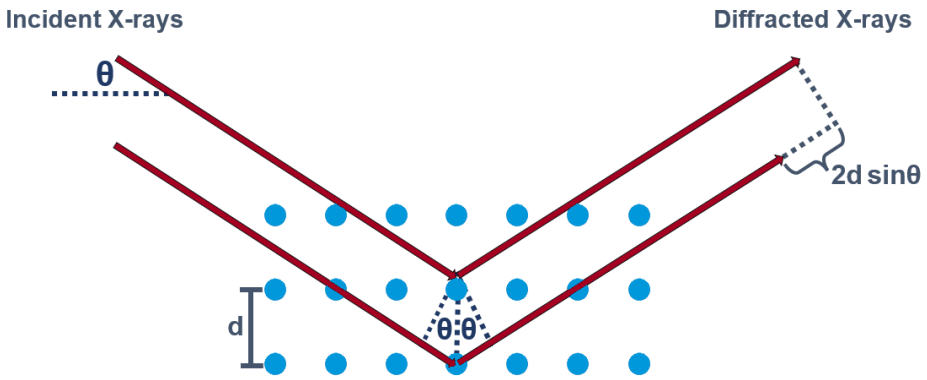


Figure 2.1. Schematic representation of Bragg's Equation (2. 1).

The X-ray diffraction technique is based on the examination of radiation diffracted from a material by an X-ray beam that is monochromatic and has a changing angle. The dispersion phenomenon is caused by the wavelength of X-rays, which is around 1 Å. Only at corners where structural interference is seen may detectors capture a signal because X-rays scattered throughout the field interact either constructively or destructively. Because of the sample's crystalline regularity, constructive interference leads to diffraction. Diffractive X-rays with varied optical lengths are produced when the X-ray beam is dispersed on different planes within the material. Diffractive X-rays with varied optical lengths are produced when the X-ray beam is dispersed on different planes within the material. The Bragg equation (2. 1) shows that the angle of incidence of the radiation for each diffraction line is associated with the interplanar spacing of the crystalline periodicity [127].

$$n\lambda = 2d\sin\vartheta \qquad (2.\ 1)$$

Where n is an integer, λ represents the wavelength of the X-rays, d is the interplanar spacing generating the diffraction and θ is the diffraction angle. Given the known X-ray wavelength in XRD experiments and the measured angles of constructive interference, the application of the Bragg equation facilitates the determination of the distance between the lattice planes of the material.

This measurement is known as "diffractogram," which is a graphical representation of X-ray intensity on the y-axis against the angle 2θ (the angle between the incident and diffracted beams) on the x-axis. Converting diffraction peaks into d-spacings enables the identification of the compound, as each compound possesses a unique set of d-spacings. Typically, this involves

comparing d-spacings with standard reference patterns. When analyzing amorphous materials using XRD, sharp peaks centered at specific θ angles are absent. Instead, amorphous materials exhibit broad features or halos centered around typical angles [128].

As previously mentioned, X-rays are generated in a cathode ray tube by heating a filament to emit electrons, which are then accelerated toward a target through voltage application, colliding with the target material. When the electrons possess enough energy to dislodge inner-shell electrons of the target material, characteristic X-ray spectra are generated and recorded. During the rotation of the sample and detector, the intensity of the reflected X-rays is registered. When the geometry of the incident X-rays aligns with Bragg's law, constructive interference occurs, manifesting as an intensity peak in the diffractogram. A detector captures and processes this X-ray signal, converting it into a count rate that is subsequently output to a device.

Analyzing the peaks through the Scherrer equation (2. 2) enables the calculation of the crystallite size of each phase present in the sample.

$$\text{Crystallite size (Å)} = \frac{k\lambda(\text{Å})}{\text{FWHM}\cos\theta} \qquad (2.\ 2)$$

In this equation, k is a constant (0.94), λ represents the X-ray wavelength in Å, FWHM is the full width at half maximum of the diffraction peak, and θ is the diffraction angle of the analyzed peak [129]. The FWHM data are previously corrected using lanthanum hexaboride (LaB_6) as a calibration standard to compensate the instrumental peak broadening. It's worth noting that the reported XRD analyses are conducted under standard conditions in the following chapters, employing a Cu anode and without a monochromator. Additionally, XRD is an extraordinarily sensitive technique, capable of detecting down to 1% w/w.

Technical details: In Italy, the crystalline phase evaluation was investigated by X-ray diffraction (XRD) on a Panalytical X'Pert PW3040 diffractometer equipped with a Cu anode for the Kα radiation (λ = 1.5418 Å) generation at 40 kV operating voltage in the 2θ range of 5-80° with a scanning step of 0.013° and an acquisition time of 0.2 s per step. The diffraction peaks were indexed according to the Joint Committee on Powder Diffraction Standards (JCPDS). Furthermore, in situ experiments using high-temperature X-ray diffraction in a reducing atmosphere were performed to thoroughly examine the evolution of the structure

under the increase of the temperature. The samples were placed on a Panalytical Empyrean diffractometer (Panalytical, Almelo, The Netherlands) equipped with a PIXcel detector and heated in an HTK1200N reactor (Anton Paar, Austria). Specifically, a non-ambient software was utilized to conduct in-operando testing on the novel $NaFe_3O_4$_CP catalytic powder (≈160 mg) at different temperatures. For the reduction simulation, a flow of 30 NmL·min^{-1} of 0.999 vol.% H_2/Ar was maintained, increasing from 25 °C to 900 °C (heating rate: +10 °C·min^{-1}). The XRD pattern was held for 30 minutes before being thermally collected. As part of the reaction simulation, the sample underwent pre-treatment with 30 NmL·min^{-1} of 0.999 vol.% H_2/Ar at 450 °C for 15 hours (XRD patterns were recorded every 4 hours). Following pre-treatment, the sample was cooled to 330 °C. Subsequently, under simulated reaction conditions, XRD patterns were taken every six hours at 330 °C using a gas mixture of 3 vol.% H_2 and 0.5 vol.% CO in N2 (30 NmL·min^{-1}). In-operando XRD data were obtained in the 20° to 80° range of the 2θ angle, using a high-resolution Bragg-Brentano detector (scan per step: 0.013° 2θ, duration per step: 0.60 s). Chapter 3 will include the information derived from the interpretation of the diffractograms.

On the other hand, in Valencia, the X-ray diffraction patterns of the powder samples were generally acquired at room temperature on a Phillips X'Pert diffractometer using monochromatic radiation corresponding to the Kα-Cu line. Typically, the diffractogram was obtained in the 2θ range of 5-90º for the samples containing iron, while in the 2θ=2-40º for the zeolites. Also in Valencia were performed XRD in situ. In particular, powder X-ray diffraction (XRD) monitored H_2-reduction (H_2-XRD) experiments were performed for selected catalysts using an Anton-Parr XRK-900 reaction chamber attached to a Panalytical Empyrean diffractometer operated at 45 kV and 40 mA using Cu Kα radiation. In these experiments, the samples were reduced under a continuous flow of 10 vol% H_2 in N_2. Then, after collecting a XRD pattern at room temperature (RT), the temperature was increased from 250 °C to 600 °C with steps of 50 °C, and the corresponding XRD patterns were collected at those given temperatures. At each temperature, two consecutive patterns of 30 minutes of duration each one were collected to ensure that a steady state was reached. After reaching the higher temperature, five consecutive patterns were recorded to ensure that the process is completed. Finally, the samples were cooled down to RT and measured again in order to analyze the final structure formed.

The XRD of the mesoporous zeolite was also uses in order to calculate the lose of crystallinity respect to the counterpart commercial zeolite. The XRD of the

mesoporous zeolite was also used to calculate the loss of crystallinity with respect to the commercial counterpart. Specifically:

- Crystallinity (%) = $\frac{\sum peak\ area\ mesoporous\ zeolite}{\sum peak\ area\ mother\ zeolite} \cdot 100$
- Loss of crystallinity (%) = 100 - crystallinity (%)

Regarding the USY zeolites utilized in this study and discussed in Chapter 6, XRD patterns were also used to calculate both framework and extra-framework aluminum. First of all, it was calculated the cell number. In order to determine the unit cell parameter of the cubic structure of zeolite FAU, some isolated and well-defined diffraction peaks in the 2 theta range, between 20 and 30 degrees, were selected. After removing the K-alpha2 component of the peaks to achieve a better accuracy, their positions were carefully determined, and those values were used to calculate their corresponding d-spacings. The Miller indices of each peak were assigned using as a reference the theoretical positions for the already know structure of the material. Then, the values of d, h, k and l were used to calculate the expected cell parameter *a* from each peak. Finally, an average *a* value was calculated from the previous values. The calculations were performed as outlined by the Equations reported below (2. 3), (2. 4) and (2. 5):

$$\frac{\mathbf{1}}{\mathbf{d^2}} = \frac{\mathbf{h^2 + k^2}}{\mathbf{a^2}} + \frac{\mathbf{l^2}}{\mathbf{c^2}} \qquad (2.\ 3)$$

$$\mathbf{a = b = c} \qquad (2.\ 4)$$

$$\mathbf{a} = \sqrt{(\mathbf{h^2 + k^2 + l^2}) \cdot \mathbf{d^2}} \qquad (2.\ 5)$$

Where:

h, k, l → Miller indices;

d → interplaner spacing or d-spacing (Å) calculated based on Bragg's law, (2. 6):

$$d = \frac{n\lambda}{2\sin\vartheta} \qquad (2.\ 6)$$

λ = 1.5406 → wavelength of incident X-ray;

n = 1 → order of diffraction;

θ → peak position in radians;

d → interplaner spacing or d-spacing (Å).

The cell number parameter obtained from Equation (2. 6), was utilized to quantify the amount of extraframework aluminum in the USY zeolite. Initially, the correlation proposed by V. Jorik [130] was employed to calculate the Framework Si/Al atomic ratio $\left(\frac{\mathrm{Si}}{\mathrm{Al}}\right)_F$, as shown in Equation (2. 7) below:

$$\left(\frac{\mathrm{Si}}{\mathrm{Al}}\right)_F = \left(\frac{192}{101.202 \cdot (\mathrm{a}_0 - 24.2115)}\right) - 1 \quad (2.\ 7)$$

This equation can also be expressed as Equation (2. 8), where N_{FAL} represents the number of framework Al atoms:

$$\left(\frac{\mathrm{Si}}{\mathrm{Al}}\right)_F = \left(\frac{192}{\mathrm{N_{FAL}}}\right) - 1 \quad (2.\ 8)$$

This means that the $\left(\frac{\mathrm{Si}}{\mathrm{Al}}\right)_{ICP}$ can be calculated following the equation (2. 9):

$$\left(\frac{\mathrm{Si}}{\mathrm{Al}}\right)_{ICP} = \left(\frac{192}{\mathrm{N_{FAL+EFAL}}}\right) - 1 \quad (2.\ 9)$$

Therefore, the number of framework and extraframework Al atoms ($N_{FAL+EFAL}$) can be calculated considering the Si/Al ratio determined by ICP, using Equation (2. 10):

$$\mathrm{N_{FAL+EFAL}} = \frac{192}{\left(\frac{\mathrm{Si}}{\mathrm{Al}}\right)_{\mathrm{ICP}} + 1} \quad (2.\ 10)$$

Given $N_{FAL+EFAL}$, it was then possible to calculate the number of extraframework Al atoms (N_{EFAL}) using Equation (2. 11):

$$N_{EFAL} = N_{FAL+EFAL} - N_{FAL} \quad (2.\ 11)$$

Finally, with N_{EFAL} and $N_{FAL+EFAL}$ known, the percentage of extraframework Al (%EFAL) could be calculated using Equation (2. 12).

$$\%\ EFAL = \frac{N_{EFAL} \cdot 100}{N_{FAL+EFAL}} \quad (2.\ 12)$$

2.5.5 Temperature programmed techniques

By subjecting samples to a thermal ramp in a controlled atmosphere, programmed temperature techniques can be used to study the behavior of reduction, oxidation, decomposition, desorption, or surface reaction of an adsorbed species. These techniques allow for the detection of species that are emitted or consumed during the processes occurring on the sample. This work has employed a variety of methodologies to gather data on catalysts including Reduction (TPR), Desorption (TPD), and Temperature Programmed Combustion (TPC).

2.5.5.1 H_2 temperature programmed reduction (H_2-TPR)

Technical details: In Italy, to investigate the reducibility of the catalyst, H_2-TPR was conducted using a Thermo Scientific 1100 TPDRO equipped with a TCD detector. Approximately 50 mg of catalyst powder was positioned within a quartz reactor between two layers of quartz wool. An inert pre-treatment involved heating the sample to 550 °C with a ramp of 10 °C·min^{-1} in an Ar flow, holding at this temperature for 50 minutes, and then purging the reactor with He. During the analysis, the sample underwent heating from room temperature to 900 °C with a 10 °C·min^{-1} ramp, all while exposed to a 20 mL·min^{-1} flow of 5% H_2 in Ar.

The reduction behavior of certain metallic catalysts and catalytic supports catalysts were ascertained in Valencia using H_2-TPR. Within a quartz U-tube, a fixed bed of 50 mg of material in particle size (0.2-0.40 mm) was loaded between quartz wool. After being exposed to an Ar flow for 30 minutes at ambient temperature, the circulating gas was changed to 10% H_2(vol)/Ar (50 mL/min) and

the samples were heated to 900 ºC at a rate of 10 ºC·min^{-1}. A thermal conductivity detector (TCD), which had been previously calibrated using the reduction of CuO as a reference, was used to monitor the H_2 consumption.

2.5.5.2 NH_3 temperature programmed desorption (NH_3-TPD)

NH_3-TPD technique, is not able to discriminate between Brønsted and Lewis acid sites.

Technical details: In Italy to investigate the acidity of the catalysts, NH_3-TPD was carried out using the AMI 300 lite TPDRO instrument. A U-shaped tubular reactor was filled with about 50 mg of sample, sandwiched between two layers of quartz wool and in contact with a thermocouple that was used to track the catalytic bed's temperature. After that, the system was put in a furnace that was heated to the program's set point temperature. The analysis began by pretreating the sample with a flow of 25 mL·min^{-1} of He at 350 °C (rate of 10 °C·min^{-1}) for 2 hours. Subsequently, acid sites on the surface were saturated by flowing a mixture of 0.25 vol.% NH_3/He (30 mL·min^{-1}) for 1 h at 50 °C. After removing physisorbed ammonia by flushing with pure He for 30 minutes at 100 °C, desorption was started by gradually heating the reactor to 900 °C with a 10 °C·min^{-1} ramp under a 30 mL·min^{-1} flow of He. By plotting the TCD signal in mV against the desorption temperature, it was possible to identify peaks corresponding to weak acid sites (desorbing NH_3 at a lower temperature) and those corresponding to strong acid sites (at a higher temperature). Subsequently, the TCD signal was integrated over time to obtain the area under the curve (mV·s), corresponding to desorbed ammonia. At the end of each test, pulses (typically 10) of 0.25 mol % NH_3 in He were carried out: knowing the concentration of the gas sent to the sampling loop and its volume, it was possible to determine the µmol of NH_3 contained in each pulse. These values were then divided by the average area under the pulse curve, obtaining the calibration factor Fc in (µmol·mV^{-1}·s^{-1}). Finally, the calibration factor was multiplied by the area of the TCD desorption signal, obtaining the µmol of ammonia desorbed from each sample.

In Valencia, NH_3-TPD profiles were recorded using an Autochem 2910 apparatus (Micromeritics) connected to a quadrupole mass spectrometer (OmniStar from Balzers Instruments). Before ammonia adsorption, approximately 100 mg of sample was pretreated by heating at 450 °C for 30 minutes in pure O_2, followed by 15 minutes in Ar, and then 15 minutes in He. Calibrated pulses of

NH_3 were then introduced at 175 °C until the sample was saturated. The chemisorbed ammonia was desorbed by heating from 175 °C to 900 °C at a rate of 10 °C·min^{-1}. The m/z = 17 signal from the mass spectrometer was used to generate the NH3 desorption profiles.

2.5.5.3 CO_2 temperature programmed desorption (CO_2-TPD)

Technical details: To explore the basic sites on the catalyst's surface, the study also included an investigation of the interaction between CO_2 and the fresh/spent catalysts through CO_2-TPD measurements. Approximately 100 mg of the sample was positioned between layers of quartz wool in a quartz tube reactor and subjected to a helium purge (30 mL·min^{-1}) at 350 °C (10 °C·min^{-1} ramp) for 2 h. Subsequently, the sample was cooled to 50 °C in a helium environment and exposed to 10 vol.% CO_2/He (30 mL·min^{-1}) at 50 °C for 1 h. Following saturation, the system was purged in the He flow (30 mL·min^{-1}) for 30 minutes to eliminate physisorbed CO_2. Desorption was then initiated by incrementally raising the temperature from 50 to 900 °C (10 °C·min^{-1} ramp) while maintaining a helium flow of 30 mL·min^{-1}.

2.5.5.4 Temperature Programmed Combustion (TPC)

Temperature-programmed combustion (TPC) studies were used to quantify the content of carbonaceous deposits in some catalysts.

Technical details: About 50 mg of sample were put in a U-shaped quartz tube for the analysis, and the reactor was heated to 750 °C at a rate of 10 °C·min^{-1} from ambient temperature using a flow of 100 mL·min^{-1} of 5 vol.% O_2/N_2. The concentrations of CO and CO_2 in the gas leaving the reactor were measured with an ABB Uras 14 gas analyzer.

2.5.6 Transmission Electron Microscopy (TEM)

Transmission Electron Microscopy (TEM) is an advanced microscopy technique that enables to image and analyze materials in great detail at the nanoscale. To create detailed images and obtain data about the structure, composition, and crystallography of a thin specimen, TEM works by passing electrons through it [131]. It operates on the same basic ideas as conventional light

microscopes, but instead of photons, it uses electrons. TEM is unique in that it can achieve extremely high resolution, orders of magnitude higher than that of light microscopes. Because electrons have a wavelength that is significantly smaller than that of light, TEM can reveal intricate internal structures, sometimes even at the atomic level, thanks to their remarkable resolution. The operational process involves directing a high-energy electron beam through an extremely thin sample. During this process, interactions between electrons and the atoms within the sample yield crucial information. These interactions enable the observation of features such as crystal structures, as well as structural characteristics like dislocations and grain boundaries. A modern TEM consists of several essential components, including an illumination system, a specimen stage, an objective lens system, a magnification system, one or more data recording systems, and a chemical analysis system [132]. At the heart of the illumination system lies the electron gun or a field emission source. The illumination system also incorporates condenser lenses, which play a pivotal role in generating a precise electron probe for imaging purposes. The specimen stage assumes a critical role in conducting structural analyses, facilitating in-situ observations of phenomena induced by processes like annealing, electric fields, or mechanical stress. This functionality offers the opportunity to characterize the physical properties of individual nanostructures. On the other hand, the objective lens serves as the central component of a TEM, ultimately defining the limits of image resolution. The magnification system includes intermediate and projection lenses, allowing for impressive magnifications of up to 1.5 million times. Finally, the chemical analysis system employs energy-dispersive X-ray spectroscopy (EDS) for the quantitative determination of the specimen's chemical composition. EDS relies on counting X-rays emitted from the region of the specimen illuminated by the electron beam, with the emission spectrum varying based on photon energy.

Technical details: To further investigate the morphology of certain catalysts, transmission electron microscopy (TEM) characterization was conducted using an FEI Tecnai G2 F20 S-Twin instrument operated at an acceleration voltage of 200 kV (instrument used in Italy) or a JEOL JEM 1400 Flash microscope running at 120 kV (instrument used in Valencia). In both cases, the materials were dispersed in high-purity dichloromethane, ultrasonically treated, and after a brief decantation, a droplet was taken from the top of the solution and placed on a copper grid that had been lightly coated in holy carbon before TEM examination. For the iron catalysts supported on carbon nanotubes, the size and location of iron nanoparticles have been determined using TEM microscopy (Transmission Electron Microscopy) operating in the dark field mode. X-ray dispersion

spectroscopy (EDX) was occasionally used in conjunction with the microscopic method to obtain composition maps of specific sample sections that had previously been captured in imaging mode. Ultimately, the crystalline planes in specific metal nanoparticles were examined using the high resolution mode (HR, High Resolution), which was also utilized to evaluate phenomena such as surface passivation or re-oxidation in Fe nanoparticles and investigate their position in relation to carbon carriers. Concerning the passivation treatment on the outside of the iron nanoparticles, it produces a layer of oxide. This reduces the rate at which oxygen diffuses into the nanoparticle, keeping the remaining portion of the nanoparticle in its reduced state and enabling the passivated catalyst to be exposed to the environment without spontaneous oxidation. Fe^0 phase oxidation is a highly exothermic process that can produce hot spots on the catalyst surface, which encourages metal phase agglomeration and re-distribution [133]. In order to study iron catalysts in their reduced state, they were first reduced for 10 hours at 400 °C and subsequently passivated in an atmosphere of 1% O_2/N_2, under room temperature in a quartz fixed bed reactor. They were then kept in that passive environment until the sample was ready for microscopy. The size distributions of Fe nanoparticles were determined by measuring 500-1000 nanoparticles using *ImageJ* on several micrographs taken at various positions on the sample holder grid.

The goal of the TEM analysis made in Valencia was to gather information on the distribution of particle lengths in various regions of the grid, considering the number of particles both inside and outside the nanotubes. After determining the total count, the percentage frequency was calculated.

To calculate the percentage frequency for each length interval, the following formula was utilized, equation (2. 13):

$$\text{Percentage Frequency} = \frac{\text{Number of Counts}}{\text{Total Sum of Counts}} \times 100 \qquad (2.\ 13)$$

Here, "Number of Counts" represents the count of particles within a specific length interval, while "Total Sum of Counts" is the cumulative count sum for all lengths.

2.5.7 Scanning Electron Microscopy (SEM)

The scanning electron microscope, is an extraordinary instrument used in various scientific fields to examine solid samples with an extremely high level of detail. Unlike traditional optical microscopes that use visible light, SEM is a technique employing a focused electron beam to interact with a sample, thereby generating an image depicting its topography and relative composition. Firstly, the sample to be analyzed must be properly prepared, often coated with a thin layer of conductive material to prevent issues with electrical charge during analysis. The heart of the instrument is an electron source, such as a tungsten filament, which produces a high-energy electron beam. This electron beam is focused onto the sample, and when it strikes its surface, various interactions occur. Some electrons are ejected from the sample's surface and are captured by specific detectors. These secondary electrons (SE) and other generated signals, such as backscattered electrons (BSE) and characteristic X-rays, are then processed and used to create an image of the sample's surface and display on a monitor thanks to specialized detectors capture. The formation of an SEM image primarily involves the detection of signals resulting from interactions between the electron beam and the scanned sample. SEM offers a resolution of 10 nm, making it necessary to employ more advanced techniques for analyzing smaller particles [134]. Field emission scanning electron microscopy (FESEM) operates on the same principles as SEM, but employs a field emission electron source instead of a thermionic electron source. In FESEM, the electron beam is emitted through a potential gradient rather than thermal energy. This distinction allows FESEM to produce superior-quality images with higher resolution and a broader range of imaging capabilities compared to SEM, achieving resolutions as fine as 2-3 nm.

Technical details: Scanning electron microscopy (SEM) analyses were performed using a FEI (Hillsboro, OR, USA) model QUANTA INSPECT 200LV microscope. FESEM measurements were carried out by Zeiss MERLIN, Gemini-II column, Oberkochen, Germany. The sample for SEM analysis was prepared following a standard procedure. After thoroughly cleaning the stubs, a small piece of black polymeric was applied as a base to adhere the sample. Once the powder was gently placed on the adhesive part of the tape, light pressure was applied to the sample so that it adhered firmly to the polymeric tape to ensure its stability during subsequent handling.

2.5.8 Energy-Dispersive X-Ray Spectroscopy

Energy-dispersive X-ray spectroscopy (commonly known as EDS, EDX, or XEDS) is a technique employed to identify the elemental composition of a specimen. This technique entails exposing the specimen to X-rays or charged particles, provoking the excitation of electrons within the specimen, leading to the emission of X-rays characterized by specific energy levels [135]. The emitted X-ray energy can be quantified using an energy-dispersive spectrometer, enabling the determination of the specimen's elements. EDS is frequently employed in tandem with scanning electron microscopy (SEM) to scrutinize the surface of specimens. EDX is capable of providing both qualitative and quantitative insights into a specimen [136].

Technical details: Energy dispersive X-ray spectroscopy was used to examinate the atomic composition of some samples. The FESEM and SEM analysis equipment employed are reported in Section 2.5.7.

2.5.9 X-Ray Photoelectron Spectroscopy (XPS)

An effective analytical method for examining the chemical and electrical characteristics of a material's surface is X-ray photoelectron spectroscopy, or XPS. The electrons that are located of the atoms are excited when X-rays are directed towards a sample's surface, and the kinetic energy of the ensuing released electrons is measured. The elemental composition, chemical state, and bonding inside the material's surface are then determined using this data. Because XPS can detect surface variations with remarkable sensitivity and can provide atomic-level information, it is useful for a wide range of applications, such as the analysis of biological systems, electrical devices, and catalysts. The method's foundation is the photoelectric effect, which was discovered in the late 19th century and later explained by Albert Einstein.

A sample is subjected to soft X-rays with energy less than around 6 keV in order to conduct the analysis. The resulting electrons' kinetic energy is then measured (Figure 2.2, a). When the energy from the X-ray is converted to an electron at the sample's core, photoelectron emission happens. Equation (2. 14) can be used to describe this phenomenon:

$$h\nu = BE + KE + \Phi_{spec} \quad (2.\ 14)$$

In this equation hν denotes the energy of the X-ray, BE represents the binding energy of the electron (how strongly it is bound to the atom or orbital it is associated with), KE is the kinetic energy of the emitted electron, and Φ_{spec} is a constant referred to as the spectrometer work function. The binding energy of an electron is an intrinsic property of the material and remains unaffected by the X-ray source used for emission. However, the kinetic energy of the emitted photoelectrons varies depending on the X-ray source, as defined by the above equation. In an XPS experiment, any electron with a binding energy lower than the energy of the X-ray source will be emitted and detected.

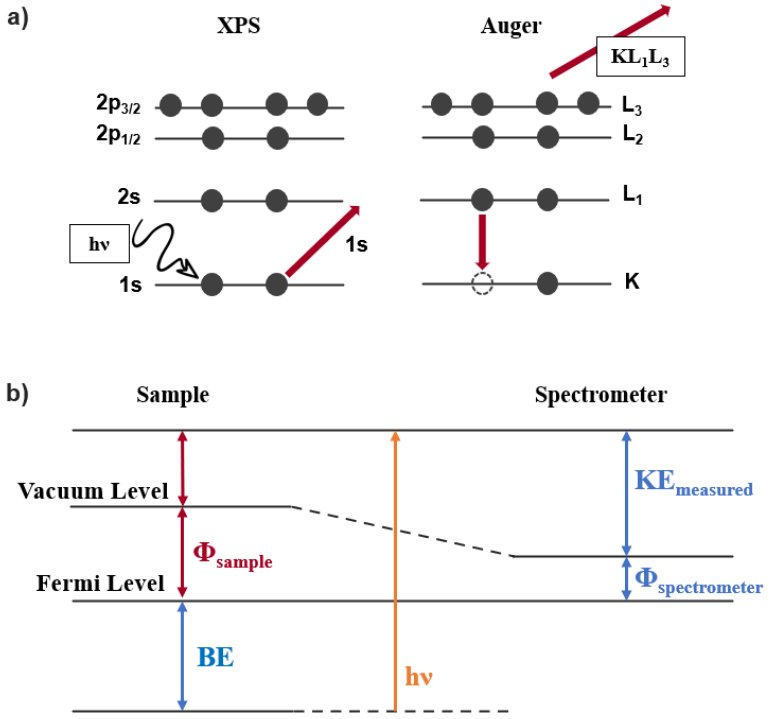


Figure 2.2. a) Processes that result from X-ray bombardment of a surface include emission of a photoelectron on the left and emission of an Auger electron on the right; b) Energy level diagram illustrates the basic XPS equation (2. 14) schematically.

In XPS, an excited and removed core electron leaves behind a "hole" in the core. A valence orbital electron can fill the hole and cause this excited and ionized state to relax. Energy released by this process can appear as either the emission of an Auger electron (Figure 2.2, b) or X-ray fluorescence. Particularly interesting, Auger electrons are frequently employed in XPS for qualitative investigation. The

binding energies of particular orbitals in the parent atom dictate the kinetic energy of an Auger electron and are not reliant on the energy of the X-ray source. Thus, the X-ray excitation energy has no effect on the kinetic energy of the Auger electron.

Technical details: In Italy, X-ray photoelectron spectroscopy (XPS) was utilized to investigate the catalyst's surface using a PHI 5000 Versa Probe device. For survey scans, a band-pass energy of 187 eV, a 45° take-off angle, and a 100 μm X-ray spot diameter were utilized; for high-resolution (HR) spectra, a band-pass energy of 23 eV was utilized. The semi-quantitative atomic concentration and fitting techniques were gathered using CasaXPS 2.3.23, a specially designed tool from Casa Software Ltd. in Wilmslow, UK.

2.6 Catalytic tests conducted in Italy

In Italy, the catalytic tests were conducted using a test bench (Figure 2.3) equipped with three supply lines, each controlled by a flow regulator. The system includes a Programmable Logic Controller (PLC) that manages temperature setpoints and controls the opening and closing of pneumatic valves (PV). These actions depend on whether the reactive mixture is directed into the reactor (PV-02 and PV-04 open, PV-03 closed) or through the bypass line (PV-03 and PV-02 open, PV-04 closed). Similar control and safety systems are in place on the feed line and at the entrance of the gaseous mixture into the reactor. PV-01 regulates the feed and takes action if the PT-01 sensor detects pressure exceeding the maximum of 28 bar. In case of a malfunction, a secondary safety measure is activated: the PSV-01 valve, set to target a pressure of 33 bar. The control and safety system PV-05/PT-05/PIC-05 and PSV2 functions similarly, programmed for the same pressure conditions.

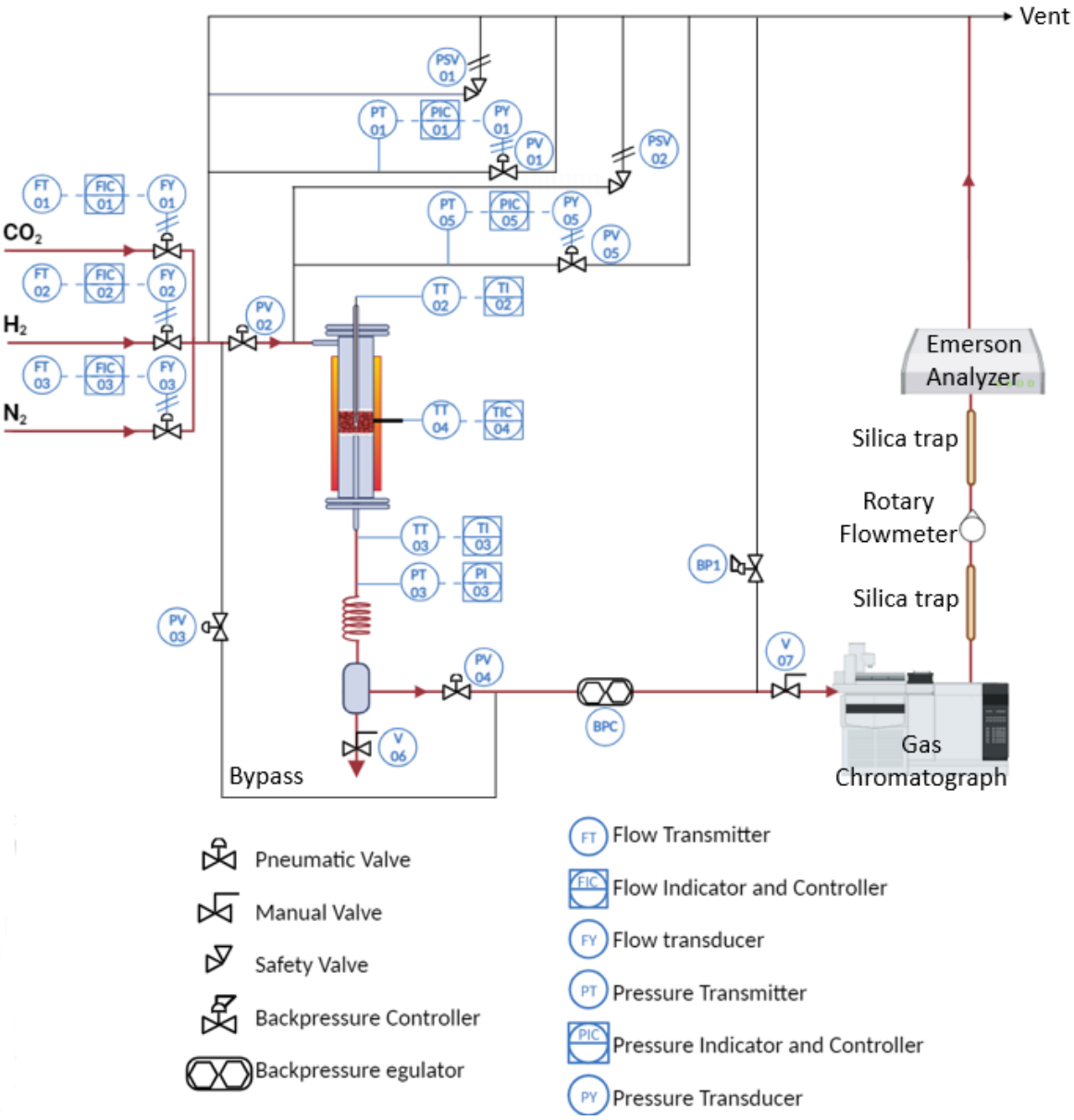


Figure 2.3. Italy test bench plant.

A back pressure controller (BPC) maintains the pressure according to the present value. Positioned after the reactor, the BPC prevents pressure fluctuations that could affect instrument performance. Overall, the catalytic performance evaluation is conducted in a fixed-bed stainless steel reactor with an 8 mm inner diameter and incorporates an inner tube (thermowell) with a 3.2 mm diameter. Inside this thermowell, a sliding thermocouple (TT 02) is positioned, allowing for

continuous monitoring of the temperature profile during the catalytic process within the annular section of the reactor. In addition, the reactor is heated by a refractory furnace, which is equipped with an additional thermocouple: TT 04. The catalyst's position, immobilized by quartz wool, is optimized for consistent testing conditions as depicted in Figure 2.4.

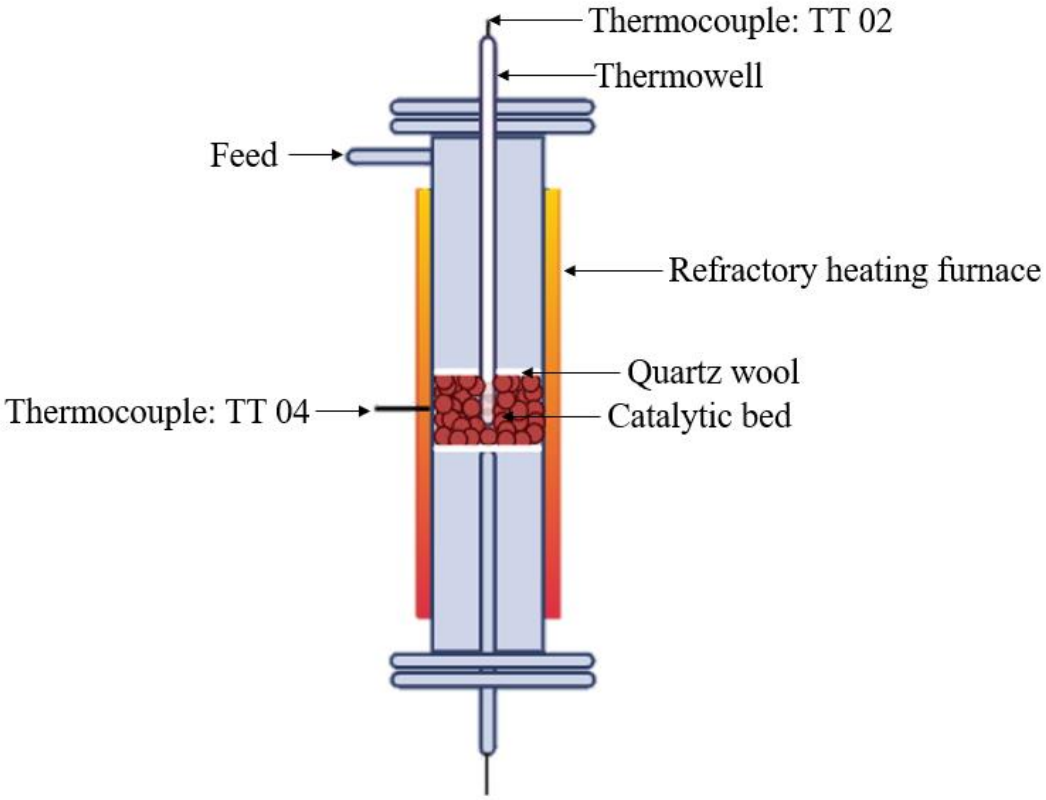


Figure 2.4. Italy Reactor Configuration.

To ensure consistent testing conditions, the catalyst load is standardized at 1.0 g for assessment of iron catalyst and at 2.0 g when the iron catalyst is combined with zeolite in a 1:1 mass ratio. This maintains a constant space velocity in the experiments with respect to the iron catalyst. The catalyst undergoes in-situ pretreatment with a 50 vol.% H_2/N_2 mixture at 360 °C for 3 h.

The catalytic tests were conducted at 330 °C, 2.3 MPa pressure, and a flow rate of 22 $NL \cdot g^{-1}_{Fe3O4} \cdot h^{-1}$ ($H_2/CO_2/N_2$=15/5/3, where N_2 is used as internal standard for GC, while H_2/CO_2=3 mol/mol). The gaseous hydrocarbon products generated during these tests were meticulously analyzed and quantified using an

online gas chromatograph (Agilent Technologies, 7890B GC System). This device was equipped with:

- Heated transfer line (maintained at 120 °C, atmospheric pressure)
- Two-column separation system arranged in series:
    1. HP-5 column, with 5% phenyl-methylpolysiloxane stationary phase, designed for heavier hydrocarbons.
    2. HP-PLOT Q column, composed of polystyrene-divinylbenzene, utilized for hydrocarbon components up to C_{10}.
- Two detectors:
    1. thermal conductivity detector (TCD)
    2. flame ionization detector (FID).

The separation method is chosen for improved chromatogram resolution without significantly prolonging elution times and helium was employed as the carrier gas at a constant flow of 2 mL/min.

The analysis program includes (Figure 2.5):

- Initial equilibration: 40 °C for 3 minutes;
- Ramp 1: Gradual temperature increase of 2 °C·min^{-1} until reaching 58 °C;
- Ramp 2: Steep temperature increase of 30 °C·min^{-1} until reaching 250 °C, with 8.3 minutes at this temperature;
- Ramp 3: Rapid temperature increase of 60 °C·min^{-1} until reaching 60 °C; with a 4-minute maintenance. A valve switch directs the eluent flow to the second column (HP-PLOT Q);
- Ramp 4: Moderate temperature increase of 7 °C·min^{-1} until reaching 250 °C, with 8.8 minutes at this temperature;
- A 10-minute post-run at 250 °C is implemented to cleanse the columns.

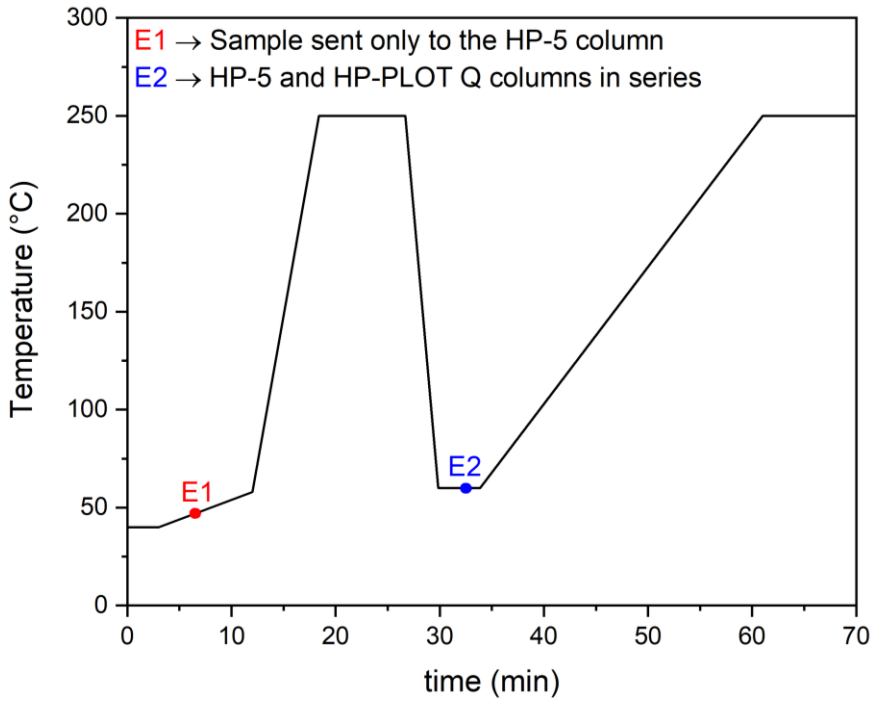


Figure 2.5. Details of the analysis program, outlining temperature ramps and isothermal intervals employed to achieve an effective separation of mixture components.

In addition, a real-time monitoring of CO, CO_2, and H_2 molar fractions, carried out using an in-line gas analyzer (Emerson X-STREAM). This analyzer was outfitted with two nondispersive infrared (NDIR) sensors and a thermal conductivity detector (TCD).

Instead, regarding the heavier hydrocarbons, they were condensed at room temperature and at a pressure of 2.3 MPa. The liquid extracted from the tests exhibited two distinctive phases: an aqueous phase composed of water and polar compounds, and an oily phase consisting of C_{6+} hydrocarbons (Figure 2.6). Subsequently, the oily phase underwent qualitative analysis using GC-MS. As a result, the selectivity for C_{6+} compounds was determined as complementary to 100 % in relation to the continuously analyzed gaseous products and the presence of oxygenated compounds. These latter were, in turn, analyzed through high-performance liquid chromatography (HPLC) and total organic carbon (TOC) techniques.

The analytical technique enabling a detailed analysis and identification of the extracted oil's composition is gas chromatography-mass spectrometry (GC-MS). This is a serial system that combines a gas chromatograph with a mass spectrometer, facilitating the identification of compounds (Figure 2.6).

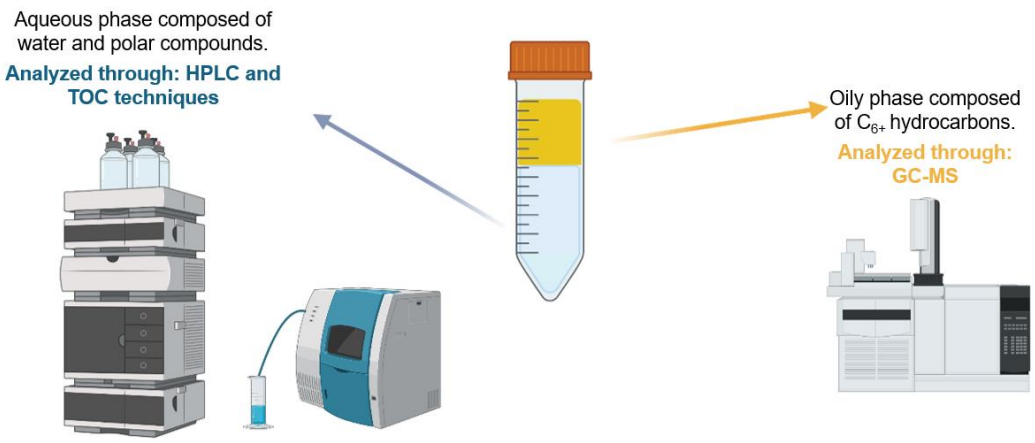


Figure 2.6. System for the Analysis of Liquid Reaction Products.

The operating principle is as follows: the injected sample undergoes vaporization and it is mixed with the carrier gas, serving as the mobile phase. This gaseous mixture crosses the chromatographic column, where its components are separated based on their distinct affinities with the stationary phase. To remove the compounds retained on the column, a temperature ramp can be implemented. This temperature ramp weakens the bonds between the mobile and stationary phases, promoting the release of products at different retention times. Upon exiting the column, the mixture enters the mass spectrometer, featuring an ionization system that imparts an electric charge to the molecule, causing its decomposition into elementary components. Compounds not ionized are removed using a vacuum system. The obtained ions are separated based on their mass and charge, allowing the final detector to measure the different fragments of each compound and assemble them to provide comprehensive information about the molecule under examination. The instrument possesses a library of compounds for comparison with the analyzed one, yielding a series of molecules that closely mirror the conducted analysis. The detector provides the operator with information about the type of compound and the reliability of the result, expressed in terms of the probability that the analyzed molecule matches the description given by the equipment. In the case study, to analyze the hydrocarbon mixture referred to as 'oil,' the gas chromatograph with a mass detector used was the 5975C Series GC/MSD System by Agilent Technologies.

The instrument is equipped with:

- *A split/splitless (SSL) injection system:* in this instance a split mode of 1:10 enabling the entering mixture to be divided into two parts: one that is

transmitted to the column and the other that is not evaluated. The highly concentrated samples under examination allowed for better resolved peaks and prevented column saturation, which is why the split mode was selected.

- *Capillary Column:* It's a J&W 122-5532 column with dimensions of 30 m x 25 mm x 0.25 μm. This column is made of silica and has a 5% phenyl-methylpolysiloxane stationary phase. It works well across a broad temperature range, from -60 °C to 300 °C.
- *Mass Spectrometer (MSD):* This instrument directs ions to the detector using a quadrupole mass analyzer. The ionization system has a hyperbolic quartz electrode coated with a thin layer of gold. When heated, it emits electrons toward the sample for ionization. The ionized molecules then move towards the detector, while the ones not affected by the electron beam (remaining neutral) are removed by the vacuum pump.
- *Vacuum System:* It consists of two turbomolecular pumps, creating high vacuum conditions ($p \sim 10^{-5}$ mbar).

To separate the compounds, after injection, the system initiates a temperature ramp to desorb the components interacting with the stationary phase at different elution times. It was necessary to find an optimal temperature ramp for the hydrocarbon compounds obtained from the reaction. The process can be summarized as follows:

Injection of the mixture with a helium flow (8.35 mL/min for the entire process), Figure 2.7.

- Initial equilibration: 40 °C for 3 minutes;
- Ramp 1: Heating at 1 °C·min^{-1} until reaching 60 °C;
- Ramp 2: Heating at 3 °C·min^{-1} until 100 °C;
- Ramp 3: Heating at 5 °C·min^{-1} until 150 °C;
- Ramp 4: Heating at 10 °C·min^{-1} until 250 °C;
- Ramp 5: Heating at 20 °C·min^{-1} until 300 °C;
- Post-run at 300 °C for 10 minutes to clean the lines.

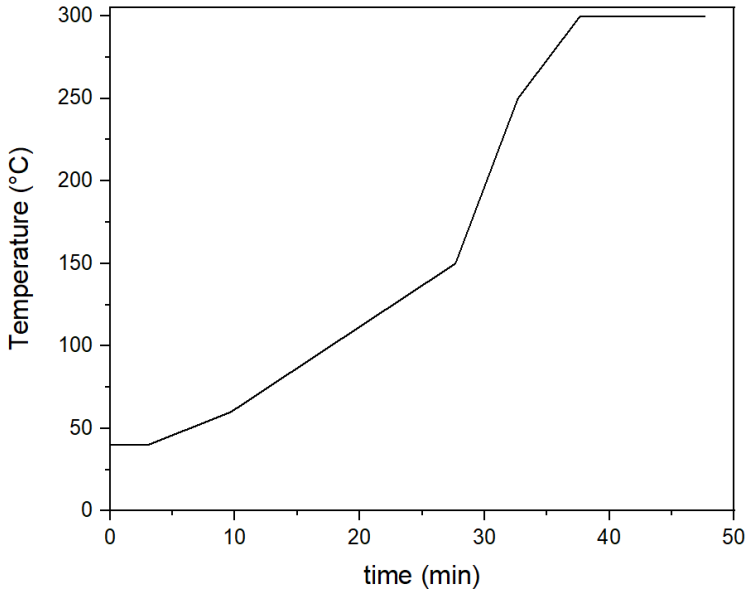


Figure 2.7. Details of the analysis program, outlining temperature ramps employed to achieve an effective separation of mixture components.

Concerning the analysis of water, as mentioned earlier, examinations were carried out utilizing HPLC and TOC. High-Performance Liquid Chromatography (HPLC) is a chromatographic method functioning under high pressures. Unlike the previously described gas chromatography, the separation of the mixture takes place in the liquid phase. The injected sample undergoes vaporization and mixing with the carrier gas to form the mobile phase. This gaseous blend, subjected to elevated pressures (up to 300 atm) through a pump, is introduced into the chromatographic column. Within the column, components segregate based on their interactions with the stationary phase. Elution can be either isocratic or gradient, wherein the concentration of the mobile phase varies to hasten the departure of components that interact more significantly with the stationary phase.

The equipment employed was a Shimadzu HPLC analyzer, specifically the Prominence model, composed of various modules including a degassing unit DGU-20A, a gradient elution system, an LC-20AT pump, an automatic injection system SIL-20 A HT-Autosampler, a control system CBM-20A, and a RID detector that gauges the refractive index change of the eluent in response to the presence of the analyte.

Another examination conducted on water was Total Organic Carbon (TOC), measuring the “total organic carbon”. This instrument assesses the overall amount of carbon dispersed in water in the form of organic components such as

hydrocarbons and alcohols. To calculate this parameter, the total amount of organic and inorganic carbon (TC) is determined. The sample is conveyed to an internal combustion chamber where oxygen is supplied while maintaining a temperature between 600 and 700 °C. In this setting, all organic compounds react with excess oxygen to combine with all the carbon dissolved in the water. The resultant combustion gases, having been cooled and transmitted to an analyzer, facilitate the measurement of the quantity of CO_2 generated.

Upon ascertaining the total carbon (TC), the determination of inorganic carbon follows acidification of the sample, which reacts according to the following reaction:

$$CO_3^{2-} + H^+ \rightarrow CO_{2(g)} + H_2O$$

The formed CO_2, measured in relation to the organic fraction, provides the inorganic carbon (IC). Therefore, Total Organic Carbon (TOC) is derived as the disparity between TC and IC Equation (2. 15).

$$TOC = TC - IC \qquad (2.\ 15)$$

The instrument TOC-VCSH purchased by Shimadzu was used with a flow of150 $mL \cdot min^{-1}$ of purified air at 680 °C. The obtained gas undergoes cooling and dehumidification, with the CO_2 detection system adopting a Non-Dispersive Infrared (NDIR) methodology. The machine is programmed to conduct repeated measurements, up to a maximum of five times on the same sample, aiming to minimize errors.

2.6.1 Data processing

The aim of the following subsection is to describe the methodology employed in processing raw experimental data.

As previously described (Section 2.6), the plant is equipped with a gas chromatograph (GC) featuring two detectors (FID and TCD) connected on-line. This setup allows for continuous sampling and analysis of the gas mixture produced. An additional layer of online monitoring is provided by an elemental analyzer (connected in series to the GC), which measures the concentration of various gases exiting the reactor, with particular emphasis on the percentage of

CO. Regarding liquid products, they are extracted after each trial and analyzed using GC-MS, TOC, and HPLC, as described in Section 2.6.

The data processing was developed based on the various measurements provided by the instruments, aiming to obtain both quantitative information (through the elemental analyzer, GC-TCD/FID, HPLC, and TOC) and qualitative (GC-TCD/FID, GC-MS, and HPLC). This allowed for a comprehensive understanding of CO_2 conversion and selectivity to CO, CH_4, and higher (C_{2+}) hydrocarbons up to C_6. The selectivity for the liquid oil extracted in each trial could not be calculated due to the inability to quantify and identify the wide range of hydrocarbon products in detail. However, qualitative information was obtained through GC-MS analysis, which, using a mass spectrometer and a dedicated library, enabled differentiation between paraffins, olefins, and aromatics.

The calculations, summarized below, aim to determine the conversion of CO_2 and the selectivity towards the obtained products. The calculation method is based on the data measured and monitored by the online-connected elemental analyzer and GC-TCD/FID. Specifically:

- TCD measures the concentration of CO_2, CO, and nitrogen, kept constant during the trial.
- FID determines the distribution of gaseous hydrocarbon products.
- The elemental analyzer measures the concentration of CO in the output.

Initially, the reactive mixture is directed to the bypass for analysis of its actual composition using gas chromatography (GC). This mixture results from the blending of on-line gas streams whose flows are controlled by mass flow controllers. During this stage, the gas chromatograph conducts three samplings of the mixture and provides measurements graphically displayed on the chromatogram in the form of peaks.

Each peak on the chromatogram corresponds to a distinct compound, and the graphical integration of each peak determines the amplitude of the total area beneath it. The calibration curves for each identified component are then employed to convert the peak amplitude to the corresponding molar concentration of the component within the analyzed gas mixture, according to the following equation (2. 16):

$$A_{c_i} = m \cdot \left(\frac{\%y}{100}\right)^a + q \quad (2.\ 16)$$

This equation represents a power-law where m, a, q respectively stand for the slope, exponent, and y-intercept; while A and %y represent respectively the peak area and the percentage molar concentration associated with each identified component. It's worth noting that if, during calibration, the exponent 'a' turns out to be approximately equal to 1 (1±0.05), it can effectively be assumed to be 1, transitioning from a power-law to a linear law.

Consequently, the data obtained from gas chromatograph measurements are utilized to estimate the average composition of the reactive mixture: for each compound, the arithmetic mean of the results from the three measurements is calculated. To specify, from the integration of the TCD signal, it is possible to determine the initial concentrations of CO_2 and N_2 ($y_{CO_2,in}$ and $y_{N_2,in}$), and, given the total volumetric flow rate ($\dot{V}_{tot,in}$), was allowed to calculate their respective initial volumetric flow rates ($\dot{V}_{CO_2,in}$ and $\dot{V}_{N_2,in}$), the equations (2. 17) and (2. 18) below resume the calculation made.

$$\%y_{CO_2,in} = \frac{Area_{CO_2}}{m_{CO_2}} \rightarrow \dot{V}_{CO_2,in} = \dot{V}_{tot,in} \cdot y_{CO_2,in} \quad (2.\ 17)$$

$$\%y_{N_2,in} = \frac{Area_{N_2}}{m_{N_2}} \rightarrow \dot{V}_{N_2,in} = \dot{V}_{tot,in} \cdot y_{N_2,in} \quad (2.\ 18)$$

In this way, estimating the molar compositions and the total outlet flow, it is possible to assess for each component the corresponding molar flow, equation (2. 19).

$$\dot{n}_{i,out} = y_{i,out} \cdot \left(\frac{\dot{V}_{out}}{22.414}\right) \quad (2.\ 19)$$

Where 22.414 $L \cdot mol^{-1}$ represents the molar volume of an ideal gas under standard temperature and pressure (STP) conditions, which correspond to 0 °C (273.15 K) and 1 atm.

Once the N_2 flow is calculated, it is known that nitrogen is inert to the reaction and thus remains constant. This is crucial as the retention times of CO and N_2 are similar, and therefore, the peak detected by the TCD will be cumulative of both concentrations. Knowing the CO concentration is essential to remove its contribution and measure the nitrogen percentage change, from which the total flow can be determined. To achieve this, the percentage of CO measured by the analyzer at the reactor system's output is considered. The following equations (2. 20), (2. 21) and (2. 22) summarize the calculations performed.

$$Area_{CO} = \%y_{CO(analyzer)} \cdot m_{CO} \tag{2. 20}$$

$$Area_{N_2} = Area_{CO+N_2} - Area_{CO} \tag{2. 21}$$

$$y_{N_{2,OUT}} = \frac{Area_{N_2}}{m_{N_2}} \tag{2. 22}$$

The overall outlet molar flow rate ($\dot{n}_{out}$) was calculated under the assumption that the inert nitrogen molar flow rate remained constant throughout the process, as expressed in equation (2. 23), where $\dot{n}_{in}$ (mol·s^{-1}) represented the total inlet molar flow rate, and $y_{N_2,in}$ and and $y_{N_2,out}$ denoted the inlet and outlet N_2 molar fractions.

$$\dot{n}_{tot,out} = \frac{y_{N_2,in}}{y_{N_{2,out}}} \cdot \dot{n}_{tot,in} \tag{2. 23}$$

The amount of CO_2 that has been converted into products (ζ_{CO_2}), and the selectivity (σ_i) for the generic i-th product were calculated according to equations(2. 24) and (2. 25), respectively:

$$\zeta_{CO_2} = \frac{\dot{n}_{CO_2,in} - \dot{n}_{CO_2,out}}{\dot{n}_{CO_2,in}} \tag{2. 24}$$

$$\sigma_i = \frac{\dot{n}_{C,i,out}}{\dot{n}_{CO_2,conv}} = \frac{N_{C,i} \cdot \dot{n}_{i,out}}{\dot{n}_{CO_2,in} - \dot{n}_{CO_2,out}} \tag{2. 25}$$

Where $\dot{n}_{CO_2,in}$ and $\dot{n}_{CO_2,out}$ are inlet and outlet carbon dioxide molar flow rate, respectively. $N_{c,i}$ represents the number of carbon atoms in a produced

species, since selectivity is evaluated on carbon atoms balance instead of a stochiometric relation between reactants and products.

Regarding the quantitative description of the gaseous hydrocarbon mixture at the output, reference is made to the FID signal, sensitive to C-H bonds. In this case, the calibrated components do not cover the entire spectrum of produced hydrocarbons. For the calibrated compounds, knowing the calibration factor (m), the percentage concentration is calculated as shown in equation (2. 26):

$$y_{C_n} = \frac{Area_{FID}}{m_{C_n}} \tag{2. 26}$$

In terms of the FID response factor, calibration was performed for the most significant light hydrocarbons, including methane, ethylene, ethane, propylene, propane, 1-butylene, n-butane, 1-pentene, and n-pentane, using certified cylinders. For other compounds, the response factor of the FID was estimated based on the procedure proposed by Scanlon and Willis [137]. For the non-calibrated compounds, a proportionality between the area of the uncalibrated compound X and that of a calibrated reference compound R is exploited in the equation (2. 27) reported below:

$$A_R : y_{R\%} = A_X : y_{X\%} \rightarrow y_{X\%} = f \cdot A_X \cdot \frac{C_R}{A_R} = f \cdot A_X \cdot m_R \tag{2. 27}$$

Where f is a "relative molar response coefficient", A_X is the area under the peak of the eluted compound, and m_R is the calibration factor of the reference. In it important to note that the coefficient f is calculated according to following system:

$$\begin{cases} f(R.wt) = MW_X ECN_R / MW_R ECN_X \\ f(R.mol) = F(R-wt) \cdot MW_R / MW_X \end{cases} \rightarrow f(R.mol) = \frac{ECN_R}{ECN_X}$$

Where MW represents the molecular weight of the compound in question, f is the relative response coefficient that can be calculated on a molar or mass basis, and ECN is the effective carbon number of the compound.

The molar response coefficient, f(R.mol), is calculated for different compounds by referring to calibrated components that closely match the carbon number of the component in question. This allows the calculation of

concentrations, $y_{X\%}$, for all components in the gas mixture. Once known, their flow rate and selectivity are then calculated.

For each hydrocarbon class (j, grouping all molecules having the same number of carbon atoms, including isomers) the olefinic share for hydrocarbon classes between C_2 and C_5 has been defined and calculated as the ratio between olefins amount and the whole hydrocarbon production (i.e., paraffins plus olefins), equation (2. 28).

$$OS_j = \frac{\dot{n}_{j,O}}{\dot{n}_{j,O} + \dot{n}_{j,P}} \tag{2. 28}$$

The total gas selectivity is calculated as the sum of carbon produced in the form of CO and hydrocarbons; its complement to one corresponds to the total liquid selectivity. So, in order to determine the total selectivity towards oil, it is necessary to subtract from the liquid selectivity the carbon converted into polar components dissolved in the aqueous solution. Through TOC analysis, it is possible to determine the total amount of carbon dissolved in the aqueous phase. The total carbon content may be affected by acetone used during the plant washing phase between tests. To eliminate this contribution, the carbon derived from acetone, calculable from HPLC analysis, is subtracted from the carbon content calculated by TOC. Therefore, the selectivity for C_{6+} compounds was calculated as the complement to 100 with respect to the continuously analyzed gaseous products and the amount of oxygenated compounds.

2.7 Catalytic tests conducted in Spain

An additional series of experiments was conducted at the Instituto de Tecnología Química in València (ITQ). Figure 2.8 illustrates a simplified schematic of the reactor and other elements of the reaction system. The fixed-bed reactor used in these experiments was designed and fabricated at the ITQ using 310 stainless steel, featuring an inner diameter of 10.3 mm and a length of 40 cm [138]. This reactor is particularly noteworthy for its dual temperature control system, ensuring a consistent temperature distribution along the catalytic bed, even during exothermic reactions. It is heated by two 400 W electric resistences, each autonomously regulated by electronic devices (Philips KS40) with PID

adjustment. Inside the reactor, there is a 316 stainless steel thermowell running longitudinally along the central axis, with an external diameter of 3 mm. Three type K thermocouples (0.05 mm diameter, Inconel® 600 alloy) are positioned within the thermowell, evenly spaced along the entire length of the catalytic bed. The upper and lower thermocouples correspond to the measurement points of the PID control systems connected to the higher and lower heating electric resistences, respectively. In contrast, the central thermocouple serves as a mobile probe, recording the longitudinal temperature profile along the catalytic bed at any point during operation. Notably, it operates independently of any control loop.

Additionally, the reaction system incorporates three mass flowmeters for gases (H_2, CO_2, and Ar), each with three downstream check valves, a hydraulic manometer, a three-way valve, and a safety valve connected to a vent outlet. It's crucial to emphasize the capability of diverting gases through a bypass line, directly connected to the pressure regulation valve (Badger-Meter), preventing their entry into the reactor. This feature is significant for analyzing the reagent mixture before each catalytic test. Moreover, for the experimental campaigns, the CO_2 flowmeter was directly connected to a certified high-pressure cylinder (supplied by Abelló-Linde) with the desired H_2/CO_2/Ar composition (in this case, with a volumetric ratio of 6/2/1, where Ar was used as internal standard for GC analysis).

Naturally, prior to initiating catalytic testing, all flowmeters underwent calibration at room temperature and atmospheric pressure. In order to do this calibration, a calibrated bubbler that measures the linear displacement rate of bubbles produced by gas passing through a water column that contains surfactant downstream of the flowmeters was used. Across the entire flow range employed for calibration, the flowmeters exhibit a linear response.

The test bench is also equipped with two traps, identified as “trap 1” (T1) and “trap 2” (T2), have been strategically placed (Figure 2.8). These traps are pressurized during experiments and maintained at temperatures of 150 °C and 100 °C, respectively. Continuing along the flow line, a pneumatic pressure regulation valve has been allocated, along with a connecting line that links the reactive system to the gas chromatography equipment, the gas chromatograph, and, finally, a vent line. Additionally, to prevent the condensation of any products, the line connecting the reactor to the gas chromatograph is heated to 200 °C. Moreover, in order to ensure that any deposits from the less volatile products analyzed online are removed, a low-pressure N_2 auxiliary line is used to purge the connection line

between the pressure regulation valve and the gas chromatograph in between analyses.

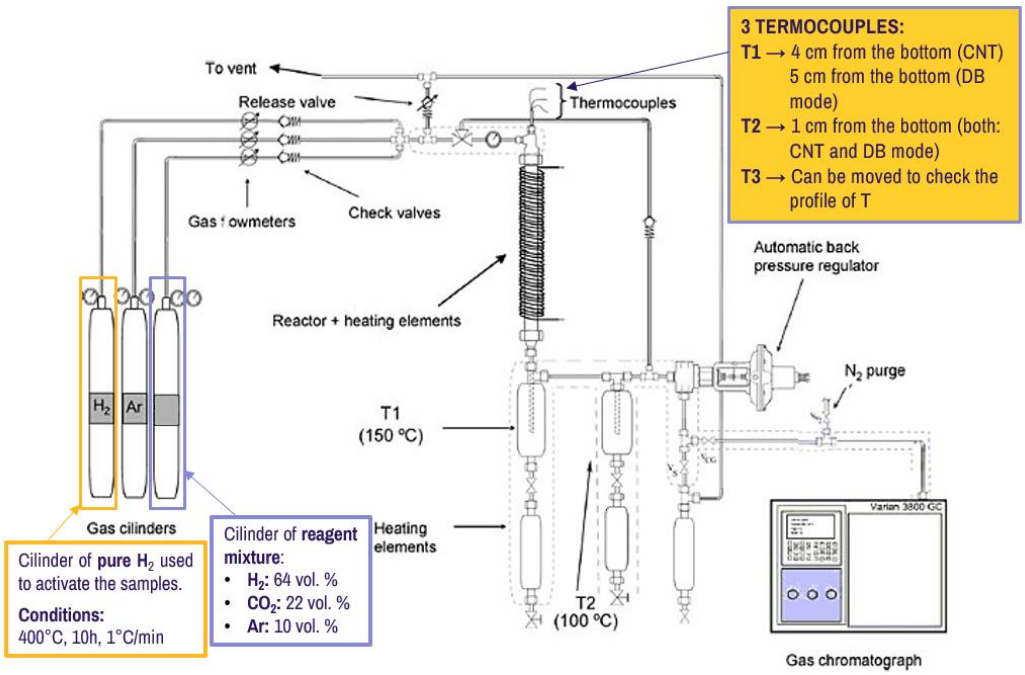


Figure 2.8. Valencia test bench plant.

The entire reaction system is safely enclosed within a cabinet featuring a powerful extraction mechanism. Additionally, the laboratory setup incorporates both a stationary CO detector (Drager Regard-1) with a sensitivity of 1 ppm and a portable CO sensor (Drager Micropac St-Ds) with a sensitivity set at 5 ppm.

2.7.1 Experimental procedure in catalytic tests

Prior to going into great detail about the catalytic tests that were performed on the Valencia test bench, it is crucial to note that three separate works were carried out; the main aspects of each are highlighted below:

1. Evaluate the sodium migration in iron-based catalysts supported on carbon nanotubes with different diameters, varying iron percentages, and iron location (in or out the carbon nanotubes), and with different degrees of contact (granule mixing and powder mixing) with the commercial zeolite CBV 5524G (refer to Chapter 4).

2. Assess sodium migration by varying the characteristics of MFI-type ZSM5 zeolites. Specifically, examine the effects of Si/Al ratio, mesoporosity, crystal size, passivation of surface layers with SiO_2, and the exchange of Brønsted acid sites with sodium (refer to Chapter 5).

3. Evaluate the effect of different zeolite frameworks (USY, BEA, ZSM-5, ZSM-22, MCM-22 and ITQ-2) on the selectivity for liquid hydrocarbon compounds. In this case, catalytic tests were performed in a dual-bed mode to avoid alkali migration effects, using a bulk iron-based catalyst (refer to Chapter 6).

Of course these points will be thoroughly deeply covered and fully examined in the chapters to follow.

The details of the reactor loading protocols, the thermal treatment conditions for catalyst reduction, and the catalytic test conditions are provided below. Additionally, the outcomes of the analysis and product identification are also provided.

2.7.2 Reactor loading protocols

Various reactor loading protocols have been adopted to align with the specific objectives of each experimental campaign. The procedures mainly differ between experiments involving carbon nanotubes (Procedure A) and those focused on studying the effect of zeolite in a double-bed mode (Procedure B).

Procedure A:

For the first two experimental campaigns, catalytic tests were conducted using two distinct integration methods for combining the iron catalyst and the zeolite: *granule mixing* and *powder mixing*.

- In the *granule mixing* approach, 0.7 g of CNT pellets and 0.7 g of zeolite pellets were physically mixed, both with a granulometry of 0.2–0.4 mm. The mixture of pellets was then carefully diluited with the appropriate amount of SiC granules (Carlo Erba) with a particle size of 0.6-0.8 mm to obtain a total bed volume of 5 cm^3 (height 4 cm) in the reactor.
- In the *powder mixing* mode, 1 gram of the desired carbon nanotubes was thoroughly mixed for 5 minutes in a mortar with 1 gram of the selected zeolite. The powder mixture was then pelletized (0.2-0.4 mm) and 1.4 g of

obtained pellets were and diluted with SiC (0.6–0.8 mm) until reaching a height of 4 cm in the reactor. Zeolite-free catalytic tests were carried out by loading 0.7 g of CNT-supported Fe catalyst pellets (0.2–0.4 mm) diluted with SiC (0.6–0.8 mm) to achieve a catalyst bed volume of 5 cm^3.

Figure 2.9 illustrates the different bed configurations used in the tests with only Fe/CNT and bifunctional Fe/CNT+ zeolite catalysts.

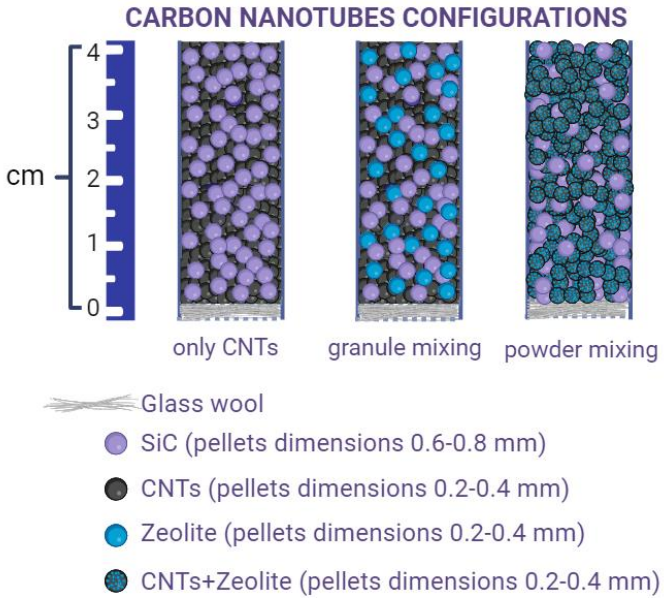


Figure 2.9. Carbon nanotubes configurations.

Procedure B:

In the third experimental campaign, were simulated the *granule mixing* and the *dual bed* mode:

- Concerning *granule mixing* 0.7 g of 1NaFe (synthesis described in Section 2.4.1) and 0.7 g of the desired zeolite (0.2–0.4 mm) were diluted with SiC granules (0.6–0.8 mm) until a total bed volume of 6.4 cm^3 was reached.
- Regarding *double-bed* mode 0.7 g of zeolite pellets (sieved with particle sizes of 0.2–0.4 mm) were physically mixed with SiC pellets (0.6–0.8 mm) and loaded into a fixed bed reactor to obtain a total bed volume of 3 cm^3 (height 2.4 cm). Subsequently, a layer of quartz wool was inserted (occupied height 0.5 cm), and finally, 0.7 g of 1NaFe pellets (sieved to the same size as zeolite particles: 0.2–0.4 mm) were loaded and physically

mixed with the appropriate amount of SiC pellets to obtain a volume of the iron bed + SiC of 2.6 cm^3 (height 2.1 cm). The test with the 1NaFe bulk catalyst alone was conducted by simulating a double bed mode, loading only SiC in the lower part and maintaining a total bed volume of 6.3 cm^3 (height 5 cm).

To facilitate understanding of the reactor loading, a representative image is provided below (Figure 2.10. Bulk iron configurationsFigure 2.10).

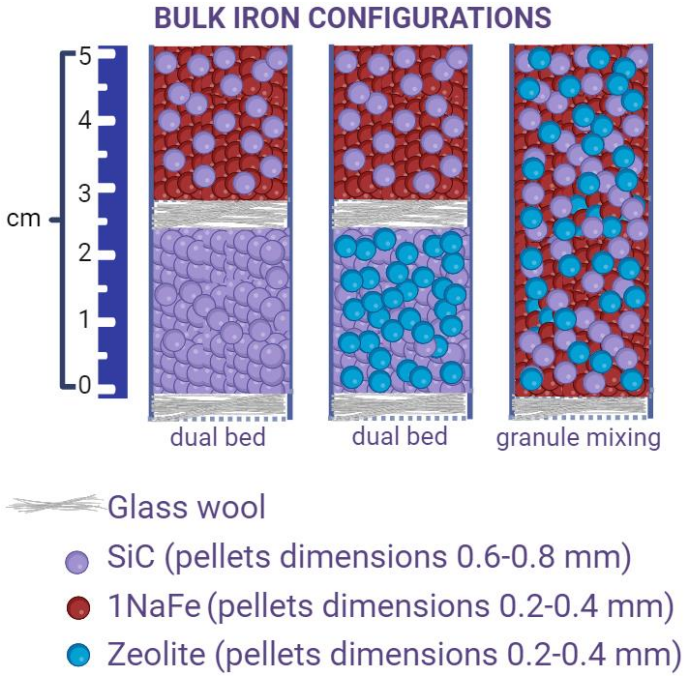


Figure 2.10. Bulk iron configurations.

Nevertheless, in both the procedures, the catalytic bed was supported by a base composed of compacted glass wool with a thickness of 0.5 cm. Furthermore, in order to ensure the homogeneity of the catalytic bed and to avoid differences in local volumetric concentration of the catalyst along the bed, which can lead to hotspots in regions with a higher local catalyst/SiC ratio due to the exothermic nature of the CO_2 hydrogenation reaction, the bed loading was carried out in three aliquots containing equal masses of catalyst and SiC. Once the reactor was sealed, it underwent a leak test for 30 min, feeding Ar until the total pressure was 2.0 MPa (working pressure during the catalytic experiment).

2.7.3 Activation and Start-up of the Catalytic Experiment

Before starting the catalytic test, each catalyst was in-situ reduced in a flow of H_2 (200 $cm^3 \cdot min^{-1} \cdot g_{cat}^{-1}$), in this case g_{cat} is referred independently to 0.7 g of Fe/CNT or 1NaFe, at a temperature of 400 °C (thermal ramp of 1 °C·min^{-1}) for 10 hours at atmospheric pressure. Subsequently, the reactor was cooled to 100 °C, always in a flow of H_2, and a mixture of reaction gases (H_2:CO_2:Ar with a volumetric ratio of 6:2:1) was introduced into the reactor at the desired flow rate. Ar was included as an internal standard for gas chromatography. The reaction pressure was slowly increased to 2.0 MPa. Finally, the temperature of the reactor was raised to 320 °C or 340 °C (10 °C·min^{-1}), depending on the chosen reaction condition. More detailed information about the catalytic tests will be provided in the paragraph below.

2.7.4 Catalytic Tests

The catalytic tests were carried out at 340 °C, in order to evaluated the effect of the temperature on products selectivity. Furthermore, as highlighted before, the temperature control within the catalytic bed was achieved using two thermocouples connected to independent PID controllers, while a third vertically sliding thermocouple was used to confirm the absence of temperature gradients (T= 320 or 340 ± 1 °C) along the catalyst bed. Initial FTS stability were determined at using a constant gas hourly space velocity (GHSV) of 3.1 $L_{(H2+CO2)} \cdot g_{1NaFe}^{-1} \cdot h^{-1}$, where $g_{Fe/CNT}$ is referred to the g of Fe/CNT catalyst proper impregnated with Fe and Na, while a (GHSV) of 11.6-19.2 $L_{(H2+CO2)} \cdot g_{1NaFe}^{-1} \cdot h^{-1}$ was used for the experimental catalytic campaign followed in dual bed with bulk iron 1NaFe. The GHSV condition chosen was maintained for approximately 27 hours of reaction. After this time, the reactor was cooled at 100 °C and depressurized. Then, a flow of Ar was passed through the reactor for 10 h at 300 °C (5 °C·min^{-1}), in order to clean the surface of the catalysts from the physisorbed products.

Approximately every 1.5 h during the reaction experiment, the gas stream exiting the catalytic system was depressurized and regularly analyzed online using a Varian 3800 gas chromatograph (GC) equipped with three columns, TCD, and FID detectors. The online GC analyses resulted in carbon mass balances in the 98-

102% range. As a matter of fact, no experiments involved the collection of oil in the two high-pressure traps during the 27-hour reaction.

2.7.5 Identification and Analysis of Products

For the analysis of reaction products, a Varian 3800 gas chromatograph was used, equipped with a system of 3 packed columns, a capillary column, and two detectors: a Thermal Conductivity Detector (TCD) and a Flame Ionization Detector (FID).

The packed columns system (13X molecular sieve and two Porapak HysepQ columns), connected to the TCD detector, allows the separation and quantification of permanent gases, including CO, CO_2, Ar, CH_4, C_2H_6, C_2H_4, C_3H_8, C_3H_6.

Instead, the CP-Sil 5-CB connected to the FID detector allows the analysis of hydrocarbons from C_1 to C_{20}, distinguishing between n-paraffins, α-olefins, linear internal olefins, alcohols, and other oxygenated compounds, isoparaffins, aromatics and isoolefins (the latter only in the C_4-C_6 range). All these products were previously identified using commercial standards (Supelco Park, Aldrich).

The products analyzed online with the reaction system were injected as gas directly using injection loops in the channels of the TCD and FID detectors. The carrier gas flow was 40 mL in the TCD and 30 mL in the FID detector. The analysis program includes (Figure 2.11):

- Initial equilibration: 35 °C for 17 minutes.
- Ramp 1: Gradual temperature increase at 10 °C·min^{-1} until reaching 250 °C, holding for 12 minutes at this temperature.

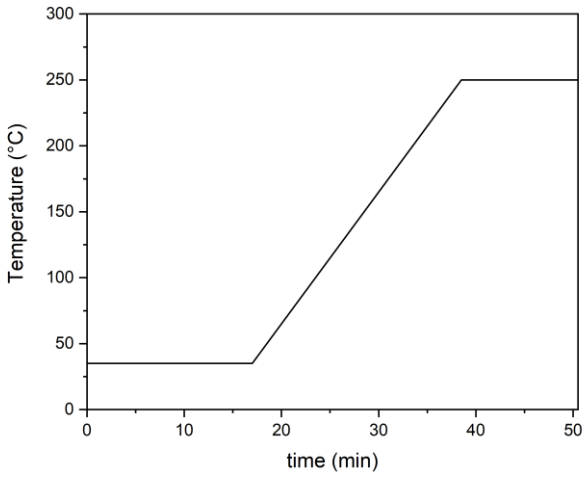


Figure 2.11. Details of the analysis program, outlining any temperature ramps or isothermal intervals employed to achieve an effective separation of mixture components. This on-line analysis detects hydrocarbons in the C_1-C_{20} range.

2.7.6 Data processing

The quantitative interpretation of chromatographic results was based on the detection of Ar as an internal reference gas in the TCD detector, equation (2. 29). Therefore, the CO_2 conversion for a chromatographic analysis was calculated from the chromatographic areas for CO_2 and Ar (TCD detector) and the chromatographic areas for a feed gas analysis in the absence of a catalyst:

$$\zeta_{CO_2} = \frac{\dot{n}_{CO_2,in} - \dot{n}_{CO_2,out}}{\dot{n}_{CO_2,in}} \cdot 100 = \frac{\left(\frac{A_{CO_2}}{A_{Ar}}\right)_{in} - \left(\frac{A_{CO_2}}{A_{Ar}}\right)_{out}}{\left(\frac{A_{CO_2}}{A_{Ar}}\right)_{in}} \cdot 100 \qquad (2.\ 29)$$

Where ζ_{CO_2} represents the CO_2 conversion, $\dot{n}_{CO_2}$ represents the molar flow rate of CO_2 at the inlet (in) and outlet (out) of the reactor, while A represents the area obtained by integrating the chromatographic peaks of CO_2 or Ar.

For the calculation of the molar flow rate of each of the gases detected in the TCD channel at the reactor outlet, the molar flow rate of Ar introduced in the feed

was used as a reference, according to Equation (2. 30) for a gas i, where i=CO_2, CO, CH_4, C_2H_4, C_2H_6, C_3H_6, C_3H_8:

$$\dot{n}_{i,out} = \left(\frac{\frac{A_i}{A_{Ar}}}{f_{i,Ar}} \right)_{TCD} \cdot \dot{n}_{Ar,in} \qquad (2.\ 30)$$

Where $f_{i,Ar}$ is the molar chromatographic response factor for compound i with respect to Ar.

The molar flow rate of each of the reaction products detected in the FID detector channel was calculated using the molar flow rate of CH_4 determined in the TCD detector channel as the base, according to equation (2. 31). In this case, the ratio of chromatographic areas in the FID channel was used, along with the mass chromatographic response factor for compound i with respect to CH_4 (f_{i,CH_4}) and the corresponding molecular weights (PM) as described in equation (2. 31):

$$\dot{n}_{i,out} = \left(\frac{\frac{A_i}{A_{CH_4}}}{f_{i,CH_4}} \right)_{TCD} \cdot \frac{PM_{CH_4}}{PM_i} \cdot \dot{n}_{CH_4,out} \qquad (2.\ 31)$$

The response factors for compounds detected in the TCD, relative to Ar, were experimentally determined by injecting gaseous samples from pressurized cylinders containing certified gas mixtures (Abelló-Linde). All response factors used in the TCD detector were calculated on a molar basis.

On the other hand, the response factors for oxygenated compounds detected in the FID were experimentally obtained by injecting liquid standard samples containing oxygenated compounds (grouped by chemical similarity) and n-heptane, prepared by weighing using commercially available compounds of known purity (>97%). Weighing was carried out under refrigeration with ice and in order of volatility to minimize errors due to evaporation during the process. The preparation of standard mixtures was performed in triplicate, in three different relative proportions, so that the response factors relative to n-heptane were obtained by averaging the three experimental results (σ<10%). The response factors obtained relative to n-heptane were converted into response factors relative to CH_4 using the value $f_{n\text{-heptane}(CH4)}$ reported in the literature for FID detectors

[139]. For non-oxygenated hydrocarbons, response factors relative to CH_4 were used, as reported in the literature [139], with a value of 1±0.04 in all cases. All response factors used for the FID detector were calculated on a mass basis.

The selectivity to product i, on a molar carbon basis, was calculated from the molar flow rates for each of the products i at the reactor outlet and the number of carbon atoms in the product i ($N_{C,i}$), according to equation (2. 32):

$$\sigma_i(\%) = \left[\frac{N_{C,i} \cdot \dot{n}_{i,out}}{\sum_i(\dot{n}_{i,out} \cdot N_{C,i})}\right] \cdot 100 \qquad (2.\ 32)$$

For each analysis, the molar carbon balance (C.B.) was calculated by accounting for the carbon atoms leaving the reactor in the form of products or unconverted CO_2, according to chromatographic calculations, and comparing this result with the molar flow of carbon fed as CO_2 in the reactant mixture, as equation (2. 33):

$$C.B\ (\%) = \left[\frac{\sum_i(\dot{n}_{i,out} \cdot N_{C,i})}{\dot{n}_{CO_2,in}}\right] \cdot 100 \qquad (2.\ 33)$$

In all the CO_2 hydrogenation tests conducted in Valencia the carbon balances were 100±2% for all the experiments.

In certain cases, the catalytic activity was expressed as the iron-time-yield (FTY), which gives the amount of CO_2 converted per hour and gram of iron, as shown in equation (2. 34):

$$FTY\ (\frac{mol_{CO_2}}{h \cdot g_{Fe}}) = \frac{\dot{n}_{CO_2,in} \cdot \zeta_{CO_2}}{M_{cat} \cdot \chi_{Fe}} \qquad (2.\ 34)$$

Where M_{cat} denotes the mass of catalyst (Fe/CNT or 1NaFe) used in the experiments, and χ_{Fe} represents the metal loading of Fe in the catalysts, determined by ICP-OES.

2.8 Comparison of test benches used in this thesis: Advantages and Limitations

The Turin test bench offered significant advantages, primarily due to its automation capabilities and the ability to remotely control the plant once the reactor was manually loaded and its integrity checked. This allowed for an optimized workflow, as the test bench could be operated and monitored remotely. Additionally, it was equipped with an automatic back pressure controller, providing precise system pressure control. However, there were notable limitations. The durability of the back pressure controller was a concern, as it was prone to damage from contamination with oil produced during reactions, which affected the pressure sensor, shutter, and BPC seals. This necessitated the condensation of C_{6+} compounds, resulting in continuous monitoring of only products up to C_5. The test bench also faced flow rate restrictions, being unable to handle low flow rates due to the limitations of the N_2 and H_2 mass flow controllers, making it unsuitable for experiments with supported materials. Temperature control was another limitation, with only two temperature controls (TT02 and TT04), restricting precise thermal management. The preparation time for catalytic tests was extended due to the reactor loading process and the mounting of the heating mantle, which had to be carefully anchored to the reactor for each test.

On the other hand, the Valencia test bench had its own set of advantages and limitations. A major advantage was the use of a manual back pressure controller placed at a high temperature (180 °C), which avoided the oil condensation issues encountered with the BPC in Turin. The system also allowed for accurate and continuous analysis of all products obtained during the reaction, thanks to heated traps and heated lines connected to the online GC-FID. The reactor loading process was easier, and the use of heating resistances instead of a mantle that needed proper anchoring sped up the assembly. The Valencia test bench also offered improved temperature control with three thermocouples, two fixed and one mobile within the catalytic bed, ensuring accurate and reproducible results. Additionally, there were no flow rate limitations from mass flow controllers, enabling work with supported materials like CNTs at low flow rates. However, the primary limitation was the lack of automation, which required manual adjustments and could be less convenient compared to automated systems in terms of optimizing work time management.

Despite the advantages and limitations of each test bench, the work carried out in both cases was challenging.

Chapter 3

3 CO_2 conversion into hydrocarbons via modified Fischer-Tropsch synthesis by using bulk iron catalysts combined with zeolites.

The study presented in this chapter was published, with modifications, as [1]:

Elena Corrao, Fabio Salomone, Emanuele Giglio, Micaela Castellino, Silvia Maria Ronchetti, Marco Armandi, Raffaele Pirone, Samir Bensaid.

"CO_2 conversion into hydrocarbons via modified Fischer-Tropsch synthesis by using bulk iron catalysts combined with zeolites". Chemical Engineering Research and Design 197 (2023) 449–465, https://doi.org/10.1016/j.cherd.2023.07.052.

3.1 Introduction

Petroleum industry has promoted economic development and societal well-being. On the other hand, the massive and growing dependence on fossil fuels has led to an uncontrolled increase in CO_2 emissions. International Energy Agency (IEA) estimated that CO_2 emissions have increased by more than 40% compared to pre-industrial levels (from 280 ppm to values above 400 ppm) [18], [19]. The most serious consequence related to increasing greenhouse gas emissions is the average temperature rise, causing an increase in sea level, ocean acidification, and climate change with increasingly frequent disastrous effects. Furthermore, fossil fuels are subject to fluctuations in supply and crude oil prices due to global

geopolitical reasons [16]. Finally, being non-renewable sources of energy, they are destined to run out over time. CO_2 could be captured and converted into fuels or high-value chemical products via reaction with green hydrogen produced by exploiting surpluses from renewable energy sources [56], [57], [58], in order to embark on a sustainable pathway to produce synthetic fuels like methane [56], [59], [60] (Power-to-Gas), methanol [61], [62], [63], dimethyl-ether [64], [65] and hydrocarbons (Power-to-Liquid) [66], [67], [68], [69], [70], [71].

The conversion of CO_2 is a challenging process due to the thermodynamic and chemical stability of CO_2 [75]. Therefore, the development of an efficient catalyst for CO_2 conversion is highly desirable. In this context, conventional Fischer-Tropsch (FTS) catalysts like Fe, Co, Ni, and Ru catalysts [65], [70], [77], [78] , have been studied for CO_2 hydrogenation to hydrocarbons. Among them, Ni- and Ru-based catalysts show high CH_4 efficiency [79], [80], but only small amounts of C_{2+} hydrocarbons are produced.

Power-to-Liquid is a good candidate for medium-term energy storage. Liquid products are easy to transport and store (whereas gaseous products require compression or liquefaction), having a higher energy density per unit volume and experiencing less mass loss during long-term storage. Moreover, liquid fuels are compatible with the existing infrastructure, making integration into transportation systems and other industries relatively straightforward without requiring extensive investments or technological overhauls. Furthermore, the technological advancements occur upstream of the consumer, resulting in high levels of acceptance from the general population.

How anticipated in chapter 1 indirect or direct routes can be carried out for the CO_2 hydrogenation into liquid fuels. The indirect route requires the use of two separate reactors: in the first one CO_2 and H_2 can be converted into CH_3OH or CO (depending on the catalyst); while in the second reactor, the reaction intermediates obtained in the first one, can be transformed into hydrocarbons. On the other hand, the direct route may be more economically advantageous than the indirect one thanks to the use of a unique reactor. The direct conversion process consists of coupling of the endothermic reverse water gas shift (RWGS) reaction with the exothermic Fischer-Tropsch synthesis (FTS) within the same catalytic particle. Fe-based catalysts have been studied extensively for their high activity and stability in hydrocarbon production [85]. They are particularly attractive due to their potential to directly convert CO_2 into fuels. This feature is due to the formation of carbides, as deeply described in Chapter 1 [87]. However, to achieve

high selectivity of light olefins, the carbon chain growth reaction needs to be effectively controlled [83]. Therefore, efforts are still underway to improve the catalytic performance of Fe-based catalysts by incorporating promoters. Among them, as discussed in paragraph 1.4.1.1 of Chapter 1, the addition of alkali promoters such as Na or K significantly enhances the formation of Fe_5C_2 sites and reduces methane production, promoting the selectivity to olefins. However, despite the numerous advantages and specific features of both promoters, sodium was chosen as promoter based on the work of Wei et al. [97] and its availability. Sodium is much more readily available compared to potassium and is generally more economical. Therefore, from a futuristic perspective, in terms of industrial applications, improving the performance of a sodium-promoted iron-based catalyst could be a very interesting and avant-garde choice.

In the context of CO_2 hydrogenation, zeolite is a crucial component of tandem catalysts in both discussed routes, as they possess unique shape selectivity and acidity that make them ideal for facilitating hydrocarbon oligomerization, isomerization, and aromatization. ZSM-5 with MFI topology is the most preferred catalyst candidate for aromatic synthesis among the solid acids used in the process because of its well-defined 3-dimensional intersecting pore system with 10-member ring channels. This feature allows it to surmount the challenges of reactant and product diffusion within the pores and maintain strong resistance to deactivation by coke. In addition to zeolite topology, the strength, density, and Si/Al atomic ratio of zeolite acid sites are critical factors in determining the catalyst effectiveness [102], [103].

If a zeolite is involved, according to the hydrogen transfer mechanism, lower olefins undergo oligomerization to produce olefins in the C_6-C_{10} range. Subsequently, the longer olefins transfer their hydrogen to another olefin molecule, leading to the generation of dienes and paraffins. The dienes then form cyclic olefins via cyclization and undergo two hydrogen transfer steps, producing cyclic dienes and aromatics, as reported in the simplified equation (3. 1). The occurrence of each hydrogen transfer step results in the formation of one paraffin molecule, which reduces the carbon utilization in terms of producing the desired chemicals (C_2-C_4 olefins and aromatics) [98], [102], [100]. It should also be added that some of organic oxygen compounds obtained on the Fe-based catalyst, especially alcohols and ethers, can react on the acid sites of the zeolite, following the reaction pathway reported in the equations (3. 2) and (3. 3). To specify, the equation (3. 2) can lead to the formation of paraffins, while the equation (3. 3) to the formation of olefins [101]. The latter may undergo further conversion to

aromatic products on the acidic sites of the zeolite as previously mentioned. Of course, the capacity of zeolite to transform light olefins and alcohols intermediate products depends on the strongness of acid sites of the zeolite.

$$C_nH_{2n} \rightarrow \frac{1}{m}C_6H_6 + \frac{3}{m}\ C_nH_{2n+2} \qquad \text{where: } m = \frac{6}{n} + 3 \qquad (3.\ 1)$$

$$C_nH_{2n+2}O\ \rightarrow\ C_nH_{2n+2}\ +\ H_2O\ +\ C \qquad (3.\ 2)$$

$$C_nH_{2n+2}O\ \rightarrow C_nH_{2n}\ + H_2O \qquad (3.\ 3)$$

More in detail, zeolites with a low Si/Al atomic ratio (less than 10), due to stronger acidity could cause the over-cracking of heavy hydrocarbons and lead to a decrease in selectivity towards liquid hydrocarbons in FT synthesis. On the contrary, zeolites with a high Si/Al (atomic ratio) (greater than 100) are characterized by a lower concentration of acid sites, which is not beneficial for the oligomerization, isomerization, and aromatization of primary CO_2-FT products. HZSM-5 with a medium number of acid sites gives the possibility to obtain a gasoline-like product [102].

Therefore, the optimal Si/Al atomic ratio for zeolites used in FT synthesis ranges typically between 40 and 80, which provides a balance between activity, selectivity, and stability of the catalyst. However, the exact Si/Al ratio depends on the specific reaction conditions and the type of syngas used in the process. For this reason, in this work a zeolite with a Si/Al ratio of 40 was chosen in order to have a good compromise in term of catalyst operation and production of gasoline-like products. In addition, to achieve the scope, also a hierarchical zeolite with the same Si/Al ratio was prepared and tested. Thus, by possessing a pore structure that is hierarchical, it means it contains both micropores, which are typically less than 2 nm in diameter, and mesopores, which typically range from 2 to 50 nm in diameter. In contrast, conventional zeolites have a predominantly microporous structure. There are numerous advantages to use a hierarchical zeolite over a conventional one. Firstly, due to the larger pore size, a hierarchical zeolite is able to enhance mass transport by enabling faster movement of reactant and product molecules through the catalyst. This results in improved catalytic activity and selectivity. Additionally, the mesopores present in hierarchical zeolites offer better accessibility to active sites for intermediate products, thereby enhancing catalytic performance in reactions involving larger molecules. Moreover, the presence of mesopores helps to mitigate the diffusion limitations that can lead to catalyst deactivation in conventional zeolites [102], [103].

Therefore, the aim of this work is to initially investigate and optimize the catalysts hydrogenation of CO_2. Hence, multifunctional materials built of a Fe-based metal oxide with Na, as promoter, with two different synthesis and with different amount of Na have been studied. Subsequently, the best metallic phase was tested in physical mixture mode in with a combination of commercial and hierarchical zeolite. Finally, the novelty of the present work lies in core-shell structures with the metallic phase positioned as the core and the zeolite as the shell. In fact, based on previous research works, capsule catalysts with a core-shell structure have demonstrated remarkable effectiveness as a catalyst for FTS. The combination of the core and shell catalysts produces a synergistic confinement effect, enabling them to break the ASF production distribution and achieve high selectivity for the desired products. By carefully selecting and optimizing the materials used for the core and shell, these capsule catalysts can perform bifunctional catalysis and consistently outperform physical mixture catalysts [100], [140]. Overall, efforts to improve the catalytic performance of Fe-based catalysts and optimize their configuration to lead to the development of more efficient and selective processes for converting CO_2 into valuable fuels require further studies.

The catalysts employed in this study are summarized in the following table (Table 3. 1) additional information are instead reported in Table 2. 1.

Table 3. 1. Principal samples details involved in this study.

Name used	Nominal Si/Al at. ratio	Nominal Na/Fe_3O_4 ratio (wt. %)	Preparation Method
$1\%NaFe_3O_4$_WI	-	1	Wet Impregnation (WI)
$5\%NaFe_3O_4$_WI	-	5	Wet Impregnation (WI)
$NaFe_3O_4$_CP	-	Dependent on washing water	Coprecipitation (CP)
HZSM5	40	-	Commercial Zeolite
HZ	40	-	Hydrothermal Synthesis
$NaFe_3O_4$_CP@HZSM5	40	Dependent on washing water	Cladding Method
$NaFe_3O_4$_CP@HZ	40	Dependent on washing water	Cladding Method

3.2 Results and discussion

3.2.1. Characterization of the catalysts

Table 3. 2 provides chemical composition and textural properties of the investigated catalysts. XRF analysis for the two zeolites showed that the Si/Al atomic ratio was close to the nominal value for both commercial and hierarchical samples. In addition, the HZ had a higher surface area (around 463.8 $m^2 \cdot g^{-1}$) than the commercial one (around 393.7 $m^2 \cdot g^{-1}$), a higher average pore size, and a greater total pore volume, confirming its mesoporous structure. Sodium content of the 1%$NaFe_3O_4$_WI and 5%$NaFe_3O_4$_WI samples was close to the nominal value, whilst $NaFe_3O_4$_CP sample obtained by coprecipitation had a sodium content of 4.7 wt.%. Interestingly, this sample exhibited the highest surface area (approximately 80 $m^2 \cdot g^{-1}$) while the surface area of the two samples obtained by impregnation was about 50 $m^2 \cdot g^{-1}$. This variation could be attributed to the different preparation methods, which may have caused the effective dispersion of sodium components on the Fe_3O_4 microspheres. In addition, the $NaFe_3O_4$_CP sample small size and large surface area are likely due to the numerous inter-particle pores present within it. This, in turn, has the potential to significantly affect the mass transport rates of both the feed and FTS products [141]. Finally, the surface area of the core-shell structures was also closely related to the Fe_3O_4-based and zeolite used; and, as expected, the XRF analyses confirmed that the Fe_3O_4:zeolite mass ratio was 1:1.

Table 3. 2. Chemical composition and textural properties of fresh catalysts.

	Na/Fe_3O_4 (wt.%)[a]	Si/Al[a]	BET surface area ($m^2 \cdot g^{-1}$)	Pore Volume ($cm^3 \cdot g^{-1}$)[b]	Pore size (Å)[c]
1%$NaFe_3O_4$_WI	1.3	-	50.1	0.28	199
5%$NaFe_3O_4$_WI	4.5	-	53.1	0.15	115
$NaFe_3O_4$_CP	4.7	-	87.2	0.27	94
HZSM5	-	38.0	393.7	0.11	38
HZ	-	39.5	463.8	0.29	102
$NaFe_3O_4$_CP@HZSM5	4.8	37.5	267.1	0.17	73
$NaFe_3O_4$_CP@HZ	4.7	39.6	371.4	0.28	77

[a] Calculated via XRF analysis;

[b] BJH Desorption cumulative volume of pores between 17 Å and 3000 Å width;

[c] BJH Desorption average pore width (4V/A).

The results of the N_2 adsorption-desorption analysis conducted on all the samples were documented in Figure 3. 1, Figure 3. 2 and Figure 3. 3.

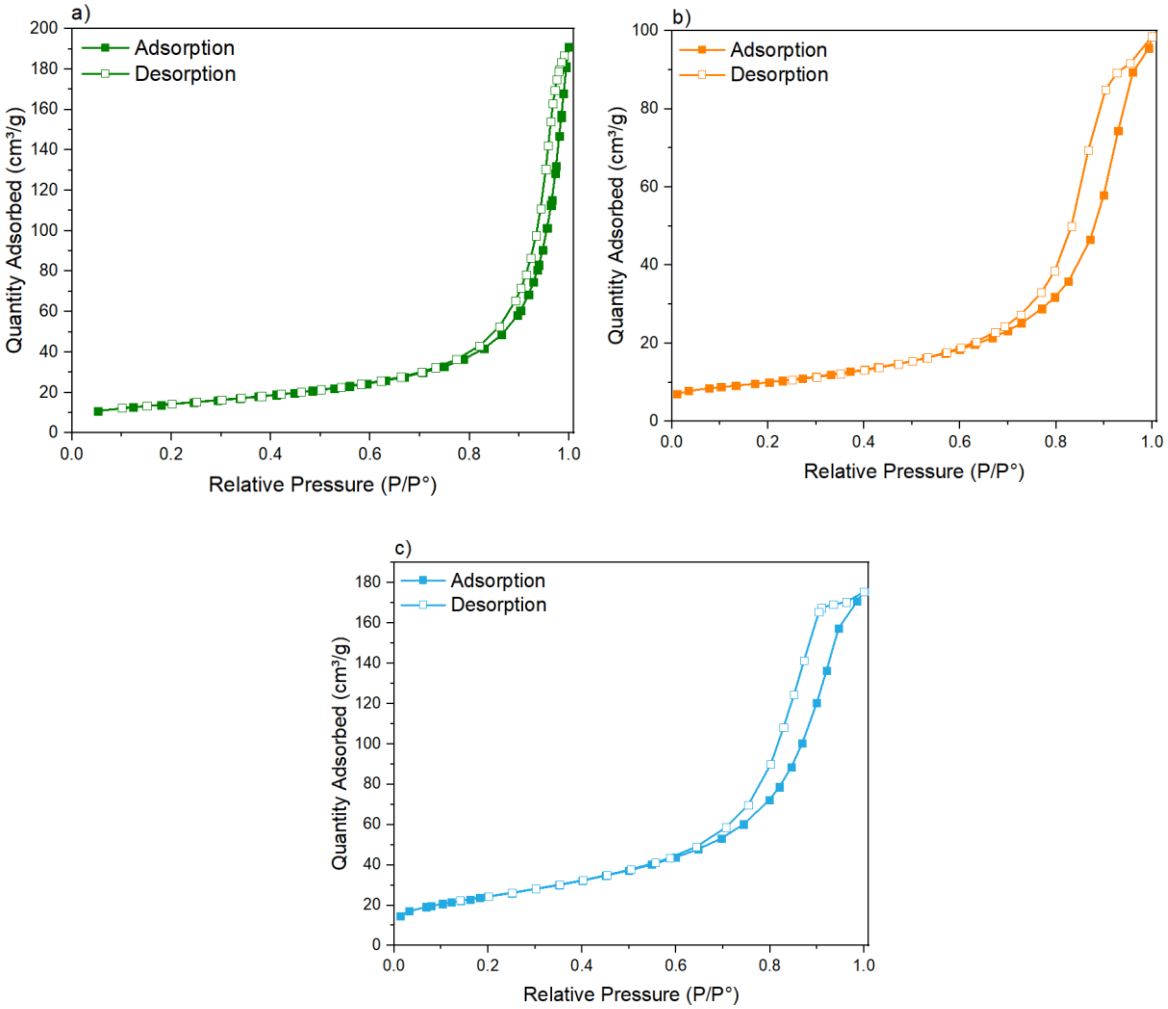


Figure 3. 1. N_2 adsorption-desorption isotherms of the calcined: a) 1%$NaFe_3O_4$_WI, b) 5%$NaFe_3O_4$_WI and c) $NaFe_3O_4$_CP.

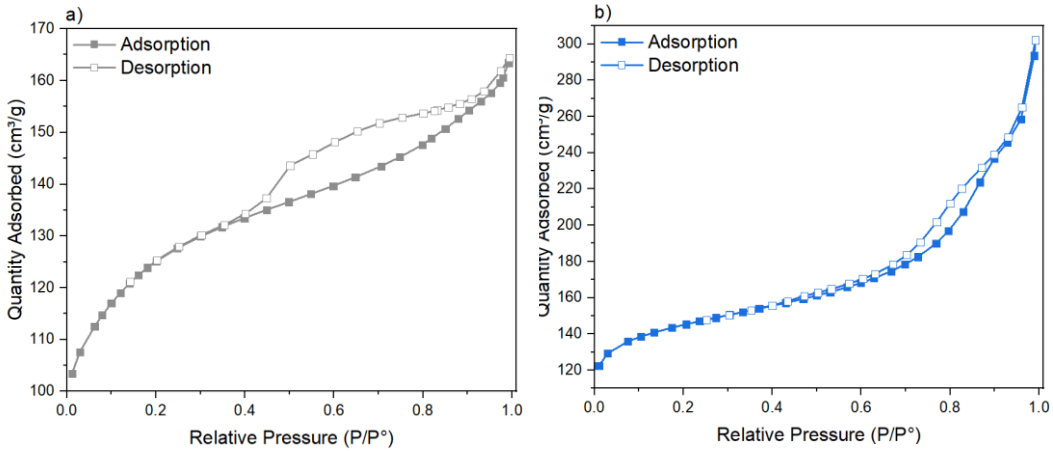


Figure 3. 2. N_2 adsorption-desorption isotherms of the calcined: a) HZSM5 and b) HZ.

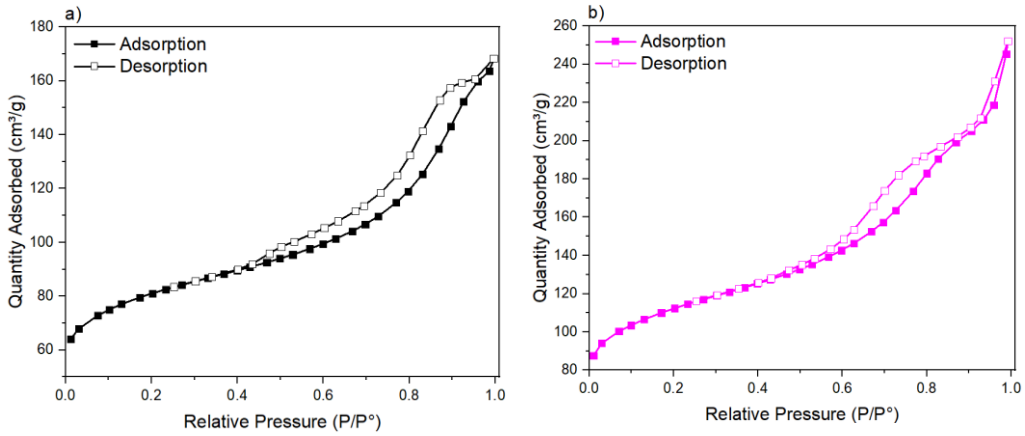


Figure 3. 3. N_2 adsorption-desorption isotherms of the calcined: a) $NaFe_3O_4$_CP@HZSM5, b) $NaFe_3O_4$_CP@HZ.

These measurements showed that all the fresh catalysts had a type IV isotherm. However, there were some differences in the hysteresis loop observed. The samples containing iron (Figure 3. 1) exhibited an H1-type hysteresis loop, indicating the formation of porous materials due to the agglomeration of uniformly sized spheres [119]. Meanwhile, the zeolite samples (Figure 3. 2) exhibited a type IV isotherm with an H4-type hysteresis loop due to the presence of a significant number of slit-shaped pores, which were categorized as supermicropores and mesopores [110], [142]. Thereby, Figure 3. 4 compares the pore distribution of the homemade hierarchical zeolite (HZ) and the commercial

zeolite (HZSM-5). The HZ showed a wide distribution of pore sizes ranging from 50 Å to 200 Å, with a peak at around 90 Å, while the commercial zeolite had a negligible distribution.

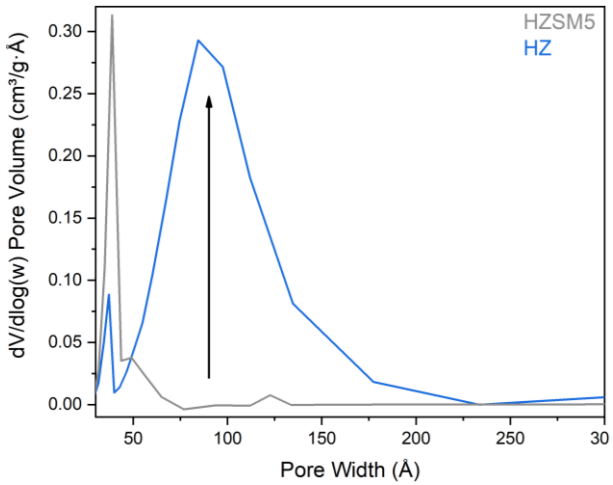


Figure 3. 4. Pore size distribution.

Figure 3. 5 a) displays the XRD patterns of the fresh Fe_3O_4-based catalysts. Samples 1%$NaFe_3O_4$_WI, 5%$NaFe_3O_4$_WI and $NaFe_3O_4$_CP exhibited the crystal planes (220), (331), (540), (511), and (440) of the typical magnetite Fe_3O_4 observed at 30.1°, 35.5°, 43.1°, 57.0°, and 62.6°, respectively. In the 5%$NaFe_3O_4$_WI sample, Na nitrate peak was detected, most likely due to the poor dispersion of Na on the surface of Fe_3O_4. Conversely, no diffraction peak associated with Na was observed in the other two samples, indicating good dispersion of sodium. This suggests that the dispersion of sodium is affected by the different content and synthesis preparations, as seen in 1%$NaFe_3O_4$_WI and $NaFe_3O_4$_CP samples [110] [143]. On the other hand, Figure 3. 5 b) illustrates that the XRD patterns of the spent Fe_3O_4-based catalysts exhibited clear peaks of Fe_3O_4 and Fe_2C_5. According to the literature, these two phases are respectively considered as the responsible for the CO_2 conversion to CO and its subsequent hydrogenation to Fischer-Tropsch products [102], [144]. Scherrer formula was used to determine the crystallite size of the fresh and spent Fe_3O_4 nanoparticles, based on the broadening of the most intense peak (311) at 2 Theta: 35.52 ° on 1%$NaFe_3O_4$_WI, 5%$NaFe_3O_4$_WI and $NaFe_3O_4$_CP samples [119]. The results of this calculation are provided in Table 3. 3, showing that the coprecipitated

$NaFe_3O_4$_CP sample has the smallest crystallite size, while the 1%$NaFe_3O_4$_WI sample has the largest crystallite size (11.4 nm and 17.8 nm, respectively).

Table 3. 3. Crystalline size fresh iron phase calculated with Scherrer equation, based on the broadening of the most intense peak (311) at 2 Theta: 35.52 °.

	Crystalline size *fresh* Fe_3O_4 *(nm)*	Crystalline size spent Fe_3O_4 *(nm)*
1%Na-Fe_3O_4_WI	17.8	31.6
5%Na-Fe_3O_4_WI	11.7	22.0
Na-Fe_3O_4_CP	11.4	16.6

This trend also holds for the spent catalysts, whose size increases to 16.6 and 31.6 nm for impregnated and coprecipitated sample, respectively. The same growth trend from the fresh to the spent catalyst is noticeable for the 5%$NaFe_3O_4$_WI sample, whose values are close to those obtained for the $NaFe_3O_4$_CP sample.

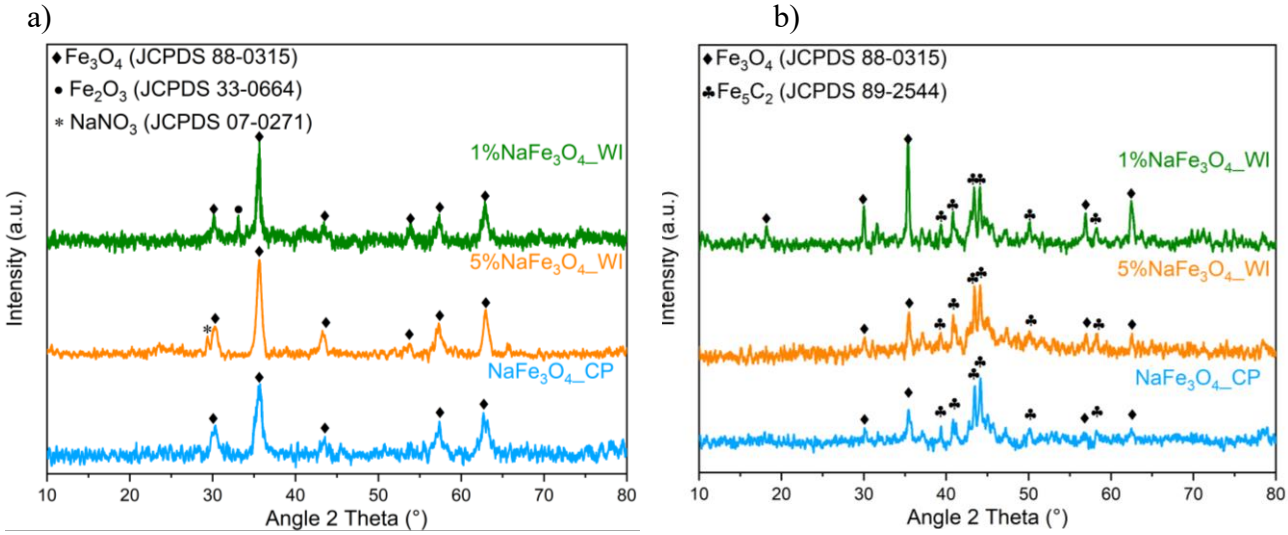


Figure 3. 5. XRD patterns of the a) fresh and b) spent Fe_3O_4-based catalysts: 1%$NaFe_3O_4$_WI, 5%$NaFe_3O_4$_WI and Na-Fe_3O_4_CP.

Figure 3. 6 a) shows that homemade hierarchical zeolite (HZ), commercial zeolite (HZSM5), and the two core-shell structures ($NaFe_3O_4$_CP@HZSM5 and $NaFe_3O_4$_CP@HZ) exhibit diffraction peaks at 2θ values of 7.98°, 8.88°, 14.85°,

23.96°, and 24.38°, which are characteristic of the MFI topology structure (JCPSD No. 44-0002) [43]. Notably, the core-shell structures ($NaFe_3O_4$_CP@HZSM-5 and $NaFe_3O_4$_CP@HZ) show no evident peaks attributed to the iron phase. In fact, the peaks associated with the Fe_3O_4 phase, due to their significantly lower intensity compared to the zeolite peaks, are effectively masked by the intense zeolite peaks. Therefore, indicate that in both cases the zeolite is well dispersed on the surface of $NaFe_3O_4$_CP. Figure 3. 6 b), on the other hand, shows the XRD patterns of the spent catalysts, where the characteristic peaks of the MFI topology structure are present. However, it is interesting to note the appearance of the peaks attributable to Fe_3O_4 (35.52°) and iron carbides (Fe_5C_2) at 42°-48° 2θ. In addition, the $NaFe_3O_4$_CP@HZSM5 sample deserves particular attention, as it is the only spent catalyst that exhibits a narrow and intense peak located at 44.6°; this peak has been attributed to the presence of metallic iron and could explain the lower activity of the catalyst during the modified Fischer-Tropsch reaction.

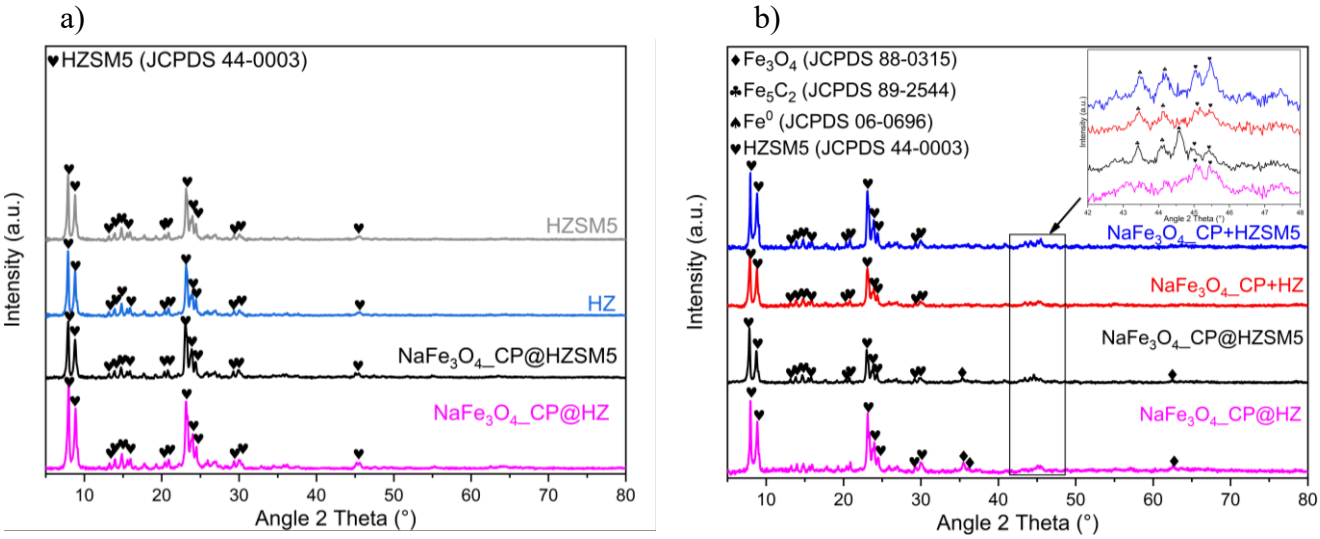


Figure 3. 6. XRD patterns of a) fresh zeolites and core-shell structures and b) spent granule mixed catalysts and core-shell structures.

However, the presence of weak peaks related to iron carbide in Figure 3. 6 (b) indicates that the higher crystallinity of the zeolite inhibits the intensity of the peaks related to iron phases. To effectively study the evolution of phases during the modified Fischer Tropsch, XRD in situ was performed on $NaFe_3O_4$_CP fresh catalyst. In particular, the patterns obtained by high temperature XRD for fresh

Fe_3O_4-based catalyst under reducing atmosphere H_2/Ar are reported in Figure 3. 7.

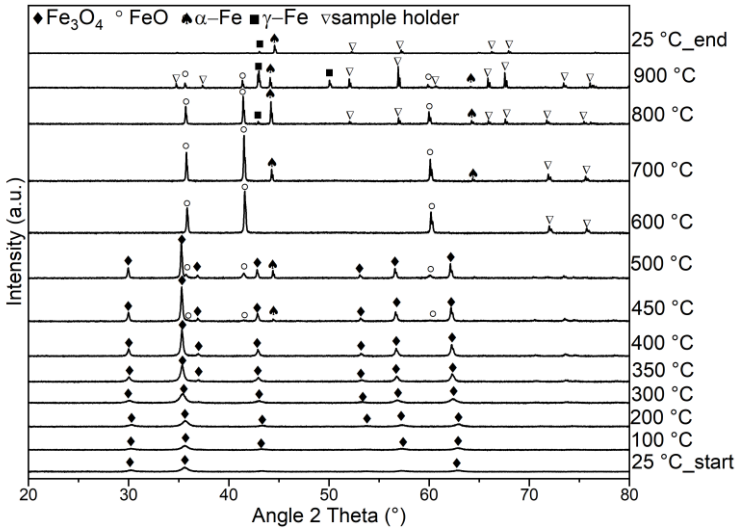


Figure 3. 7. In situ XRD patterns of fresh $NaFe_3O_4$_CP catalytic powder under reducing atmosphere H_2/Ar from 25 °C to 900 °C.

From room temperature to 400 °C only peaks related to Fe_3O_4 are present. At 450 °C the FeO and α-Fe phases appear, as shown by its characteristic peak at 2θ value of 41.6° and 44.6° respectively, while at 600 °C the Fe_3O_4 phase disappears. The patterns at 800 °C and 900 °C exhibit diffraction peak at 2θ value of 42.9° confirming the presence of the iron phase γ-Fe next to FeO and α-Fe. In Figure 3. 8 a) the patterns obtained by high temperature XRD under isothermal conditions at 450 °C for fresh $NaFe_3O_4$_CP catalyst under reducing atmosphere H_2/Ar are shown. The patterns collected every 4 h show the presence of Fe_3O_4, FeO and α-Fe and their progressive growth over time. XRD patterns of fresh $NaFe_3O_4$_CP catalyst collected every 6 h at 330 °C under reducing atmosphere H_2/CO/N_2 and previously treated at 450 °C under reducing atmosphere H_2/Ar, are reported in Figure 3. 8 b). Distinct pattern of Fe_3O_4 and increasing over time peaks attributable to iron carbides (Fe_5C_2, Fe_7C_3) at 43°-46° 2θ are detectable [145], [146], [147], [148].

a) b)

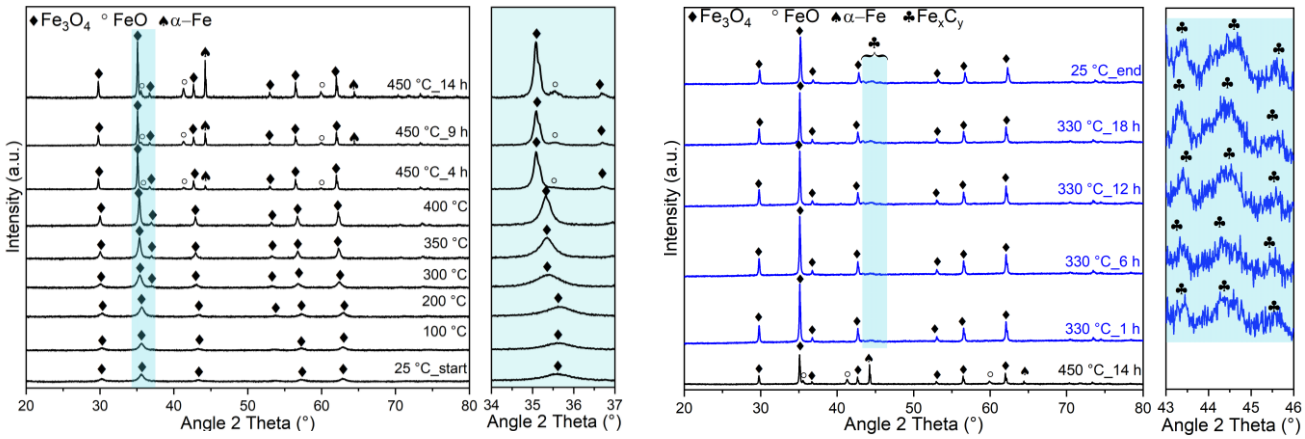
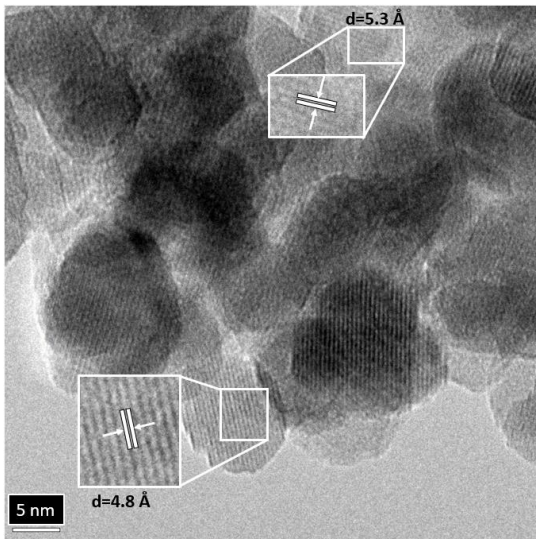


Figure 3. 8. In situ XRD patterns of fresh $NaFe_3O_4$_CP catalytic powder under reducing atmosphere a) H_2/Ar from 25° to 450 °C, black profiles; b) H_2/Ar at 450 °C for 14 h, black profile and H_2/CO/N_2 at 330 °C for 18 h, blue profiles.

The presence of iron oxide phase in the fresh catalysts and iron carbide in spent ones was also investigated and evaluated measuring the interplanar distance of the crystal planes through HR-TEM analysis, as reported in Figure 3. 9 and Figure 3. 10.

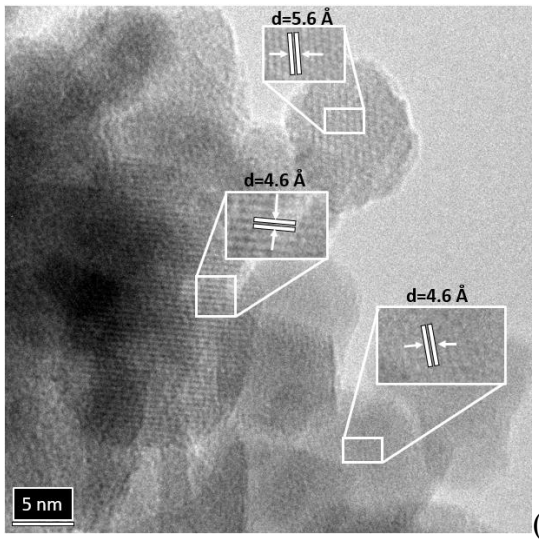
Fresh 1%$NaFe_3O_4$_WI (Magnification: 400 kX)



(a)

4.8 and 5.3 Å → [h k l] = 1:1:1 (Fe_3O_4)

Spent 1%$NaFe_3O_4$_WI (Magnification: 500 kX)

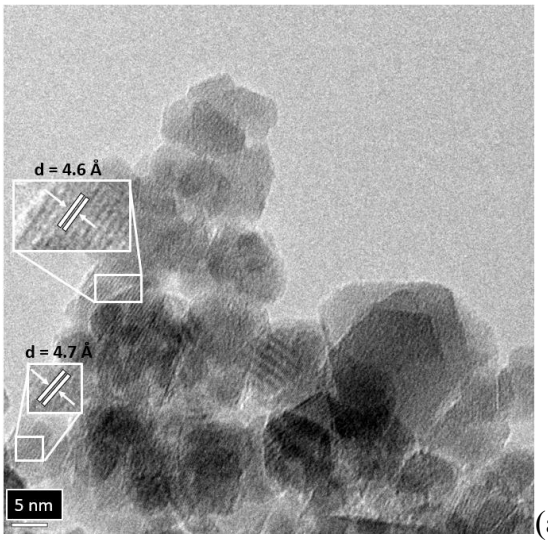


(b)

5.6 Å → [h k l] = 2:0:0 (Fe_2C_5)

Figure 3. 9. HR-TEM images of a) fresh and b) spent 1%$NaFe_3O_4$_WI.

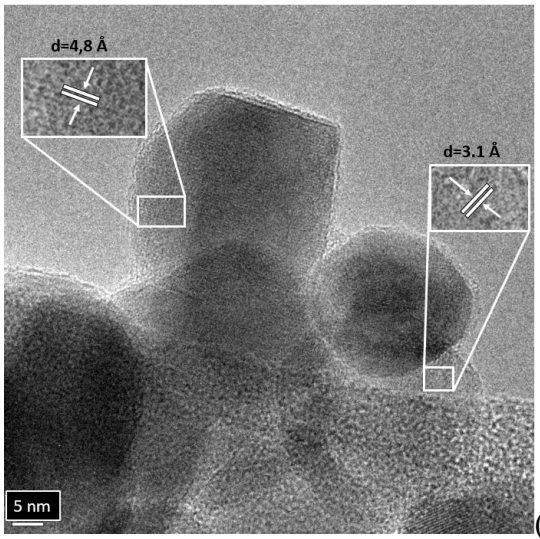
Fresh $NaFe_3O_4$_CP (Magnification: 300 kX)



(a)

4.6 and 4.7 Å → [h k l] = 1:1:1 (Fe_3O_4)

Spent $NaFe_3O_4$_CP (Magnification: 600 kX)



(b)

3.1 Å → [h k l] = 1:1:1 (Fe_2C_5)

4.8 Å → [h k l] = 1:1:1 di Fe_3O_4

Figure 3. 10. HR-TEM images of (a) fresh and (b) spent $NaFe_3O_4$_CP.

After the examination of the images, it becomes evident that the lattice spacing of the fresh nanoparticles, ranging from 4.6-5.3 Å, corresponds to the (111) face of Fe_3O_4. Conversely, the lattice spacing of the nanoparticles in the spent 1%$NaFe_3O_4$_WI catalyst is approximately 5.6 Å, which corresponds to the (200) face of Fe_5C_2. In the case of the spent $NaFe_3O_4$_CP catalyst, the lattice spacing of the nanoparticles is approximately 3.1 Å, corresponding to the (111) face of Fe_5C_2. Furthermore, the TEM image reported in Figure 3. 11 shows a particle from the spent sample of $NaFe_3O_4$_CP, where it is visibly evident that at the end of the catalytic test, the Fe_3O_4 nanoparticles are surrounded by a layer of carbon, demonstrating how the catalyst undergoes modification during the catalytic test [70], [149].

Spent $NaFe_3O_4$_CP (Magnification: 150 kX)

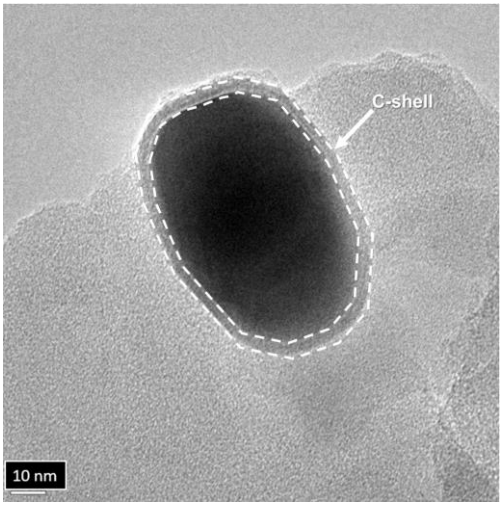


Figure 3. 11. HR-TEM images of spent $NaFe_3O_4$_CP.

On the other hand, TEM and SEM images, collected respectively in Figure 3. 12 and Figure 3. 13, depict homemade HZ, made of globular shape aggregates ranging from 200 to 400 nm and consisting of nanoparticles.

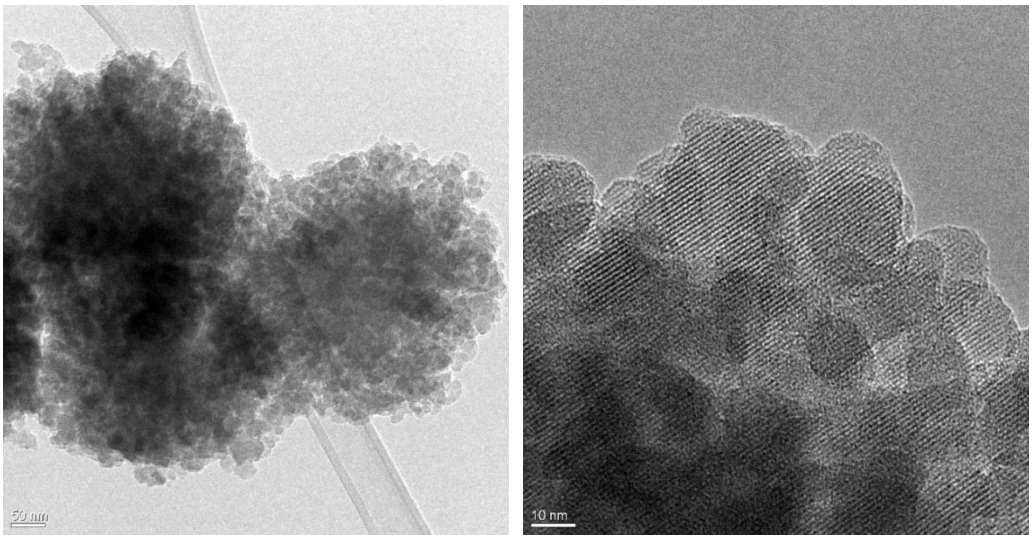


Figure 3. 12. TEM images of the homemade HZ sample.

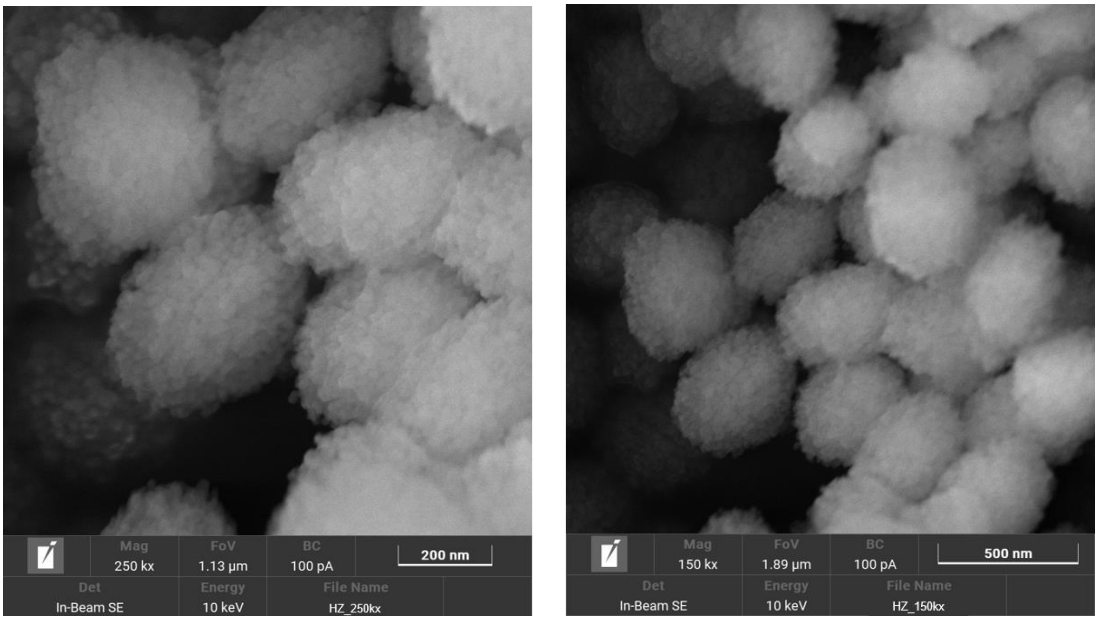


Figure 3. 13. SEM images of the homemade HZ sample.

These nano-units form agglomerates containing ZSM-5 nanocrystals, measuring 10-20 nm, with a similar morphology to that of the reference HZSM-5 sample (pictures not reported). The size of these aggregates is dependent on the chosen seed silanization agent, which in this case is 3-APTMS. The micrographs show the presence of additional porosity, which is created by the voids between the nanocrystals. The crystallographic planes of ZSM5 zeolite are visible throughout the particles, indicating a degree of orientation among adjacent nano-units and suggesting their likely intergrowth. This is remarkable considering the small size of the nano-units and confirms that these hierarchical MFI samples are highly crystalline materials [142].

H_2-TPR profiles were used to investigate the reduction behavior of iron-based catalysts with different Na contents and distributions. In particular, Figure 3. 14 a) and b) show that all catalysts exhibit three broad peaks with the maximum respectively in the range of 362-438 °C, 600-639 °C, and 788 °C, which are associated with the reduction processes of Fe_2O_3 to Fe_3O_4, Fe_3O to FeO, and FeO to metallic Fe, respectively [150]. Focusing on Figure 3. 14 a), the sample obtained by coprecipitation with NaOH ($NaFe_3O_4$_CP) showed the lowest reduction temperature (362 °C), compared to the catalysts obtained by impregnation (1%$NaFe_3O_4$_WI and 5%$NaFe_3O_4$_WI), which exhibited the first reduction peak shifted to higher temperatures, at 438 and 418 °C, respectively.

This result indicates that a different distribution and quantity of sodium would affect the reduction of Fe_2O_3 to Fe_3O_4 and Fe_3O_4 to FeO. The results obtained from the deconvolution of the three peaks of H_2-TPR supports this assumption and are reported in Table 3. 4.

Table 3. 4. Quantitative analysis of the H_2-TPR measurements.

	T maximum (°C)	**H_2 uptake ($mmol \cdot g^{-1}$)**	**H_2 uptake/theoretical H_2 uptake (%)**
1%$NaFe_3O_4$_WI	438	1.5	8
	600	2.0	11
	788	13.9	80
5%$NaFe_3O_4$_WI	418	1.8	10
	618	7.4	41
	788	8.8	48
$NaFe_3O_4$_CP	362	1.6	9
	639	9.5	55
	788	6.2	36
$NaFe_3O_4$_CP@HZSM5	370	1.4	8
	617	9.2	53
	724	6.6	38
$NaFe_3O_4$_CP@HZ	453	1.5	9
	663	8.7	50
	809	7.1	41

It is worth highlighting that a higher sodium content, whether added directly by coprecipitation or subsequently by impregnation, does not significantly affect the H_2-uptake of the first peak, from 1.5 $mmol \cdot g^{-1}$ for 1%$NaFe_3O_4$_WI to 1.6 $mmol \cdot g^{-1}$ and 1.8 $mmol \cdot g^{-1}$ for $NaFe_3O_4$_CP and 5%$NaFe_3O_4$_WI. This result is not surprising since, according to the XRD results (Figure 3. 5), there are no obvious peaks attributable to the Fe_2O_3 phase, except in the sample of 1%$NaFe_3O_4$_WI. Instead, the $_{H2}$-uptake of the second peak (Fe_3O_4 becoming FeO)

is particularly low (2.0 mmol·g-1) for the sample 1%$NaFe_3O_4$_WI if compared to 5%$NaFe_3O_4$_WI and $NaFe_3O_4$_CP where the H_2-uptake was 7.4 mmol·g^{-1} and 9.5 mmol·g^{-1}, respectively. Table 3. 4 and Figure 3. 14 b) show that for the core-shell structure the peaks are shifted towards higher temperatures. Furthermore, the total H_2 consumption of the first two peaks is in both cases lower than the value obtained for the parent active phase alone. This aspect is even more evident in core-shell type structures, where the first reduction peak is shifted towards slightly higher temperatures compared to the parent active phase used ($NaFe_3O_4$_CP) as the core. In fact, the first peak shifted to 370 °C for the sample $NaFe_3O_4$_CP@HZSM5 and 453 °C for $NaFe_3O_4$_CP@HZ catalyst, while the H_2-uptake decreased from 11.1 mmol·g^{-1} for the $NaFe_3O_4$_CP phase alone to 10.6 mmol·g^{-1} and 10.2 mmol·g^{-1} for the corresponding core-shell structures. A possible explanation deals with that the proximity between the iron phase and zeolite, that may influence the reducibility of the catalyst, and therefore its catalytic performance. This could also be related to the mass transfer phenomena of H_2 in the layer of zeolite that surround the oxide, which would delay the consumption of H_2 and thus lead to a shift to higher temperatures and/or Na migration.

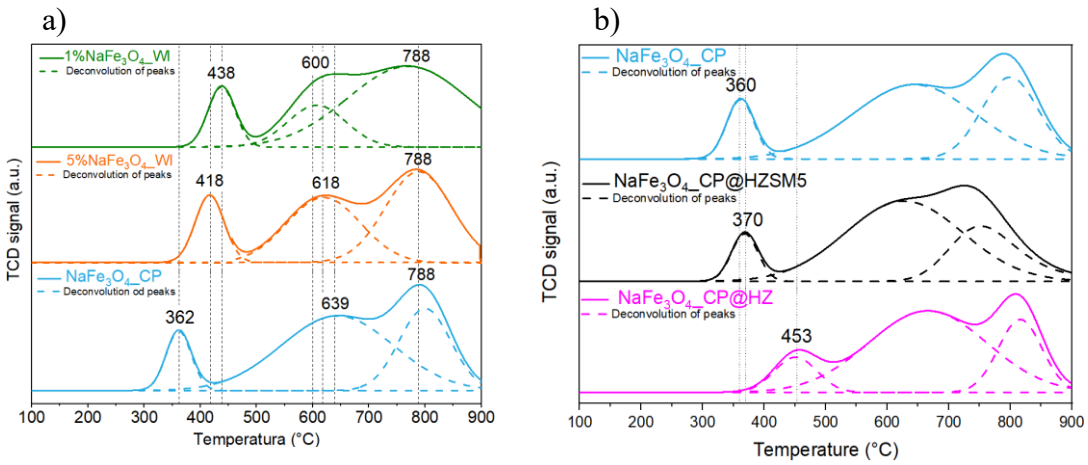


Figure 3. 14. H_2-TPR profiles of fresh catalysts: (a) 1%Na-Fe_3O_4_WI, 5%Na-Fe_3O_4_WI 5%Na-Fe_3O_4_CP; (b) $NaFe_3O_4$_CP@HZSM5 and $NaFe_3O_4$_CP@HZ.

To support Na migration and/or mass transfer phenomena, NH_3-TPD tests were carried out to evaluate and compare the acidity of the core-shell structures with the parent zeolite used as the shell, as shown in Figure 3. 15. The commercial zeolite (HZSM5) and the hierarchical one (HZ) exhibit a total acidity of 263 µmol·g^{-1} and 273 µmol·g^{-1}, respectively (Table 3. 5);

Table 3. 5. Quantitative analysis of the NH_3-TPD measurements.

	Weak acid sites $\mu mol \cdot g^{-1}_{zeolite}$ **(170-200 °C)**	**Medium acid sites** $\mu mol \cdot g^{-1}_{zeolite}$ **(~244°C)**	**Strong acid sites** $\mu mol \cdot g^{-1}_{zeolite}$ **(350-400 °C)**	**Total acid sites** $\mu mol \cdot g^{-1}_{zeolite}$
HZSM-5	137.28	-	125.94	263.22
HZ	135.96	-	136.74	272.70
NaFe3O4_CP@HZSM5	77.81	190.86	-	268.66
NaFe3O4_CP@HZ	75.89	192.58	-	268.47

The concentration of acid sites within the hierarchical zeolite is comparable to that of the commercial zeolite, providing evidence that the synthesis was successful. The NH_3-TPD profiles of $NaFe_3O_4$_CP@HZSM5 and $NaFe_3O_4$_CP@HZ core-shell structures present a single, wider peak with a shoulder at a lower temperature of about 10-40 °C compared to the respective zeolite used as the shell. In addition, the peak at a higher temperature (350-400 °C) is completely absent. This result can be justified by the migration of sodium (promoter) from the mixed iron oxide phase towards the zeolite, since NaZSM-5 zeolite results in the absence of strong acid sites capable to adsorb NH_3 molecules, owing to the absence of a proton (H^+) linked to the O atom in the −Al−O−Si− group [151]. On the other hand, the concentration of acid sites of fresh and spent sample is similar, indicating that the total amount of acid sites remain constant (Table 3. 4).

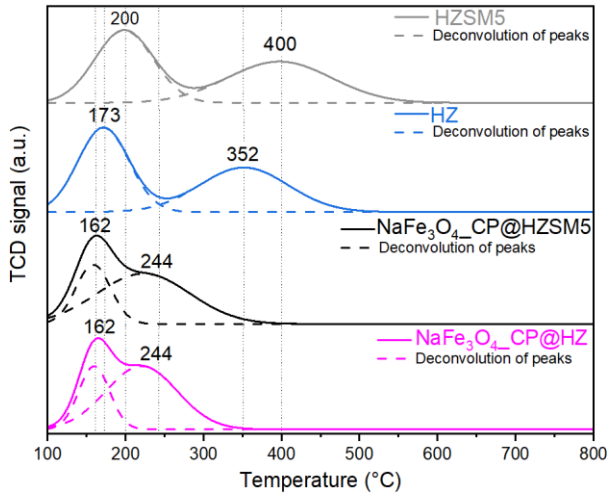


Figure 3. 15. NH_3-TPD fresh catalysts profiles.

The degree of coverage for the core-shell $NaFe_3O_4$_CP@HZSM5 was investigated via FESEM-EDS analysis, as reported in Figure 3. 16. The samples were prepared by cutting a section of sample with a scalpel and placing the hemisphere on the appropriate stub. The procedure was facilitated by the electrostatic properties of iron-phase situated in the core, which allowed the pellet to be precisely positioned. As can be seen from Figure 3. 16, the sample was perfectly coated with zeolite.

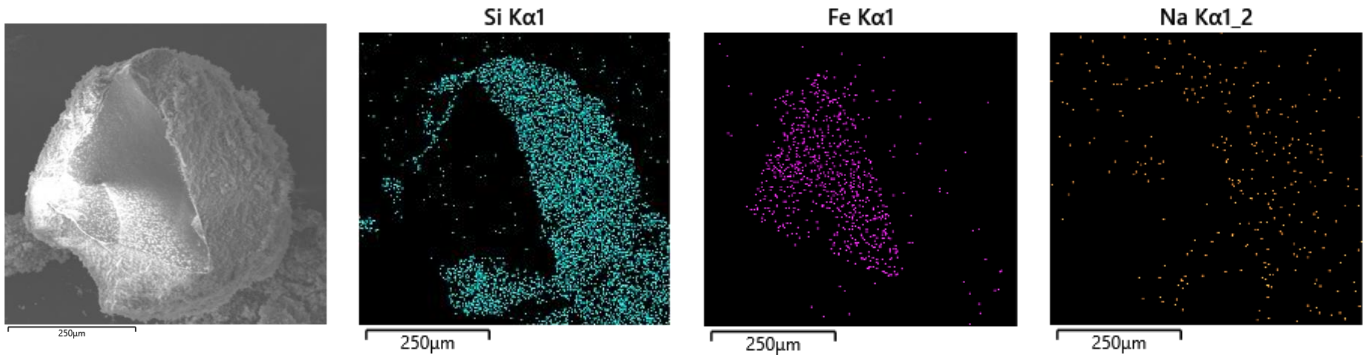


Figure 3. 16. FESEM-EDS images of the sample: $NaFe_3O_4$_CP@HZSM5.

Basic properties of fresh and spent catalysts were investigated by CO_2-TPD measurements. Figure 3. 17 a) and Figure 3. 18 a) show the CO_2 desorption profiles for fresh iron-oxide phase catalysts and fresh core-shell $NaFe_3O_4$_CP@HZSM5, respectively, while Figure 3. 17 b) and Figure 3. 18 b) show the desorption profiles for the corresponding spent catalysts. The fresh catalysts exhibit a desorption peak at relatively low temperature, especially in the case of $NaFe_3O_4$_CP catalyst (156 °C), attributed to the desorption of weakly

adsorbed CO_2. This peak is virtually absent in the 5%$NaFe_3O_4$_WI catalyst. However, intense and broad peaks appear in the temperature range of 400-900 °C in the TPD profiles of the 1%$NaFe_3O_4$_WI and 5%$NaFe_3O_4$_WI catalysts. These peaks result from the desorption of CO_2 that interacts strongly with the surface basic sites. The presence of sodium is crucial in improving the surface basicity, as indicated by these results. Furthermore, the total CO_2 uptake amount of 5%$NaFe_3O_4$_WI shows that the surface basicity increases with increasing sodium content (Table 3. 6). However, the surface basicity does not depend only on the amount of sodium, but also on its distribution on the catalyst surface [119]. Additionally, with the introduction of zeolite (core-shell structure $NaFe_3O_4$_CP@HZSM5), the first peak shifts to a temperature about 100 degrees higher if compared with the core phase profile ($NaFe_3O_4$_CP). Focusing on the CO_2-TPD profiles, spent catalysts (Figure 3. 17 b) and (Figure 3. 18 b), in all cases, there is at least one peak at a temperature above 520 °C. The absence of CO_2 desorption peaks below 400 °C indicates the absence of relatively weak basic sites on the surface of spent catalysts, which implies that the weaker basic sites on the surface of fresh catalysts have become stronger compared to their spent counterparts [152]. Moreover, the number of basic sites for all spent catalysts increases significantly after the CO_2 hydrogenation reaction (Table 3. 6). It should also be noted that the higher the Na load in the catalyst, the greater the amount of desorbed CO_2. Finally, comparing the amount of CO_2 per unit of mass of Fe_3O_4 of spent catalysts with and without a zeolite, it is possible to see that the amount of desorbed CO_2 decreases significantly in the core-shell $NaFe_3O_4$_CP@HZSM5 structure (Table 3. 6). This could imply that the presence of zeolite in intimate contact with the $NaFe_3O_4$_CP phase negatively affects the adsorption of CO_2.

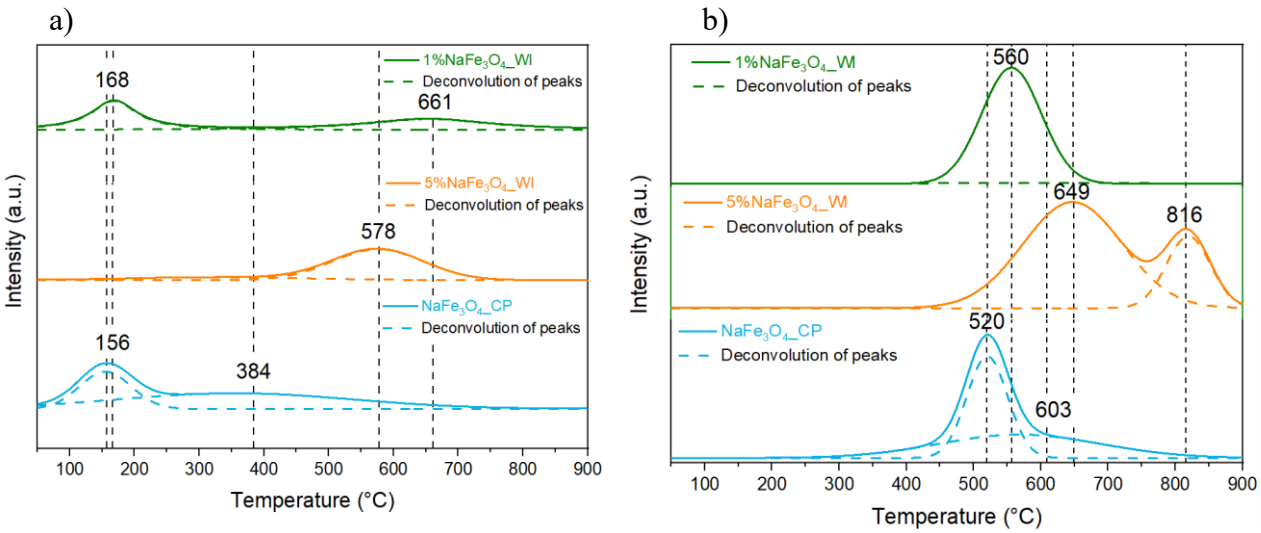


Figure 3. 17. CO_2-TPD profiles a) fresh iron-oxide and b) spent iron-oxide samples.

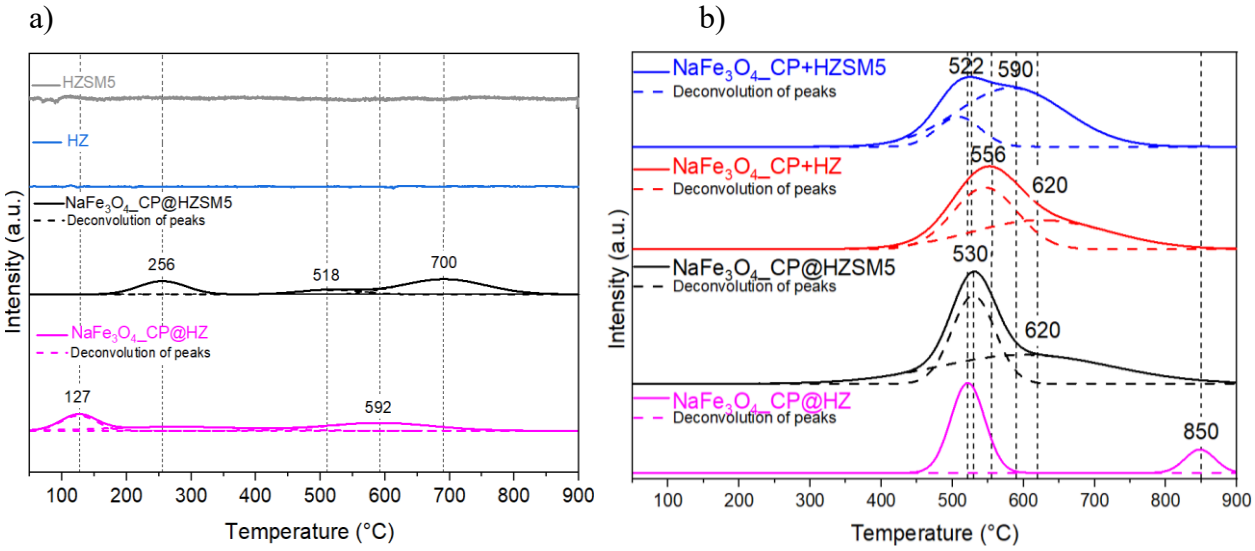


Figure 3. 18. CO_2-TPD profiles a) fresh core-shell catalyst; b) spent core-shell structures and physical mixture.

Table 3. 6. CO_2-TPD fresh and spent iron-oxide phases.

	Fresh sample ($mmol/g_{iron\text{-}oxide\ phase}$)	**Spent sample** ($mmol/g_{iron\text{-}oxide\ phase}$)
1%$NaFe_3O_4$_WI	0.2	3.6
5%$NaFe_3O_4$_WI	0.7	3.9
$NaFe_3O_4$_CP	0.5	3.9
$NaFe_3O_4$_CP+HZSM5	-	3.7
$NaFe_3O_4$_CP+HZ	-	4.2
$NaFe_3O_4$@HZSM5	0.3	3.1
$NaFe_3O_4$@HZ	0.1	3.4

To better understand where Na was located and if the core-structures were well covered by the zeolite, XPS measurements have been performed on samples: 1%$NaFe_3O_4$_WI, 5%$NaFe_3O_4$_WI, $NaFe_3O_4$_CP, $NaFe_3O_4$_CP@HZSM5 and $NaFe_3O_4$_CP@HZ, both fresh and spent ones. In particular, survey scans have been recorded firstly, to infer the presence of chemical elements and to calculate their relative atomic concentration (at.%); scans are reported in Figure 3. 19.

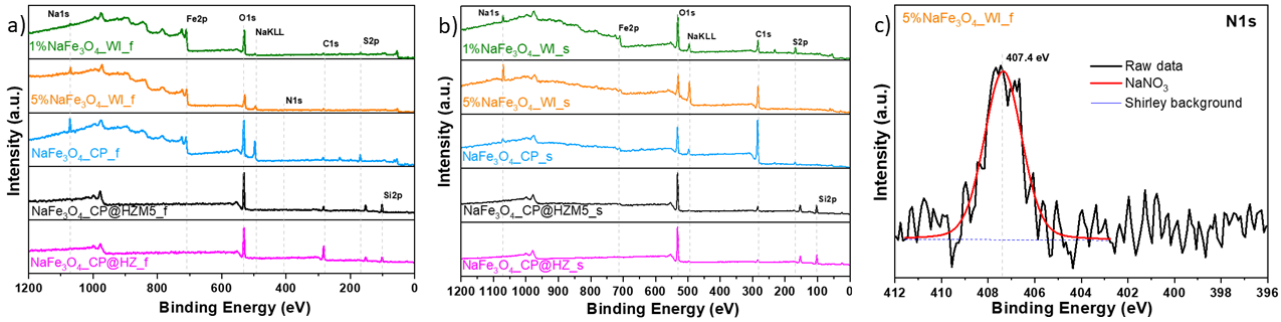


Figure 3. 19. XPS spectra related to survey regions for fresh a) and spent b) samples. C) HR N1s region deconvoluted to show the chemical shift of N due to $NaNO_3$ bond in 5%$NaFe_3O_4$_WI_f sample.

The chemical composition obtained for each sample is resumed in Table 3. 7. According to literature [153] we expected a decrease in the Fe concentration after the catalytic tests, due to the formation of a passivation layer made principally by Carbon species. This trend is clearly noticeable for samples 1%$NaFe_3O_4$_WI, 5%$NaFe_3O_4$_WI and $NaFe_3O_4$_CP, while the core-shell structures did not show a clear trend, as iron oxide is cover by zeolite shell. C content for sample $NaFe_3O_4$_CP@HZSM5 can be considered mostly stable, while for sample $NaFe_3O_4$_CP@HZ Carbon content decreases after catalytic tests. Fe signal appeared after catalytic tests in both zeolite covered samples, with very low intensity (≤ 1.0 at.%), maybe due to shell erosion or fractures, which make Fe_3O_4 core exposed. Na1s signal has a not clear trend as well: it increases for wet impregnated samples, after catalytic tests, while decreases for co-precipitated one; it is almost constant for core-shell structures (according to Fe content). Some remnants due to precursors have also been detected (i.e. Cl and S). It has to be underlined that only for sample 5%$NaFe_3O_4$_WI_f a N1s peak has been detected. From subsequent HR analysis (see Figure S10), we found out that the chemical shift inferred is the one related to $NaNO_3$ (407.4 eV) [154], as already explained with XRD measurement. This contribution disappeared after catalytic tests.

Table 3. 7. XPS relative atomic concentration (at.%) for all the samples, fresh and spent ones.

SAMPLES	Relative atomic concentration (at.%)						
	C1s	O1s	Fe2p	Na1s	Si2p	Others	
1%$NaFe_3O_4$_WI	10.9	67.3	14.6	2.3	/	Cl: 0.5; S: 4.4	fresh
	37.1	46.9	3.9	4.8	/	Cl: 0.3; S: 7.0	spent
5%$NaFe_3O_4$_WI	19.9	48.8	21.1	7.8	/	N: 2.4	fresh

	61.9	23.7	3.2	11.2	/	/	spent
$NaFe_3O_4$_CP	11.4	53.5	9.6	14.2	/	Cl: 1.6; S: 9.7	fresh
	76.6	19.4	0.8	1.5	/	S: 1.7	spent
$NaFe_3O_4$_CP+HZSM5	18.2	61.3	/	/	20.5	/	fresh
	20.0	57.2	1.0	0.8	21.0	/	spent
$NaFe_3O_4$_CP+HZ	47.1	41.4	/	/	11.5	/	fresh
	9.3	60.3	0.4	1.1	28.0	Al: 0.9	spent

Focusing on the HR spectra acquired for all the elements, which are crucial to understand the behavior of catalysts surfaces, we can appreciate several modifications due to catalytic tests. In Figure 3. 20 (a, d) Fe2p spectra are reported, for both fresh and spent samples: the shape of curves for the WI fresh samples is the one reported for Fe_3O_4 [155], with the typical satellite due to Fe^{3+} species at ≈ 719 eV. The $Fe2p_{3/2}$ peak position is at 710.3 eV (± 0.1 eV), as expected. For sample $NaFe_3O_4$_CP_f, the peak appears less sharp towards the lower binding energy, with an enlargement of the FWHM, due to the increase of the Fe^{2+} component (at 709.0 eV), which is furthermore evidenced by the quasi-disappearance of the satellite at 719 eV, which is due to Fe^{3+}. After the catalytic tests new components arise, in accordance to XRD results. In particular two components have been detected: a first one at 706.7 eV due to $Fe(^0)$ and a second one at 708.7 eV due to FeC_x [156]. Both components are more intense in samples 5%$NaFe_3O_4$_WI_a and in the core-shell ones. In accordance to Fe2p changes also C1s peaks show different chemical shifts after the catalytic activity. Before tests, the C signal are quite noisy, due to the low intensity of the signals. After the tests the signals are sharper and deconvolution procedures (not shown) could be applied to them. Apart from the C-C due to adventitious carbon at 284.8 eV, several peaks due to C-O interaction are present at higher binding energy values, as reported in Figure 3. 20 (b, e). Only sample 5%$NaFe_3O_4$_WI_a shows a component at 288.6 eV, due to COOH species. If we look at the lower binding energies side, we can infer the appearance of two components: one due to FeC_x bond at 283.1 eV and another one at 284.5 eV, which can be due to C-C sp^2 arrangement or to C-Fe* charge transfer effects [157] which appears when charge is transferred from the metal surface atoms to the more electronegative carbon atoms in the a-C matrix, which, in our case, can be represented by the outer C amorphous shell, as shown in TEM analysis previously. The last region we have analyzed is the one related to Na1s peak, Figure 3. 20 (c, f). Two main chemical shifts have been evidenced: a first one at lower binding energies at 1071.6 (±0.2) eV and a second one at higher binding energies at 1072.8 (± 0.2) eV. Based on the article proposed by K.P. de

Jong et al. from the a Na1s signal it is possible to evaluate the possible migration of sodium. In fact, the position of Na1s signal has to be at 1071.4 eV, whereas the core-shell structures, after the heat treatment, showed a shift of the Na1s signal to 1073.0 eV, which is in the range of the sodium ion exchanged zeolite (1072.8 eV). This shift towards higher binding energy after the heat treatment supports the hypothesis of migration of sodium ions from the iron catalyst to the zeolite, resulting in loss of promotion effect on the iron catalyst as well as decreased acidity of the zeolite [104].

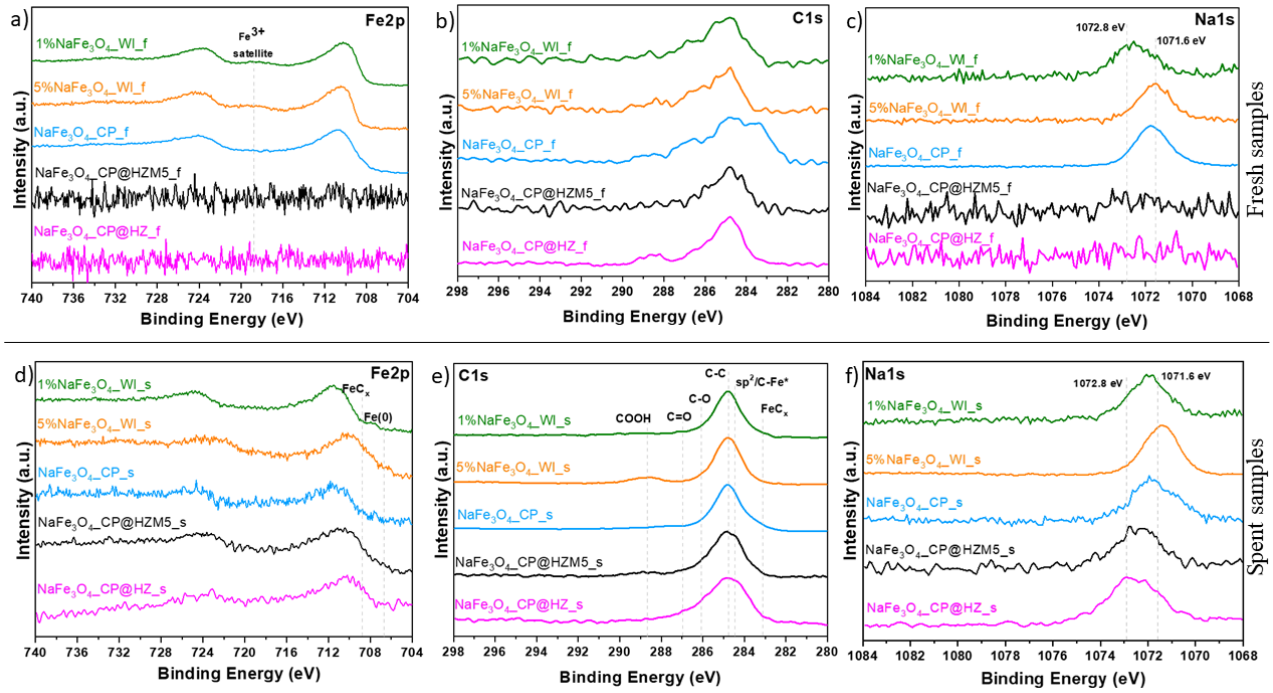


Figure 3. 20. XPS HR spectra: Fe2p doublet (a, d), C1s region (b, e) and Na1s region (c, f) for fresh (upper row) and spent (lower row) samples.

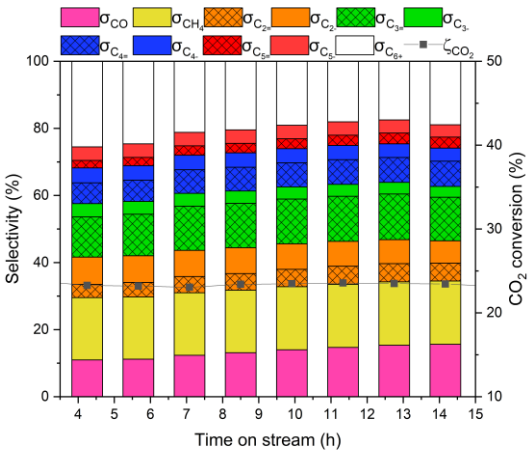
3.2.2. Catalytic tests

This section presents the outcomes of the catalytic experiments performed on iron-oxide phases synthesized through different techniques and with varying sodium content. Stability tests were carried out at 330 °C, a pressure of 2.3 MPa, and a flow rate of 21.96 $NL \cdot g_{Fe3O4} \cdot h^{-1}$ with an inlet composition of 65 vol.% H_2, 22 vol.% CO_2, and 13 vol.% N_2 over about 14 hours. The aim of these tests is to shed light on the behavior of the catalytic performances when the contact between

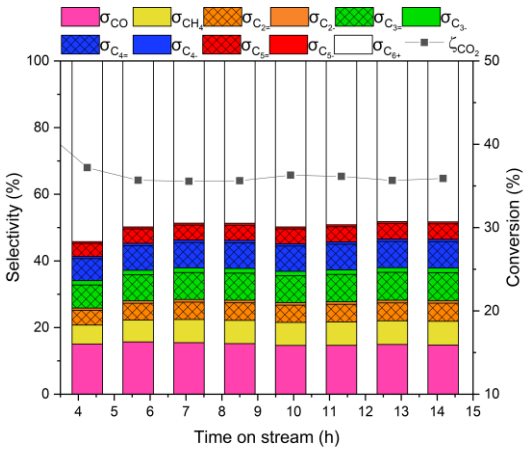
the iron phase and the zeolite is intimate, thanks to the core-shell structure, and to provide an interpretation for the obtained results.

First of all, the three iron-based catalysts were tested. As reported in the synthesis section, the samples named 1%$NaFe_3O_4$_WI, 5%$NaFe_3O_4$, and NaFe3O4_CP were obtained using two different synthesis methods (impregnation for 1%$NaFe_3O_4$_WI and 5%$NaFe_3O_4$ and coprecipitation for $NaFe_3O_4$_CP) and varying the sodium content from 1 wt.% (gNa/gFe_3O_4) in 1%$NaFe_3O_4$_WI, to 5 wt.% (gNa/gFe_3O_4) in 5%$NaFe_3O_4$_WI sample. To simplify the discussion of the catalytic tests, the results corresponding to 11 hours of testing are shown in Figure 3. 22, while the TOS monitoring profiles are shown in Figure 3. 21 a), b), and c).

a) 1%$NaFe_3O_4$_WI



b) 5%$NaFe_3O_4$_WI



c) $NaFe_3O_4$_CP

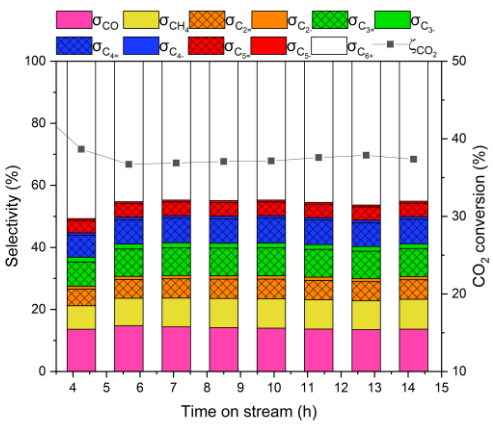


Figure 3. 21. Time-on-stream (TOS) tests up to ≈ 14 hours, temperature: 330 °C, pressure: 2.3 MPa, and flow rate: 22 $NL \cdot g^{-1}_{Fe3O4} \cdot h^{-1}$ with an inlet $H_2/CO_2/N_2$ molar ratio equal to 15/5/3: a) 1%$NaFe_3O_4$_WI; b) 5%$NaFe_3O_4$_WI; c) $NaFe_3O_4$_CP.

As can be seen from Figure 3. 22, the catalytic performance increases with increasing sodium content. CO_2 conversion passes from 22% in the 1%$NaFe_3O_4$_WI sample to 36-38% in the 5%$NaFe_3O_4$_WI and $NaFe_3O_4$_CP samples. demonstrating that the amount of loaded Na seems (rather than the synthesis method) seems to affect the catalytic performance [119]. On the other hand, although the CO selectivity is approximately the same (ranging from 13 to 15% in all three samples), the methane selectivity is suppressed with increasing sodium content, in agreement with the open literature [158]. The CH_4 selectivity decreases from 19% for the 1%$NaFe_3O_4$_WI catalyst to 7-9% for the other two catalysts. Furthermore, it is worth noting that as the sodium content increases, the selectivity for olefins in the C_2-C_5 range increases significantly, reaching 88-87% for 5%$NaFe_3O_4$_WI and $NaFe_3O_4$_CP samples, respectively (Table 3. 8).

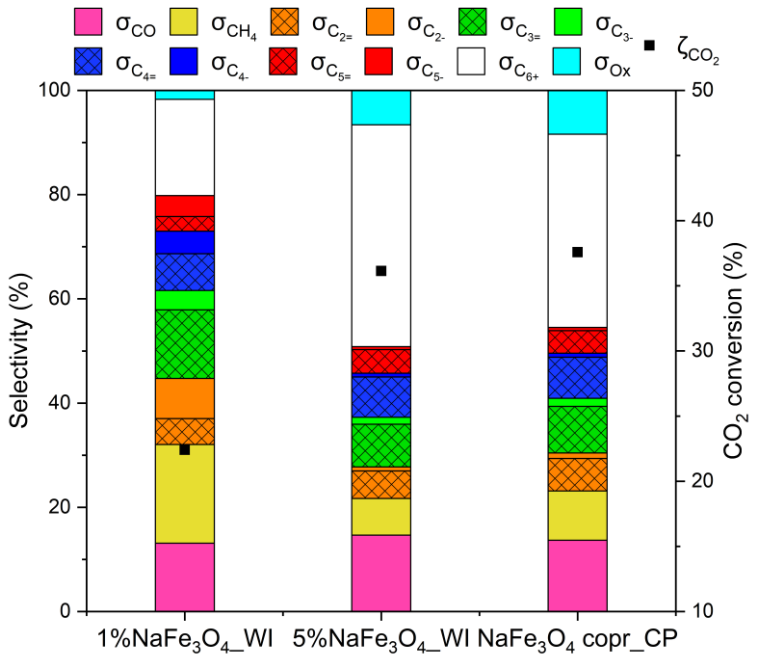


Figure 3. 22. Comparison catalytic performance of 1%$NaFe_3O_4$_WI, 5%$NaFe_3O_4$_WI and $NaFe_3O_4$_CP catalysts at 330 °C. Reaction conditions: 2.0 MPa, 21.96 $NL \cdot gFe_3O_4 \cdot h^{-1}$, TOS = 14 h.

Table 3. 8. Results catalytic tests.

	CO_2 conv	CO sel	CH_4 sel	C_2-$C_5^=$ sel	C_2-C_5^0 sel	C_{6+} sel	Ox sel	O/(O+P)[a]
	(%)	(%)	(%)	(%)	(%)	(%)	(%)	(%)
1%$NaFe_3O_4$_WI	22	13	19	28	20	18	2	59
5%$NaFe_3O_4$_WI	36	15	7	26	3	43	7	88
$NaFe_3O_4$_CP	38	14	9	27	4	37	8	87
$NaFe_3O_4$_CP+HZSM5	35	19	8	5	20	45	2	21
$NaFe_3O_4$_CP+HZ	40	12	8	4	18	57	1	18
$NaFe_3O_4$_CP@HZSM5	22	12	24	10	35	19	0	23
$NaFe_3O_4$_CP@HZ	25	18	19	12	31	19	0	27

[a] Olefin share calculated for the fraction C_2-C_5.

GC-MS chromatogram obtained by injecting the collected oil produced with the $NaFe_3O_4$_CP sample is shown in Figure 3. 23, where the prevalence of olefinic compounds can be appreciated.

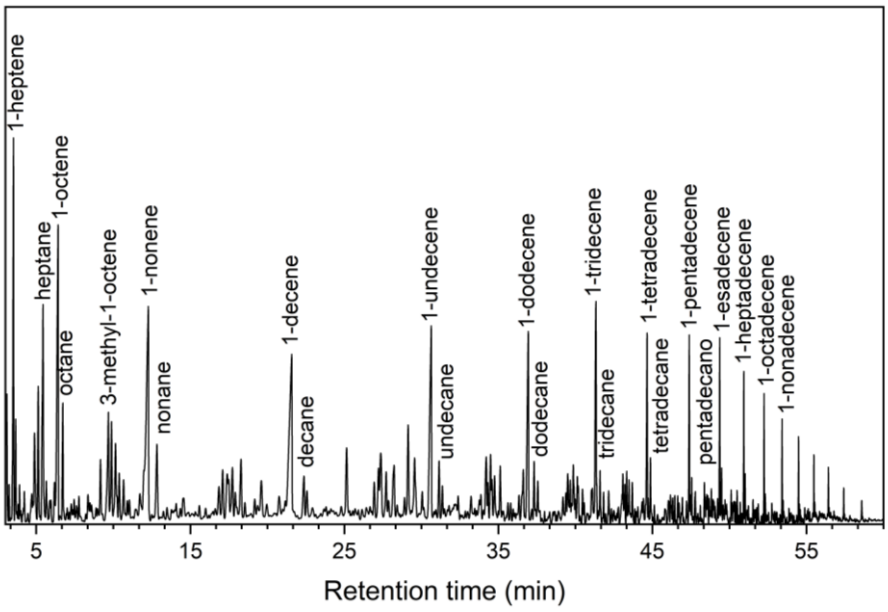


Figure 3. 23. Mass chromatogram $NaFe_3O_4$ _CP.

Another interesting aspect is the selectivity of oxygenated compounds present in the collected aqueous fraction during condensation, calculated taking into account the amount of cleaning solvent (acetone) used to clean the reactor and the lines of the test bench. Specifically, the amount of acetone resulting from HPLC analysis was subtracted from the $mg \cdot L^{-1}$ of carbon obtained through TOC analysis (Table 3. 9), divided for the hours of TOS and subtracted as a complement to 100 with respect to the gaseous products analyzed continuously using GC-FID (Table 3. 8 and Figure 3. 22).

Table 3. 9. Results derived from TOC and HPLC.

	TOC $\mathbf{mg_C \cdot L^{-1}}$	**HPLC**[a] $\mathbf{mg_C \cdot L^{-1}}$
1%$NaFe_3O_4$_WI	7133	896
5%$NaFe_3O_4$_WI	30335	6662
$NaFe_3O_4$_CP	5960	338
$NaFe_3O_4$_CP+HZSM5	9015	2565
$NaFe_3O_4$_CP+HZ	4854	2151
$NaFe_3O_4$_CP@HZSM5	1581	863
$NaFe_3O_4$_CP@HZ	998	249

[a]$mg \cdot L^{-1}$ of acetone resulting from reactor and lines cleaning.

Finally, focusing on the comparison of these last two catalysts, it is interesting to note that, although they were obtained using different syntheses, the catalytic results obtained with the same sodium content are very similar, regardless of the preparation method [119]. For this reason, for simplicity of preparation, only the $NaFe_3O_4$_CP sample was tested in physical mixture mode and in core-shell structures with two different MFI-type zeolites: the commercial zeolite (HZSM-5) and the homemade hierarchical zeolite (HZ).

The interest in combining the iron-based catalyst with zeolite lies in the desire to obtain a liquid fuel with aromatic compounds, in order to confer desirable properties to the final product, such as high octane number and improved engine combustion efficiency. Additionally, aromatic compounds are important for cleaner combustion because they have a higher tendency to burn completely than other gasoline components, thus reducing emissions of polluting exhaust gases. On the other hand, excessive amounts of aromatics can increase particulate

emissions, so their presence in gasoline must be carefully controlled. To control the content of aromatic compounds, it is important to use zeolites with an appropriate Si/Al atomic ratio. In fact, based on literature data, a zeolite with a Si/Al atomic ratio of 40 was chosen for this work. In Figure 3. 26 are reported the catalytic data of the tests that include the zeolite, while the TOS monitoring profiles are shown in Figure 3. 24 (a, b) and Figure 3. 25 (a,b).

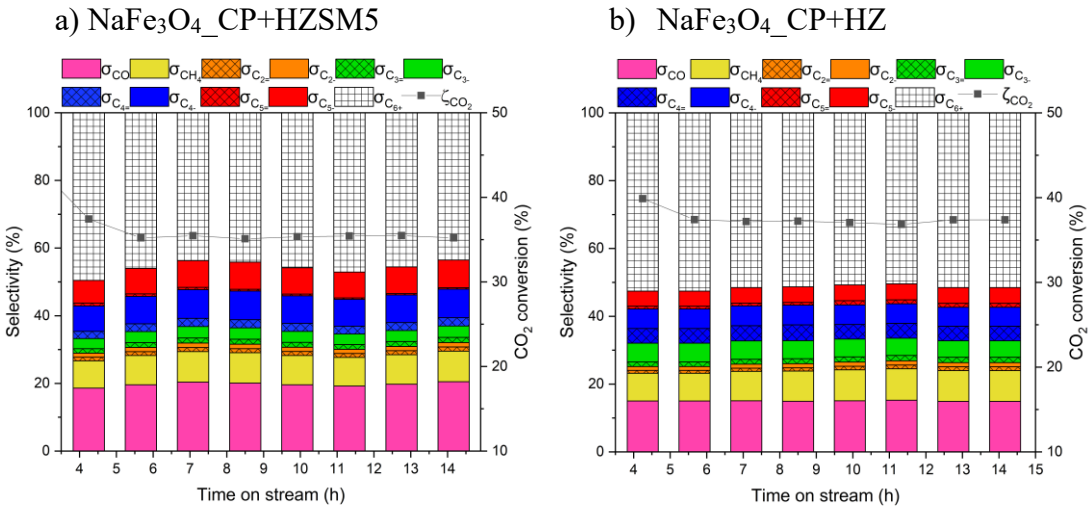


Figure 3. 24. Time-on-stream (TOS) tests up to ≈ 14 hours, temperature: 330 °C, pressure: 2.3 MPa, and flow rate: 22 $NL \cdot g^{-1}_{Fe3O4} \cdot h^{-1}$ with an inlet $H_2/CO_2/N_2$ molar ratio equal to 15/5/3: a) $NaFe_3O_4$_CP+HZSM5; b) $NaFe_3O_4$_CP+HZ.

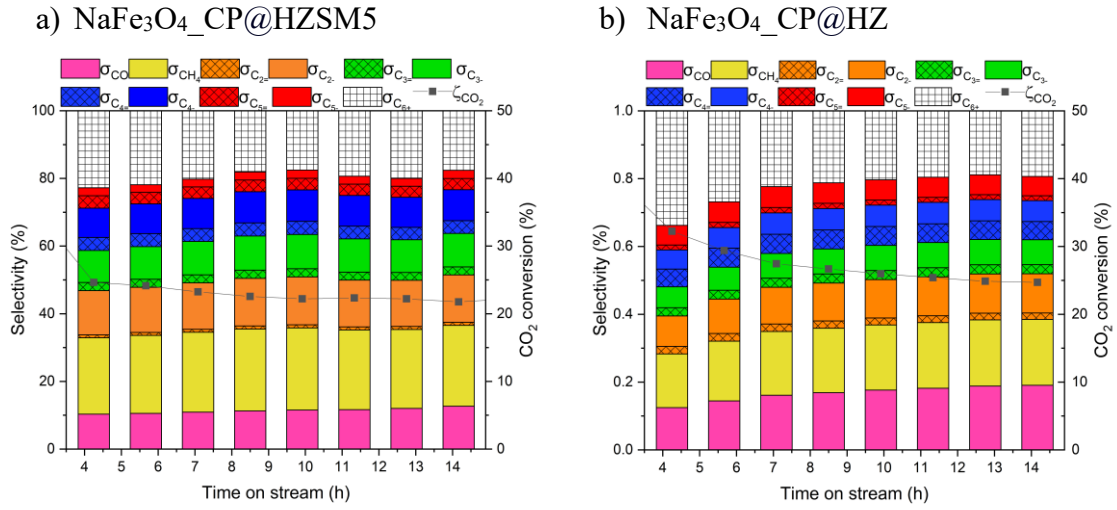


Figure 3. 25. Time-on-stream (TOS) tests up to ≈ 14 hours, temperature: 330 °C, pressure: 2.3 MPa, and flow rate: 22 $NL \cdot g^{-1}_{Fe3O4} \cdot h^{-1}$ with an inlet $H_2/CO_2/N_2$ molar ratio equal to 15/5/3: a) $NaFe_3O_4$_ CP@HZSM5; b) $NaFe_3O_4$_CP@HZ.

Looking to the results resumed in Figure 3. 26, it can be appreciated that the $NaFe_3O_4$_CP catalyst tested in physical mixture with both the commercial and homemade hierarchical zeolites showed higher catalytic activity than the corresponding core-shell sample having the same active phase and zeolite. Specifically, the catalyst called $NaFe_3O_4$_CP+HZ turned out to have the best catalytic performance. This catalyst achieved a conversion of 40%, compared to a conversion of 35% for the $NaFe_3O_4$_CP+HZSM5 catalyst, a CO selectivity of 12% compared to 19% for the $NaFe_3O_4$_CP+HZSM5 catalyst, and an 8% CH_4 selectivity for both catalysts. The C_{6+} selectivity was 57%, compared to 45% for the $NaFe_3O_4$_CP+HZSM5 catalyst. Furthermore, for the most performing catalyst ($NaFe_3O_4$_CP+HZ) light olefins (C_2-C_5) selectivity and olefin share are the lowest among the investigated samples, being equal to 4% and 18%, respectively (Table 3. 8). Limited olefins content and increased paraffins production, along with the formation of C_{6+} compounds, is a clear demonstration of the zeolite ability to oligomerize, isomerize, and aromatize.

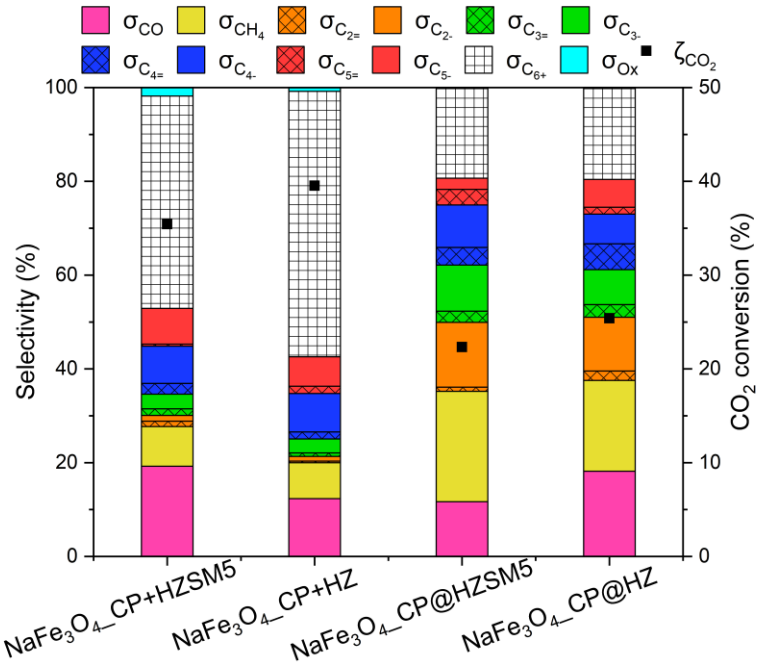


Figure 3. 26. Comparison of catalytic performance among physical mixture and core-shell of $NaFe_3O_4$_CP with commercial and homemade hierarchical zeolite. Reaction conditions: 330°C, 2.3 MPa, and a flow rate of 21.96 $NL \cdot g_{Fe3O4} \cdot h^{-1}$ TOS=14 h.

Another interesting aspect is that the content of oxygenated compounds decreased when an acid zeolite is present within the catalyst (decreasing from 8% for the $NaFe_3O_4$_CP phase alone to below 2% for the catalysts containing both $NaFe_3O_4$_CP and zeolite). Indeed, oxygenated compounds can be transformed directly into olefins and/or hydrogenated to paraffins. In addition, the superior catalytic performance of the hierarchical zeolite can be attributed to the presence of mesopores, which facilitate the desorption of aromatic and/or long-chain products due to the larger pore size. As can be appreciated from the chromatograms of the oil collected at the end of the 14-hour test and reported in Figure 3. 27 and Figure 3. 28, the majority of the compounds present in the C_{6+} fraction are aromatic compounds, both when using a commercial or a hierarchical homemade zeolite, while looking to the TOC results, the hierarchical zeolite represents the one with lower content of oxygenated compounds, Table 3. 9.

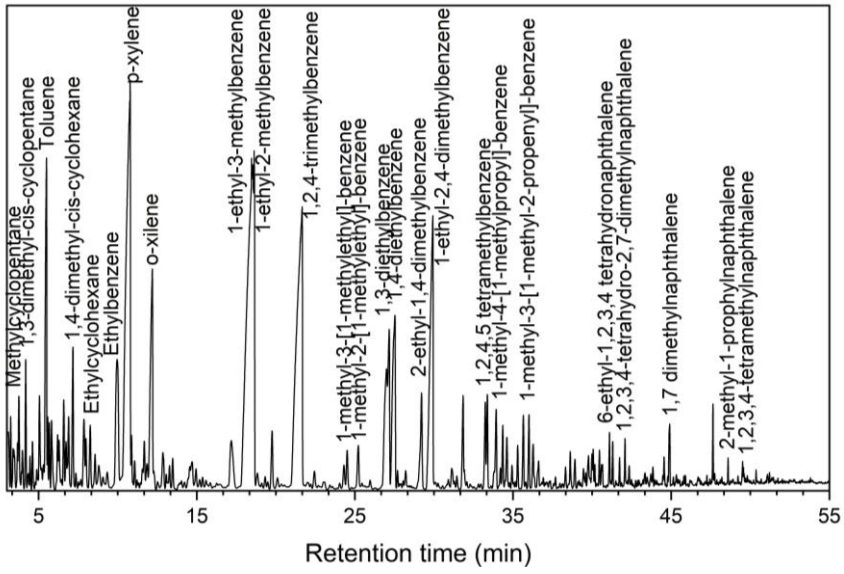


Figure 3. 27. Mass chromatogram $NaFe_3O_4$ _CP+HZSM-5.

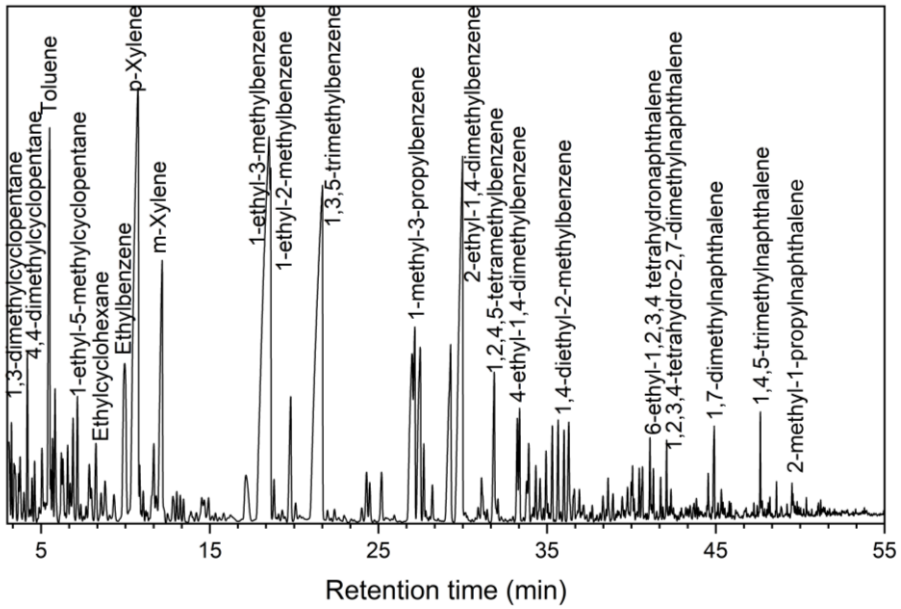


Figure 3. 28. Mass chromatogram $NaFe_3O_4$ _CP+HZ.

Focusing on the core-shell configurations (Figure 3. 26), it is clear that the catalytic activity towards modified Fischer-Tropsch Synthesis (FTS) is lower than the one obtained with the corresponding physical mixtures and the iron-based catalyst alone (as indicated in Table 3. 8). $NaFe_3O_4$_CP@HZSM5 catalyst, for instance, exhibits a 13% lower conversion rate than the corresponding $NaFe_3O_4$_CP+HZSM5, and the same 13% decrease is observed when comparing $NaFe_3O_4$_CP@HZ with $NaFe_3O_4$_CP+HZ. Moreover, both core-shell structures demonstrate an increase in selectivity towards CH_4 and olefins/paraffins, and a significant reduction in C_{6+} compounds when compared to the corresponding catalysts tested in physical mixture. These outcomes can be attributed to the decrease in alkaline content in the iron catalyst, caused by the migration of alkali metals towards the zeolite [159]. Additionally, previous research has suggested that a small distance between the iron (-carbide) catalyst and the acidic sites of a bifunctional catalytic system may facilitate the migration of alkali metal ions from the iron (-carbide) catalyst to the zeolite, owing to the high mobility of these ions. This may lead not only to decreased activity and selectivity of the catalyst, but also neutralize the acidic sites of the zeolite, resulting in lower selectivity towards olefin aromatization [159].

To rule out deactivation of the core-shell structures due to coke deposition, all spent catalysts were subjected to temperature programmed combustion (TPC) analysis to quantify the amount of carbon deposited on the surface of the samples during catalytic tests. Table 3. 10 presents the correlation between the quantity of

carbon moles in the spent catalyst (generated during TPC analysis) and the percentage of converted carbon moles. When the hierarchical zeolite is involved, the amount of coke deposit in the carbon is lower, confirming the importance of mesopore in the structure of the zeolite. In addition, based on the results of coke deposition, the core-shell structures lower activity is not due to deposited coke. In fact, the resulting coke is lower if compared to the catalysts that showed higher catalytic activity. The results emphasize that the core-shell structures are probably affected by diffusion problems and/or sodium migration issues. Moreover, it is possible that these two effects are interconnected, and investigating the underlying reasons for the limited activity of these structures presents an intriguing research opportunity.

Table 3. 10. TPC results.

	g_{coke}/g_{cat} (a.u.)	mol $C_{spent\ catalyst}$/mol $C_{converted}$ (%)
1%$NaFe_3O_4$_WI	0.05	0.63
5%$NaFe_3O_4$_WI	0.15	1.16
5%$NaFe_3O_4$_CP	0.11	0.82
$NaFe_3O_4$_CP+HZSM5	0.07	0.60
$NaFe_3O_4$_CP+HZ	0.07	0.47
$NaFe_3O_4$_CP@HZSM5	0.02	0.25
$NaFe_3O_4$_CP@HZ	0.02	0.21

3.3 In closing

The synthesis of stable and high-performing multifunctional catalysts for hydrocarbon mixture production via CO_2 hydrogenation (i.e., modified Fischer-Tropsch process) was investigated. Based on the results obtained, there does not seem to be a significant difference between iron-based catalysts with the same sodium content obtained through impregnation and coprecipitation. Thus, in terms of energy saving, the use of the iron-based catalyst obtained through coprecipitation represents a valid alternative, since it can be synthesized in a single step (without pre-calcination before use) and requires a smaller amount of water. Physical mixture between Na-promoted Fe-based metallic phase and acid zeolites

led to the best performance in terms of conversion and heavier hydrocarbons selectivity (mainly due to oligomerization and aromatization). Furthermore, it is evident that the use of a hierarchical zeolite is a valid alternative to increase the amount of products within the gasoline range. With the presence of mesopores that facilitate the release of products, the isomerization capacity is higher if compared to a conventional zeolite. As a future perspective, it will also be interesting to conduct in situ and/or post-reaction characterizations that allow us to study, confirm, and/or refute the migration of alkali metals, partly supported by the ex-situ XPS and NH_3-TPD analyses reported in this article. Alternatively, it will be necessary to study a support, possibly hydrophobic, such as carbon-based supports, that prevent the migration of sodium.

Chapter 4

4. Strategies to inhibiting alkali migration

This chapter explores in detail the impact of iron and sodium confined in nanotube channels (CNTs) with an outer diameter (OD) of 10-20 nm on alkali migration. The Na-Fe/CNT samples were tested in two different contact modes with commercial zeolite CBV5524G (MFI27): granule mixing (GM) and powder mixing (PM). For a direct comparison, a carbon nanotube (CNT) was prepared with the same amount of iron (10 wt.%) and sodium (Na/Fe atomic ratio of 0.025). However, in this configuration, iron and sodium were intentionally distributed on the surface of the CNT (OD: 10-20 nm). This approach has been crucial to assessing whether confinement effectively limits or mitigates the migration of sodium from iron catalyst sites to zeolite acid sites. Based on the results obtained, the iron content was increased from 10 wt. % to 15 wt. %, while keeping the Na/Fe atomic ratio constant. The study also examined the effect of confinement on CNTs with larger diameters of 40-60 nm and 60-100 nm.

4.1. Introduction

As extensively detailed in Chapter 1, the hydrogenation of CO_2, using green hydrogen produced from the surplus of renewable energy, holds promise for the sustainable production of value-added chemicals and fuels. Realizing this potential necessitates the use of high-performance catalysts. In this context, Fe, Co, and Ru-based catalysts for Fischer Tropsch Synthesis (FTS) have been extensively studied [77], [160]. Among them, iron-based catalysts have attracted a lot of attention because of their low detrimental effects, low cost, excellent selectivity toward olefins and high activity, gaining the interest of both industry and academic researchers. The product selectivity of FTS follows the Anderson-Schulz-Flory (ASF) distribution rule, in which product selectivity decreases as the

carbon number increases, which results in high selectivity for undesirable products consisting mainly on linear olefins and normal paraffins [161], [162]. However, these products cannot be used as gasoline without costly separation procedures and octane number addition [162]. For this reason, recently, researchers have achieved increased selectivity towards targeted products by combining oxides and zeolites, overcoming the ASF trend. Furthermore, iron-based not only is active for the RWGS and FTS reactions, but it also performs noticeably better when it is impregnated with alkali metals, such as sodium [70], [97], [110], by suppressing methane production. However, the presence of alkaline metals in iron-based catalysts can compromise their performance if not properly separated from the zeolite [90], [105], [106], [108], [163], [164]. For this reason, iron-based catalysts and zeolites are currently the focus of extensive research and offer promising avenues for further study. In fact, it is demonstrated that promoters, such as sodium, can migrate to the acidic sites of the zeolite, compromising the overall catalytic performance of the system [108]. The impact of this migration on composite catalysts is a subject of significant interest. The loss of sodium promotion from iron sites can negatively affect the conversion and the selectivity of both CO and CH_4. On the other hand, the ion-exchange of the protons of the acid sites of the zeolite with sodium results in a decrease in the ability of the zeolite to aromatize.

To overcome this inconvenience, could be interesting the use of an appropriated support. In this context it is crucial to emphasize that the nature and structure of the support, can influence metal dispersion, varying the effectiveness and selectivity of these iron-based catalysts. However, despite the fact that metals supported on silica, alumina, or titanium have historically been the main focus of research on catalysts for CO_2 hydrogenation, the investigation of carbon-based supports, such as carbon nanotubes (CNTs) and activated carbon, has increased recently [165].

This is because carbon materials are superior support candidates than traditional oxide supports because of their special qualities, which include an inert surface, good electrical conductivity, high mechanical and chemical stability, and a well-refined nanochannel structure that allow the confinement of sodium and iron. In particular, thanks to their particular structure, the CNT support may have an impact on the dispersion, distribution, reduction, carbonization, and, in the end, on the catalytic performance [166], [167].

A research team, led by Daniel R. Minett from the University of Bath, has demonstrated the efficacy of Fe@CNT supports in both the Reverse Water Gas Shift (RWGS) reaction and the Fischer Tropsch (FT) process, utilizing CO_2 as a raw material for hydrocarbon production. In this specific context, the significant surface area, thermal stability, and strong adhesion of carbon nanotubes to metal particles make them the preferred choice as catalytic supports. Carbon nanotubes (CNTs) have gained widespread use as platforms for converting carbon monoxide into hydrocarbons, facilitating superior dispersion of catalyst nanoparticles like iron. Notably, iron nanoparticles, when deposited on carbon nanotubes (CNTs) through initial moisturization techniques, have proven to be efficient FT catalysts with minimal deactivation rates. CNTs have also exhibited higher activity per unit volume compared to alternative platforms [168].

In addition, carbon nanotubes, with their distinctive features like uniform pore size distribution, meso and macro pore structure, inert surface properties, and resistance to acidic and basic environments, can significantly contribute to various catalytic reactions. The unique tubular structure of carbon nanotubes (CNTs), composed of graphene layers, induces a shift in p-electron density from the concave inner surface to the convex outer surface, according to theoretical studies. This results in an electron-deficient interior surface and an electron-enriched exterior surface, potentially influencing the structure and electronic properties of substances in contact with each surface. Furthermore, investigations into non-catalytic gas-phase reactions suggest that confinement within narrow channels could increase the density of reactants, creating a locally higher pressure. However, a potential drawback associated with depositing catalytic sites within these narrow channels is an increased restriction on mass transfer [165], [169].

In the utilization of CNT supports, the impact of the pore size and diameter of carbon nanotubes on the catalytic performance of FT catalysts remains unclear. Typically, the pore size of supported catalysts can affect the distribution of particle sizes, dispersion, degree of reduction, and rates of mass transfer [169].

This study is directed towards preventing sodium alkali migration of sodium from iron to the acid sites of zeolite. Initially, it was assessed the effectiveness of confining Na-impregnated iron inside Carbon Nanotubes (CNTs) with an outer diameter (OD) ranging from 10 to 20 nm, labeled as CNT-S-O10FeNa. The catalyst underwent testing using two different contact modes with an MFI-type zeolite named MFI27: granule mixing (GM) and powder mixing (PM). To gain a comprehensive understanding of whether confinement played a role in preventing

sodium migration, a CNT with an identical outer diameter (10-20 nm) and the same amount of iron and sodium content was prepared and tested. However, in this instance, iron and sodium were deliberately positioned on the surface of the CNT to enhance their interaction with the acidic sites of the zeolite, and this sample was identified as CNT-S-C10FeNa.

After confirming that effective confinement prevents sodium migration and improves catalytic performance over time, it was explored the impact of increase the content of iron inside the CNT. Specifically, it was prepared an additional CNT (10-20 nm) with a higher iron content (increased from 10% to 15%) while maintaining a constant atomic ratio of Na/Fe at 0.025. This new CNT was designated as CNT-S-O15FeNa. Furthermore, it was evaluated the influence of sodium and iron confinement in CNTs with a larger outer diameter, utilizing a CNT with an outer diameter of 40-60 nm (CNT-M-O15FeNa) and one with an outer diameter of 60-100 nm (CNT-L-O15FeNa), maintaining the iron content at 15% in these cases as well.

The catalysts employed in this study are summarized in the following table (Table 4. 1) additional information are instead reported in Table 2. 2.

Table 4. 1. Principal samples details involved in this study.

Name used	Outer diameter
CNT-S-C10FeNa	10-20
CNT-S-O10FeNa	10-20
CNT-S-O15FeNa	10-20
CNT-M-O15FeNa	40-60
CNT-L-O15FeNa	60-100

4.2. Results and discussions

4.2.1 Catalysts characterization

Table 4. 2 provides information on the metal composition of the Na-Fe/CNT catalysts employed in this study, determined through ICP-OES analyses. The results show that the Fe and Na contents were fairly similar and close to the

targeted metal content, specifically 10 and 15 wt. % of Fe, depending on the catalyst, along with a Na/Fe molar ratio of 0.025.

Table 4. 2 Textural properties of carbon nanotubes catalyst impregnated with Fe and Na measured by N_2 physisorption and chemical analysis of carbon nanotubes impregnated with Fe and Na catalyst.

Sample	BET area	Total pore volume[a]	Fe (wt. %)	Na (wt. %)	Na/Fe at. ratio
CNT-S-original	113	0.88	-	-	-
CNT-M-original	93	0.26	-	-	-
CNT-L-original	64	0.28	-	-	-
CNT-S-C-MAT[b]	139	0.87	-	-	-
CNT-S-O-SAT[c]	179	0.81	-	-	-
CNT-S-C10FeNa	156	0.66	12.15	0.14	0.027
CNT-S-O10FeNa	155	0.45	11.46	0.12	0.024
CNT-S-O15FeNa	150	0.44	17.59	0.19	0.026
CNT-M-O15FeNa	92	0.34	16.53	0.17	0.025
CNT-L-O15FeNa	86	0.25	17.55	0.16	0.022

[a] Single point adsorption total pore volume of pores less than 2405.945 Å diameter at P/Po=0.991981005.

[b] The nomenclature CNT-S-C-MAT indicates the sample obtained from the original CNT-S nanotube subjected to mild acid treatment (MAT). In other words, the starting nanotube (CNT-S-original) underwent treatment with HNO_3, 35 vol. %, for 20 h, at 140 °C.

[c] The nomenclature CNT-S-O-SAT indicates the sample obtained from the original CNT-S nanotube subjected to strong acid treatment (SAT). In other words, the starting nanotube (CNT-S-original) underwent treatment with HNO_3, 68 vol. %, for 20 h, at 140 °C.

All samples were subjected to N_2 adsorption; the adsorption profiles are reported in Appendix 1, Figure A1. 1, Figure A1. 2 and Figure A1. 3. Specifically, Figure A1. 1 shows the adsorption profiles of the original small-pore (CNT-S-original), medium-pore (CNT-M-original), and large-pore (CNT-L-original) CNTs. Figure A1. 2 also presents the adsorption profiles of the small-pore CNT treated with acid, under both weak and strong conditions. The graph in Figure A1. 3 shows the N_2 adsorption profiles for the samples containing iron inside the CNTs, specifically the CNT-S-O10FeNa, CNT-S-O15FeNa, CNT-M-O150FeNa, and CNT-L-O15FeNa samples, as well as the sample with iron on the nanotube surface (CNT-S-C10FeNa).

By comparing the results obtained for CNT-S-original, CNT-S-C-MAT, and CNT-S-O-SAT, as shown in (Table 4. 2), an increase was observed in the BET surface area following the acid treatment. This increase is more pronounced in the sample subjected to strong acid treatment (CNT-S-O-SAT), while it is less evident in the CNT-S-O-MAT sample treated with mild acid [112]. The BET surface area changes from 113 $m^2 \cdot g^{-1}$ to 179 and 139 $m^2 \cdot g^{-1}$, respectively.

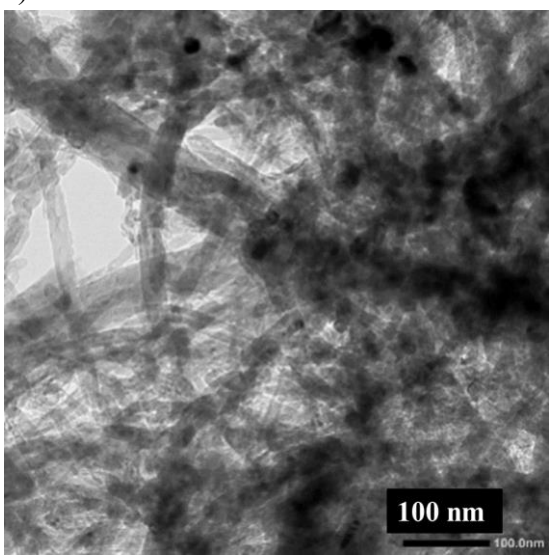
The CNT-S-C10FeNa sample, which is made up of CNT-S-C-MAT, has a surface area that goes from 139 $m^2 \cdot g^{-1}$ to 156 $m^2 \cdot g^{-1}$. This is probably because of the iron outside of the nanotubes [165]. In addition, considering the total pore volume, there are no evidence of pore blockage.

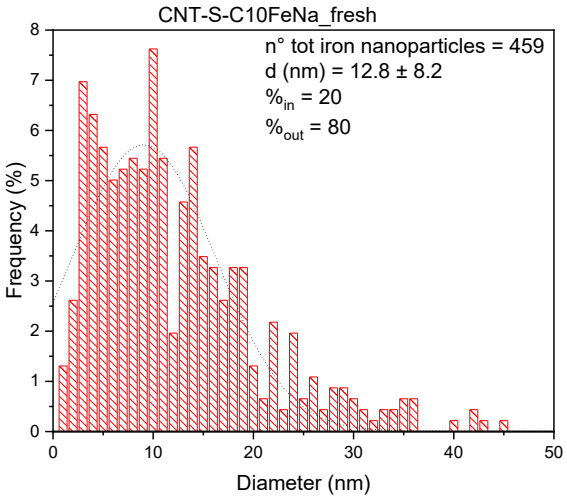
Conversely, CNT-S-O10FeNa and CNT-S-O15FeNa samples, in comparison with the iron-free CNT (CNT-S-O-SAT), exhibit a reduced total pore volume, decreasing from 0.88 $cm^3 \cdot g^{-1}$ to 0.45 and 0.44 $cm^3 \cdot g^{-1}$, suggesting pore blockage resulting from the deposition of iron inside the CNT and a lower BET surface area, respectively 155 and 150 $m^2 \cdot g^{-1}$ compare with the iron outside the CNT [165].

Moreover, when examining the CNT-M-original samples alongside CNT-M-O15FeNa and CNT-L-original alongside CNT-L-O15FeNa, there is a noticeable rise in surface area in both instances.

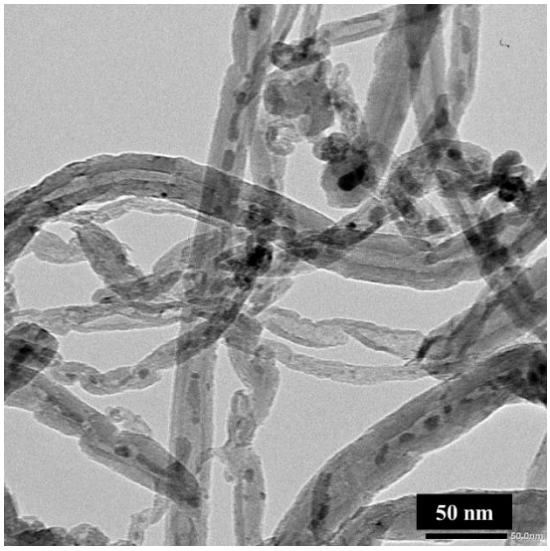
TEM analyses were conducted on three different types of catalyst samples: fresh samples (F), reduced and passivated catalysts (R/P), and post-reaction catalysts (S). The reduced and passivated catalysts underwent a reduction process in pure hydrogen for 10 hours at 400 °C, followed by passivation in a diluted air stream containing 1% oxygen (R/P). For all samples, an increase in the percentage of Fe particles out of the CNT, was observed with the progression of the heat treatments, accompanied by an increment in the average particle diameter. This growth was found to be more contained in samples with a higher percentage of Fe inside the nanotube (CNT-S-O10FeNa) and significantly more pronounced in samples where iron is predominantly or entirely outside the nanotube (CNT-S-C10FeNa, CNT-M-O15FeNa, and CNT-L-O15FeNa).

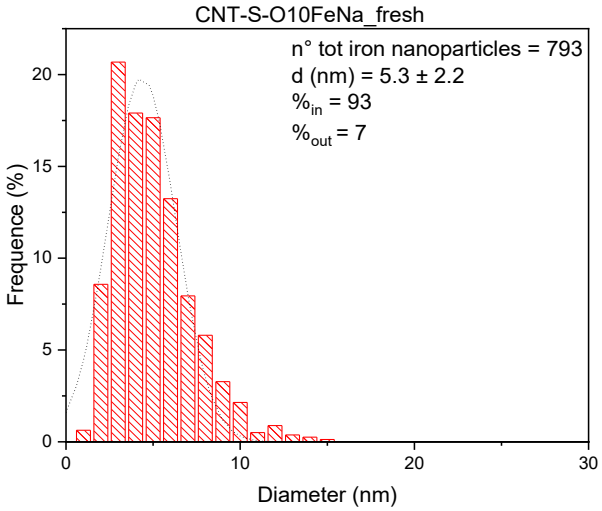
a)


100 nm
100.0nm

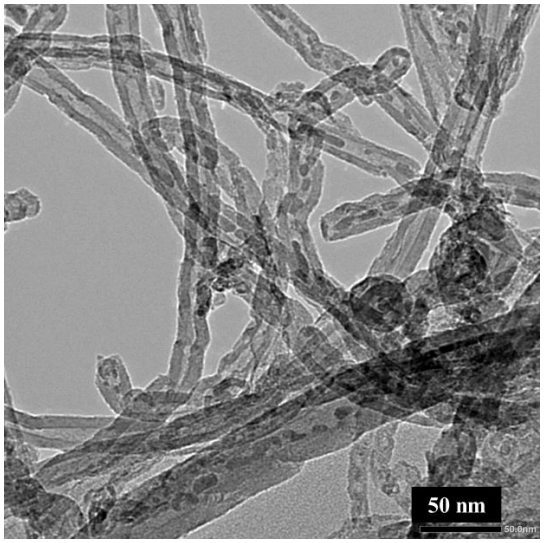

CNT-S-C10FeNa_fresh
n° tot iron nanoparticles = 459
d (nm) = 12.8 ± 8.2
%in = 20
%out = 80
Frequency (%)
Diameter (nm)
0
1
2
3
4
5
6
7
8
0
10
20
30
40
50

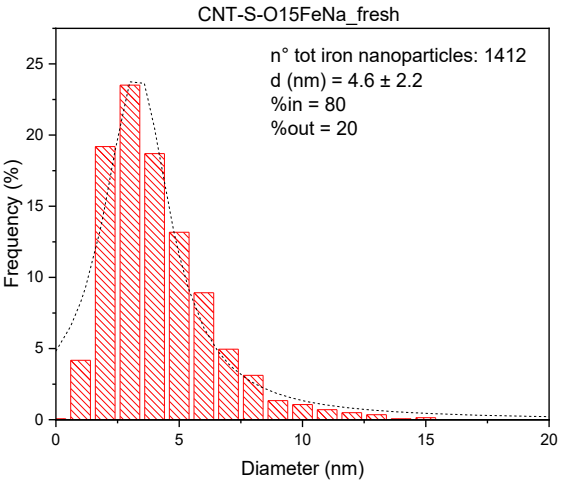
b)


50 nm

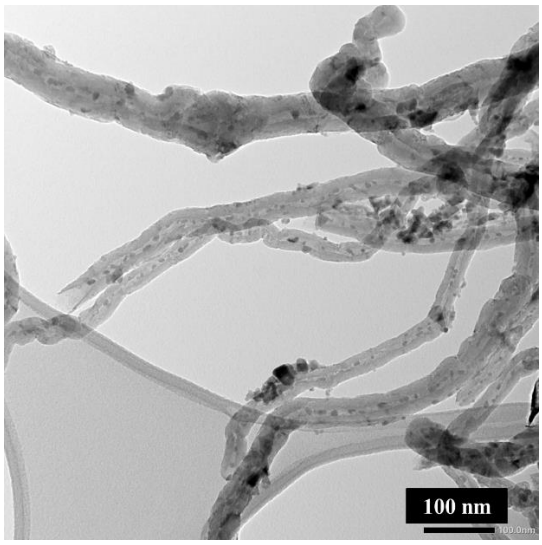

CNT-S-O10FeNa_fresh
n° tot iron nanoparticles = 793
d (nm) = 5.3 ± 2.2
%in = 93
%out = 7
Frequence (%)
Diameter (nm)
0
5
10
15
20
0
10
20
30

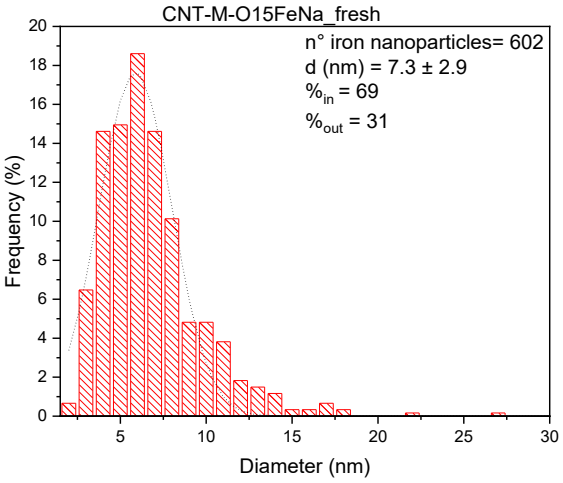
c)


50 nm


CNT-S-O15FeNa_fresh
n° tot iron nanoparticles: 1412
d (nm) = 4.6 ± 2.2
%in = 80
%out = 20
Frequency (%)
Diameter (nm)
0
5
10
15
20
25

d)


100 nm


CNT-M-O15FeNa_fresh
n° iron nanoparticles= 602
d (nm) = 7.3 ± 2.9
%in = 69
%out = 31
Frequency (%)
Diameter (nm)
0
2
4
6
8
10
12
14
16
18
20
5
10
15
20
25
30

e)

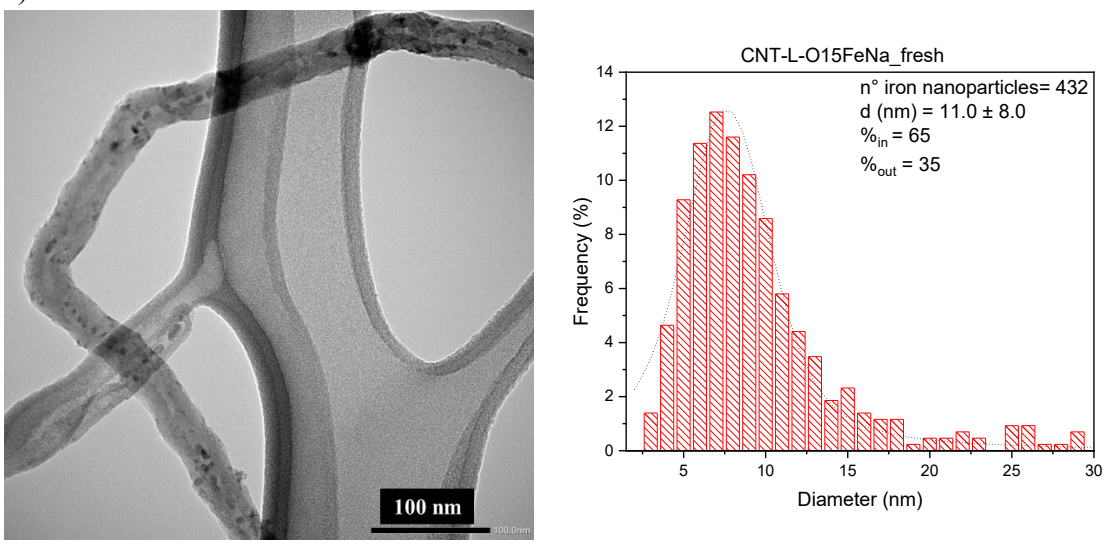


Figure 4. 1 TEM images and nanoparticles distributions for the fresh CNT samples: a) CNT-S-C10FeNa_fresh, b) CNT-S-O10FeNa_fresh, c) CNT-S-O15FeNa_fresh, d) CNT-M-O15FeNa_fresh and e) CNT-L-O15FeNa_fresh.

The Figure 4. 1 shows the TEM images of each fresh sample, along with the relative pore size distribution. The average distribution of iron nanoparticles has been calculated using the previously mentioned equation (2. 13), while the mean diameter was obtained by calculating the arithmetic mean of the sizes of the counted and measured nanoparticles. Remarkably, 93% of the iron in sample CNT-S-O10FeNa was contained, suggesting significant capillary filling. On the other hand, the CNT-S-C10FeNa sample exhibits extremely restricted confinement as desired, with only 80% of the iron located outside the pores. However, by increasing the iron content from 10 wt. % to 15 wt. %, while maintaining the same outer diameter of the CNTs (OD 10-20 nm), a lowering of the percentage of confined nanoparticles to 80% is observed in the CNT-S-O15FeNa sample. Furthermore, it can be seen that the confinement decreases further as the diameter of the CNTs increases. For example, in the CNT-M-O15FeNa sample, only 69% of the iron is confined, whereas in the CNT-L-O15FeNa sample, the percentage drops to 58%.

By analyzing the XRD patterns of the fresh catalysts shown in Figure 4. 2, we can observe diffraction lines at 26.3° and 43.8°, which are attributed to the (0 0 2) and (1 0 1) reflections of carbon nanotube (CNT) supports. The peaks at 2θ of 33.1°, 35.6°, 54.0° and 62.4° are assigned to the hematite phase (Fe_2O_3, JCPDS

24-0072), while the peaks at 2θ of 35.4°, 43.1°, and 62.5° can be attributed to the magnetite phase (Fe_3O_4, JCPDS 88-0315).

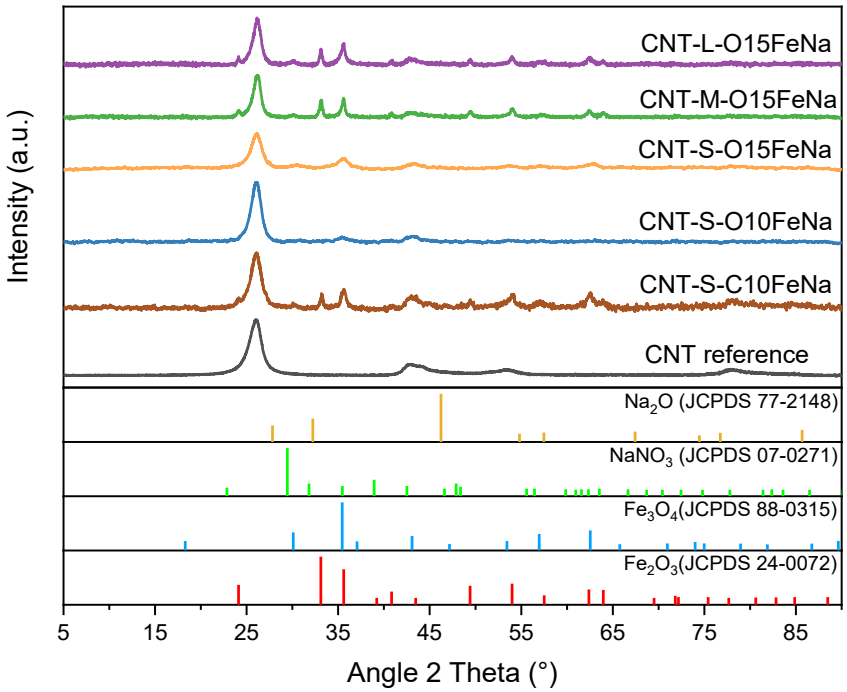


Figure 4. 2. XRD profiles of fresh carbon nanotubes.

It is evident that the width of the XRD peaks of iron oxide for the CNT-S-C10FeNa catalyst, containing 80% of iron nanoparticles outside the CNT tubes based on TEM analysis, is smaller than that of the counterpart CNT-S-O10FeNa with confined iron nanoparticles. This indicates larger sizes of iron oxide nanoparticles positioned outside the CNT with the same iron content. Additionally, CNT-S-O10FeNa presents only the characteristic broad and weak peaks of magnetite. This feature is likely due not only to the better dispersion of iron in the support [170], but also to the confinement inside the CNT, preventing the growth of iron oxide nanoparticles [112], resulting in high detectability on the XRD pattern (with a minimum limit for particles to diffract being 4 nm).

Comparing the CNT-S-O10FeNa samples with the CNT-S-O15FeNa sample, it is observed that, at the same nanotube diameter and with an increase in iron content, there are narrower peaks attributed to the Fe_3O_4 phase, indicating larger crystallite sizes. This result is further confirmed by TEM analysis, revealing that

only 80% of iron nanoparticles are confined inside the fresh catalyst, while the remaining 20% are positioned externally.

As the amount of iron in the support increases (from 10 to 15%), we can observe not only a decrease in the half-height of the magnetite peaks but also, as the outer diameter (OD) increases from 10-20 to 60-100, the reappearance of peaks related to the hematite phase. Two factors contribute to this observation: firstly, increasing the iron content in the CNT effectively increases the amount of iron on the surface (as confirmed by TEM analysis); secondly, as the external and internal diameter of the CNT increases, it seems to become more challenging to introduce iron into the support due to capillarity forces. To clarify, when comparing samples with the same iron content (15 wt. %) and different diameters, an increase in particle size is observed (Table 4. 3), attributed to both the larger diameter of the nanotubes and the lower number of confined iron particles in the CNT. For instance, in the CNT-M-O15FeNa sample, only 69% of iron nanoparticles are confined inside, as indicated by the distribution of nanoparticles obtained from TEM images.

The values of crystallite size, calculated for various catalysts by integrating the peak at 35.7° and applying the Scherrer equation, are reported in Table 4. 3. The results of nanoparticle sizes obtained through XRD and TEM analyses are consistent and in line with expectations. Any discrepancies, such as the slightly higher value measured by XRD, can be attributed to instrumental limits in detecting iron nanoparticles below 4 nm using XRD.

Table 4. 3. Fe_3O_4 particle sizes of catalysts supported on carbon nanotubes (CNTs).

	Particle sizes Fe_3O_4 (nm)	
	XRD	**TEM**
CNT-S-C10FeNa	14	12.8±8.2
CNT-S-O10FeNa	5	5.3±2.2
CNT-S-O15FeNa	6	4.6±2.2
CNT-M-O15FeNa	15	7.3±2.9
CNT-L-O15FeNa	19	11.0±8.0

The cristallite size from XRD pattern, reported in Table 4. 3 was calculated following the Scherrer equation reported in Chapter 2.

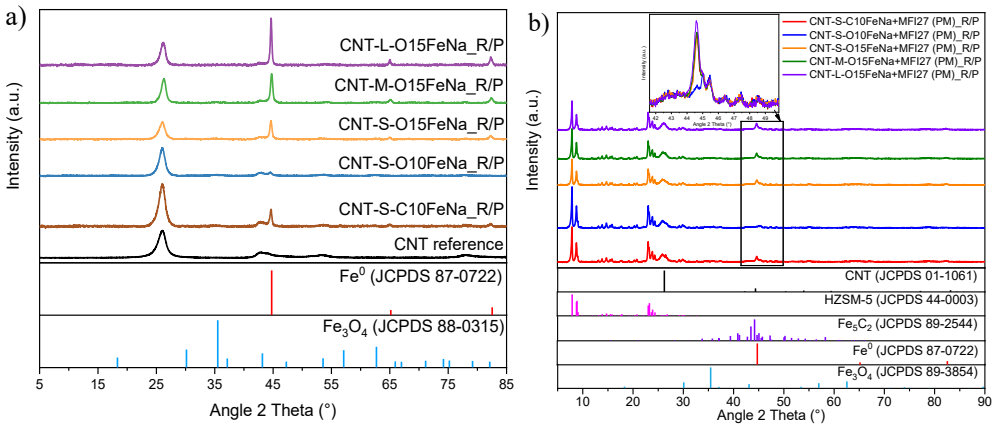


Figure 4. 3. XRD profile of CNT samples alone a) and in powder mixing with the commercial zeolite MFI27 b), both after reduction in H_2 at 400 °C for 10 h.

In Figure 4. 3, the XRD patterns of the samples subjected to in situ reduction with pure H_2 at 400 °C for 10 h are shown. In this case, the theories presented for the fresh catalysts would also seem to be valid. Specifically, in the CNT-S-O10FeNa sample, the peaks of magnetite are practically nonexistent, while the peak of metallic iron appears at 30 °C. However, this peak is much less intense than in the other catalysts. Once again, it is hypothesized that not only is iron more evenly dispersed within the carbon support, but also that particles below 4 nm do not diffract. The minimal particle growth confirmed by TEM analysis demonstrates how confinement hinders nanoparticle growth. As for all the other samples, all three peaks related to metallic iron are present. Furthermore, the theory that an increase in the outer diameter leads to a greater number of nanoparticles outside the nanotubes seems to be confirmed, as the intensity of the peaks related to metallic iron increases. Finally, comparing the patterns of the CNT-S-C10FeNa and CNT-S-O15FeNa samples, the intensity of the metallic iron phase peaks is practically the same. It is also apparent in this case that, although in the second sample the iron was confined within the CNTs, the higher metal content implies a greater number of nanoparticles outside the CNTs compared to the CNT-S-O10FeNa sample.

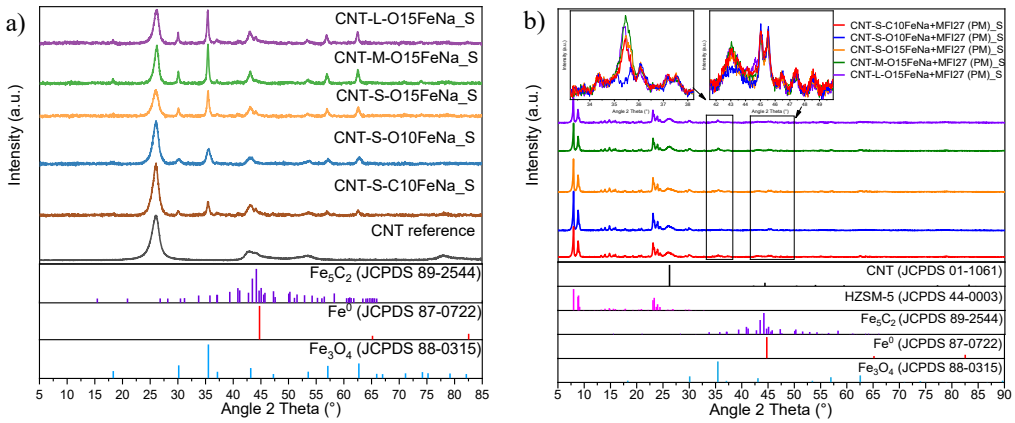


Figure 4. 4. XRD pattern spent catalysts a) without zeolite and b) with zeolite.

Analyzing the diffractograms of spent catalysts obtained through X-ray diffraction (XRD) and depicted in Figure 4. 4 a) and b), a peak at 44.8° is observed, attributed to metallic iron (JCPDS 87-0722). This peak is present in all samples, except for CNT-S-O10FeNa and CNT-S-O10FeNa+MFI27 (PM). The absence of this peak in these samples may be linked, as previously noted for fresh catalysts, to a better dispersion of iron and its effective confinement within the nanotubes. Regarding the assessment of the presence of carbides in the 40°-46° range for all samples, a challenge arises due to a broadened peak in this region, attributed to the reference CNT.

Figure A1. 4, Figure A1. 5 and Figure A1. 6 display the X-ray diffractograms in situ recorded at increasing temperatures in the range of 250 °C to 600 °C during the H_2 reduction treatment for respectively the CNT-S-C10FeNa, CNT-S-O10FeNa, and CNT-M-O15FeNa samples without (a) and with the MFI27 zeolite (b). Additionally, the figure illustrates the temperature-related evolution of the normalized area for the main diffraction peaks of each crystalline species. In the analysis of the phase evolution for the CNT-S-C10FeNa and CNT-M-O15FeNa samples, there is initially the reduction of Fe_2O_3 to Fe_3O_4, followed by the reduction of Fe_3O_4 with the subsequent formation of FeO and Fe. Noteworthy is the observation that the CNT-S-O10FeNa sample appears to reduce more rapidly compared to the other two samples. Specifically, with the same test duration and at the temperature of 600 °C, it is evident that 85% of the iron has been reduced, compared to 80% for the CNT-M-O15FeNa sample and 60% for the CNT-S-C10FeNa sample. This latter result aligns with data obtained through H_2-TPR analysis (Figure 4. 5) and existing literature, suggesting a greater ease of iron reduction within the nanotube compared to iron on the carbonaceous support

surface. Regarding the in situ XRD performed on the 1:1 mixture of CNT and MFI27 zeolite sample powders, Figure A1. 4, Figure A1. 5 and Figure A1. 6 (b), the pronounced intensity of the zeolite peaks, compared to the iron peaks outside (CNT-S-C10FeNa) and inside (CNT-S-O10FeNa and CNT-M15FeNa), did not provide conclusive information compared to that obtained through H2-TPR.

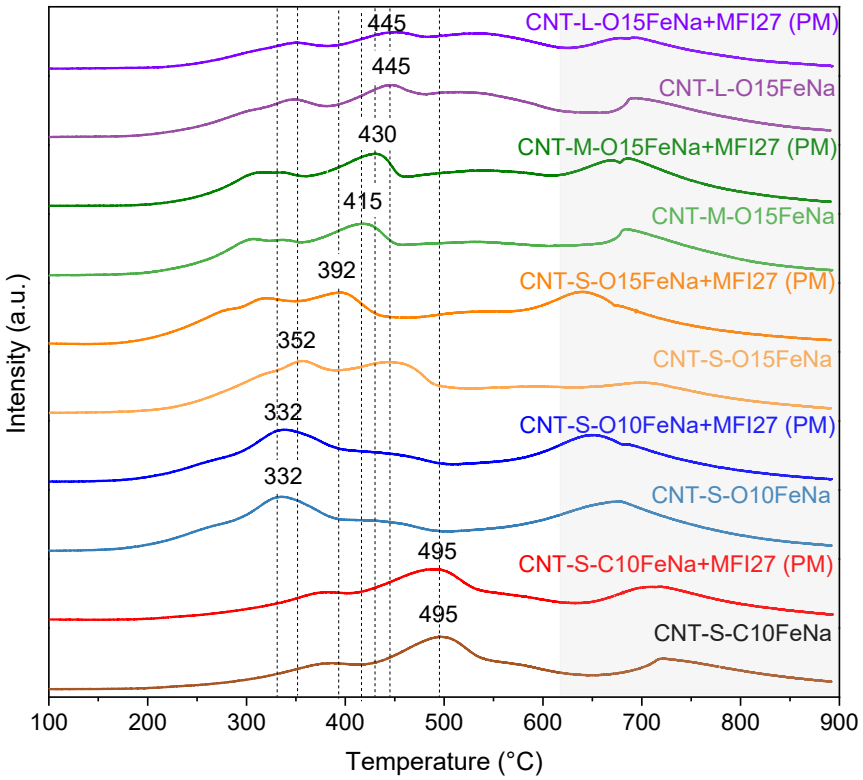


Figure 4. 5. H_2-TPR profiles.

The H_2-TPR profiles for the Fe/CNT samples with and without zeolite are shown in (Figure 4. 5). Of interest are the reduction temperatures of the iron oxides, which undergo the following phase transitions as reported in the literature: $Fe_2O_3 \rightarrow Fe_3O_4 \rightarrow FeO \rightarrow Fe$ [171]. Specifically, the sample CNT-S-O10FeNa containing 10% of iron inside the CNT exhibits the first reduction peak at lower temperature than the sample CNT-S-C10FeNa with 10% of iron outside (334 °C versus 382 °C). On the other hand, the sample CNT-S-O15FeNa exhibits the first reduction peak at intermediate temperature rather than the other samples due to

the higher iron content (15%) causing approximately 20% of iron to be outside (based on TEM analysis), unlike the CNT4O10FeNa sample where almost all particles are inside the CNT (around 93%). Focusing on the samples with an outer diameter of nanotubes measuring 40-60nm and 60-100nm, and containing 15% iron, specifically CNT-M-O15FeNa and CNT-L-O15FeNa, it is observed that the reduction peak associated with the transformation of Fe3O4 to FeO occurs at a temperature of approximately 430 °C. This observation is consistent with the results obtained through TEM analysis, suggesting that, akin to the findings for CNT-S-C10FeNa and CNT-S-O15FeNa, a portion of the iron is localized on the surface of the nanotubes. Lastly, the peak at a temperature above 650 °C is attributed to the gasification of the CNT [150] [172] [173]. On the other hand, looking to the volume of H_2 consumed during the analysis, it results that the catalyst with the higher consume of volume is the sample CNT-S-O10FeNa, while the sample with the lower consume is the CNT-S-O15FeNa+MFI27 (PM) probably due to the presence of the zeolite. This could explain the lower activity of this sample Table 4. 4. In any case, all the sample show a low consume of H_2, consequently a low reduction of the iron, in the presence of the zeolite.

Table 4. 4. Results H_2-TPR.

	T_{max} (°C)	**Volume (ml/g_{CNT} STP)**	**H_2 consumed (mmol/g_{CNT})**	**H_2 consumed (mmol/$g_{Fe\ ICP}$)**
CNT-S-C10FeNa	495	78.6	3.5	2.2
CNT-S-C10FeNa+MFI27 (PM)	495	43.6	1.9	1.2
CNT-S-O10FeNa	334	70.1	3.1	2.2
CNT-S-O10FeNa+MFI27 (PM)	337	44.4	2.0	1.4
CNT-S-O15FeNa	356	47.0	2.1	1.0
CNT-S-O15FeNa+MFI27 (PM)	396	19.2	0.9	0.4
CNT-M-O15FeNa	415	75.6	3.4	1.6
CNT-M-O15FeNa+MFI27 (PM)	430	39.4	1.8	0.9
CNT-L-O15FeNa	445	96.8	4.3	2.0
CNT-L-O15FeNa+MFI27 (PM)	445	45.6	2.0	0.9

4.2.2 Catalytic tests

Following individual testing of the Na-Fe/CNT, they underwent experiments in two different contact configurations with a commercial zeolite supplied by Zeolyst, designated CBV5524G, and referred to in this study as MFI27. The two contact configurations employed for testing the Fe/CNT with the zeolite were granule mixing (GM) and powder mixing (PM). The second chapter of this work presents comprehensive details on the procedures utilized in the catalytic experiments, encompassing specific reactor loading methods.

The catalytic results obtained with the series of Fe/CNT catalysts are reported in Table 4. 5, where are reported respectively the medium value of the last 6 h collected of the overall product selectivity and hydrogen distribution for CO_2 conversion. In all cases, the space velocity (CO_2+H_2)L·g_{CNT}^{-1}·h^{-1}) was set at 3.1, with H_2/Ar/CO_2 in a volume ratio of 68/10/22%, a flow rate of 40 ml/min, pressure (P) at 20 bar, temperature (T) at 340 °C, and time on stream (TOS) at 27 h.

Table 4. 5. Hydrocarbons distribution for CO_2 hydrogenation at 340 °C, 20 bar, GHSV = 3.1 $L_{CO2+H2}/(g_{cat}·h)$, H_2/CO_2 = 3.1 mol/mol. Data averaged for TOS = 21 – 27 h.

	Hydrocarbons distribution (%C)						Arom/C_{5+}	C_2-C_4
	C_1	$C_2^=$-$C_4^=$	C_2^0-C_4^0	C_{5+} aliph	C_{5+} arom	Total C_{5+}	(%C)	O/P ratio
CNT-S-C10FeNa	16	38	9	37	0	37	0	4.1
CNT-S-C10FeNa+MFI27 (GM)	22	1	39	23	15	38	40	0.02
CNT-S-C10FeNa+MFI27 (PM)	47	1	41	9	2	11	17	0.01
CNT-S-O10FeNa	20	25	15	40	0	40	0.0	1.6
CNT-S-O10FeNa+MFI27 (GM)	27	1	40	21	11	32	35	0.02
CNT-S-O10FeNa+MFI27 (PM)	26	1	39	22	12	34	35	0.02
CNT-S-O15FeNa	14	33	9	44	0	44	0	3.6
CNT-S-O15FeNa+MFI27 (GM)	21	1	32	23	23	46	49	0.02
CNT-S-O15FeNa+MFI27 (PM)	27	1	42	21	9	30	31	0.02
CNT-M-O15FeNa	12	33	8	47	0	47	0	4.0
CNT-M-15FeNa+MFI27 (GM)	19	2	38	23	18	41	43	0.04
CNT-M-O15FeNa+MFI27 (PM)	30	1	42	19	8	27	29	0.03
CNT-L-O15FeNa	12	36	7	45	0	45	0	5.4
CNT-L-O15FeNa+MFI27 (GM)	18	1	37	22	22	44	49	3.3
CNT-L-O15FeNa+MFI27 (PM)	47	1	39	10	3	13	21	1.2

By comparing the CNT-S-C10FeNa and CNT-S-O10FeNa samples, it can be seen that the latter sample has a higher selectivity to CH_4 and a lower selectivity to light olefins. This seems to be consistent with a better dispersion of iron and sodium particles in the nanotubes [111]. However, comparing the results obtained from all the tests conducted on the catalysts without zeolite, does not seem to be a substantial difference between the "open" and "close" samples Figure 4. 6 a) and d). This trend is confirmed by Bao's article, where it was demonstrated that only by increasing the pressure above 30 bar is it possible to appreciate a significant difference in terms of conversion and iron time yield [111].

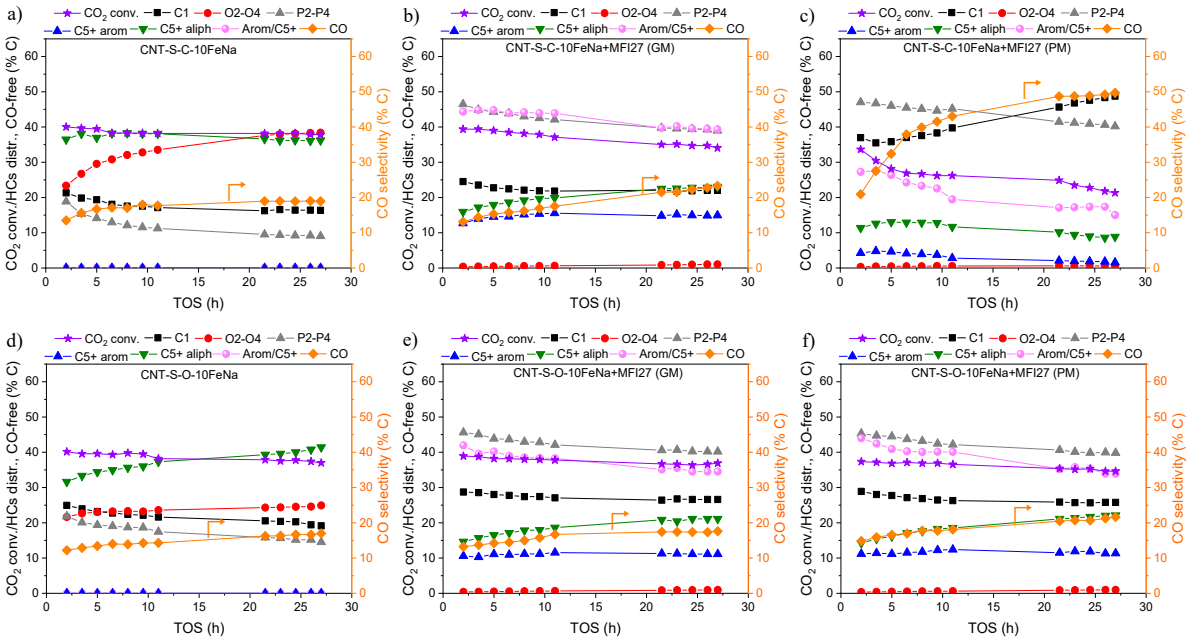


Figure 4. 6. TOS monitoring of CO_2 hydrogenation at 340 °C, 20 bar, GHSV = 3.1 $L_{CO2+H2}/(g_{CNT}\cdot h)$, H_2/CO_2 = 3.1 mol/mol for: a) CNT-S-C10FeNa, b) CNT-S-C10FeNa+MFI27 (GM), c) CNT-S-C10FeNa+MFI27 (PM), d) CNT-S-O10FeNa, e) CNT-S-O10FeNa+MFI27 (GM) f) CNT-S-O10FeNa+MFI27 (PM). To specify: (a, b, c) Na promoted Fe outside CNT and (d, e, f) Na promoted Fe inside CNT.

Furthermore, as it is known from the literature, the presence of sodium as a promoter in iron-based catalysts in the FT reaction has been studied to increase the selectivity towards C_{5+}. However, the selectivity towards C_{5+} increases over time during the reaction because the accumulation of carbon on the catalyst leads to the formation of iron carbides [110]. These carbides are active in the synthesis of long-chain hydrocarbons and less active in the synthesis of short-chain hydrocarbons. Additionally, sodium promotes CO adsorption and catalyst

activation, increasing the reaction rate. This leads to a higher production of long-chain hydrocarbons over time.

Instead, by comparing the TOS always shown in Figure 4. 6 b), c), e) and f), related to "close" and "open" CNT catalysts with zeolite in the two different contact modes, it is possible to appreciate the differences, especially in terms of CO_2 conversion, CO selectivity and CH_4 selectivity. To better understand the effect of possible migration, it is good to refer to the following Figure 4. 7.

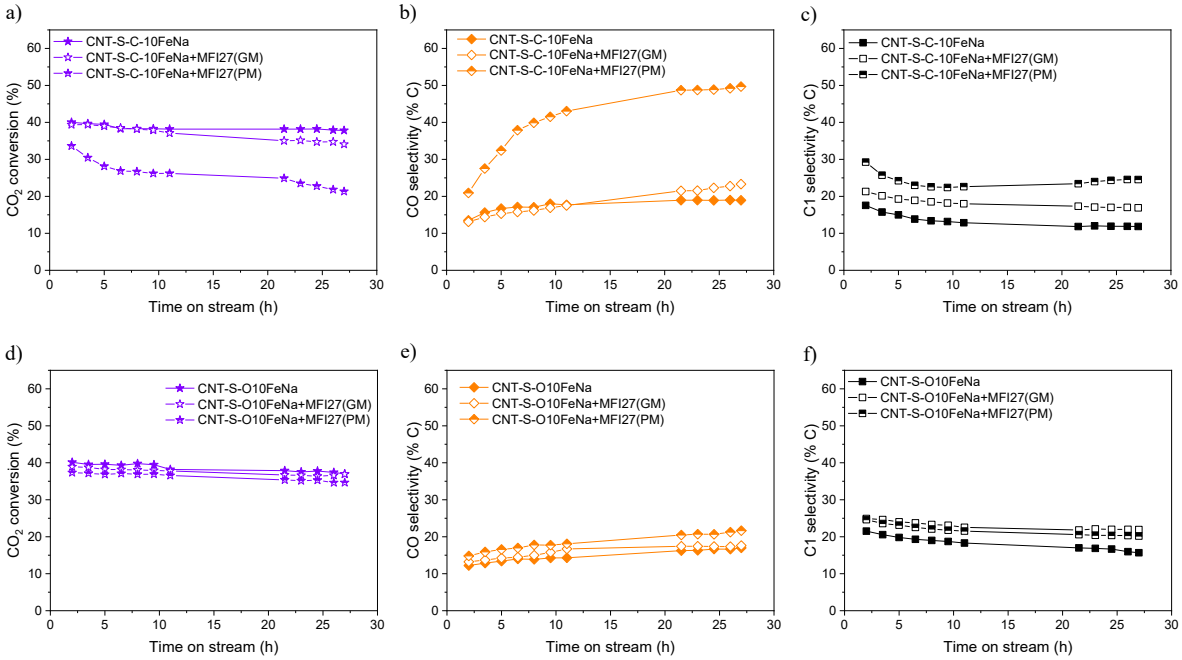


Figure 4. 7. Comparison of CO_2 conversion, CO selectivity and metal selectivity for the CNT-S-C-10FeNa sample with "close caps" (first line) and the CNT-S-O-10FeNa sample with "open caps" (second line). In particular each graph is compared the single Na-Fe/CNT (full symbol), the granule mixture Na-Fe/CNT+zeolite (empty symbol) and the powder mixture Na-Fe/CNT+zeolite (half-full symbol).

By analyzing the graphs shown in Figure 4. 7 (a, b, and c) concerning the CNT-S-C-10FeNa sample (iron predominantly placed on the outer surface of the canal) tested alone and with MFI27 zeolite in both GM and PM contact modes, a significant reduction in the conversion time of CO_2, a significant increase in the selectivity to CO, and a higher selectivity to CH_4 if these results are compared to CNT-S-C10FeNa tested without the zeolite are observed. These changes become more evident as the contact between the Na-Fe/CNT sites and the acid sites of zeolite increases, with more marked deviations in the sample tested in PM than

that tested with GM. However, considering Figure 4. 7 (d, e and f), it is observed that the changes previously discussed become negligible for the CNT-S-O10FeNa sample, in which the iron has been deliberately confined within the channels. This suggests that iron confinement in CNTs acts as an effective barrier, limiting the migration of sodium from active iron sites to the acid sites of zeolite.

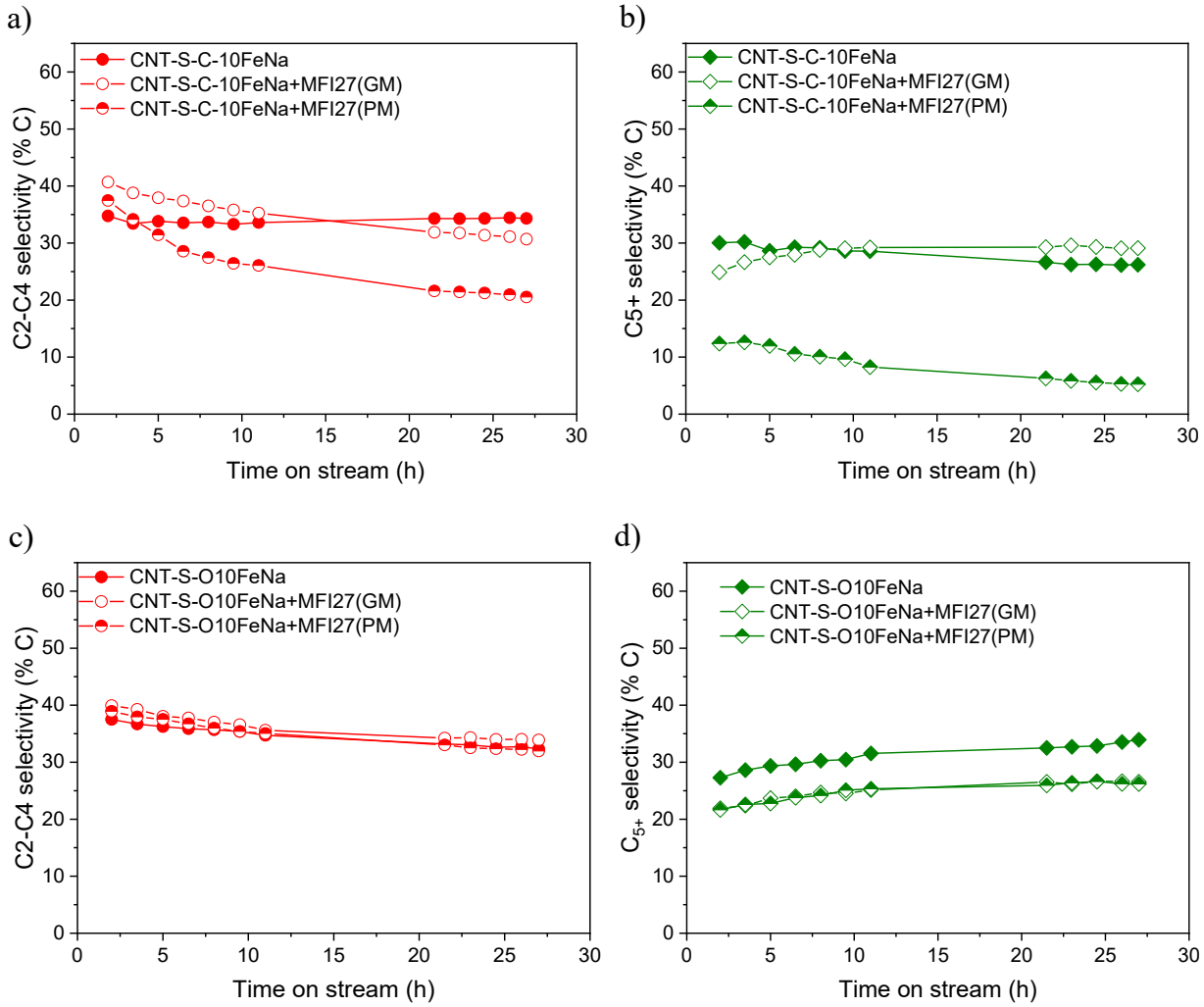


Figure 4. 8. Comparison of total C_2-C_4 (paraffins+ olefins) and total C_{5+} selectivity for the CNT-S-C-10FeNa sample with "close caps" (first line) and the CNT-S-O-10FeNa sample with "open caps" (second line). In particular each graph is compared the single Na-Fe/CNT (full symbol), the granule mixture Na-Fe/CNT+zeolite (empty symbol) and the powder mixture Na-Fe/CNT+zeolite (half-full symbol).

Looking at the Figure 4. 8, the comparison of total C_2-C_4 and total C_{5+} selectivity for the CNT-S-C-10FeNa and CNT -S-O10FeNa samples, reflects the same comments made for Figure 4. 7. In other words, it is observed that for the sample with unconfined iron there are sharp deviations in the test performed in PM mode, while these deviations become negligible when considering the CNT-S-O10FeNa catalyst.

Based on the results and benefits observed with the iron confinement, it was decided to increase the iron concentration from 10 wt. % to 15 wt. %, first of all maintaining the same CNT with OD 10-20 nm and later increasing the diameter of the CNT to 40-60 nm and 60-100 nm. The results achieved over time are represented in the graphs shown in Figure 4. 9.

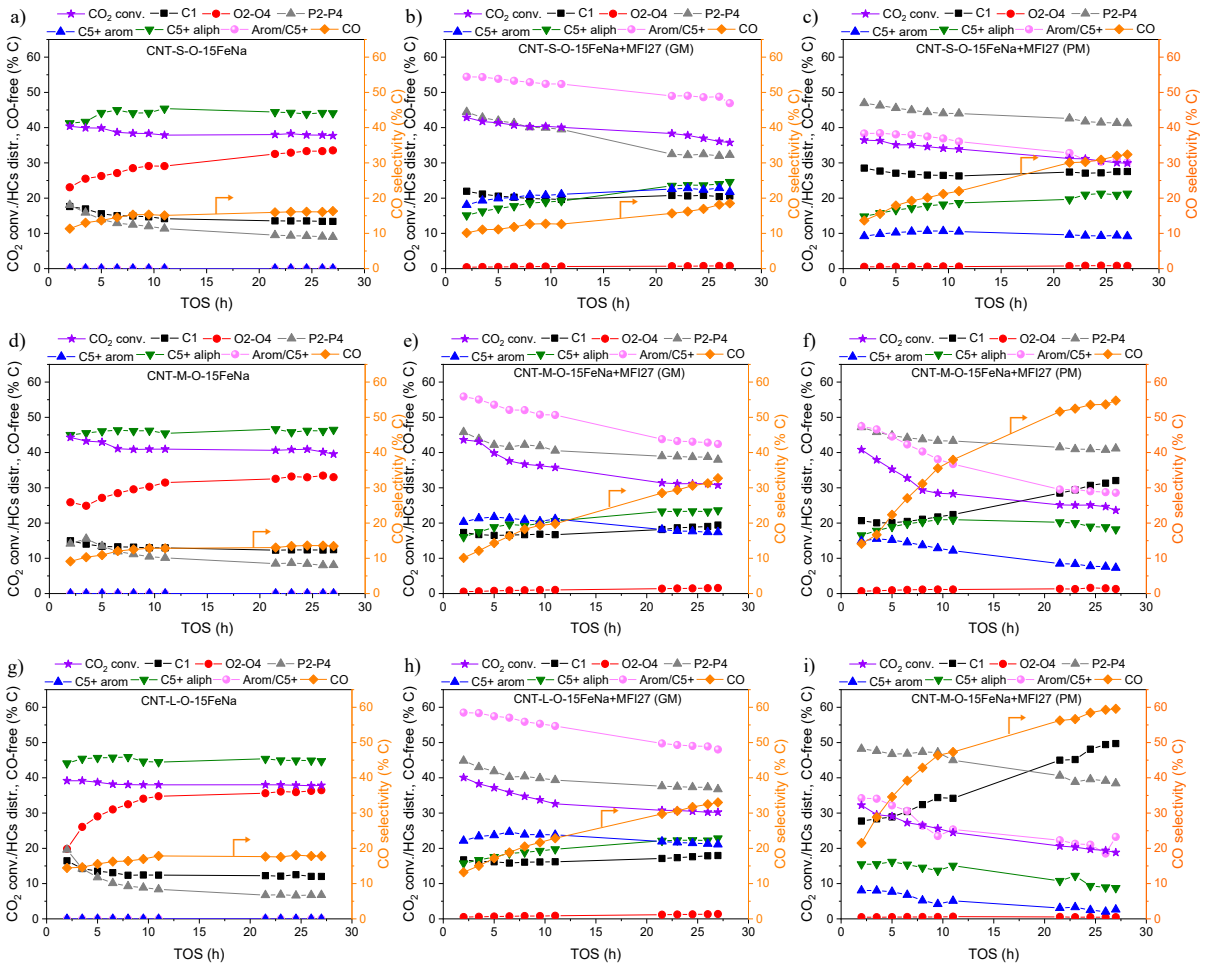


Figure 4. 9. TOS monitoring of CO_2 hydrogenation at 340 °C, 20 bar, GHSV = 3.1 $L_{CO2+H2}/(g_{CNT}\cdot h)$, H_2/CO_2 = 3.1 mol/mol for: a) CNT-S-O15FeNa, b) CNT-S-O15FeNa+MFI27 (GM), c) CNT-S-O15FeNa+MFI27 (PM), d) CNT-M-O15FeNa, e)

CNT-M-O15FeNa+MFI27 (GM), f) CNT-M-O15FeNa+MFI27 (PM), g) CNT-L-O15FeNa, h) CNT-L-O15FeNa+MFI27 (GM) and i) CNT-L-O15FeNa+MFI27 (PM).

Looking Figure 4. 9, the conversion appears to reach a maximum for the CNT-M-O15FeNa sample, where the CNT has an external diameter of 40-60 nm, and then decreases in the CNT-L-O15FeNa sample, with an external diameter of 60-100 nm. However, if catalysts with the same iron content, but different diameters are compared, the variation may be correlated with the average size of the iron nanoparticles and, consequently, with the Turnover Frequency (TOF), which is likely optimal for the CNT-M-O15FeNa sample. In this sample, the average size of the iron nanoparticles was found to be 5.9-4.3 nm, according to TEM analysis, and 15 nm, according to the crystallite size obtained from XRD analysis. Another reason why this sample might exhibit higher conversion compared to the other samples with the same percentage of iron could be related to the amount of iron on the surface of the nanotube. This characteristic may bypass potential diffusion issues related to the confinement of iron inside the CNT. Similarly, the CNT-M-O15FeNa sample shows the lowest selectivity to CO, presumably for the same reasons mentioned above. Furthermore, the CNT-M-O15FeNa sample, initially showing the highest conversion, also experiences a more rapid deactivation, a phenomenon likely attributed to the sintering of particles not confined within the CNT. This is corroborated by TEM analysis, indicating that, by the end of the reaction, these unconstrained particles constitute 54% of the total, Figure 4. 1, (d).

Moreover, it is interesting to carefully monitor over time the trends of CO_2 conversion, CO selectivity, and CH_4 selectivity for the CNT-S-O15FeNa, CNT-M-O15FeNa, and CNT-L-O15FeNa samples, in relation to the migration of sodium from iron to the acidic sites of the zeolite Figure 4. 10. As already highlighted by TEM analysis, the increase in iron content (from 10 to 15 wt. %), using the same CNT (OD 10-20 nm) leads to a 13% decrease in the quantity of confined iron nanoparticles, with significant repercussions on catalysis, especially for the sample tested in PM with zeolite, CNT-S-O15FeNa+MFI27 (PM).

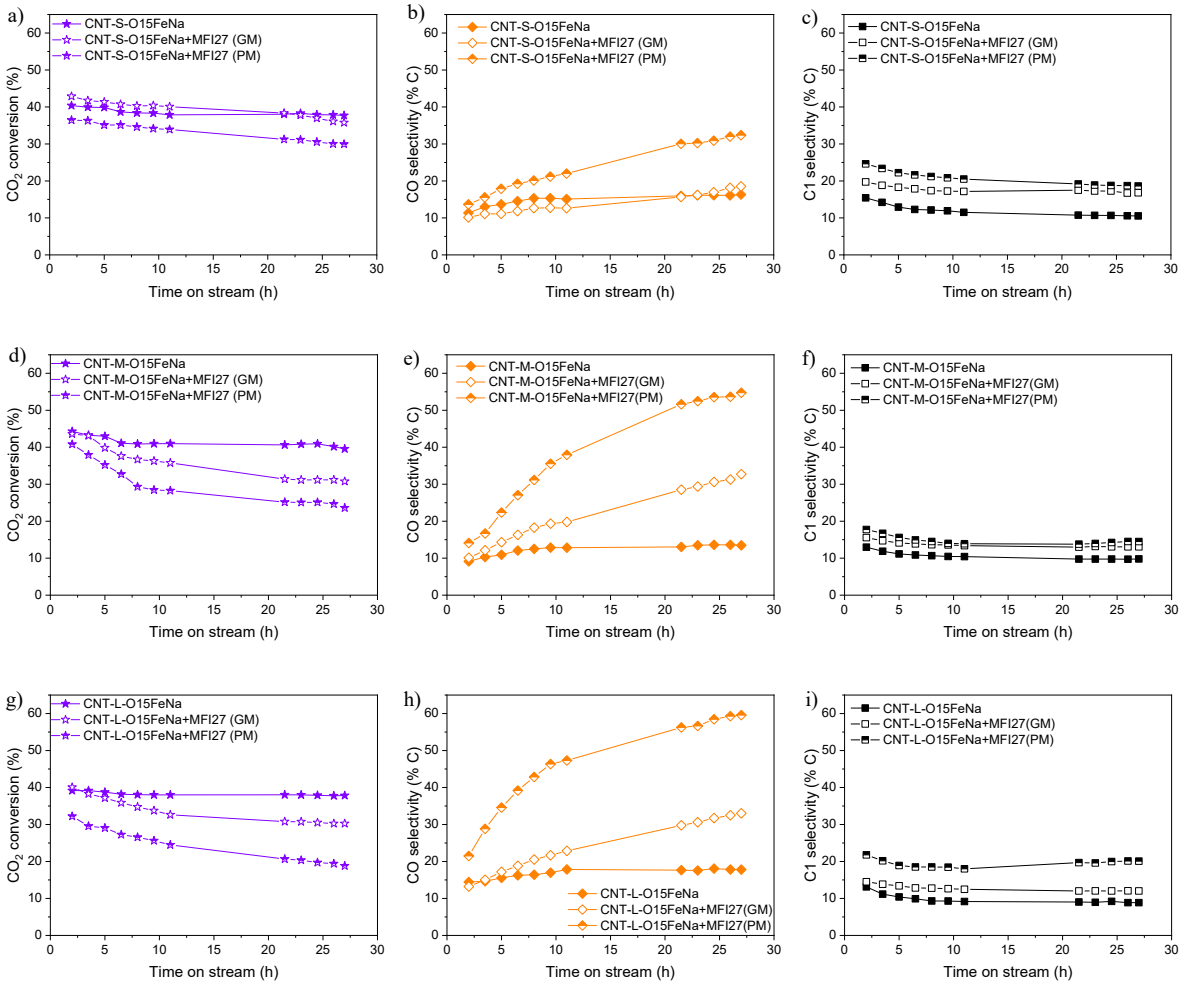


Figure 4. 10. Comparison CO_2 conversion, CO selectivity and CH_4 selectivity for the samples: CNT-S-O15FeNa (a-c); CNT-M-O15FeNa (d-f); CNT-L-O15FeNa (g-i), tested without and with zeolite in the two different mode: GM and PM.

It is also important to highlight the discrepancies compared to the trends observed for the parent CNT tested alone, compared to when zeolite is involved in the tests. These differences, undoubtedly a result of sodium migration, become progressively more apparent as CNT diameters increase because of a decrease in the number of confined nanoparticles, Figure 4. 10 (d-i). This indicates once more how well total confinement maintains the promotion of iron by the sodium and protects the zeolite's acidic sites.

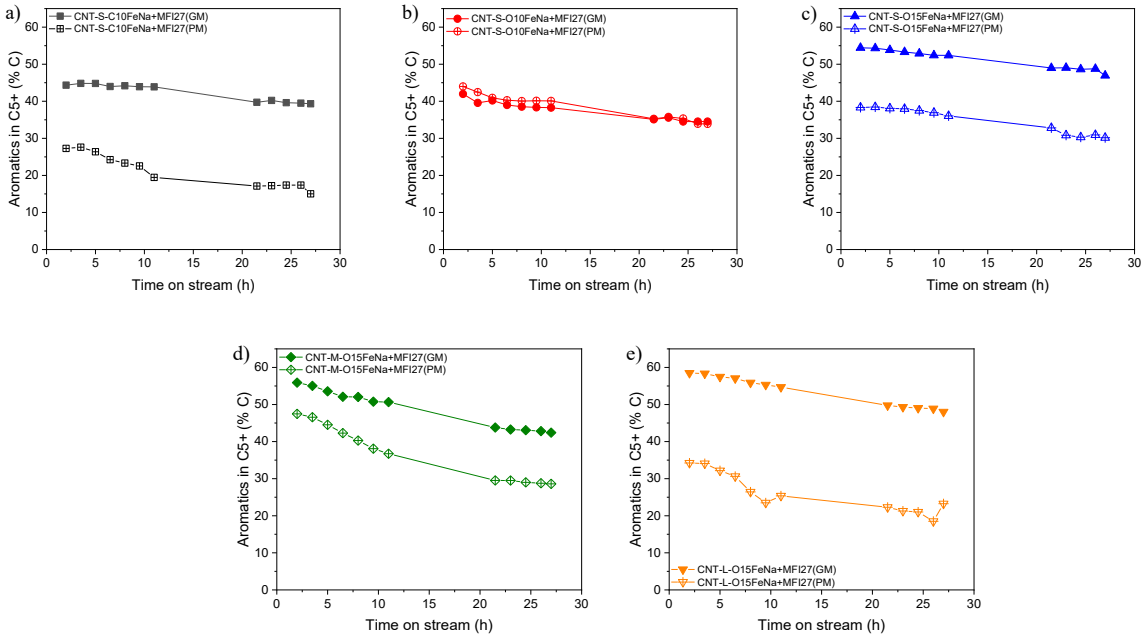


Figure 4. 11. TOS monitoring of aromatics product calculated inside C_{5+} products.

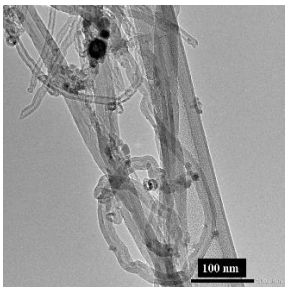
Until now, migration has been attributed exclusively to the loss of iron promotion by sodium due to its migration. However, the possibility of ion exchange of the acid sites of the zeolite with sodium should also be considered. Looking at the aromatics produced during the 27-hour test and calculated within the C_{5+} compounds produced, Figure 4. 11, it can be seen that the progression over time is virtually constant for tests involving the CNT-S-O10FeNa sample, whether tested in GM or PM with zeolite. In contrast, for all other tests, there is not only a marked decrease in aromatic products over time, but above all a more pronounced progression for tests performed in powder mixing mode. This decrease may be justified by the loss of acid sites, exchanged with sodium, capable of oligomerising, isomerising and above all aromatising the intermediate reaction products (olefins). Another interesting aspect is that for samples involving CNT-M-O15FeNa and CNT-L-O15FeNa, non-negligible deviations are already evident in tests performed in GM mode.

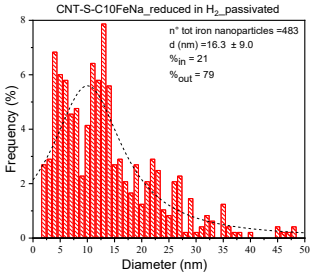
4.2.3 Reduced/Passivated and Spent Catalysts characterization

Group 1: catalysts reduced in H_2 and passivated

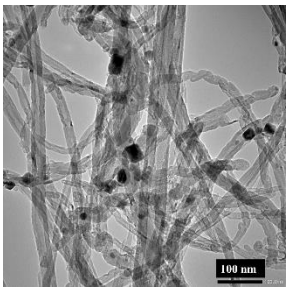
Group 2: spent catalysts

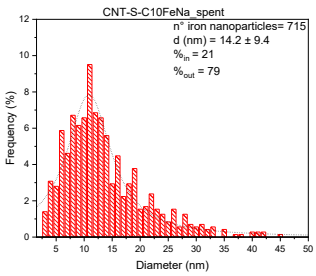
a)



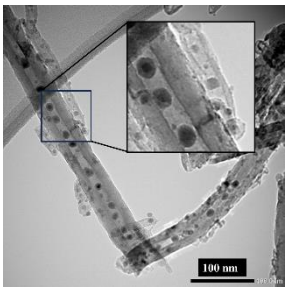


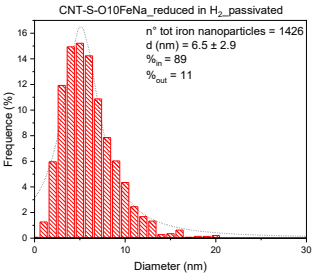
b)



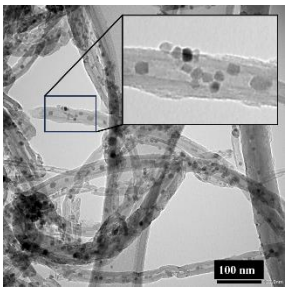


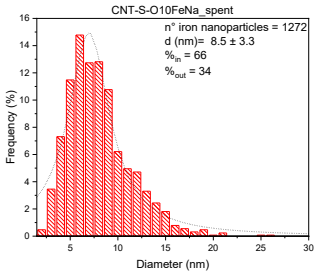
c)



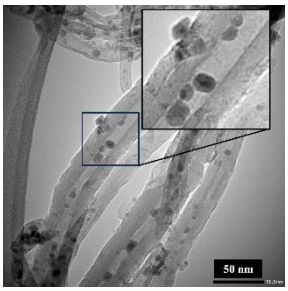


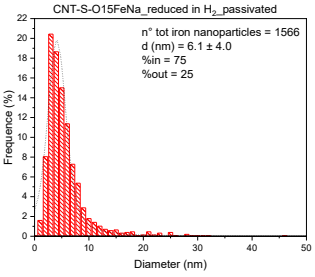
d)



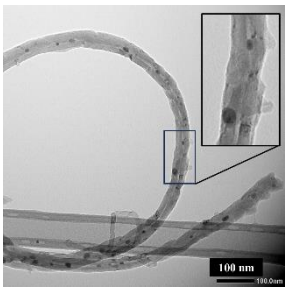


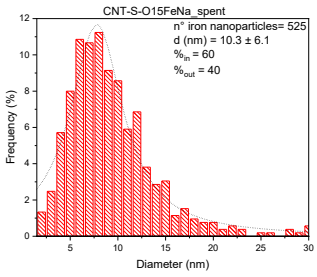
e)



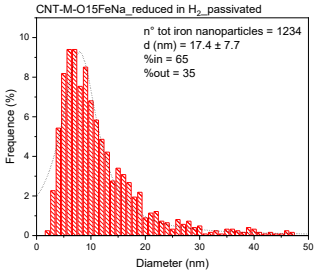


f)

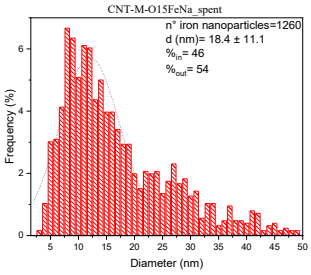




g)



h)



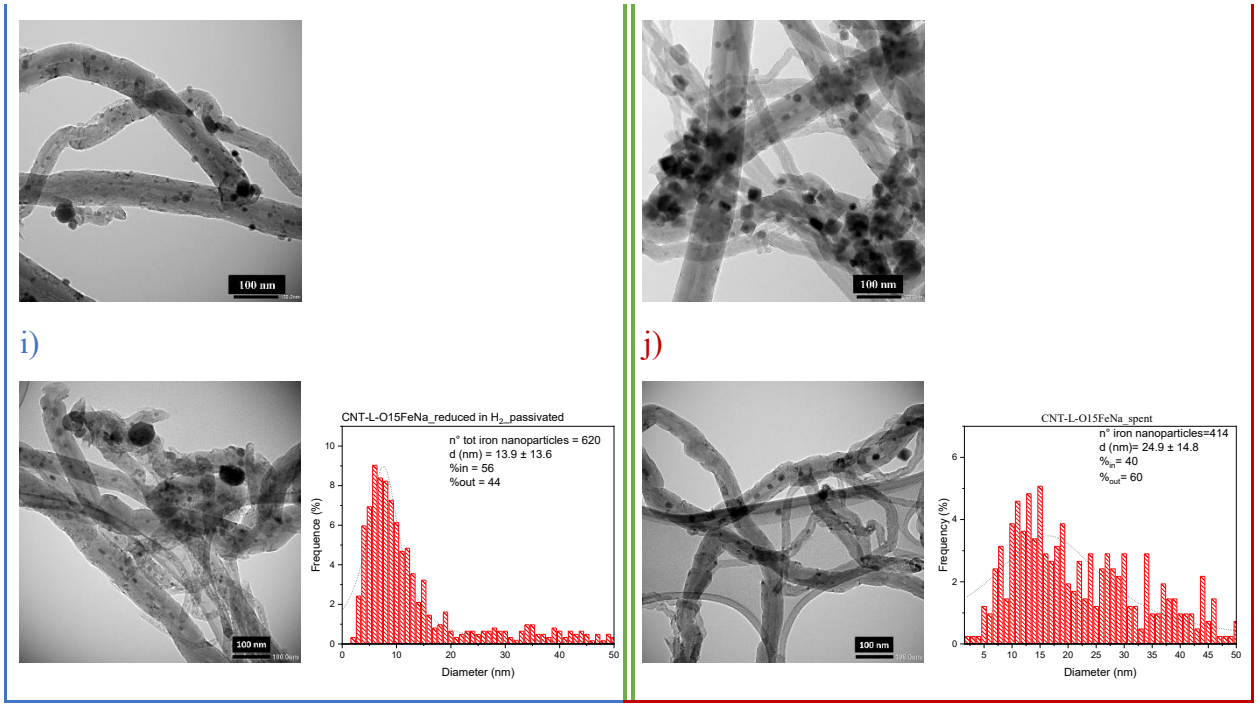


Figure 4. 12. TEM images of *Reduced/Passivated (R/P) catalysts (Group 1, blue color)*: a) CNT-S-C10FeNa_R/P, c) CNT-S-O10FeNa_R/P, e) CNT-S-O15FeNa_R/P, g) CNT-M-O15FeNa_R/P and i) CNT-L-O15FeNa_R/P; *Spent (S) catalysts (Group 2, red color)*: b) CNT-S-C10FeNa_S, d) CNT-S-O10FeNa_S, f) CNT-S-O15FeNa_S, h) CNT-M-O15FeNa_ S and j) CNT-L-O15FeNa_S.

For all samples, an increase in the percentage of Fe particles out of the CNT, was observed with the progression of the heat treatments, accompanied by an increment in the average particle diameter. This growth was found to be more contained in samples with a higher percentage of Fe inside the nanotube (CNT-S-O10FeNa) and significantly more pronounced in samples where iron is predominantly or entirely outside the nanotube (CNT-S-C10FeNa, CNT-M-O15FeNa, and CNT-L-O15FeNa).

4.3. Conclusion

The catalytic results show that the migration of sodium from iron catalytic sites to the acidic sites of zeolite MFI27 is greatly reduced when iron and sodium are confined in CNT. The CNT-S-10FeNa sample, which revealed minimal variations in the two contact modes with the zeolite, confirms the efficiency of the carbonaceous barrier in separating iron from acidic sites. This effect is especially noticeable in this sample. Additionally, as demonstrated by catalytic results and

TEM analysis, increasing the iron content from 10% to 15% lead to a decrease in confinement capacity. Additionally, it was found that as the diameter of the CNT rises, the quantity of confined iron nanoparticles decreases. A detailed analysis of the catalytic tests and comparison of the CNT tested alone with the same CNT tested in two different contact modes with the zeolite revealed significant differences in CO_2 conversion and selectivity to CO and CH_4, particularly in the granule mixing mode. In conclusion, sodium migration is more pronounced with higher exposure of iron nanoparticles on the surface of the CNT and with smaller distances between iron sites and the acidic sites of the zeolite. It is undeniable that effective confinement is crucial to prevent iron from losing its alkaline metal promotion and to preserve the zeolite's acidity from sodium ion exchange with the zeolite proton.

Based on the results obtained and the conclusions drawn, the CNT-M-O15FeNa catalyst was selected to conduct further study, as detailed in Chapter 5. This time, the study did not focus on the properties of CNTs to mitigate sodium migration, but solely on the morphological properties of various MFI zeolites. Furthermore, to simplify the system, tests were conducted only in GM mode. This choice was motivated by the fact that, even with this configuration, significant deviations were observed compared to the CNT tested individually.

Chapter 5

5. Examining Alkali Migration in Na-promoted Fe-CNT/Zeolite Systems with a Focus on Various MFI Zeolite Properties

As discussed in detail, the migration of sodium from iron to the acidic sites of the zeolite in the CO_2-FTS represents a significant challenge as it compromises the catalytic activity and selectivity towards desired products. To address this issue, several strategies have been developed, one of which was examined in Chapter 4. In that context, the study focused on confining iron and sodium within carbon nanotubes (CNTs), demonstrating that the encapsulation of sodium and iron nanoparticles inside CNTs serves as a robust barrier against alkali metal migration when the CNTs are combined with zeolite. However, its efficacy decrease with increasing iron content and CNT diameter. Given these findings, the subsequent strategy presented in this chapter aims to analyze the influence of the external surface area and the structural properties of various MFI-type zeolites to achieve a more stable structure resistant to sodium ion exchange. To specify, the idea reported in this chapter was to center the attention on the study of different properties of MFI-type zeolite combined in granule mixing mode with the CNT-M-O15FeNa sample (synthesis reported in Chapter 2 and characterization details in Chapter 4). In fact, this particular CNT sample, as revealed in the previous chapter (Chapter 4), exhibited a substantial decrease in sodium promotion over time when combined with commercial zeolite (MFI27) in granule mixing mode. It seems certain that the phenomenon is taking place because of the increased selectivity for CO and CH_4 and the decreased conversion of CO_2. To conduct this study, the focus was particularly on the characteristics of MFI-type zeolite and all the tests were carried up in granule mixing mode (GM). Hence, initial modifications to the surface structure of MFI27 zeolite, involving passivation with

SiO_2 and the partial exchange of H^+ protons with sodium, were undertaken. The sample obtained was labelled MFI34@Sil3. Subsequently, the effect of a Si/Al ratio greater than 27 in MFI zeolites was examined. However, it was observed that, despite a decrease in Brønsted acidic sites, the zeolite MFI112, with a Si/Al ratio of 112, does not limit sodium migration. Based on these results, further analysis considered, on the one hand, the effect of an MFI zeolite with a nanocrystalline structure (MFI46-nano) and, on the other hand, the performances of an MFI structure with extra-large crystals characterized by a significantly reduced external surface area (μMFI35), which demonstrated a substantial restriction in sodium migration. In order to confirm the hypothesis that a limited external surface area plays a critical role in limiting the migration of alkali metals, the μMFI35 zeolite was desilicated (μMFI27-meso)). This treatment aimed to increase the external surface area and evaluate the influence of this variation on catalytic performance. However, the CNT-M-O15FeNa+MFI27 (GM) test from the previous chapter serves as a reference point for evaluating, based on catalytic performance, the possible inhibition or mitigation of sodium migration.

5.1. Introduction

In industrial contexts, proton-zeolites are used as acid catalysts for several hydrocarbon conversion processes [174], [175], [176]. In particular, the MFI zeolite is widely employed as a heterogeneous catalyst in isomerization and aromatization reactions. It features a three-dimensional 10-membered ring (10-MR) channel structure comprising straight and sinusoidal 10-MR channels with diameters ranging from approximately 5.1 to 5.6 Å and their intersections with a diameter of about 6.3 Å. The Al sites located within zeolite cavities constitute Brønsted acid sites with intrinsically different deprotonation energies and catalytic effects. Furthermore, proton affinity is influenced by factors such as Al content, neighboring protons, the shape and size of aluminosilicate clusters, and the shape and size of micropore voids [176]. As it is known its effectiveness depends on two main features: the ability to separate molecules according to their geometry, which is made possible by the distinct crystalline pores that contain catalytically active sites, and the Brønsted acidity that results from the aluminum's presence in the silicate framework. However, the steric effect, which only permits access to molecules whose diameters are less than the pore diameter, is primarily responsible for molecular selection and the ensuing shape selectivity [177]. Furthermore, the impacts of shape selection may reduce the synthesis of

undesirable products during the transition stage by avoiding the growth of bulky intermediates in the pores. This is accomplished by preventing the formation of bulky intermediates. The form of the particles, the density of the active sites, and the distribution of aluminum in the structure are just a few of the features of zeolites that may be greatly influenced throughout the preparation process and ultimately affect how efficient they are as catalysts. Furthermore, it should be emphasized that the presence of catalytic active sites at the pore entrance and on the outside might result in unintentional non-selective catalysis. Limiting the outer surface and extra-framework material by creating big, well-crystallized zeolite crystals and lowering the aluminum concentration might be one way to prevent this [175]. Conversely, the increase in external surface area highlights both the effects of surface charge and the abundance of surface sites. These factors can influence the shape of the external crystallite, the dimensions of the unit cell, pore arrangements, and the diffusion properties of zeolitic crystals. Such aspects are significant for adsorption, gas separation processes, and catalysis, as they impact contact duration and the transfer of mass and heat [178].

To better specify, the crucial roles in transforming olefins, such as isomerization, oligomerization, and aromatization, are predominantly played by the Brønsted acid sites rather than Lewis acid sites. These acid sites have a profound impact on catalytic performance. The distribution of Brønsted acid sites is determined by the positioning of framework Al atoms within the zeolite framework. This regulates the placement of acidic protons, which counterbalance the negative charges resulting from the substitution of framework Si atoms with Al atoms at tetrahedral sites. However, the spatial dimensions and design of the pores that act as Brønsted acid sites have a substantial impact on the catalytic performance. This is because of the distribution of Brønsted acid and the confinement effects that channels or cavities have on reaction intermediates and transition states. Furthermore, Brønsted acid sites are regulated by the lattice structure and the Si/Al ratio of the zeolite [176], [179]. Zeolites show considerable Brønsted acidity when H^+ ions occupy their cation sites, which has a substantial impact on their catalytic activity. Protons, that balance charges in the OH^- groups of Si(OH)Al species inside the zeolite structure, serve as Brønsted centers during catalytic reactions. These sites actively take part in isomerization and alkylation processes, and they are in charge of breaking down hydrocarbon molecules. The concentration of Brønsted acid sites may be modified by adjusting the aluminum-to-silicon ratio in the framework, described as the Al_2O_3 to SiO_2 molar ratio. However, zeolite acidity is increased when the molar ratio of Si to Al is lower. It

is also possible to modify Brønsted acid sites by adding metallic cations in place of H^+ ions, like sodium. However, this results in the loss of Bronsted's acidity. In addition to Brønsted sites, zeolites have Lewis acid sites that are connected to cations and positively charged oxide clusters and have an impact on catalytic activity. These sites can polarize bonds of reactive molecules and contribute to hydrocarbon molecule adsorption and cracking. Brønsted acid sites can be reduced in number by either removing aluminum from the framework under steam conditions or by dehydroxylating Brønsted acid sites at high temperatures. This process creates Lewis acid sites. Zeolite catalytic activity may be impacted by Brønsted sites' increased acidity due to interactions with extra-framework aluminum (EFAL) sites [180], [181]. Numerous prior investigations have asserted that the adjacency of extra-framework aluminum (EFAL) to a Brønsted acid site (BAS) may yield synergistic Brønsted acid sites (SBAS) with increased the activity for alkane cracking reactions. While water's involvement can influence reaction rates, selectivity, and mass transfer in various reactions, the exposure of zeolites to water can trigger hydrolysis of framework aluminum atoms. Consequently, this leads to the formation of framework-associated aluminum atoms at low temperatures and EFAL species at high temperatures. Moreover, under steaming conditions, water aids in mobilizing EFAL species within zeolite pores [181].

The catalysts employed in this study are summarized in the following table (Table 5. 1) additional information are instead reported in Table 2. 3.

Table 5. 1. Principal samples details involved in this study.

Name Used	IZA	Synthesis procedure
CNT-M-O15FeNa	-	Wet impregnation
MFI27	MFI	Commercial zeolite
04NaMFI27	MFI	Commercial zeolite partially ion-exchanged
MFI34@Sil3	MFI	Commercial zeolite sylilated with amourphous
MFI112	MFI	Commercial zeolite
µMFI35	MFI	Hydrothermal synthesis
µMFI27-meso	MFI	Desilication of homemade µMFI35
MFI46-nano	MFI	Hydrothermal synthesis

5.2. Results and discussions

5.2.1 Catalysts characterization

The Si/Al atomic ratios, as determined by ICP-OES, are provided in Table 5. 2. For instance, silylation of the commercial MFI27 sample through three cycles led to an increase in the Si/Al ratio from 27.2 to 33.6, as expected with approximately 4 wt.% SiO_2 incorporation per silylation cycle. Conversely, desilication of the initial μMFI35 zeolite to produce the mesoporous μMFI27-meso sample resulted in a decrease in the bulk Si/Al ratio from 34.9 to 27.1 due to desilication carried out using NaOH and TBAOH as reagents. In addition, in the same table, it is interesting to note that the Si/Al ratio found through XPS analysis is lower for all samples. This result can be explained by the presence of extraframework aluminum, which leads to a higher concentration of aluminum on the surface of the zeolites, Table 5. 2.

Table 5. 2. Bulk chemical composition determined by ICP-OES, Si/Al atomic ratio in the near-surface region measured by XPS, and percentage of framework (FAL) and extra-framework (EFAL Al species derived from ^{27}Al MAS NMR for MFI samples.

Zeolite	ICP-OES			XPS	^{27}Al MAS NMR
	Si/Al at. ratio	Na (wt%)	Na/Al at. ratio	Si/Al at.	FAL/EFAL (%)
MFI27	27.2	0.00	0.00	22.7	91/9
0.4NaMFI27	26.6	0.56	0.44	-	-
MFI112	112.0	0.02	-	106.1	98/2
MFI34@Sil3	33.6	0.01	-	32.0	92/8
MFI46-nano	46.0	0.24	-	42.2	95/5
μMFI35	34.9	0.00	0.00	-	94/6
μMFI27-meso	27.1	0.04	0.003	-	82/18

Following XRD analysis, both commercially available and homemade zeolites displayed distinct reflections characteristic of the MFI topology, specifically at 2θ angles of 8.0°, 8.8°, 8.9°, 23.1°, 23.3°, and 23.9°, consistent with JCPDS 44-0003 (Figure 5. 1).

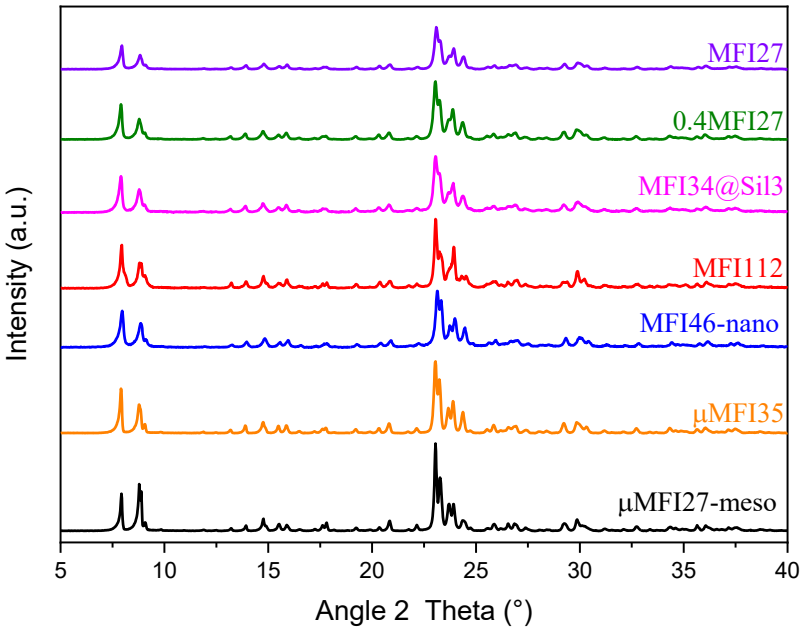


Figure 5. 1. XRD patterns obtained for commercial MFI samples, namely MFI27 and MFI112; alongside other samples home-prepared.

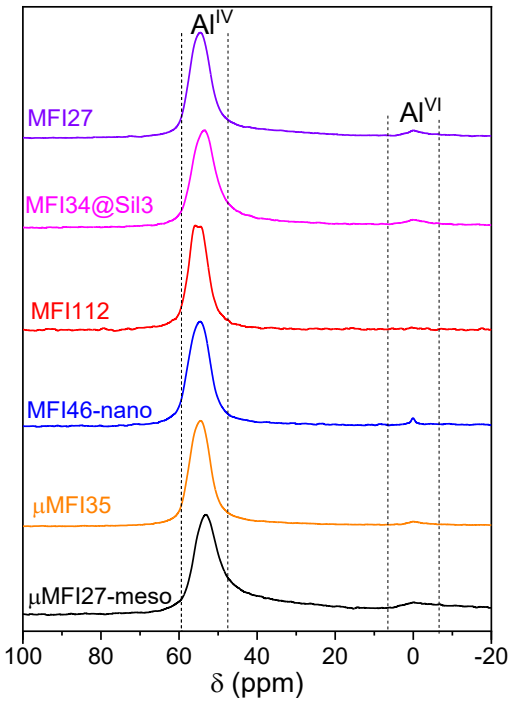


Figure 5. 2. Normalized ^{27}Al MAS NMR spectra of hydrated MFI zeolites.

In fact, heat treatment induced dealumination of framework aluminum (FAl) in zeolites, leading to the generation of extra-framework aluminum (EFAl), as demonstrated by the appearance of hexa-coordinated aluminum in the ^{27}Al MAS NMR spectra (Figure 5. 2). The H-MFI samples exhibited two clear peaks at around 55.1 ppm, which suggests the existence of tetrahedrally-coordinated FAl [182]. Following the steaming process, additional signals became apparent, including a small peak at 0 ppm, which can be attributable to hexa-coordinated EFAl [183], [184]. The % of FAL and EFAL species estimated by deconvolution of the Al^{IV} (at ca. 55 ppm) and Al^{VI} (at ca. 0 ppm) signals are given in the last column of Table 5. 2. However, there were no visible bands at roughly 30 ppm, indicating the absence of lack of either penta-coordinated EFAl or EFAl in tetrahedral coordination with two framework oxygen atoms [182], [185], [186].

Furthermore, Table 5. 3 summarizes the average crystallite sizes and textural characteristics obtained through N_2 physisorption. In terms of texture, the commercial and homemade samples exhibited BET surface areas (339-438 $m^2 \cdot g^{-1}$) and micropore volumes (0.098-0.182 $cm^3 \cdot g^{-1}$) typical of MFI zeolite, exhibiting a type IV isotherm [110], [142], Figure 5. 3. However, these zeolites showed

external surface areas ranging from 9 to 199 $m^2 \cdot g^{-1}$, indicating an expected inverse relationship with crystallite size, Figure 5. 4 and Figure 5. 5. Concerning the MFI34@Sil3 zeolite, obtained following three-cycle silylation, experienced a reduction of approximately 11% and 10% respectively in BET surface area and micropore volume, attributed to the presence of an amorphous external SiO_2 layer. Conversely, MFI46-nano zeolite exhibited significantly higher BET and external surface areas (450 and 74 $m^2 \cdot g^{-1}$, respectively) due to its nano-sized nature, confirmed by FESEM (Figure 5. 4, b) and TEM images (Figure 5. 5, a) showing aggregate sizes of 0.02-0.04 μm. However, the zeolite with the lowest external surface area (9 $m^2 \cdot g^{-1}$) and higher crystallite size (12x6x5 μm) reported in this work is the μMFI35, Table 5. 3 and Figure 5. 4 c, d).

Table 5. 3. Textural properties of MFI zeolites determined by N_2 adsorption measurements.

Zeolite	BET (m^2/g)	S_{ext} (m^2/g)	S_{micro} (m^2/g)	V_{micro} (cm^3/g)	Crystallite size (μm)
MFI27	376	42	334	0.163	0.1-0.2
0.4NaMFI27	-	-	-	-	-
MFI112	369	43	326	0.161	1-2
MFI34@Sil3	339	48	291	0.143	-
MFI46-nano	450	74	376	0.182	0.02-0.04
μMFI35	351	9	342	0.166	12x6x5
μMFI27-meso	438	199	239	0.098	5-15

[a] t-plot External Surface area ($m^2 \cdot g^{-1}$)

[b] t-plot micropore volume ($cm^3 \cdot g^{-1}$).

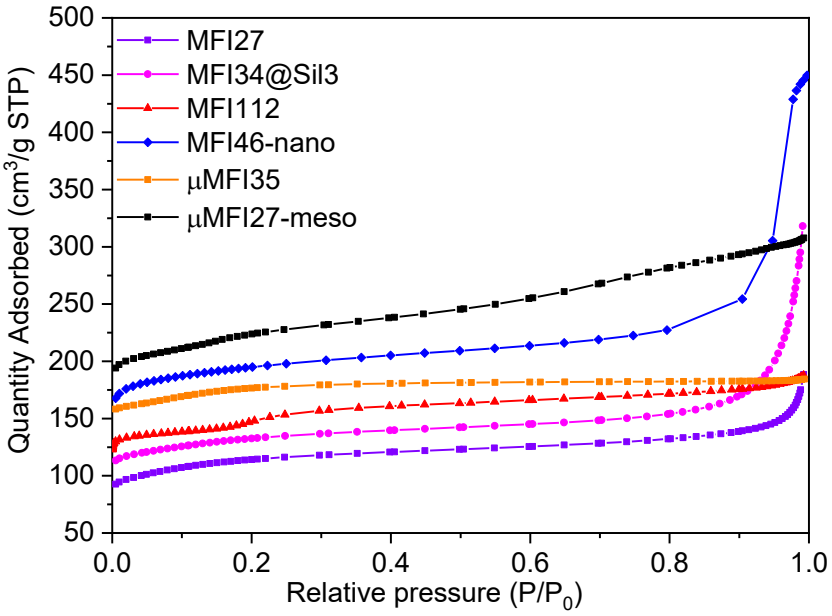
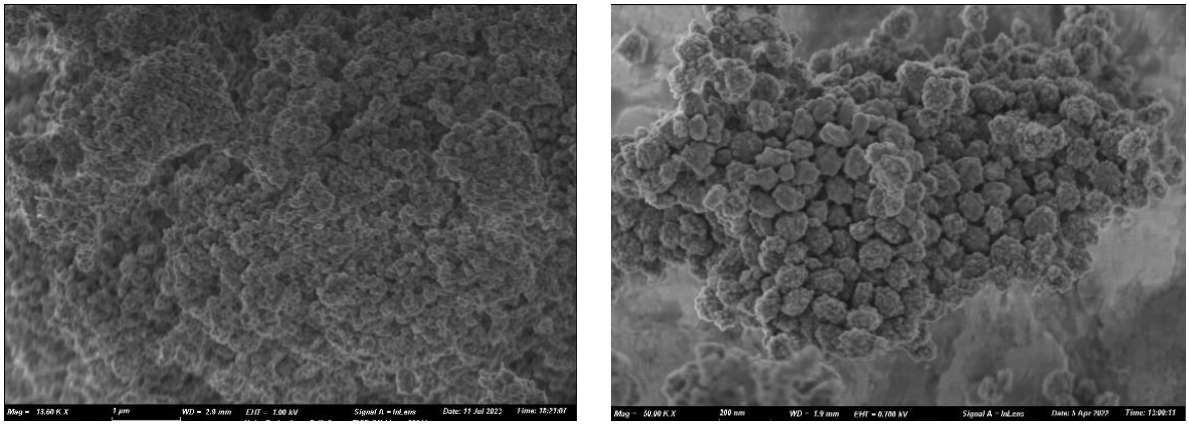
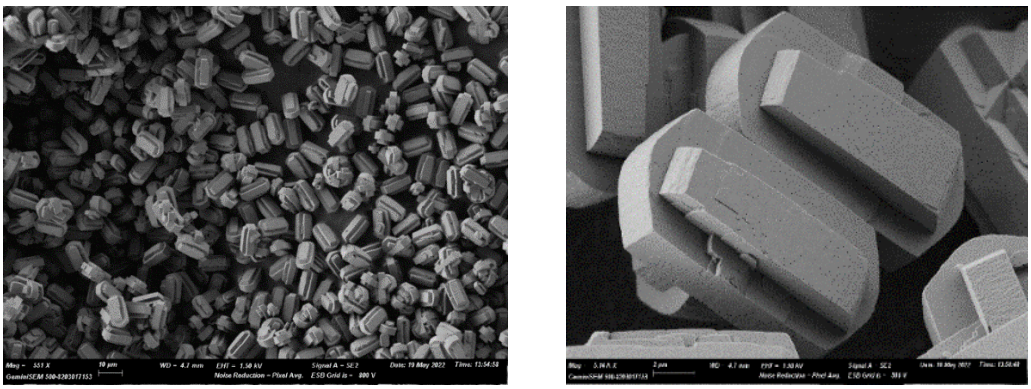


Figure 5. 3. N_2 adsorption isotherms measured at -196 °C for MFI zeolites. For the sake of clarity, the isotherms have been upshifted by 30, 40, 60, 70, and 100 $cm^3 \cdot g^{-1}$ for MFI34@Sil3, MFI112, MFI46-nano, µMFI35, and µMFI27-meso, respectively.

a) b)



c) d)



e)

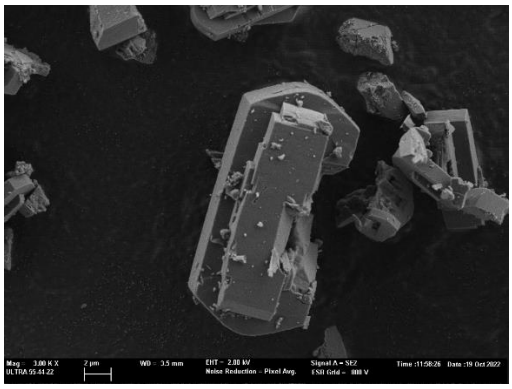


Figure 5. 4. Representative FESEM images of (a) MFI27, (b) MFI46-nano, (c, d) μMFI35 and (e) μMFI27-meso zeolites.

a) b)

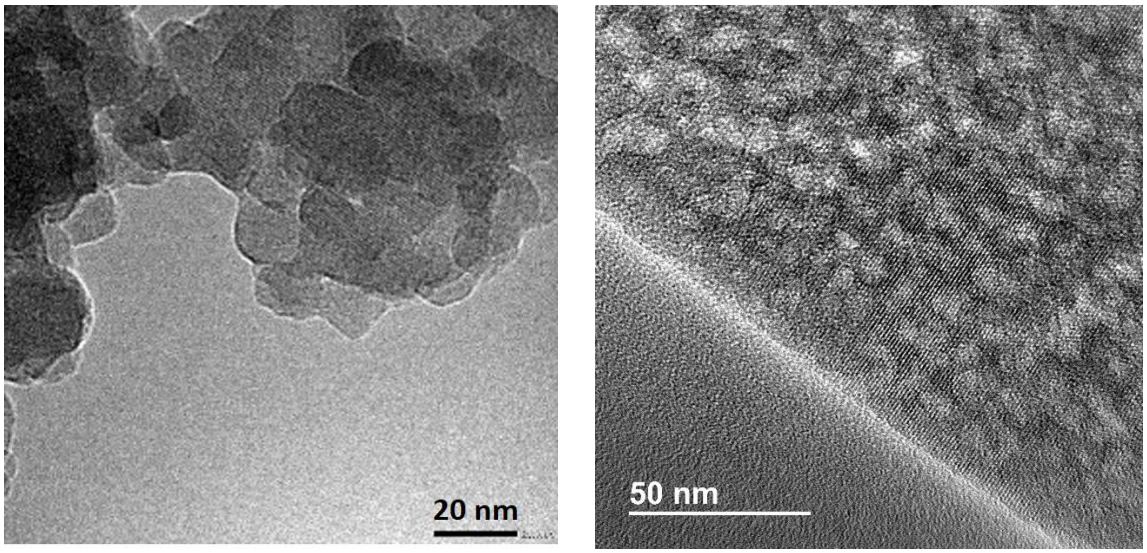


Figure 5. 5. Representative TEM images of MFI46-nano (a) and μMFI27-meso (b) zeolites.

In addition, how expected, the desilication of μMFI35 under alkaline conditions (labelled μMFI27-meso) notably increased external and BET surface areas from 9 to 199 $m^2 \cdot g^{-1}$, through accompanied by a decrease in micropore volume from 0.166 to 0.098 $cm^3 \cdot g^{-1}$, Table 5. 3. The estimated crystallite size ranged from 5000-15000 nm via FESEM, Figure 5. 4, e) observable as light grey regions in TEM images, Figure 5. 5, b).

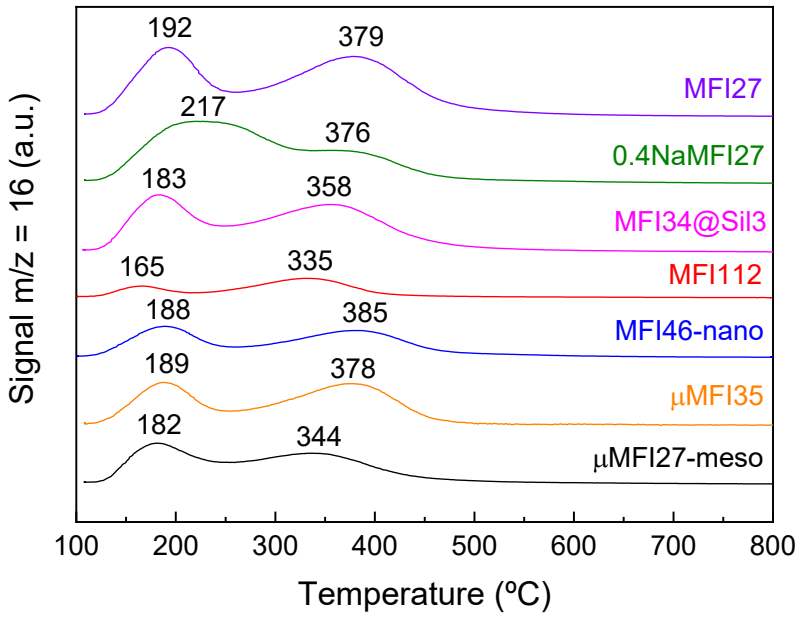


Figure 5. 6. NH_3-TPD profiles of MFI zeolites.

Figure 5. 6 illustrates the NH_3-TPD profiles for the all MFI zeolites involved in this work. As it is possible to appreciate all the profiles displays two distinct peaks: a peak at a lower temperature of around 180-200 °C, indicating the presence of weak acid sites, and a peak at a higher temperature of around 350-380 °C, signifying the strong acid sites. The high-temperature peaks of MFI27, 0.4NaMFI27, MFI34@Sil3, MFI112, MFI46-nano, µMFI35, and µMFI27-meso are detected at specific temperatures of 379, 376, 358, 335, 385, 378 and 344 °C, respectively. After analyzing the profiles, specifically comparing MFI27 with 0.4NaMFI27 and MFI34@Sil3, it is important to observe that the total acidity dropped when the zeolite is recovered by a shell of amorphous SiO_2 and/or Na^+ ions were added to the framework. This is because Na^+ has inferior electron-acceptor characteristics compared to Al^{3+} [187]. Furthermore, for these three zeolites the total amounts of acid sites were found to be 610, 511 and 491 µmol/g, respectively, Table 5. 4.

Table 5. 4. Density of acid sites of MFI samples determined by NH_3-TPD.

Zeolite	Quantity adsorbed cm^3(STP)/g	Weak[a] (μmol /g)	Strong[a] (μmol /g)	Total (μmol /g)
MFI27	13.67	219	391	610
0.4NaMFI27	11.45	280	231	511
MFI34@Sil3	11.00	160	331	491
MFI112	2.75	27	96	123
MFI46-nano	6.25	107	172	279
μMFI35	8.64	142	244	386
μMFI27-meso	7.63	113	228	341

[a] Weak acid sites: Tmax < 300 °C. Strong acid sites: Tmax > 300 °C.

In order to determine the characteristics and amounts of the Brønsted and Lewis acid sites, pyridine infrared (IR) tests were conducted on all the MFI zeolites. The presence of bands at 1545 and 1445 cm^{-1} in the IR spectra indicates the presence of Brønsted (PyH^+) and Lewis (L-Py) acid sites, respectively [187], [188]. The results of the FT-IR spectra analysis of the zeolite, obtained following the removal of pyridine at temperatures of 150, 250, 350, and 400 °C, are presented in Table 5. 5. Based on the infrared spectra of pyridine produced at a temperature of 150 °C, it was shown that only 0.4NaMFI27 and μMFI27-meso zeolites present a densities of Brønsted acid sites. Nevertheless, in all the MFI zeolites the levels of Brønsted acid sites decrease with increasing of the temperature. In particular the levels of Brønsted acid sites decline more rapidly on 0.4NaMFI27 when the temperature rose from 150 to 400 °C in comparison to MFI27. Furthermore, the variations in the concentrations of Brønsted acid sites on the MFI zeolites reveals that the acid strength increase in the following order MFI112<MFI46-nano<μMFI27-meso<MFI34@Sil3<0.4NaMFI27<MFI27.

Table 5. 5. Acidity of MFI zeolites determined by FTIR of adsorbed pyridine.

Zeolite	Acidity (µmol/g)							
	B_{150}	B_{250}	B_{350}	B_{400}	L_{150}	L_{250}	L_{350}	L_{400}
MFI27	-	308	232	164	-	35	27	26
0.4NaMFI27	68	61	58	-	12	7	5	-
MFI34@Sil3	-	164	112	70	-	34	28	25
MFI112	-	79	50	25	-	7	4	2
MFI46-nano	-	174	140	94	-	26	20	10
µMFI35	-	-	-	-	-	-	-	-
µMFI27-meso	128	139	141	-	24	17	14	-

The external acid properties of the sample MFI34@Sil3 were evaluated through FTIR spectroscopy of adsorbed 2,6-di-tert-butyl pyridine (FTIR-DTBPy), Figure 5. 7.

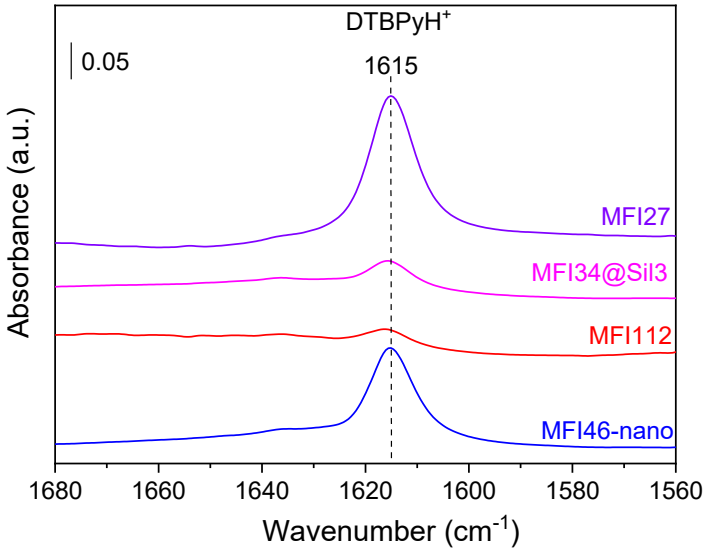


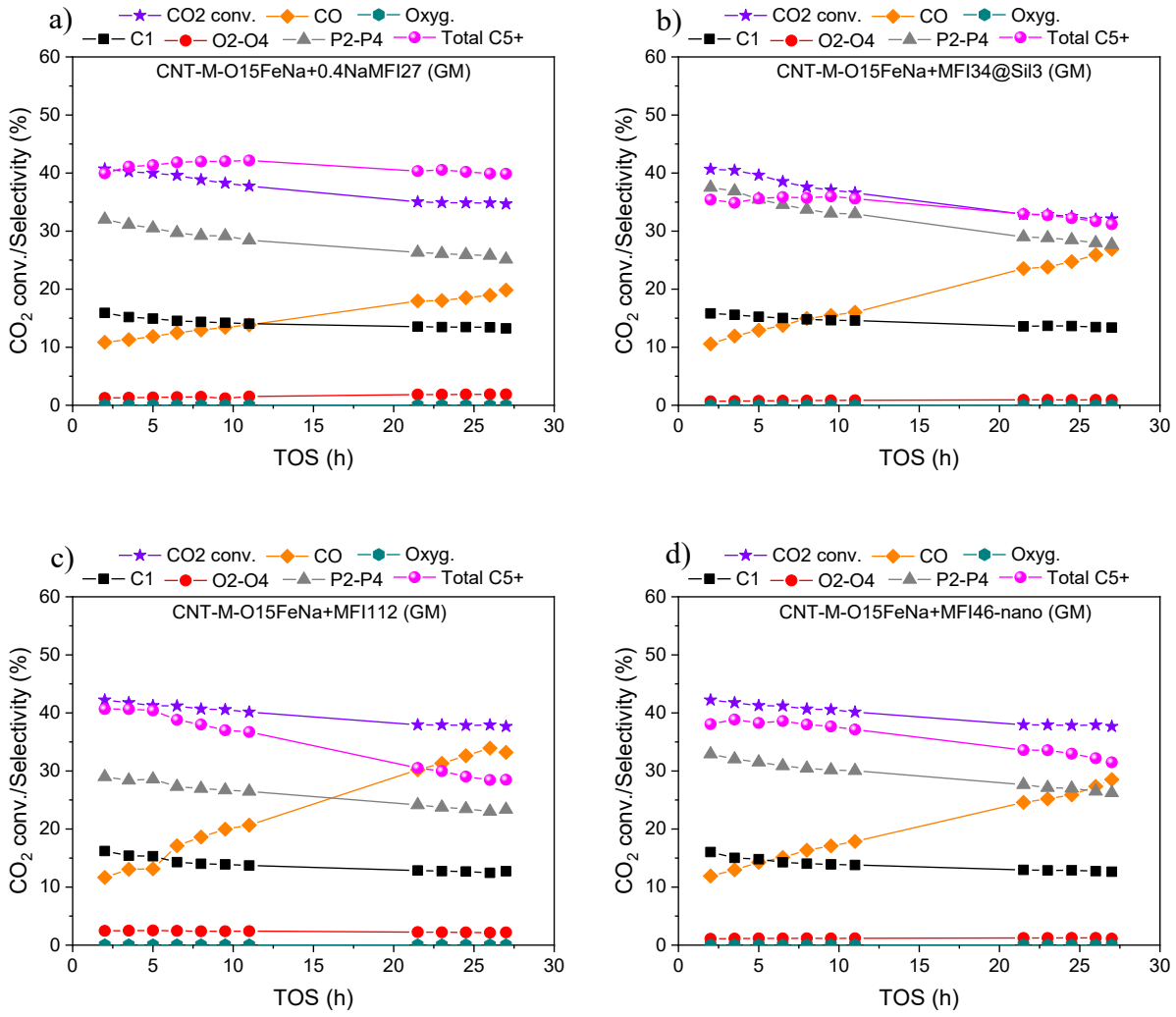
Figure 5. 7. FTIR-DTBPy spectra of MFI zeolites. Spectra normalized to sample weight.

In addition, FTIR spectroscopy of adsorbed 2,6-di-tert-butyl pyridine (FTIR-DTBPy), a bulky probe molecule unable to penetrate the 10-ring pores of H-ZSM-5, was utilized to qualitatively assess the external Brønsted acidity in selected zeolites [189]. To evaluate the influence of external Brønsted acid sites on the inhibition of sodium migration, without being obscured by the possible contribution of total Brønsted acidity, FTIR spectra of adsorbed 2,6-di-tert-butyl pyridine (FTIR-DTBPy) were measured for some previously mentioned zeolites. The corresponding spectra in the region where the IR band at 1615 cm^{-1} attributed to the ring vibration of protonated 2,6-DTBPy (2,6-DTBPyH$^+$) appears are presented in Figure 5. 7. As observed, the intensity of the band at 1615 cm^{-1} for the silylated sample MFI34@Sil3 (I_{1615} = 0.04 a.u.) was reduced by approximately 81% compared to its original MFI27 counterpart (I_{1615} = 0.21 a.u.), indicating a simultaneous decrease in the concentration of external Brønsted acid sites. Furthermore, the intensity of this band in MFI112 (I_{1615} = 0.03 a.u.) and MFI46-nano (I_{1615} = 0.09 a.u.) was lower than in MFI27 due to their lower Si/Al ratio, as evident from Table 5. 2. This suggests that MFI27 exhibits an increase in the amount of accessible external Brønsted acid sites compared to the other zeolites (Figure 5. 7).

5.2.2 Catalytic tests

Figure 5. 8 illustrates the catalytic tests conducted via granule mixing (GM), employing the catalyst CNT-M-O15FeNa alongside various MFI structures characterized by distinct structural properties. Throughout the 27-hour Time on Stream (TOS) period, a significant fluctuation in catalytic performance is evident. This variation is primarily attributed to the depletion of iron promotion induced by sodium, coupled with the reduction in surface acidic sites resulting from the ions- exchange between zeolite protons and sodium ions. The CO_2 conversion, CO selectivity, and overall hydrocarbons distribution obtained over the tandem CNT-M-O15FeNa plus different MFI zeolite systems are summarized in Table 5. 6. As can be seen, the presence of different MFI zeolite significantly changed the distribution of higher hydrocarbons, i.e. C_2-C_4 paraffins, and liquid (C_{5+}) hydrocarbons, in different extents depending on the specific H-ZSM-5 zeolite used. As a general trend, all the tandem catalysts displayed a low selectivity of light olefins ($C_2^=$-$C_4^=$) and higher selectivity of light paraffins (C_2^0-C_4^0) and C_{5+} hydrocarbons, mostly related to the formation of aromatics. Moreover, the hydrogen released in the aromatization reactions accounts for the saturation of

olefins causing the observed decrease in the selectivity of $C_2^=$-$C_4^=$ and the concomitant increase in C_2^0-C_4^0 (Table 5. 6). It is interesting to note that the catalyst containing the zeolite with the highest Si/Al ratio, MFI112, does not show substantial differences in terms of selectivity if the phenomenon of sodium migration occurs. Without such migration, one would expect a low formation of aromatic compounds and the promotion of cracking of heavier olefins produced on the iron-based component, in favor of lighter olefins. However, in this case, no evident differences related to the lower acidity of this zeolite has been observed.



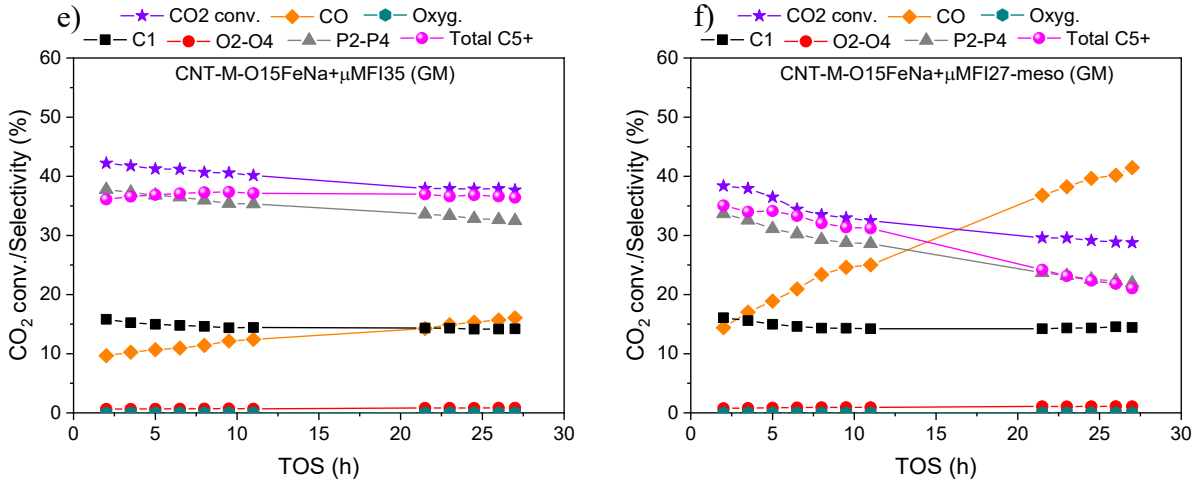


Figure 5. 8. TOS monitoring CNT-M-O15FeNa+different MFI zeolite, weight ratio 1:1, granular mixture mode: a) CNT-M-O15FeNa+0.4NaMFI27, b) CNT-M-O15FeNa+MFI34@Sil3, c) CNT-M-O15FeNa+MFI112, d) CNT-M-O15FeNa+MFI46-nano, e) CNT-M-O15FeNa+µMFI35, f) CNT-M-O15FeNa+ µMFI27-meso.

Table 5. 6. Overall product selectivity.

CATALYST	CO_2	FTY	Overall Product Selectivity (%C)						ΣC_2-C_4
	(%)	(mmol/(g_{Fe}·h)	CO	Oxyg	C1	$C_2^{=}$-$C_4^{=}$	C_2^0-C_4^0	Total	(%C)
CNT-M-O15FeNa+MFI27 (GM)	31	58	31	0	13	1	27	28	27
CNT-M-O15FeNa +0.4NaMFI27 (GM)	35	65	19	0	13	2	26	40	28
CNT-M-O15FeNa +MFI34@Sil3 (GM)	32	60	25	0	14	1	28	32	29
CNT-M-O15FeNa +MFI112 (GM)	30	57	32	0	13	2	24	29	26
CNT-M-O15FeNa +MFI46-nano (GM)	32	62	26	0	13	1	27	33	28
CNT-M-O15FeNa +µMFI35 (GM)	38	70	15	0	14	1	33	37	34
CNT-M-O15FeNa +µMFI27-meso (GM)	29	54	39	0	14	1	23	23	24

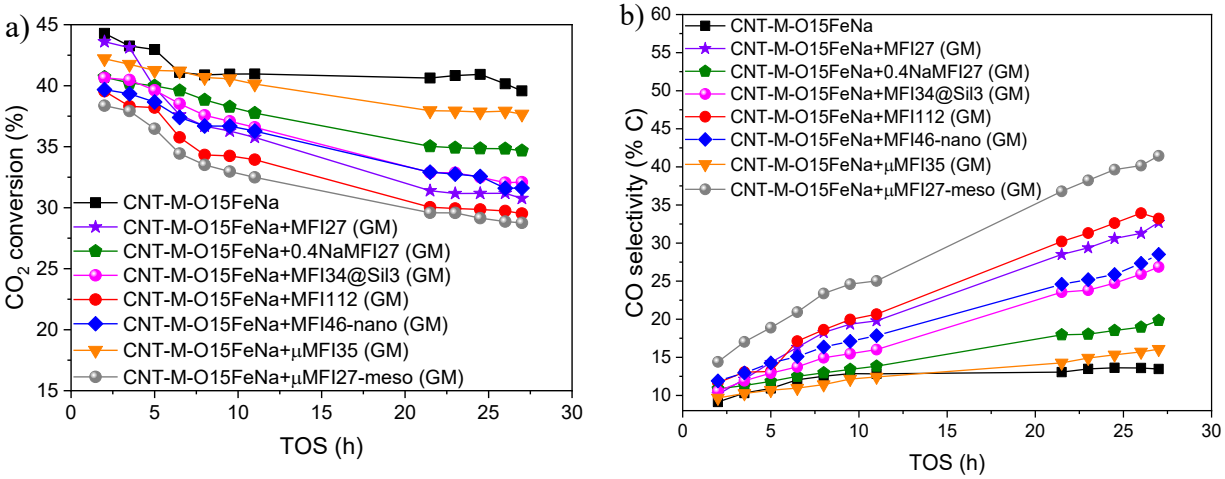
[a] H_2/Ar/CO_2=68/10/22 (% vol.), flow=250 ml/min; P=20 bar; T=340 °C; TOS=27 h;

[b] The FTY was calculated at standard condition: R=0.0821 (L·atm/(mol·K); P=1 atm; T=298.15 K;

Since Brønsted acid sites are generally the predominant type of acid sites in zeolites, as it is the case of the H-ZSM-5 samples studied here (Table 5. 5), it seems reasonable that their concentration and/or strength should play an essential role in determining the aromatics selectivity. However, if Na-migration occurs the catalytic performances could depend on other factors. Furthermore, to better understand the difference between the various zeolitic structures, it is advisable to refer to Figure 5. 9, where comparisons are presented in terms of CO_2 conversion, CO selectivity, and CH_4 selectivity among the different catalytic tests conducted. However, for a more in-depth analysis and better understanding, it is advantageous to compare the catalytic tests conducted using different MFI zeolites. In this context, the tests conducted with CNT alone and CNT in combination with zeolite MFI27 were included only for comparative purposes. To specify, the test conducted with CNT-M-O15FeNa alone is included because it represents a condition where sodium migration does not occur and it is relevant for comparison in terms of CO_2 conversion, CO selectivity, and CH_4 selectivity. This condition serves as a reference parameter to be achieved during tests with an MFI zeolite that effectively limits or inhibits sodium migration. Conversely, the inclusion of the test with CNT-M-O15FeNa+MFI27 (GM) represents a condition where sodium migration occurs. Therefore, it is justified in the comparative analysis to evaluate potential improvements in catalytic performance when using MFI zeolites with different properties and how these may contribute to mitigate, inhibit, and/or prevent this undesired phenomenon. All catalysts exhibit rather unstable performance with TOS, especially in terms of CO_2 conversion and selectivity of CO, CH_4, and total hydrocarbons. In particular a gradual decline in CO_2 conversion accompanied by an increase in the selectivity of CO and CH_4 was noticed since the early reaction stages at equivalent reaction conditions (Figure 5. 9, a-c). These trends evidenced a progressive loss of iron promotion due to migration of the alkali from the iron component to the zeolite during reaction. However, the stable behavior observed for the tandem catalysts based on CNT-M-O15FeNa+µMFI35 (GM) reported in this work suggests that alkali migration is mitigated to a noticeable extent, at least within the range of TOS studied here. Conversely, the CNT-M-O15FeNa+µMFI27-meso (GM) demonstrates a low CO_2 conversion rate (29 %) and poor selectivity for C_{5+} hydrocarbons (23%), making it the least effective among the others tests. Additionally, it shows the highest CO selectivity (39 %) as a by-product. This outcomes can be explained by the

interaction between the acidic sites of H-ZSM-5 and sodium ions present on the surface of the CNT-M-O15FeNa catalyst. This interaction reduces the alkalinity of the CNT-M-O15FeNa catalyst, thereby hindering the formation of the active phase Fe_5C_2 and reducing its capacity for carbonization. Consequently, it becomes challenging to produce low-carbon olefin intermediates [151]. Moreover, the presence of Na^+ ions, which exchange with the acidic sites of H-ZSM-5, inhibits olefins oligomerization and isomerization reactions [190]. In contrast, when the zeolite used has a large dimension (µMFI35), the CO_2 conversion and selectivity of C_{5+} products remain high and really close to the CNT-M-O15FeNa sample tested without zeolite (see test CNT-M-O15FeNa+µMFI35 (GM)).

Analyzing Figure 5. 9, it is interesting to note an intriguing trend: the selectivity towards total C_{5+} compounds gradually diminishes (Figure 5. 9, d) as the sum of aromatic and aliphatic compounds increases (Figure 5. 9, e and f). Particularly, it is evident that this decrease is primarily attributable to the decline in selectivity towards aromatics over time, indicating a progressive difficulty of the zeolite in aromatization. However, this trend is practically absent in the samples where there was no observed migration of sodium from iron to the acidic sites of the zeolite, as previously demonstrated by trends in CO_2 conversion (Figure 5. 9, a) and selectivity to CO (Figure 5. 9, b) and CH_4 (Figure 5. 9, c).



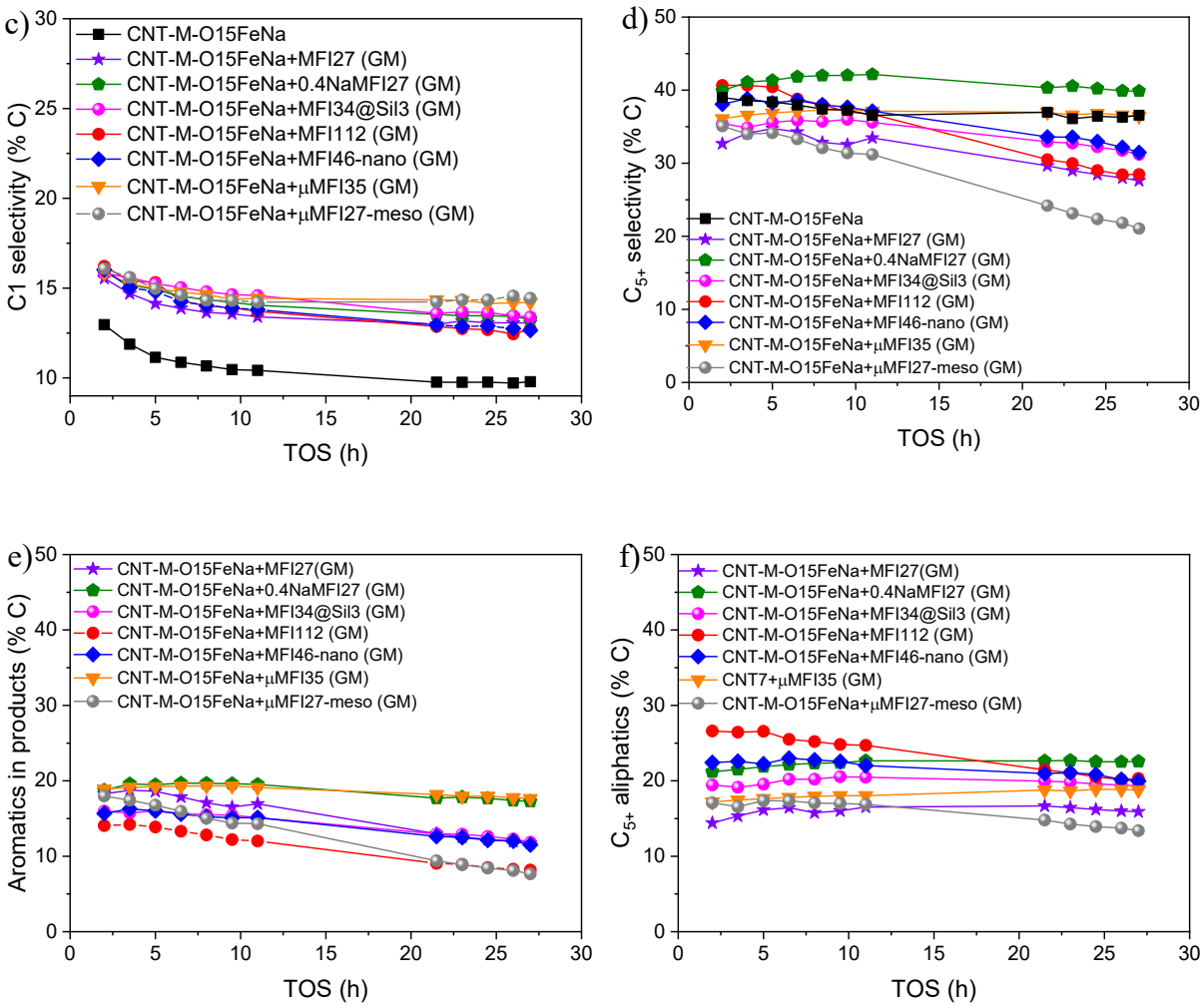


Figure 5. 9. Comparison conversion and overall selectivity.

As previously mentioned, the tendency of sodium to migrate is clearly visible and appreciable from the trends in CO_2 conversion, CO selectivity, and CH_4 selectivity over time. For this reason, to evaluate in detail the possible sodium migration over time and/or its inhibition, these three parameters have been reported in Figure 5. 10 in relative form over time.

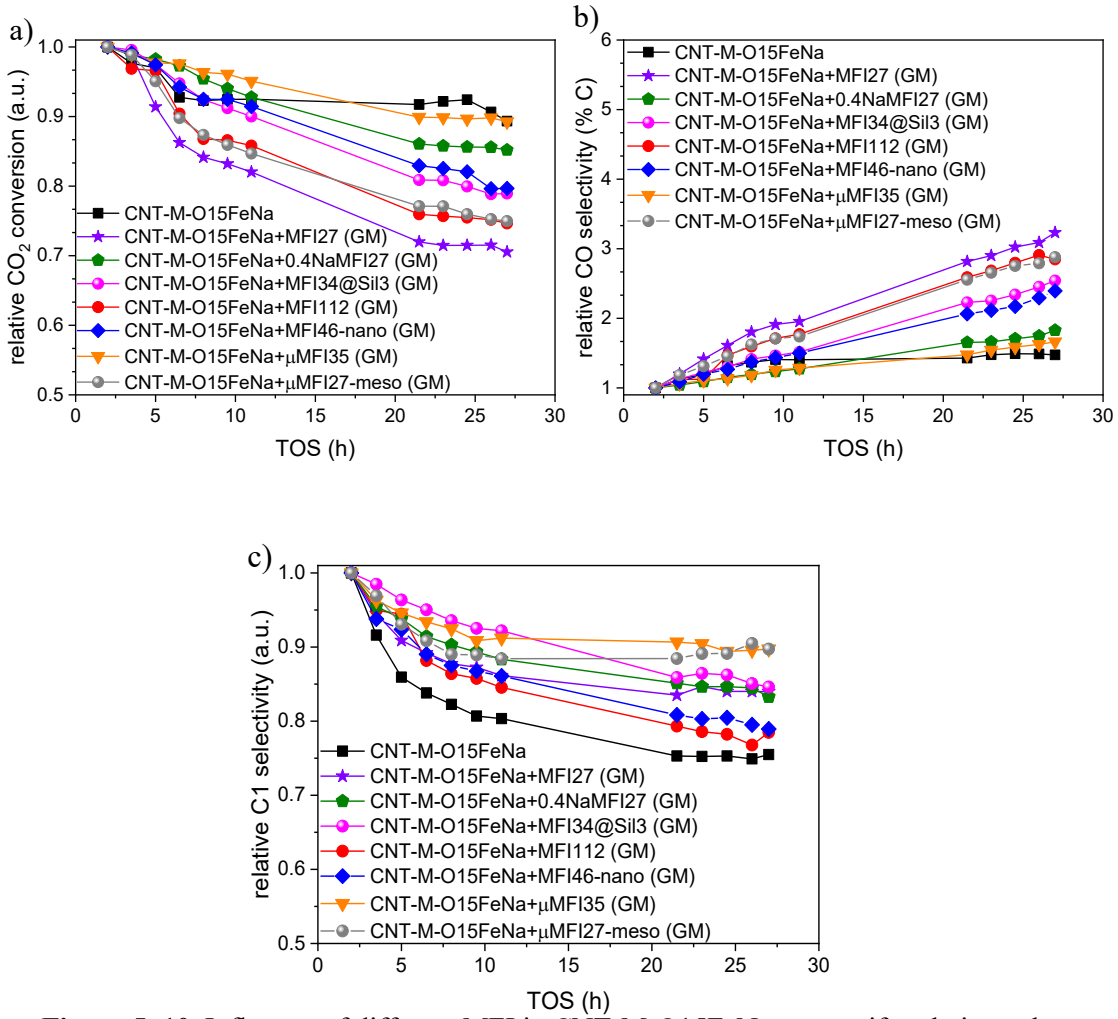


Figure 5. 10. Influence of different MFI in CNT-M-O15FeNa, to specify relative value related to itself conversion and to itself selectivity.

As can be observed, the CO_2 conversion and methane selectivity over time are practically identical to those found for the CNT-M-15FeNa catalyst tested alone, indicating an absence of sodium migration from the iron sites to the acidic sites of the zeolite. However, a detailed analysis of methane selectivity over time shows a slightly higher value. The reason for this is that some external acidic sites, despite their small surface area, can exchange ions with sodium from the iron. However, the zeolite's catalytic activity and its ability to oligomerize, isomerize, and aromatize remain intact over time due to the limited number of these external sites, Figure 5. 10.

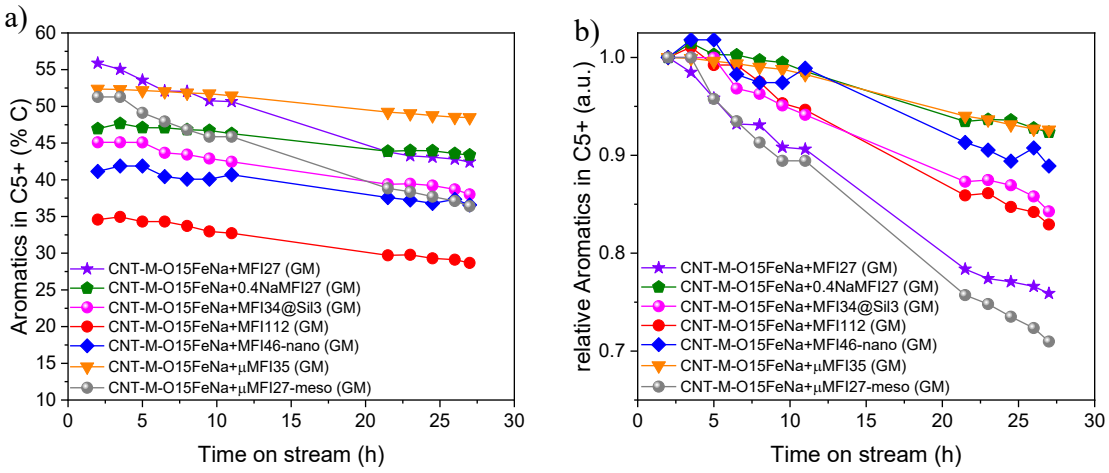


Figure 5. 11. Effect of CNT and site distance (GM) on aromatics formation.

In the analysis of the results, it is clear that the stability of aromatic production is influenced by the capacity of active sites to aromatize over time. This stability can be compromised by phenomena such as coke formation or, in the case at hand, by the ion exchange of zeolite acid sites with sodium from iron during the reaction. It is interesting to note that the Si/Al ratio of zeolites, and therefore the number of Brønsted acid sites, plays a key role in their ability to aromatize olefinic reaction intermediates and their susceptibility to sodium exchange. The catalytic data shown in Figure 5. 11 confirm this relationship: for example, the test conducted with zeolite MF112 showed the lowest quantity of aromatics from the first analysis point, while that with zeolite MFI27 highlighted the highest content of aromatics among the C_{5+} products. The μMFI35 and MFI46-nano zeolites follow the same trend, while zeolite 0.4NaMFI27 and MFI34@Sil3 confirm the expected results based on the available acid sites. However, what makes this study particularly interesting is evaluating the long-term stability of these zeolites. This stability appears to be more influenced by the exchange of Brønsted protons with sodium. Specifically, when observing the Time on Stream (TOS) relative values, it is clear that zeolite MFI27, along with the test conducted with μMFI27-meso zeolite, is the least stable. Conversely, the most stable zeolite seems to be μMFI35, followed by 0.4NaMFI27. These results suggest that zeolites with fewer surface Brønsted acid sites may inhibit sodium exchange, thereby impeding sodium migration from iron to the zeolite acid sites. A species can migrate from iron-based catalysts to H-ZSM-5, thereby reducing acidic active sites by donating

electrons to the zeolite during the reaction. Therefore, it is hypothesized that excessive proximity may promote the migration of sodium ions to H-ZSM-5, resulting in the poisoning of acidic sites on the zeolite and consequently deteriorating the formation of aromatics [105], [191]. Furthermore, tests conducted with mesoporous zeolite (μMFI27-meso) highlight inferior catalytic performance. This is because intracrystalline mesopores, located directly within individual crystals, facilitate diffusion and, consequently, ion exchange with sodium, thereby contributing to the increase in the crystal's surface area. The observed catalytic trends using μMFI35 zeolite can be explained by its large crystal size, which affects the external surface area of the material and, consequently, the potential ion exchange with Na^+ ions from the catalytic sites of iron to the acidic sites of the zeolite. It is important to note that the presence of larger crystals results in fewer grain boundaries and, consequently, a lower external surface area per unit volume compared to smaller crystals. In the case of μMFI35 zeolite specifically, this translates to an external surface area of only 13 $m^2 \cdot g^{-1}$, significantly lower than other zeolites examined in this study. It is crucial to emphasize that, in the context of ion exchange with sodium, a reduced external surface area appears to inhibit and/or mitigate the efficiency of ion exchange, limiting it. The competition between H^+ ions present in the acidic sites of the zeolite and Na^+ ions in the surrounding environment may be reduced due to the lower availability of surface area for ion exchange. Consequently, there may be a reduction in the undesired phenomenon of ion exchange of the acidic sites of the zeolite with sodium, thus providing a potential strategy to mitigate sodium migration.

5.3. Conclusion

The study focusing on the structural properties of MFI zeolite highlighted the importance of reducing the number of surface acid sites that, when exposed, can interact with sodium previously adsorbed on iron. From the analysis conducted, it was found that all of the proposed alternatives proved beneficial in limiting sodium migration. However, the analysis of CO_2 conversion and product selectivity over time, especially with regard to CO and aromatics, showed that the application of an amorphous SiO_2 layer on the outer surface of the commercial MFI27 zeolite is effective in limiting migration, although not completely inhibiting it. The same result, further improved, was achieved by the partial exchange of the zeolite's acid sites with sodium. Based on these results, it was

decided to examine a zeolite with an MFI structure but with a higher Si/Al ratio in order to reduce the number of surface acid sites. However, the results were not conclusive with regard to blocking migration. Although improvements in trends were observed, these were not conclusive. For these reasons, the effects of two zeolites with different morphological properties were analyzed: the MFI46-nano zeolite, characterized by a nanocrystalline structure (10-20 nm in size according to TEM analysis), and a μMFI35 zeolite, with crystallites five times larger than conventional zeolites (5000-15000 nm in size according to FESEM analysis) and a surface area of only 13 $m^2 \cdot g^{-1}$. This last zeolite (μMFI35), due to its surface properties, proved to be the best in mitigating sodium migration, highlighting the critical role of morphological properties and specific surface area in influencing sodium migration and overall catalytic performance. However, as a confirmation of the theory founded, was prepared and tested the same zeolite, but desilicated. Because the desilication is known to create mesoporous cavities on the surface and increase the surface area, as predicted, the catalytic performance dropped again, suggesting significant sodium migration. This study provides a solid basis for the synthesis of high-performance zeolites that are unaffected by ion-exchange with sodium.

Chapter 6

6. Impact of Different Zeolite Structures on the Catalytic Performances of NaFe-Zeolite Systems Tested in Dual-Bed Mode

As already stated in the previous chapters, the use of substantial CO_2 emissions from industrial combustion, together with the use of green hydrogen, is widely used in the process of reducing CO_2 in hydrocarbon fuels and high-value-added chemicals. This approach not only reduces the emissions of one of the main greenhouse gases and climate change, but also includes the use of green H_2, produced, for example, from the electrolysis of water using the excess of renewable energy, thus overcoming the problems of storing hydrogen. In particular, this study investigates the thermocatalytic CO_2 Fischer Tropsch conversion into liquid fuel using 1NaFe catalysts combined with various zeolite frameworks: 12-ring (FAU and BEA) and 10-ring (MFI, TON, MWW and ITQ-2), operated at 20 bar, 340 °C for 27 h on stream in a dual bed mode. Different impacts of the zeolite framework on catalytic activity and product distribution are demonstrated by experimental data, highlighting the importance of mass transfer phenomena and active site engineering in CO_2 conversion reactions, especially in the first stage of the reaction (1-2 h). This study will emphasize the effect of various frameworks with 10-ring channels on the generation of liquid fuel, while the first portion concentrates on the influence of zeolite with large pore size (12-ring). The greatest results in terms of gasoline generation were obtained in this context using the zeolite MFI27. The catalytic performance of each catalyst system is systematically evaluated in terms of CO_2 conversion efficiency, hydrocarbon selectivity, and stability under industrially relevant operating conditions. Overall, this study provides valuable insights into the design and optimization of catalyst systems for thermocatalytic CO_2-Fischer-Tropsch synthesis, thereby contributing to the development of sustainable technologies for carbon recycling and renewable energy production.

6.1. Introduction

As anticipated in chapter 1, technologies as carbon capture, utilization, and storage (CCUS) have shown great promise in mitigating climate change by converting CO_2 into useful hydrocarbon fuels and chemicals. The chemical conversion of CO_2 has become attractive and practicable with the development of green electricity and renewable hydrogen sources, such as wind, hydraulic power, biomass, and solar energy. This procedure not only lowers CO_2 levels, decreasing negative environmental effects of this greenhouse gas, but also makes hydrogen storage easier. As an indispensable part of CCUS the CCU is essential to combating global warming. The success of CCU depends on the ability to store significant amounts of CO_2 in the final products. As a result, the conversion of CO_2 into high-value hydrocarbons, mainly those containing two or more carbon atoms, has received a great deal of study attention (C_{2+}). Furthermore, the CO_2 transformation, which was made possible by the combination of renewable energy sources and green hydrogen, has attracted interest from all across the world and is now a top research priority. This represents a viable route to net-zero emissions, closing the carbon cycle and contribute to a sustainable future. Utilizing CCUS technology, especially CCU, it is possible to reduce CO_2 emissions while simultaneously producing valuable hydrocarbons [192], [193], [194], [195], [196], [197], like liquid fuel. To achieve this goal, it is necessary the use of a tandem catalyst made up of a "redox" metallic catalyst and an "acidic" zeolite. In this regard, it has been observed that combining FTS catalysts with zeolites to create a tandem catalysis is an efficient way to manipulate the product distribution toward desired products [198], especially in terms of liquid fuel products. In fact, by adding a zeolite to the system, light hydrocarbons, especially olefins, can be hydro processed to make more valuable products like aromatics, iso-paraffins, and iso-olefins [199]. This is in contrast to standalone metal catalysts that frequently produce low-value or restricted-range products. As it is known, iron-based materials impregnated with alkali metals are the most used as "redox" metallic catalyst and when combined with zeolite make high-octane gasoline-range [197].

As it was found, the distribution of hydrocarbons was influenced by the micropore size of the zeolites and, of course, by the different zeolite frameworks. Zeolite are aluminosilicates with cavities and molecular-sized pore topologies, boast high surface areas and shape/size selectivity, providing flexibility in their chemical compositions and the ability to accommodate different metals in their

frameworks. The versatile assembly of tetrahedra contributes to the diversity in zeolite structure, forming a three-dimensional framework consisting of cages and channels with molecular dimensions. Furthermore, the choice of zeolite for specific product selectivity is determined by the shape selective ability provided by its unique channel system and acid distributions [199], [200], [201], [202].

The International Zeolite Association (IZA) has recognized 255 types of natural and synthetic zeolite frameworks to date, assigning them three-letter codes.

Zeolites are classified based on channel dimensions, conventionally defined by the ring size of the aperture, distinguishing small pore zeolites (8-ring), medium pore zeolites (10-ring) and large-pore zeolites (12-ring). This microporous void space allows the access and diffusion of molecules with suitable sizes and shapes, known as shape-selectivity in zeolites. In some cases, the molecular dimensions of zeolite pore systems pose limitations for the access, formation, and diffusion of large molecules. Therefore, various strategies have been developed to enhance diffusion, such as increasing zeolite pore sizes, decreasing crystal size, forming single-layer zeolites (delamination), or introducing mesoporosity into zeolite crystals [54]. It is to highlight that structural characteristics of the zeolites enables to overcome challenges related to the diffusion of reactants and products within the pores, while maintaining robust resistance to deactivation by coke. In addition to zeolite topology, factors such as the type, strength, and concentration of acid sites, as well as the Si/Al atomic ratio and pore size distribution, are critical determinants of catalyst effectiveness [102], [103]. Figure 6. 1 depicts the framework of the zeolite employed in this work, that will help to discuss and understand catalytic results.

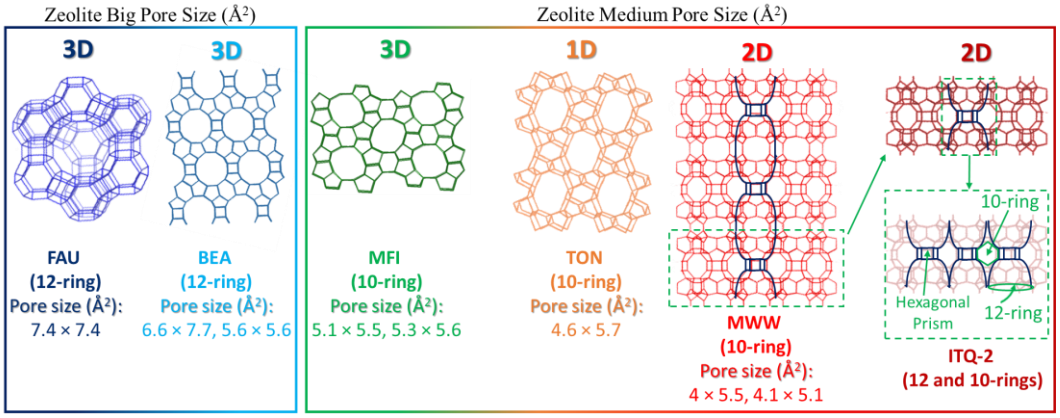


Figure 6. 1. Main characteristics of the zeolites studied in this thesis work, (framework created by 3D Drawing tool in the Database of Zeolite Structures, accessed 11 December 2023).

As it is possible to appreciate from the Figure 6. 1, this work focuses on zeolite with big pore (FAU and BEA) and zeolite with medium pore size (MFI, TON, MWW and ITQ-2). Concerning the zeolite with big pore, it is important to highlight that both zeolite are characterized by 12-oxygen rings. In particular, the FAU zeolite features tetrahedrally configured pores with a diameter of 7.4 Å. This arrangement includes large supercages at the intersection points [203].The BEA zeolite, on the contrary, presents small pore size (5.6 Å) parallel to the [001] plane, while pore size (6.6×7.7 $Å^2$) in the [100] plane [203]. The zeolite utilized in this investigation, characterized by the FAU framework, is commonly identified as USY zeolite, where USY stands for ultra-stable Y, while the zeolite featuring the BEA framework, is commonly known as BETA zeolite.

Regarding the zeolite with medium pore, the most common in CO_2 hydrogenation into liquid fuel is the MFI framework, that display an unconventional structure, featuring straight pores with cross-sectional dimensions of 5.4 × 5.6 $Å^2$ intersecting with zig-zag pores that have cross-sectional dimensions of 5.1 × 5.5 $Å^2$ [203]. Notably, it stands out as the preferred catalyst for aromatic synthesis among the solid acids utilized in the process. This preference is attributed to its well-defined three-dimensional pore system with 10-member ring channels [102], [103]. One of the key zeolites investigated in this thesis is ZSM-5 with MFI topology. Near the MFI topology was investigated the TON framework, characterized by one-dimensional silicon-rich medium-pore zeolites (10-ring), featuring pores measuring 4.6 x 5.7 $Å^2$ [203]. The zeolite with TON framework involved in this thesis is the HZSM-22.

Off course was also decided to involve a zeolite with 10-ring channels, but characterized by a two-dimensional pore system. The zeolite with MWW-type framework employed in this work is the MCM-22 zeolite. This zeolite was synthetized for the first time by Mobil researchers in the 1990s [204]. Since then, its remarkable porous structure has attracted significant attention from the scientific community. The framework of this material is characterized by two distinct pore systems, which can be accessed through 10- ring holes. One of them is three-dimensional, composed of large, cylindrical supercages (7.1 × 7.1 × 18.4 $Å^3$), with six apertures per supercage. These supercages are connected by straight and oblique channels (4.0 × 5.5 $Å^2$). Supercages are stacked on top of each other using double 6-ring openings, creating an effective barrier that prevents molecules from diffusing through. The second pore system, surrounding the double 6-ring that connects the supercages, consists of interconnected sinusoidal channels (4.1 × 5.1 $Å^2$) [205], [206], [207], [208]. Its unique properties make it very interesting for possible uses in catalysis, such as alkylations, aromatizations, methanol-to-olefin (MTO) or hydrocarbon (MTH) conversions, Fischer-Tropsch synthesis, isomerizations, and more [209].

Another zeolite studied in this work is the ITQ-2, obtained from the dealumination of MCM-22 [210], [211]. This zeolite was synthesized, for the first times, at the ITQ (Instituto de Tecnología Quimíca) in Valencia, starting from the precursor of the MCM-22 zeolite, which has an MWW-type structure. To specify, the ITQ-2 specifically comprises of thin sheets made up of a hexagon-shaped array of "cups" that can penetrate the sheet from both sides. The 12-ring that forms the aperture of these cups is around 7.0 Å in diameter. The cups come together in the middle of the layer to form a double 6-ring window that runs from bottom to top. As a result, inside the sheet, between the cups, there is a 10-ring channel system [210].

Another important aspect to taken into account is that CO_2 hydrogenation is largely dependent on the structure and acid sites of zeolite catalysts. Yet, the diffusion of reactants and products may be considerably limited by micropores. This problem can be solved by treating the zeolites with inorganic alkali salt, in order to partially dissolve silica species and form mesoporous hierarchical structures. Since their more accessible pore structure and enhanced mass transfer allow molecules and coke precursors to diffuse more easily via linked mesopores, hierarchical zeolites are commonly employed for CO_2 hydrogenation. This

increase the catalyst's activity and stability. In addition, the CO_2 adsorption capability of these zeolites is improved. In this instance, an ion exchange treatment is necessary to replace the Na^+ ions with the H^+ protons in order to counteract the load of the framework. As a matter of fact, in the case of zeolites, the oxygen atoms in the SiO_4 and AlO_4 tetrahedra are shared, and the lattice is negatively charged, countered by the ability of alkali and alkaline earth cations to flow inside the lattice channels. It is possible to substitute these counterions from the bridge Al(OH)Si (Brønsted acid sites) with other cations, including H^+ [197].

This study focuses on investigating the synergistic effects of 1NaFe catalysts with various zeolite frameworks in a dual bed configuration for thermocatalytic CO_2-Fischer-Tropsch conversion into gasoline. By systematically exploring the influence of different zeolite frameworks on catalyst performance, this research uses 1NaFe as the active phase in all catalytic experiments (synthesis and reactor charging methodology reported in Chapter 2). The first part of the work is looking at large-pore zeolites with different structures, mainly FAU and BEA (also known as USY24 and BEA17). The objective is to investigate the impact of desilication on the two zeolites, USY15M and BEA17M, synthesis detailed in Chapter 2. This study examines how acidity affects the distribution of hydrocarbon products in FAU zeolite (USY). Specifically, they were investigate several FAU zeolites with varying Si/Al ratios, denoted as USY24, USY13, and USY5. Some of the zeolites that are looked at in the second part of the study are MFI (MFI27), MFI17M (for less silica), H22-32 (for TON zeolite), M22-20 (for MWW), and ITQ2-18 (for ITQ-2). In all cases, the aim was to evaluate and compare the data within a brief timeframe of 1-2 hours on stream, taking into account the tendency of several zeolites to undergo deactivation within a few hours of catalytic testing.

The catalysts employed in this study are summarized in the following table (Table 6. 1) additional information are instead reported in paragraph 2.4.

Table 6. 1. Name used in this chapter and additional information of each zeolite.

Name used	IZA code	Additional information
USY24	FAU	Y zeolite purchased by Zeolyst International with the following code: CBV760
USY15M	FAU	Desilicated CBV760[a]
USY13	FAU	Y zeolite purchased by Zeolyst International with the following code: CBV720
USY5	FAU	Y zeolite purchased by Zeolyst International with the following code: CBV712

BEA17	BEA	BETA zeolite purchased by Zeolyst International with the following code: CP814C
BEA17M	BEA	Desilicated CP814C [b]
MFI27	MFI	H-ZSM-5 zeolite purchased by Zeolyst International with the following code: CBV5524G
MFI17M	MFI	Desilicated CBV5524G [c]
Z22-32	TON	H-ZSM-22 zeolite purchased by ACS material
M22-20	MWW	MCM-22 zeolite synthetized at ITQ [d]
ITQ2-18	-	ITQ-2 zeolite synthetized at ITQ for delamination of MCM-22 [d]

[a] Synthesis details are provided in Chapter 2, Paragraph 2.4.2;
[b] Synthesis details are provided in Chapter 2, Paragraph 2.4.3;
[c] Synthesis details are provided in Chapter 2, Paragraph 2.4.2 (utilizing the same method employed for the desilication of μMFI35);
[d] Synthesis details are provided in Chapter 2, Paragraph 2.4.4.
In addition, to better understand the different properties of the zeolites involved in, the characterization have been divided into physical and chemical analysis, not only to simplify the discussion, but also to help with the understanding.

In addition, since the active phase involved in this study is always 1NaFe, for simplicity, only the name of the zeolite involved will be reported in the catalytic tests.

6.2. Results and discussions

6.2.1 Catalysts characterization

As extensively discussed in the first chapter and emphasized in the introduction of this chapter, the production of various liquid hydrocarbons through CO_2 hydrogenation via the RWGS and FTS reaction mechanisms can be influenced by the different frameworks of the zeolites. Therefore, this study considered several zeolites with 12- and 10-ring channels. First of all, however, some basic characterizations of the iron-based catalyst 1NaFe, essential for the RWGS reaction, are illustrated.

6.2.1.1 Characterization of bulk iron impregnated with sodium: 1 NaFe

The 1NaFe catalyst underwent a series of basic characterizations to verify the success of its synthesis and evaluate its catalytic properties. It was obtained by the impregnation of Fe_3O_4 as descripted in Chapter 2.

Before beginning the experimental campaign, it was evaluated the sodium and iron content with ICP-OES analysis. As expected, the 1NaFe sample showed a 1 wt.% sodium content, Table 6. 2.

Table 6. 2. Chemical analysis of bulk iron catalyst impregnated with Na.

Sample	Fe (wt%)	Na (wt%)	Na/Fe at. ratio
Fe_3O_4	72.17	0	0
1NaFe	70.49	1.09	0.038

Additionally, we investigated the textural properties of the Fe_3O_4 and 1NaFe catalysts using N_2 adsorption. As reported in Table 6. 3 both catalysts show a good surface area, around 99 $m^2 \cdot g^{-1}$ for the Fe_3O_4 and around 81 $m^2 \cdot g^{-1}$ for the sodium-impregnated sample. The impregnation of Fe_3O_4 with Na likely caused the total pore volume to decrease from 0.36 to 0.31 $cm^3 \cdot g^{-1}$, following the same trend. However, the mean pore diameter remained around 12 nm, showing no significant changes.

Table 6. 3. Textural properties of bulk iron impregnated with Na measured by N_2 physisorption.

Sample	A_{BET} ($m^2 \cdot g^{-1}$)	V_T[a] ($cm^3 \cdot g^{-1}$)	D_p[b] (nm)
Fe_3O_4	98.67	0.36	11.94
1NaFe	80.58	0.31	12.20

[a] Single point adsorption total pore volume of pores less than 2217.660 Å diameter at P/Po = 0.991291740
[b] BJH Adsorption average pore diameter (4V/A).

In addition, it was evaluated the crystalline structure of 1NaFe, compared with its counterpart Fe_3O_4. The X-ray diffraction (XRD) pattern of the fresh samples clearly show peaks attributable to the Fe_3O_4 phase (Figure 6. 2 a). In particular, the peaks at 30.1°, 35.5°, 43.1°, 57.0°, and 62.6° (JCPDS No. 89-3854) correspond to the crystal planes (200), (103), (004), (321), and (224), respectively, and are clearly distinguishable. However, focusing on the 1NaFe sample no sodium diffraction peaks are present, indicating that the sodium is well dispersed. In addition, it was performed the XRD analysis on the 1NaFe spent catalyst, that, as

seen in Figure 6. 2 b), is predominantly characterized by peaks ascribable to Fe_2C_5 (JCPDS No. 89-2544) and Fe_3O_4 phases. These phases, Fe_2C_5 and Fe_3O_4, are known to be the active components responsible for the conversion of CO_2 into hydrocarbons by hydrogenation [97], [103], [110], [119], [156].

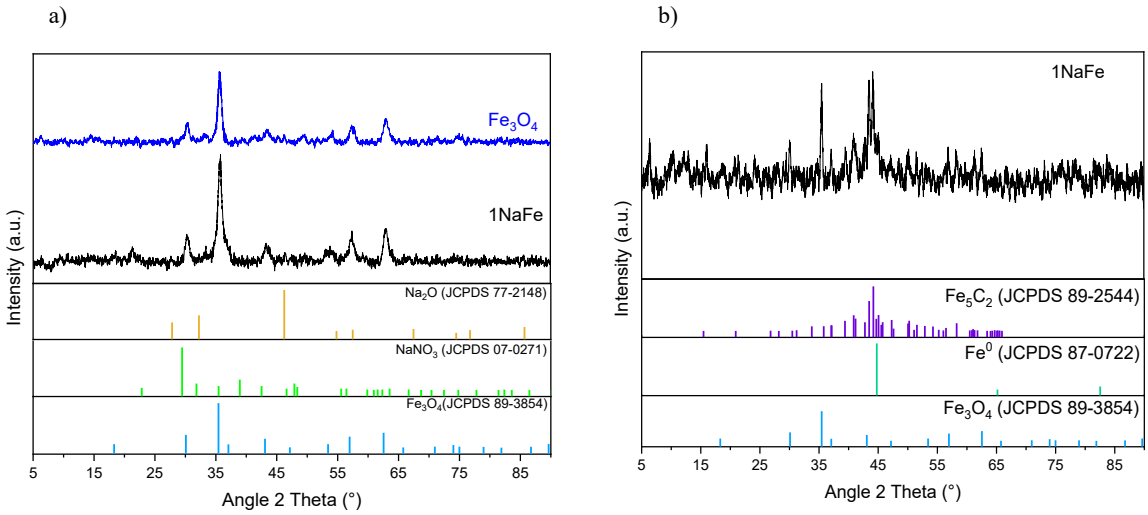


Figure 6. 2. XRD pattern of a) fresh of Fe_3O_4 and 1NaFe catalysts and b) spent of 1NaFe catalyst.

In addition it was calculated the crystallite size by taking into account the most intense peak at 35.5°, using the Scherrer equation (equation description reported in Chapter 2). It was found that the crystallite size was 11 nm for bulk iron without sodium (Fe_3O_4) and 14 nm for bulk iron impregnated with sodium (1NaFe), Table 6. 4.

Table 6. 4. Fe_3O_4 crystallite size of bulk iron catalysts.

	Cristallite size Fe_3O_4 (nm)
Fe_3O_4	11
1NaFe	14

All the catalytic tests of this Chapter were carried out using the 1NaFe catalyst, which did not require further characterizations due to its well-documented synthesis and catalytic properties in the literature [97], [110], [119], [212], [213]. This work is mostly focused on the performance of zeolites with different structures in the production of liquid hydrocarbons.

6.2.1.2 Characterization of zeolites

Before delving into a comprehensive analysis of the zeolite characterization in this study, it is crucial to provide a brief explanation of the names used to distinguish the various types of zeolite and reported in Table 6. 1. First of all, it is important to highlight the IZA code and conventional name. This combination was inspired by a desire to define the catalyst using only three letters while also ensuring a clear identification of the actual framework. In fact, it is known that the FAU zeolite could refire both on Y and X zeolites. Hence the decision to proceed using the name USY, followed by the Si/Al ratio found by the ICP-OES analysis. The sample's name, ending in M, corresponds to the desilicated sample. Also, for the zeolites with TON and MWW structures, it was decided to use another code to identify the zeolite used. The lack of a corresponding IZA code for the sample ITQ-2 necessitated the use of an alternative acronym.

6.2.1.3 Chemical-physical properties of the zeolite

The process of converting long-chain hydrocarbons derived from CO_2 hydrogenation via the RWGS and FTS reaction mechanisms in a series of zeolite beds leads to different product distributions depending on the topology structures of zeolites [193], [212]. In addition the catalytic stability could be affected by crystal morphology [110], [214]. Taking this into account, this chapter examines six zeolites with 12-ring channels (USY24, USY15M, USY13, USY5, BEA17, and BEA17M) and five zeolites with 10-ring channels (MFI27, MFI27M, Z22-32, M22-20, and ITQ2-18).

Table 6. 5 provides the chemical composition and textural properties of all calcined zeolites. The ICP-OES test showed that the desilicated samples (USY15M, BEA17M, and MFI17M) had lower Si/Al molar ratios than the zeolites (USY24, BEA17, and MFI27). The desilication process, always applied to the original zeolites, consistently results in a higher mesoporous area for the desilicated materials, leading to an increase in the area BET (Table 6. 5). However, the desilicated zeolite showed a lower micropore volume, again due to the formation of mesopores against micropores. Also, the ITQ-2 sample showed a higher BET surface area than MCM-22, which, as could be seen, is mostly due to the contribution of the larger external surface area as an effect of the delamination [215]. To support these results, the N_2 physical adsorption/desorption isotherm

curves and pore size distributions of all the different zeolite structures involved are shown in Figures A2.1–A2.5.

Table 6. 5. Chemical analysis and textural properties of zeolites.

Sample	ICP-OES	N_2-adsorption			
	Si/Al at. ratio	A_{BET} ($m^2 \cdot g^{-1}$)	A_{micro} ($m^2 \cdot g^{-1}$)[a]	A_{meso} ($m^2 \cdot g^{-1}$)[b]	V_{micro} ($cm^3 \cdot g^{-1}$)[c]
USY24	24.2	753	506	247	0.25
USY15M	15.3	856	382	474	0.19
USY13	13.2	769	553	216	0.27
USY5	5.4	688	521	167	0.26
BEA17	17.3	577	504	73	0.25
BEA17M	16.8	684	321	363	0.16
MFI27	27.2	380	338	42	0.17
MFI17M	17.2	495	220	272	0.11
Z22-32	31.8	237	194	43	0.10
M22-20	19.8	426	347	79	0.17
ITQ2-18	17.9	632	259	373	0.12

[a] t-plot Micropore Area ($m^2 \cdot g^{-1}$);
[b] t-plot External Surface Area ($m^2 \cdot g^{-1}$);
[c] t-plot micropore Volume ($cm^3 \cdot g^{-1}$).

The XRD patterns show the characteristic diffractograms of all the zeolites involved in this work, revealing well-crystalline frameworks and high purity, with no other crystalline phases observed (Figure 6. 3). However, the ITQ2-18 sample evidences some peaks typical of the M22- structure, though with lower intensity, due to the incomplete delamination during the delamination process of the layered MCM-22 precursor.

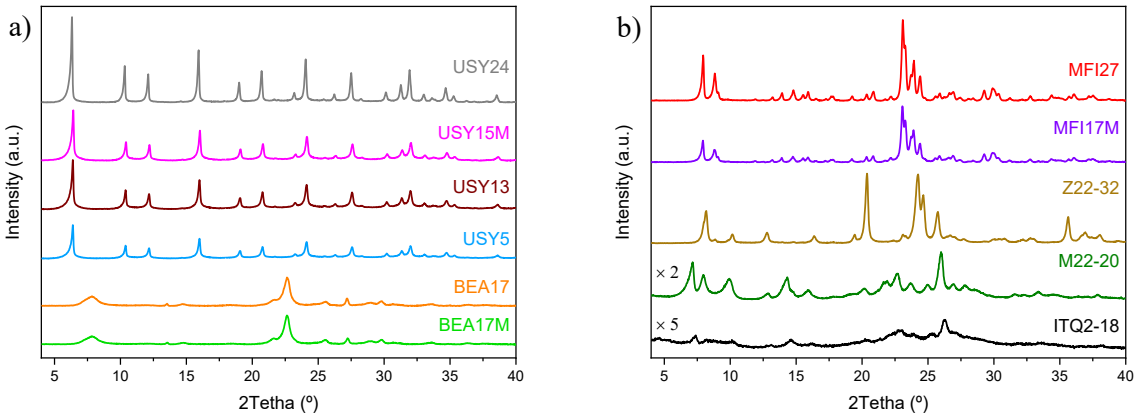


Figure 6. 3. XRD profiles of a) zeolites with 12-ring channels and b) zeolites with 10-ring channels.

Furthermore, the loss of crystallinity for desilicated samples (USY15M, BEA17M, and MFI17M) compared to their counterpart zeolites (USY24, BEA17, and MFI27) was calculated and is reported in Table 6. 6. Specifically, the loss of crystallinity for each sample was determined from integrated peak areas at specific angles (2θ). For instance, the loss of crystallinity of USY15M was determined from peak areas at 21° and 24° (2θ) compared to the counterpart zeolite USY24. The loss of crystallinity of BEA17M was determined from the integrated peak areas at 7.7°, 21.5°, 22.6°, and 25.5° (2θ) and compared with the counterpart zeolite BEA17. Similarly, the loss of crystallinity of MFI17M was determined from the integrated peak areas at 8°, 8.8°, 23.1°, and 24.4° (2θ) and compared with the counterpart zeolite MFI27.

Table 6. 6. Loss of crystallinity of mesoporous zeolites.

Sample	Loss of crystallinity (%)
USY15M	11
BEA17M	5
MFI17M	19

Acidic zeolites play a crucial role in directing reaction pathways and impacting product distribution [214], [216]. NH_3-TPD analysis was employed to assess the acid properties of different zeolite structures, with profiles shown in Figure 6. 4.

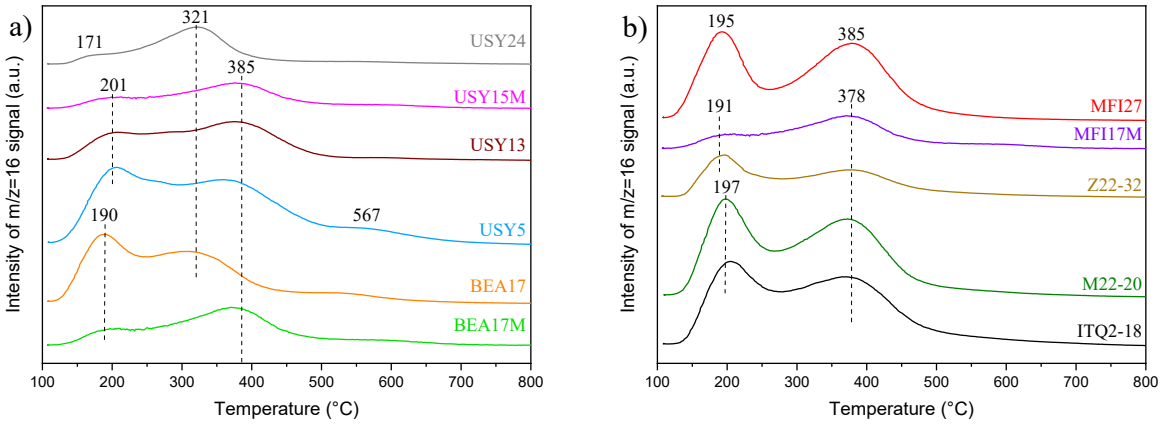


Figure 6. 4. NH_3-TPD profiles of a) zeolites with 12-ring channels and b) zeolites with 10-ring channels.

The desorption peak temperature reflects acid intensity, while peak area signifies acid content, detailed in Table 6. 7. Low-temperature desorption peaks (100-290 °C) indicate weak acid centers, whereas high-temperature peaks (290-570 °C) denote strong acid centers. Gaussian fitting reported on the Appendix 1, Figure A2.6 reveal three ammonia desorption peaks, indicative of weak, medium-strong, and strong acid centers. Medium-strong acid centers are predominantly situated on the outer surface, while strong acid centers primarily reside at pore intersections.

Table 6. 7. Zeolite Acidity Determined by TPD-NH_3.

Sample	Weak acid sites (µmol/g)	Medium acid sites (µmol/g)	Strong acid sites (µmol/g)	Total acid sites (µmol/g)
USY24	49	-	213	262
USY15M	69	-	230	300
USY13	70	95	258	423
USY5	97	93	351	542
BEA17	159	-	457	616
BEA17M	237	-	447	684
MFI27	219	-	391	610
MFI17M	201	-	255	456
Z22-32	178	-	216	394
M22-20	178	-	343	521
ITQ2-18	132	-	339	471

Further characterization of acidic properties was conducted using pyridine as a probe molecule. Py-IR analysis at various temperatures (250 °C, 350 °C, and 400 °C) revealed Brønsted and Lewis acid sites, Figure A2.7-A2-17. IR absorption peaks at 1545 cm^{-1} and 1445 cm^{-1} correspond to pyridine chemisorption on Brønsted and Lewis acid sites, respectively, while the peak at 1490 cm^{-1} indicates chemisorption on both sites. The distribution of Brønsted and Lewis acid sites is presented in Table 6. 8.

Table 6. 8. Acidity of zeolites determined by IR-pyridine (µmol py·g^{-1}), at different pyridine desorption temperatures.

Sample	Brønsted			Lewis		
	250 °C	350 °C	400 °C	250 °C	350 °C	400 °C

USY24	120	65	46	19	12	11
USY15M	91	65	24	39	22	17
USY13	173	95	58	50	32	24
USY5	234	166	71	66	38	29
BEA17	248	202	125	60	58	55
BEA17M	206	140	60	98	89	77
MFI27	295	230	169	25	21	18
MFI17M	191	135	79	118	90	77
Z22-32	107	71	33	13	7	5
M22-20	187	157	121	35	29	26
ITQ2-18	112	78	31	38	25	24

Characterization via ^{27}Al MAS NMR was utilized to assess aluminum coordination in the final acid solids. Most aluminum species exhibit tetrahedral coordination, evidenced by the intense band centered at 50–55 ppm in the ^{27}Al MAS NMR spectra (Figure 6. 5).

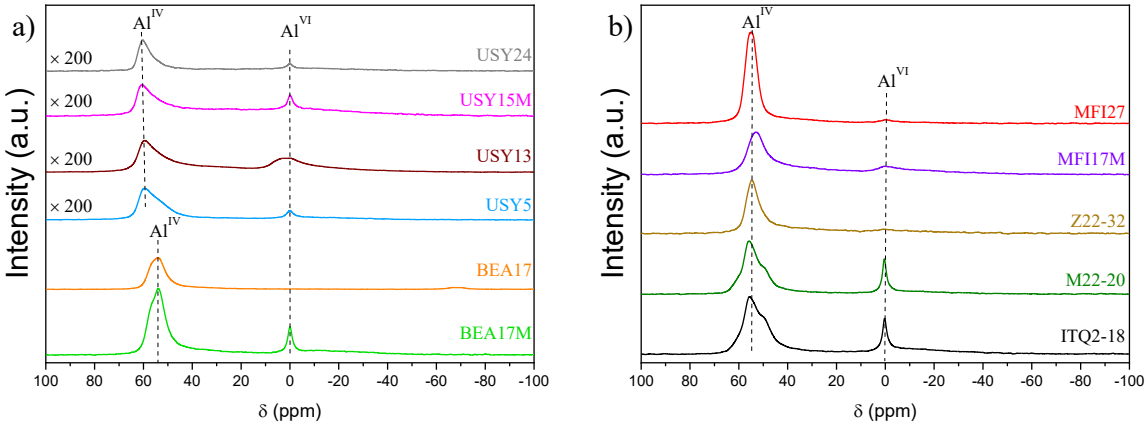


Figure 6. 5. ^{27}Al MAS NMR spectra of fully hydrated zeolites: a) zeolites with 12-ring channels and b) zeolites with 10-ring channels.

However, a smaller band at 0 ppm shows that octahedrally coordinated Al (Al^{VI}) is present in extraframework positions (EFAL) in all zeolites (about 0-40%, Table 6. 9). Comparing desilicated samples with their counterparts reveals an increase in EFAL content. For instance, in USY15M zeolite, EFAL constitutes 40%, compared to 37% in the counterpart USY24 zeolite. This trend is consistent for BEA17M and MFI17M zeolites.

Table 6. 9. Percentage of extraframework and framework Al estimated from ^{27}Al MAS NMR (FAL = framework Al, EFAL = extraframework Al).

Sample	EFAL (%)	FAL (%)
USY24	37	63
USY15M	40	60
USY13	33	67
USY5	60	40
BEA17	0	100
BEA17M	26	64
MFI27	7	93
MFI17M	25	65
Z22-32	16	84
M22-20	26	74
ITQ2-18	30	70

The EFAL amount for the USY zeolites was also calculated using the Jorik equation, as detailed in Chapter 2, and the results are reported in Table 6. 10. The %EFAL values were very close to the values found by ^{27}Al MAS NMR, confirming the results found by spectroscopy.

Table 6. 10. XRD-based framework and extraframework composition of USY-type zeolites.

Zeolite	a_0 (Å)	Si/Al$_F$[a]	N_{FAL}[b]	N_{EFAL}[b]	$N_{FAL+EFAL}$	%EFAL
USY24	24.266	33.9	5.5	2.1	7.6	27.8
USY15M	24.260	38.1	4.9	6.7	11.6	57.8
USY13	24.298	20.9	8.7	4.8	13.5	35.3
USY5	24.345	13.2	13.5	16.2	29.7	54.5

[a] Framework Si/Al atomic ratio.

[b] N_{FAL} and N_{EFAL} are the number of framework and extraframework Al atoms, respectively. N_{FAL} was determined from the unit cell size parameter (a_0) using the correlation reported by Jorik and co-workers [130].

6.3. Catalytic tests

6.3.1 Influence of catalytic bed configuration: granule mixing versus dual bed

As stated in the introduction, all performance evaluations of medium- and large-pore zeolites were carried out over 1NaFe+zeolite (DB) system combining the metallic component with the chosen zeolite in a dual bed arrangement, and with a mass ratio of 1:1. Under the specified experimental conditions: 2.0 MPa,

340 °C, H_2/CO_2=3, and 19.2 $L \cdot g^{-1} \cdot h^{-1}$, at a time on stream of 27 h (Chapter 2 provides a detailed description of the reactor loading mode). The decision to carry out all the tests in dual bed mode was made in order to avoid the risk of sodium migration from iron to the acidic sites of the zeolite, which has been thoroughly examined in Chapters 3, 4, and 5. However, prior to starting the experimental campaign, the 1NaFe catalyst was tested alone to ensure consistency. This was achieved by resembling a dual bed mode using SiC, as outlined in Chapter 2. Figure A2. 18 documents the findings from the 27-hour experiment. Subsequently, in order to guarantee clarity, an experiment was conducted using the 1NaFe catalyst and the zeolite USY24 in two distinct contact modes: granule mixing and dual bed Figure 6. 6, where it appears evident that the catalytic properties of the iron-based catalyst impregnated with sodium decrease over time when investigated in close proximity to the zeolite (granule mixing). This decline is caused by a reduction in the acidic sites of the zeolite and a loss of iron promotion, which ultimately impacts the catalytic properties [90], [97], [104], [106]. During the 27 h test of the granule mixing catalyst, an increase in CO and CH_4 selectivity and a decrease in conversion over time were observed. Nevertheless, these alterations were virtually non-existent during the dual bed test due to the separation of the zeolite and the sodium-impregnated iron-based catalyst (1NaFe) in dual bed mode.

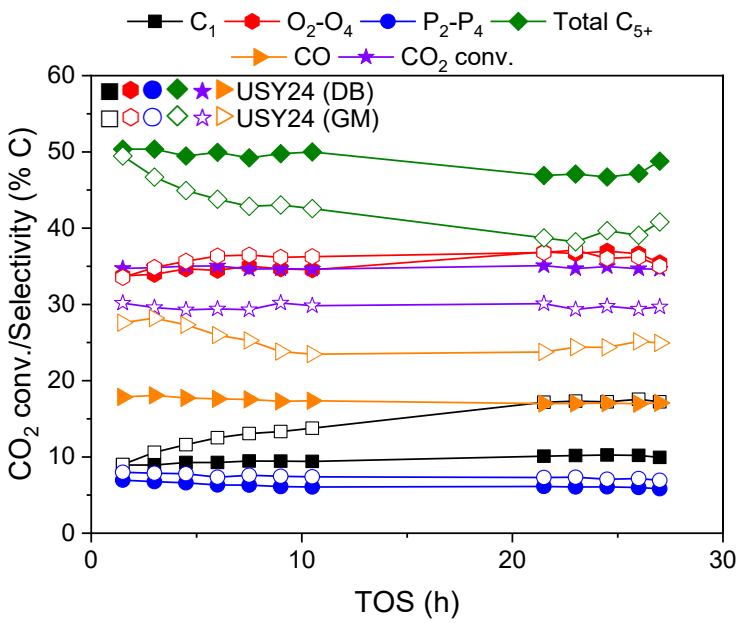
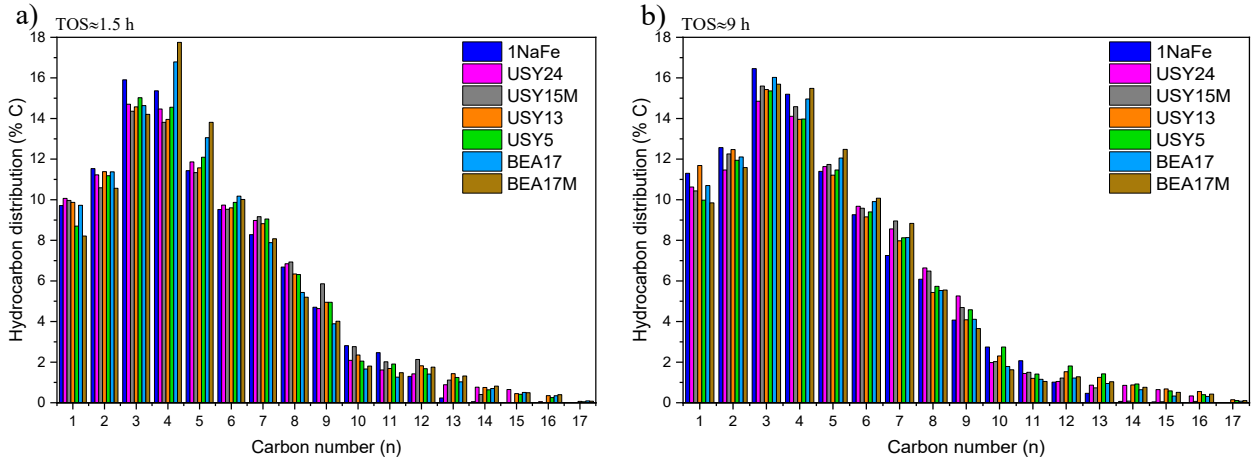


Figure 6. 6. TOS monitoring of 1NaFe tested in two different configurations: dual bed (DB, full symbols) and granule mixture (GM, empty symbols).

As a result, the decision was reached to proceed with the investigation of the various zeolite structures through experiments in dual bed mode.

6.3.1.1 Effect of 12-ring zeolites tested in dual bed mode

As anticipated in the introduction, comparisons between the catalytic tests were made over short time on stream (~1.5) due to the rapid deactivation of some zeolite structures caused by coke deposition and lose of acid sites. Focusing on the large-pore zeolites (12-ring), it can be observed from Figure 6. 7 that there are no significant variations in carbon number product distribution comparing the standalone 1NaFe with the 1NaFe catalyst tested in dual bed mode with large-pore zeolite. Looking to the Figure 6. 7, the only noticeable differences are seen in the case of BEA17 zeolite and in its desilicated form, which show a higher selectivity of approximately 3-4% for C_4 and C_5 hydrocarbon chains at 1.5 h of TOS compared to the standalone 1NaFe catalyst. This could be attributed to the ability of BEA-type zeolites to undergo cracking of longer hydrocarbon chains. However, this effect seems to disappear after 9 h of catalytic testing, probably due to the deactivation of some catalytic sites caused by coke formation. There is no evidence when FAU zeolite is involved, neither when desilication is introduced in the zeolite or when its acidity varies in terms of carbon number product distribution.



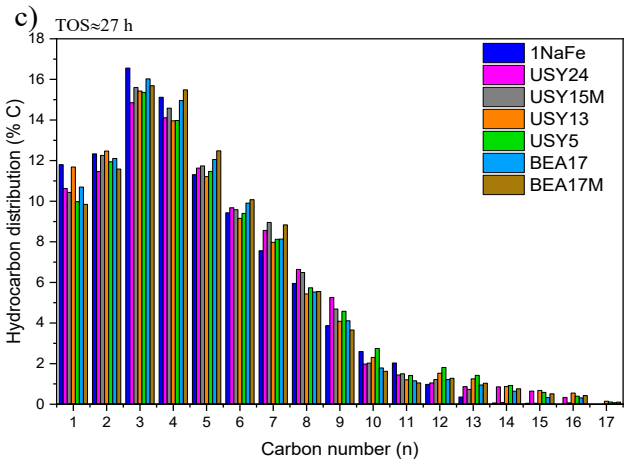


Figure 6. 7. Product distribution calculated after 1.5 h (a), 9 h (b) and 27 h (c) over time on stream, for carbon number of standalone 1NaFe and 1NaFe combined in dual bed mode with 12 MR zeolites: USY24, USY15M, USY13, USY5, BEA17 and BEA17M.

To better understand the subtle differences between the various zeolitic frameworks, each structure needs to be compared to the sole active phase. Also in this case, the comparison was made after 1.5 h and after 9 h of catalytic testing. The iron catalyst used alone (located in the first column on the left, as shown in Figure 6. 8, a) resulted in a CO_2 conversion of 35 %, with a selectivity towards methane (CH_4), light olefins (O_2–O_4), paraffin (P_2–P_4), long-chain hydrocarbons (C_{5+}), and CO selectivity of 9, 32, 8 and 51 % respectively. The CO_2 conversion rate remained very constant in all instances (35-33 %), indicating that none of these zeolites has the ability to activate CO_2. Figure x does not exhibit significant alterations in hydrocarbon distributions. To accentuate the impact of the zeolite on hydrocarbon distributions, Figure 6. 8 b) specifically displays the changes in selectivity for each hydrocarbon component in relation to the standalone 1NaFe catalyst. Most zeolites (Figure 6. 8, a) boost the selectivity of lighter olefins O_2-O_4 by around 10-13%, respectively for BEA17 and BEA17M, this trend is quite reduced after 9 h yet Figure 6. 8 c) and d) and accentuated after 27 h as it is possible to appreciate from Figure 6. 8 e) and f). However, these results are not surprising because based on a review of several literature sources, it can be inferred that BEA and FAU zeolite have hydrocracking activity on heavy hydrocarbons, resulting in the production of lighter hydrocarbons [196], [199].

a) b)

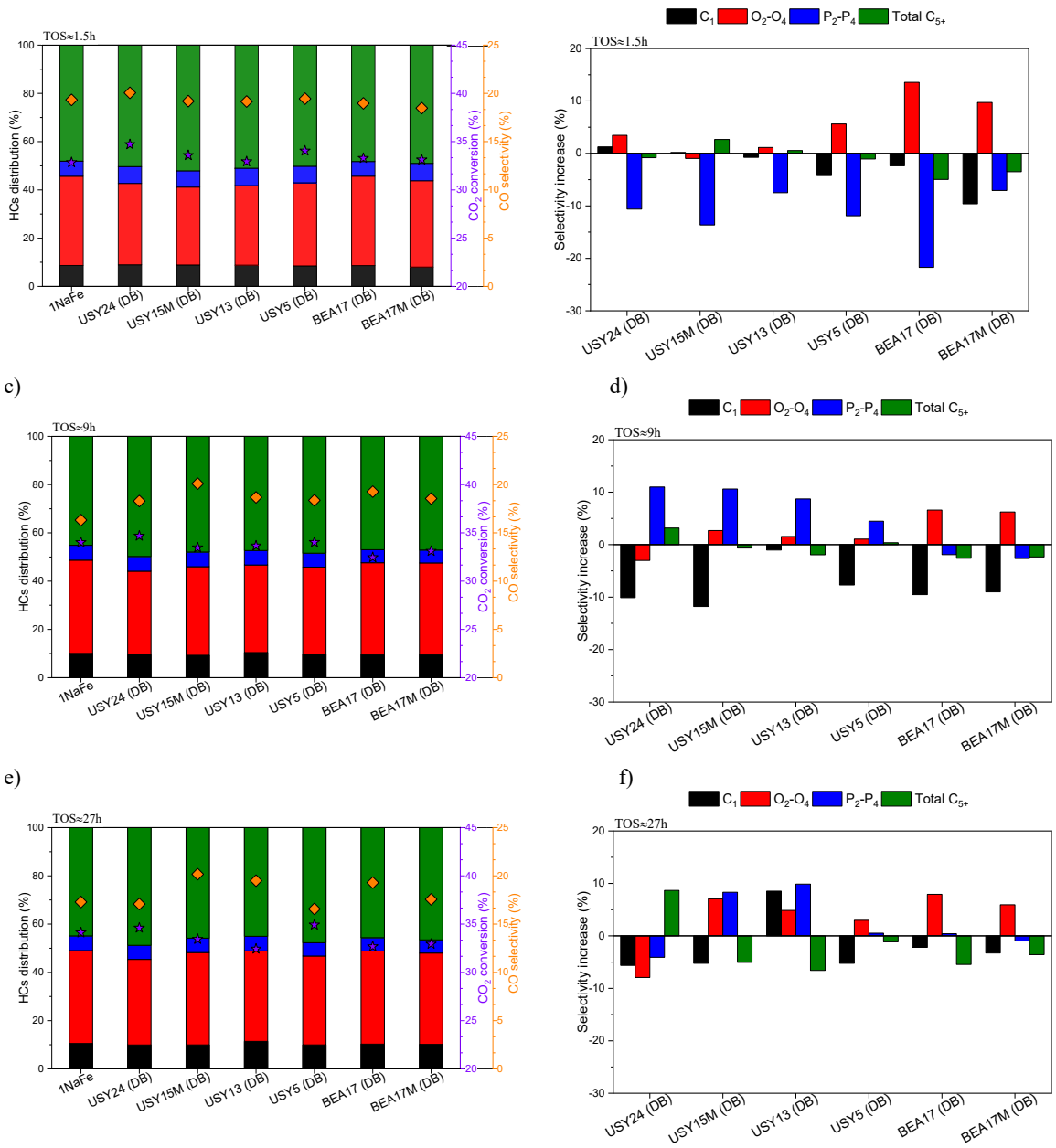


Figure 6. 8. a), c) and d) A comparison of catalytic data obtained with various zeolites; b), d) and e) explanation in detail of the (net) increase (or decrease) in selectivity of specific hydrocarbon groups when zeolites are introduced in comparison to the 1NaFe catalyst used alone. Reaction parameters include 2.0 bar, 340 °C, H_2/CO_2 = 3, and 19.2 $L \cdot g^{-1} \cdot h^{-1}$, with a time on stream of 27 h.

Based on the obtained results, it is evident that, when comparing the tests conducted at 1.5 hours of catalytic testing, the inclusion of large-pore zeolites does not lead to a significant change in the distribution of hydrocarbons compared to

the individual testing of the 1NaFe catalyst. However, there is a slight decrease in C_{5+} compounds, except for the USY15M sample. As a result, it is unsurprising that gasoline synthesis over time exhibits a generally reduced yield of C_5-C_{11} compounds when employing zeolite catalysts, with the exception of the USY15M zeolite. However, despite these conditions, we observe a decrease in gasoline production after 20 h of the reaction (Figure 6. 9). This finding is consistent with other studies that have shown that enlarging the pore diameters of zeolites greatly enhances the movement of reactants and intermediates, leading to more effective hydroprocessing. As a result, the improved mass transfer facilitates the effective removal of products from the catalyst, minimizing further interaction with intermediates and reactants and enhancing the overall efficiency of the process [217].

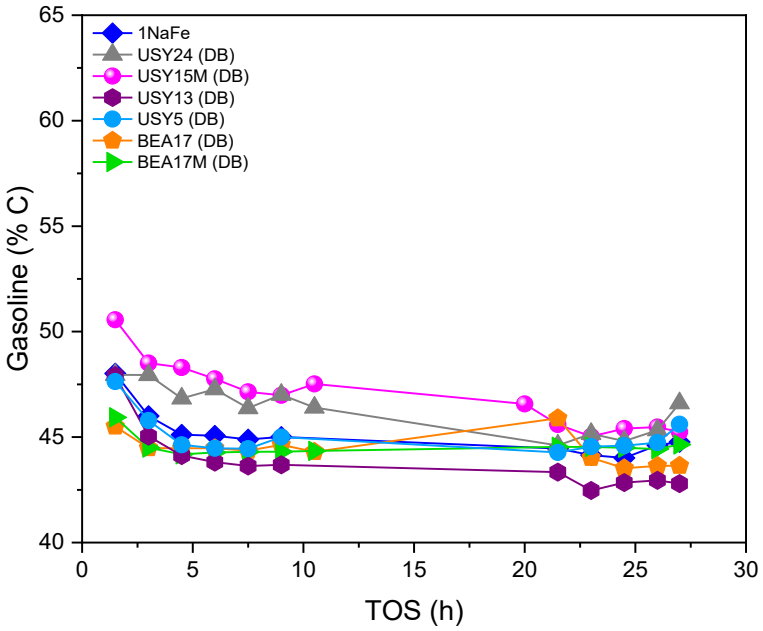


Figure 6. 9. Product selectivity to gasoline product (C_5-C_{12}) over zeolite with large-pore-size. Reaction parameters include 2.0 bar, 340 °C, H_2/CO_2 = 3, and 19.2 $L \cdot g^{-1} \cdot h^{-1}$, with a time on stream of 27 h.

According to the previously shown data, it is evident that zeolites with large-pore do not have the potential to combine short hydrocarbon chains into oligomers. Hence, it is necessary to assess their capacity for aromatization and

isomerization. In this scenario, distinctions are taken into account at brief time intervals to prevent potential deactivation caused by the development of coke. Figure 6. 10 depicts the amount of aromatic compounds found in the C_{5+} fraction. The varying acidity levels of zeolites with FAU structures have a minimal impact on the creation of aromatic chemicals. However, desilication seems to promote the process of aromatization. Using USY15M zeolite leads to a 19 % rise in aromatic content compared to C_{5+} compounds, which is around a 3 % increase compared to the typical FAU zeolite utilized in this study. When examining zeolites with a BEA structure, it is seen that there are no substantial differences in the amount of aromatic compounds present between conventional and desilicated zeolites.

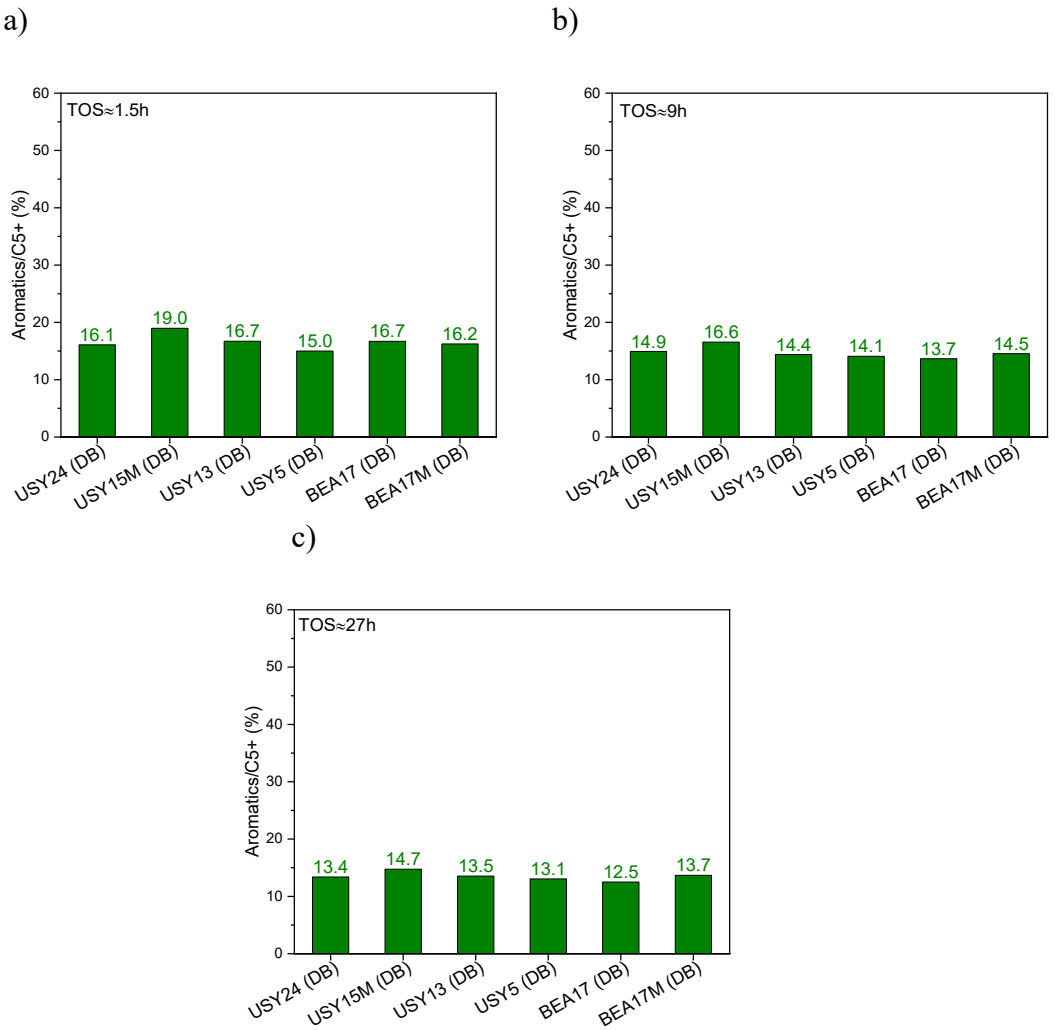


Figure 6. 10. Effect of zeolite topology over aromatics selectivity calculated in the C_{5+} fraction. Results reported: a) beginning of TOS (1.5 h), b) middle of the TOS (9 h), c)

end of the TOS (27 h). Reaction parameters include 2.0 bar, 340 °C, H_2/CO_2 = 3, and 19.2 $L \cdot g^{-1} \cdot h^{-1}$, with a time on stream of 27 h.

The exceptional capability of large-pore zeolites to isomerize is highlighted by their impressive propensity to produce branched C_5 compounds, as seen in Figure 6. 11. How it is possible to appreciate, a very low amount of branched hydrocarbons were produced over the base catalyst alone (1NaFe). The formation of branched hydrocarbons drastically increased on addition of the zeolite to the iron bulk catalyst, particularly at the initial reaction stages. After a thorough examination of the graph, it is evident that both USY and BEA zeolites demonstrate, at the beginning of the test, a significant degree of isomerization. However, the capacity of USY zeolites declines as acidity increases, reaching its maximum with zeolite USY15M. This suggests that desilication has a role in enhancing the preference for producing branched products. The same phenomenon is found in the case of BEA17 zeolite, and particularly in its desilicated form, BEA17M, which exhibits a similar pattern to the one observed between ordinary USY24 and its desilicated version. Nevertheless, although large-pore zeolites have a remarkable capacity for isomerization, a thorough examination of the trend over time reveals a fast decline in branching C_{5+} chains, even in the first phases of the reaction, most likely attributable to zeolite deactivation. The existence of the supercages in the USY zeolites lead to a faster deactivation compared to BEA-type zeolites, making this phenomenon particularly noticeable in FAU zeolite.

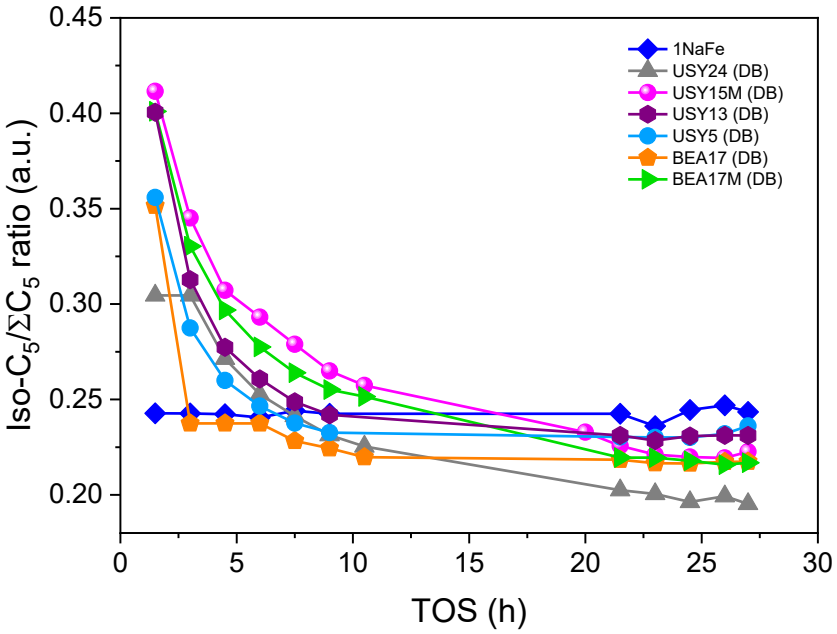


Figure 6. 11. Effect of different zeolite frameworks with 12-ring on the isomerization of C_5 compounds. Reaction parameters include 2.0 bar, 340 °C, H_2/CO_2 = 3, and 19.2 $L \cdot g^{-1} \cdot h^{-1}$, with a time on stream of 27 h.

Upon evaluating the profiles during the 27-hour reaction (Figure 6. 12), it is evident that there are no abrupt fluctuations in terms of conversion and selectivity towards CO, CH_4, O_2-O_4, P_2-P_4, and C_{5+}, as previously emphasized. Large-pore zeolites do not have a substantial capacity to change the arrangement of carbon atoms in comparison to sodium. Instead, what differs is their capability to isomerize, which diminishes with time as a result of zeolite deactivation produced by the development of coke. This limits the number of active sites on the zeolite.

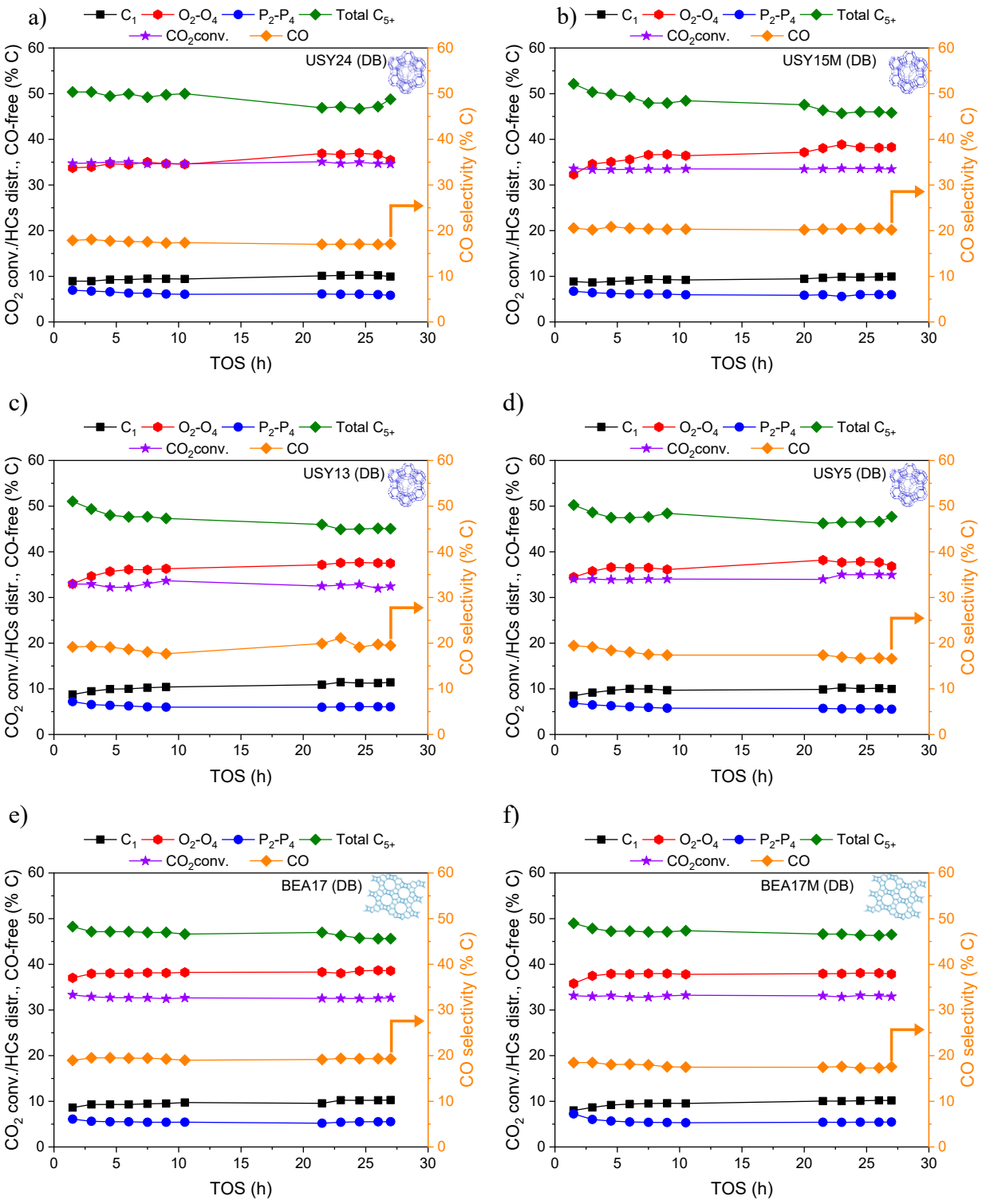


Figure 6. 12. Catalysts activity and products distribution over 1NaFe tested in dual bed mode with large-pore size zeolite: a) USY24, b) USY15M, c) USY13, d)USY5, e)

BEA17 and f) BEA17M. Reaction parameters include 2.0 bar, 340 °C, H_2/CO_2 = 3, and 19.2 $L \cdot g^{-1} \cdot h^{-1}$, with a time on stream of 27 h.

6.3.1.2 Effect of 10-ring zeolites tested in dual bed mode

Given these factors, the attention has been redirected towards investigating medium-pore zeolites. The MFI-type framework is highly popular because of its renowned capacity to oligomerize, isomerize, and aromatize, which makes it an exceptional choice for gasoline production. Furthermore, the impacts of two-dimensional (MCM-22 and ITQ-2) and one-dimensional structures zeolite (ZSM-22), namely respectively M22-20, ITQ2-18 and Z22-32, will be assessed alongside the three-dimensional zeolitic structure. The data on liquid fuel production using medium-pore zeolites (10-ring) clearly demonstrates that zeolites with an MFI-type framework significantly enhance the yield of gasoline compared to using only bulk phase 1NaFe (Figure 6. 13). A comparison between conventional MFI27 zeolite and its desilicated counterpart, MFI17M (synthesis reported in Chapter 2), reveals a 2% increase in gasoline production with desilicated MFI17M zeolite. Specifically, there's a shift from around 59 % for standard MFI27 to 61 % for desilicated MFI17M. Moreover, zeolites incorporating this framework exhibit remarkable stability during a 27-hour time-on-stream (TOS) period. Further examination of Figure 6. 13 shows that 10-ring zeolites exhibit a significant increase in gasoline production compared to using only the active phase 1NaFe, especially in the initial stages of the catalytic experiment. For instance, after 1.5 hours of reaction time, M22-20 demonstrates a benzene selectivity of approximately 52.5%; in its delaminated form (ITQ2-18), this selectivity up to 53%. However, both instances show an abrupt decline in selectivity after three hours of TOS. A similar trend is observed for zeolite Z22-32.

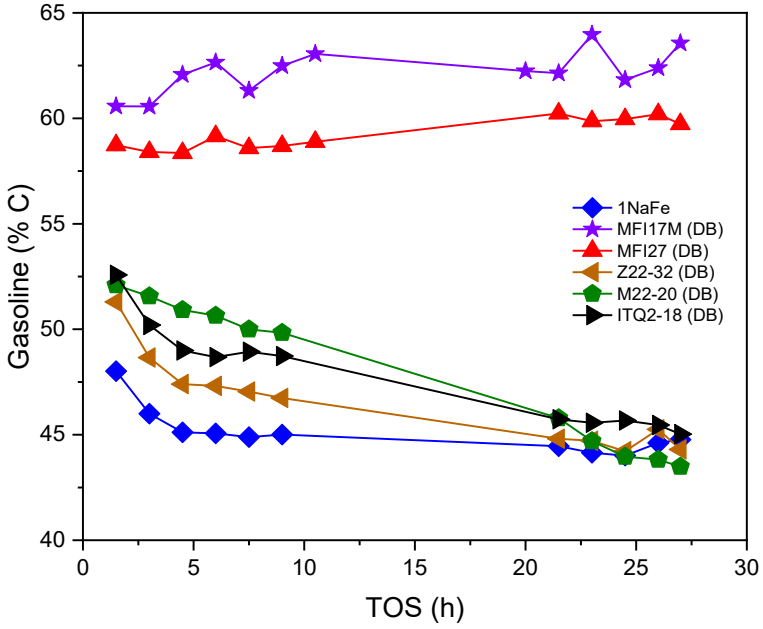


Figure 6. 13. Product selectivity to gasoline product (C_5-C_{12}) over zeolite with medium-pore-size. Reaction parameters include 2.0 bar, 340 °C, H_2/CO_2 = 3, and 19.2 $L \cdot g^{-1} \cdot h^{-1}$, with a time on stream of 27 h.

As it is possible to appreciate from Figure 6. 14 (a), after 1.5 hours of reaction time, the conventional MFI27 zeolite produces aromatics in the C_{5+} fraction at a rate of 52.5%, while the desilicated MFI17M zeolite yields 45.8%. Interestingly, while the production of aromatics in the C_{5+} fraction remains stable over time for the desilicated zeolite (comparing data at 1.5 h, 9 h, 21.5 h, and 27 h), Figure 6. 14 (a-d), possibly due to the presence of three-dimensional channels, the conventional zeolite experiences an 8% decline after 27-hour of reaction time, dropping from 52.5 % to 46.2 %. The stability of MFI17M may be attributed to mesopores, which reduce susceptibility to deactivation by coke through enhanced diffusion of products over its acidic sites. In contrast, a notable decrease in aromatic production is observed for other medium-pore zeolites, such as Z22-32 (mono-dimensional channels) and M22-20 and ITQ2-18 (bi-dimensional channels). Comparing data at 1.5 h and 27-hour of Time on Stream (TOS), all three zeolites experience a loss of 8-9 %.

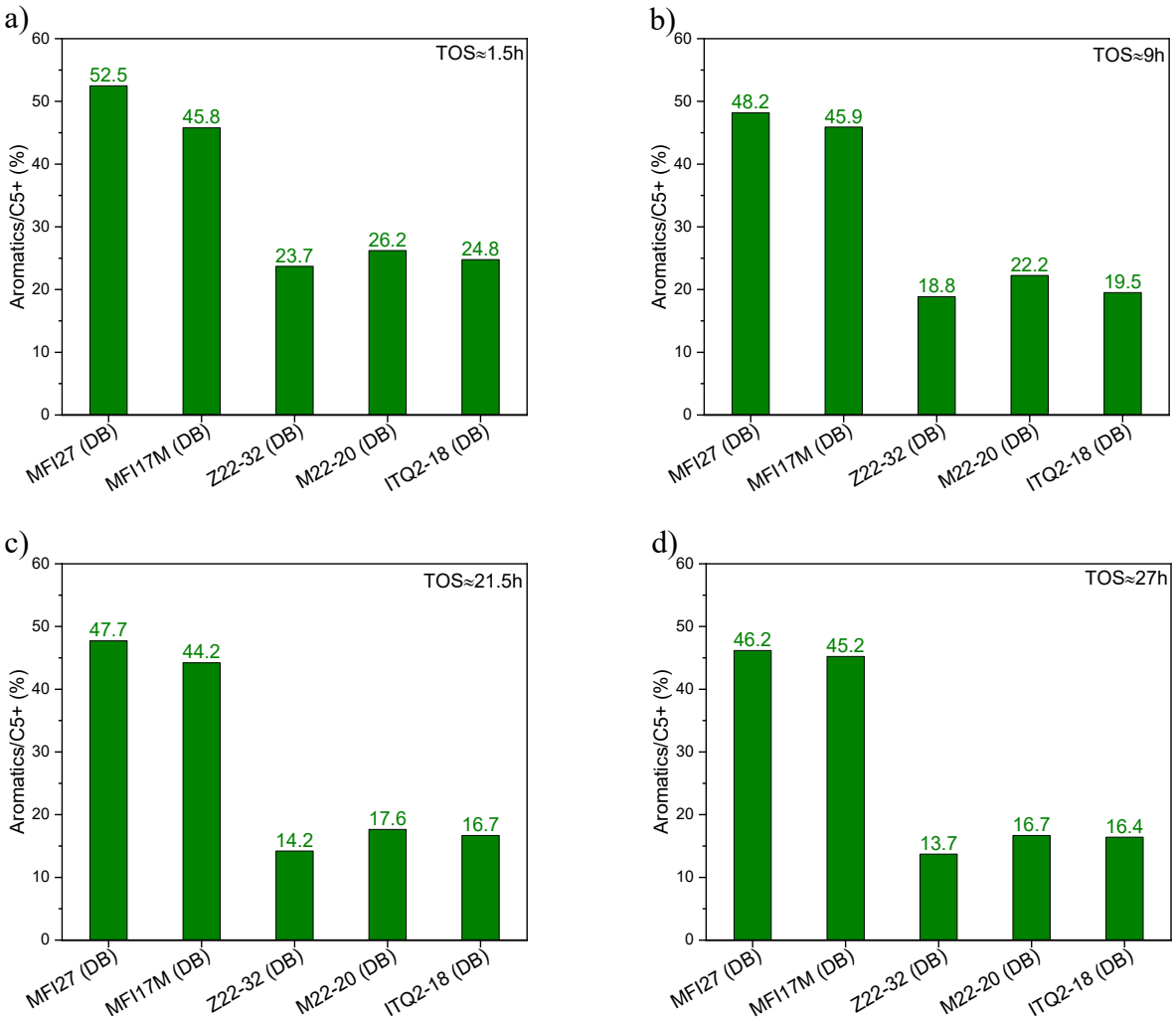


Figure 6. 14. Effect of zeolite topology over aromatics selectivity calculated in the C_{5+} fraction. Results reported: a) beginning of TOS (1.5 h), b) middle of the TOS (9 h), c) end of the TOS (27 h). Reaction parameters include 2.0 bar, 340 °C, H_2/CO_2 = 3, and 19.2 $L \cdot g^{-1} \cdot h^{-1}$, with a time on stream of 27 h.

Similar to large-pore zeolites, the ratio of iso-C_{5+} compound production to the sum of C_{5+} products was evaluated for medium-pore zeolites. Observing Figure 6. 15, it is evident that all 10-ring zeolites exhibit a significant isomerization capacity compared to the bulk iron phase 1NaFe, especially during the early hours of Time on Stream (TOS). In particular, both MFI27 zeolites and its desilicated counterpart, MFI17M, not only maintain a stable trend over time but also stand out for their pronounced isomerization capability. Of note is the behavior of ITQ2-18 zeolite at 1.5 hours of TOS, which emerges as the best among the studied zeolites in terms of isomerization during the considered period. However, this

capacity diminishes rapidly during the reaction, presumably due to its cup-shaped structure. As discussed earlier, ITQ2-18 is derived from the delamination of M22-20, but it should be emphasized that delamination is not always complete due to structural defects and the presence of extra-framework Al, which can compromise the efficiency of ITQ2-18 synthesis. The cup-shaped surface of ITQ2-18, accessible through 12-ring, could be responsible for its rapid deactivation in terms of isomerization, as this shape may hinder molecule diffusion, limiting access to acidic sites. Similarly, M22-20 zeolite shows effective isomerization at the beginning of the reaction but undergoes a similar deactivation over time. In contrast, Z22-32 zeolite appears to have a more limited isomerization capacity, likely due to the presence of mono-dimensional channels, which are easily blocked by coke, hindering access to acidic sites.

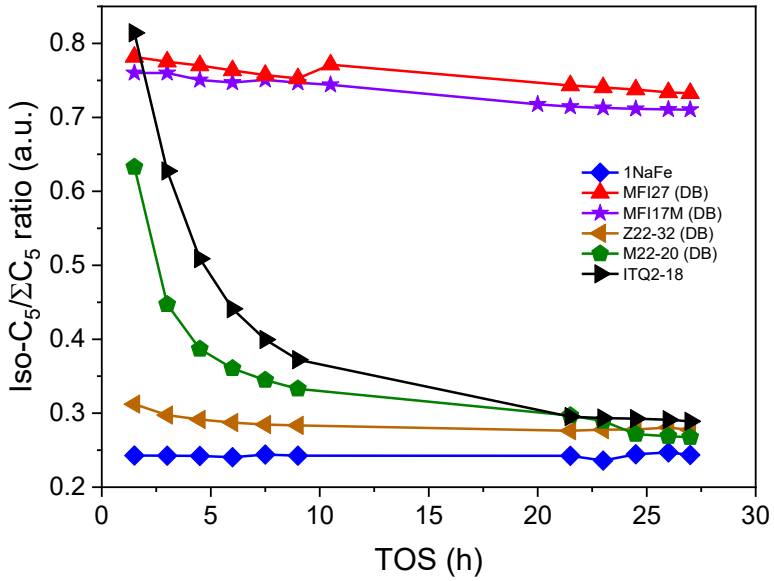
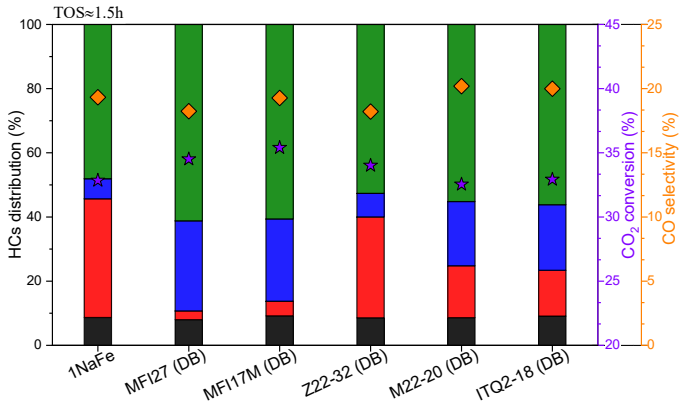


Figure 6. 15. Effect of different zeolite frameworks with 10-ring on the isomerization of C_5 compounds. Reaction parameters include 2.0 bar, 340 °C, H_2/CO_2 = 3, and 19.2 $L \cdot g^{-1} \cdot h^{-1}$, with a time on stream of 27 h.

For an in-depth analysis of the data, Figure 6. 16. illustrates the dual-bed configuration of 1NaFe/zeolite (with medium porosity) multifunctional systems. We combine the systems at a 1:1 mass ratio. Figure 6. 16.a) shows the standalone iron catalyst in the first column on the left, labeled 1NaFe, as a comparison to the involvement of zeolites. Within this context, it is observed that the conversion of CO_2 remains mostly unchanged in all cases. However, there is a noticeable

decrease in the ratio of light olefins in almost all zeolites (MFI27, MFI17M, M22-20, and ITQ2-18). Moreover, an increase in the production of C_{5+} chains and P_2-P_4 paraffinic chains may be seen in these zeolites, especially in the MFI27 and MFI17M zeolites, which have 10-ring structures, and the potential to combine smaller molecules into larger ones to produce heavy hydrocarbons [199]. As a support, Figure 6. 16.b) illustrates the changes in selectivity for each hydrocarbon component across different zeolites compared to the 1NaFe catalyst used alone. This emphasizes the influence of zeolites on hydrocarbon distribution. The data shows that the Z22-32 zeolite, despite having a medium pore size, has only minor variations in selectivity. As previously mentioned, this phenomenon is probably caused by the shape of type 1D pores, which quickly become inactive and so hinder large changes in the distribution of products.

a)



b)

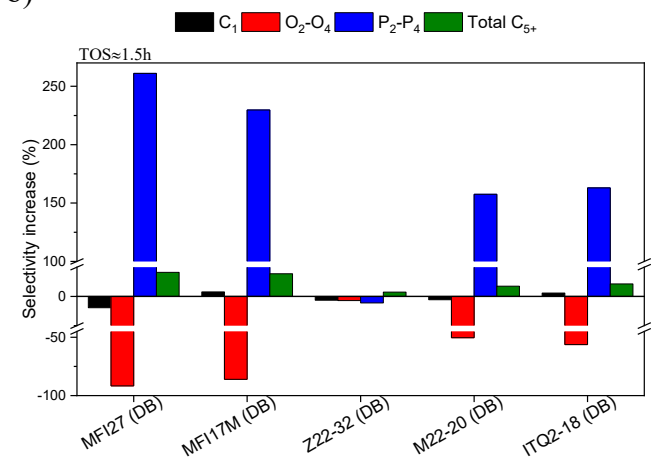
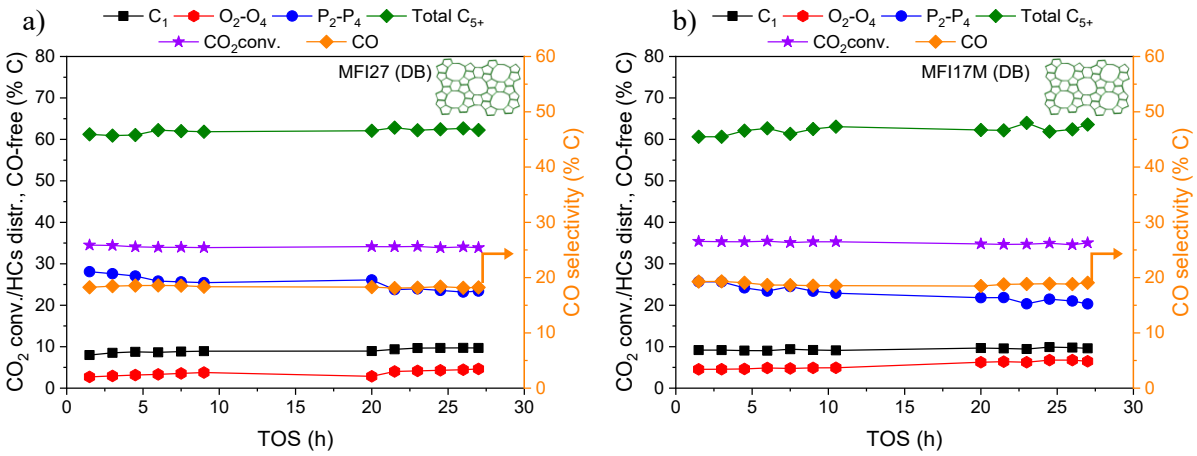


Figure 6. 16. a) A comparison of catalytic data obtained with various zeolites; b) explanation in detail of the (net) increase (or decrease) in selectivity of specific hydrocarbon groups when zeolites are introduced in comparison to the 1NaFe catalyst

used alone. Reaction parameters include 2.0 bar, 340 °C, $H_2/CO_2 = 3$, and 19.2 $L \cdot g^{-1} \cdot h^{-1}$, with a time on stream of 27 h.

After analyzing the reaction profiles of investigations involving medium-pore zeolites in Figure 6. **17**, it is clear that MFI27 and MFI17M zeolites exhibit exceptional long-term stability compared to other medium-pore size zeolites mentioned in this research. Indeed, as the reaction progresses, Z22-32, M22-20, and ITQ2-18 zeolites maintain their ability to convert CO_2. However, they exhibit a reduction in their initial capacity to isomerize, oligomerize, and aromatize the O_2-O_4 olefins. The reason for this is that the conversion of CO_2 is not affected by the particular zeolite utilized but rather depends only on the "redox" catalyst used; in this work, the so-called 1NaFe is often highlighted. After a 27-hour reaction period, there is a discernible decrease in favorability towards C_{5+} compounds and a corresponding rise in favorability towards light olefins when using M22-20 and ITQ2-18 zeolites. When Z22-32 zeolite is employed, the distribution of hydrocarbons remains rather stable over time. This result supports the hypothesis that this zeolite rapidly loses its activity upon coming into contact with the reacting mixture. In fact, it is sufficient a long chain to obstruct the one-dimensional pores of the zeolite, triggering depletion of the zeolite's acidic sites that are crucial for controlling the distribution of reaction intermediates (olefins) towards the desired products.



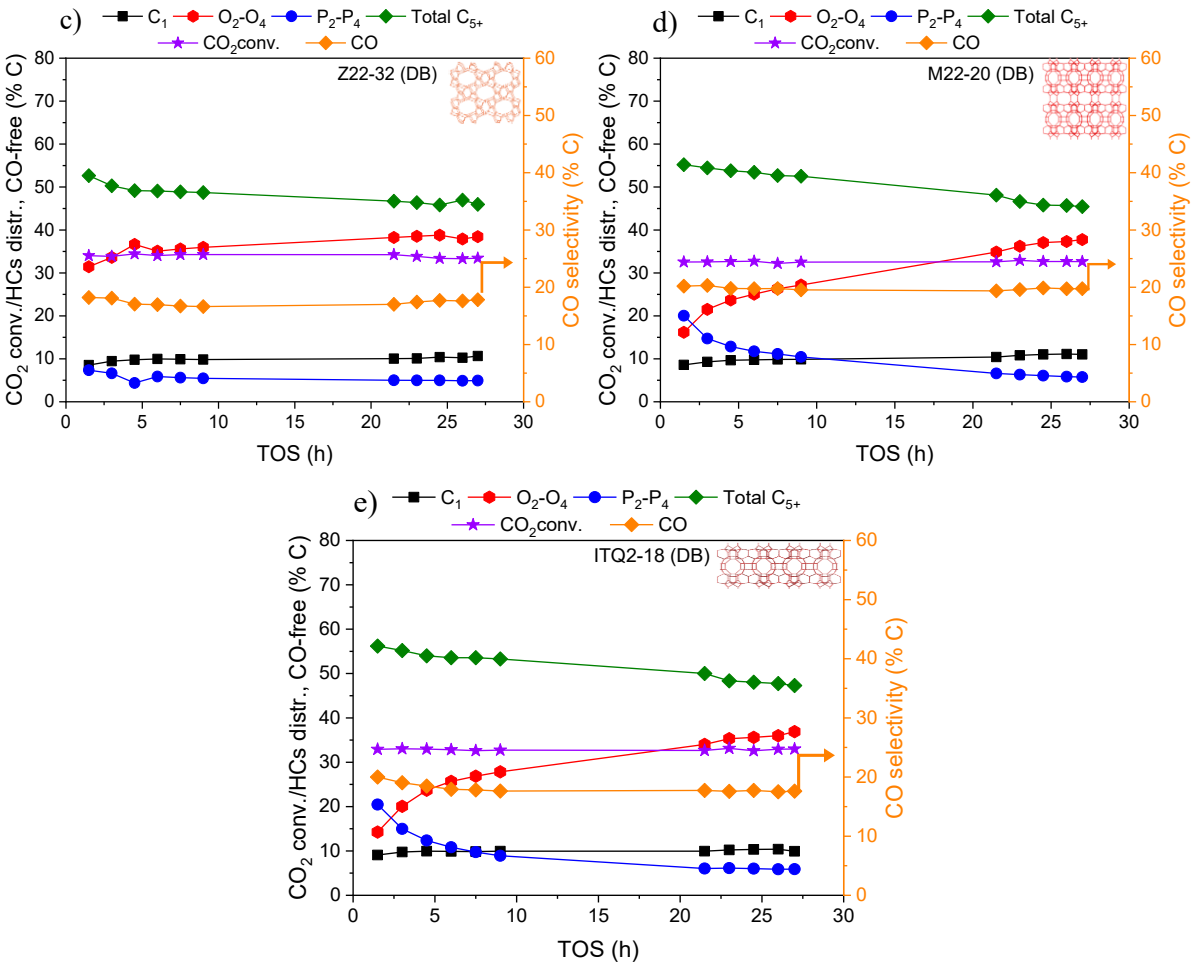


Figure 6. 17. Catalysts activity and products distribution over 1NaFe tested in dual bed mode with large-pore size zeolite: a) MFI27, b) MFI17M, c) Z22-32, d) M22-20 and e) ITQ2-18. Reaction parameters include 2.0 bar, 340 °C, H_2/CO_2 = 3, and 19.2 $L \cdot g^{-1} \cdot h^{-1}$, with a time on stream of 27 h.

6.3.1.3 Summary consideration of 10 and 12-ring zeolite tested in dual bed mode

Table 6.11. Hydrocarbons distribution at 1.5 h.

Sample	(% C) [a]	HCs distribution (% C)				C_{5+} distribution (% C) [b]			$O/(O+P)_{C2-C4}$ (wt. %)
	CO	C_1	$C_2^=$-$C_4^=$	C_2^0-C_4^0	C_{5+}	C_5-C_{12}	C_8-C_{16}	C_{13}-C_{22}	
1NaFe DB	19	9	37	6	48	99	28	1	85
1NaFe+USY24 DB	18	9	34	7	50	95	28	5	82
1NaFe+USY15M DB	20	9	32	7	52	97	30	3	82
1NaFe+USY13 DB	19	9	33	7	51	94	29	6	81
1NaFe+USY5 DB	19	8	35	7	50	95	28	5	83

1NaFe+BEA17 DB	19	9	37	6	48	94	26	6	85
1NaFe+BEA17M DB	18	9	37	6	48	94	26	6	86
1NaFe+MFI27 DB	18	8	3	28	61	96	32	4	8
1NaFe+MFI17M DB	19	9	5	26	60	100	31	0	14
1NaFe+Z22-32 DB	18	9	31	7	53	97	26	3	80
1NaFe+M22-20 DB	20	9	16	20	55	94	30	6	44
1NaFe+ITQ2-18 DB	19	9	14	20	56	91	31	9	40

[a] Selectivity of CO calculated from TCD detector; [b] C_{5+} distribution (%C): C_5-C_{12} gasoline range, C_8-C_{16} Jet fuel range, C_{13}-C_{22} diesel range.

Table 6.11 shows the hydrocarbon distributions at 1.5 h of TOS, obtained by the online GC analyses. Comparing the base (1NaFe), with the 1NaFe tested in dual bed modality with different zeolites, it is possible to appreciate, as expected, that the zeolite component did not further contribute to the formation of methane by cracking at the conditions used, maintaining a CO selectivity around 18-20% and a methane selectivity of around 8-10%.

6.3.2 Characterization of spent zeolites

Studies on the coke accumulation of spent zeolites were conducted using various analytical techniques, including ICP, elemental analysis, TG, and TPO analysis. The Si/Al ratio was calculated to confirm the stability of the zeolite and results are reported in Table 6. 4. TG analysis revealed two weight loss steps during the heating process under an air atmosphere Figure 6. 18 a) and b). The initial step, occurring before 400 °C, indicated the removal of adsorbed water from the zeolite channels. However, the subsequent step, after 400 °C, corresponded to the combustion of zeolite coke. In terms of the coke values detected through TG analysis for zeolites with 12-ring channels, the results were nearly identical in all cases, ranging between 20% and 24%, Table 6.12. Notably, focusing on the 10-ring channels zeolites, after a 27-hour reaction, the total coke deposition on MFI27 and MFI17M was 4.2 and 4.5% respectively. In contrast, the values found were significantly lower for the spent M22-20 (13.7%) and ITQ2-18 (23.5%) zeolites (Table 6.12). The TG analysis detects a particularly interesting coke value for the zeolite Z22-32. Such a low value would appear insufficient to justify this zeolite's low catalytic activity and its significant deactivation over the 27-hour catalytic test. However, due to its one-dimensional (1D) structure, characterized by channels extending in only one direction, even a minimal percentage of coke is enough to explain its deactivation. When coke forms and deposits in these one-way channels, even in small amounts, it can easily block access to the catalytic sites, which quickly turns off the zeolite. This particular vulnerability to coke formation is due to the limited accessibility to the active sites and the difficulty of

removing carbon deposits from the narrow and linear channels. Therefore, the 1D structure, while having some advantages in terms of catalytic selectivity, is disadvantageous when it comes to resistance to coke deactivation. This explains why the Z22-32 zeolite, despite its low coke content, exhibits a significant loss of catalytic activity during the prolonged test. Based on this considerations, it is possible to highlight that pore structure strongly correlates with this disparity; larger available space near acid sites typically leads to faster coking rates. The MFI's interconnected channel structure imposes steric constraints on bulky intermediate formation, resulting in a low coking rate. Conversely, the spacious cavities of BEA and the supercages of FAU zeolites facilitate chain growth reactions, promoting coke formation and zeolite deactivation [213], [218].

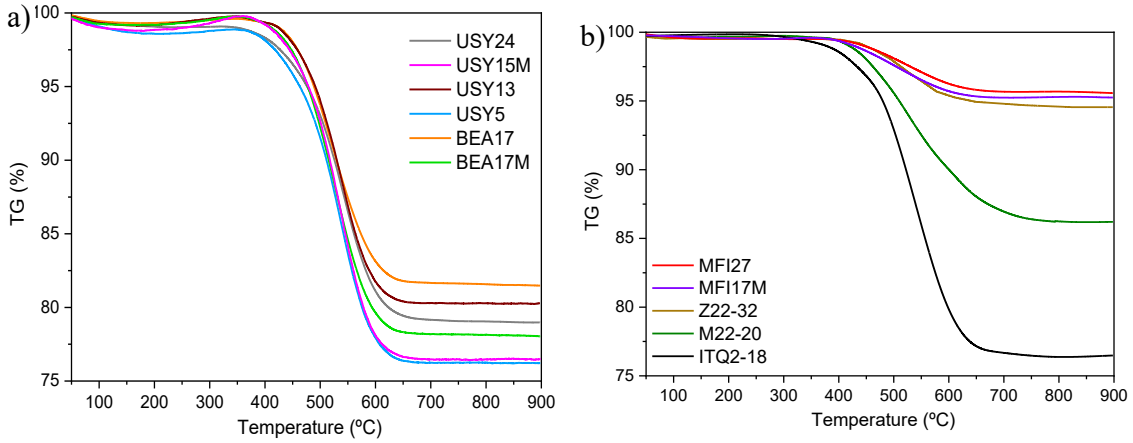


Figure 6. 18. TG profiles for a) spent large pore (12-ring) and b) medium pore (10-ring) zeolites.

Elemental analysis also determined the amount of carbonaceous residues in spent zeolites. Interesting to note, is that the elemental analysis (C+H) shows a strong correlation with the thermogravimetric analyses' calculation of the total coke content, Table 6. 4 [219].

Table 6.12. Chemical composition (ICP) and coke content (elemental analysis, TG analysis) of spent zeolites.

	ICP-OES	**Elemental analysis**			**TG analysis**
Zeolite	Si/Al ratio	C (%)	H (%)	C+H (%)	Δ Mass Loss (wt. %)[a]
USY24	24.8	18.8	1.6	20.5	21.0
USY15M	14.6	21.0	1.6	22.5	23.5

USY13	13.5	17.9	1.4	19.3	19.7
USY5	5.3	19.0	1.6	20.6	23.8
BEA17	17.3	17.2	1.5	18.7	18.5
BEA17M	17.2	19.6	1.6	21.1	21.9
MFI27	25.7	3.4	0.5	3.9	4.2
MFI17M	16.1	5.5	0.6	6.1	4.5
Z22-32	31.8	4.5	0.6	5.2	5.3
M22-20	20.0	17.7	1.5	19.2	13.7
ITQ2-18	18.0	19.8	1.5	21.3	23.5

[a] Coke content determined from the weight loss in the temperature range of 400-900 °C of TG curves.

Also, TPO-MS analysis (Figure 4a) clearly showed CO_2 (m/z = 44) signals on all of the used zeolites, Figure 6. 19. How it is possible to appreciate, all the zeolites exhibit a main desorption peak in the temperature range of 416-494 °C (low-temperature or LT coke) along with a much less intense desorption at temperatures of 550–700 °C (high-temperature or HT coke). The more reactive type of carbon, which oxidizes at lower temperatures (LT coke), is attributed to reaction intermediates, while the more inert coke, which burns at higher temperatures (HT coke), is associated with polyaromatic compounds formed on the Brønsted acid sites within the zeolite channels [220]. It is believed that this latter type of carbon is the main cause of catalyst deactivation in the reaction stage following the induction period. Table 6.13 provides the temperatures of maximum CO2 formation (T_{max}) for LT and HT coke, along with their respective contributions, based on the areas of their respective peaks in the deconvoluted TPO-MS profiles (CO_2 signal). All zeolites have similar burning temperatures for LT (416-494 °C) and HT (550-700 °C) coke types, which means that the carbon deposits are made of similar chemicals. From the deconvolution profiles in Figure x, were calculated the amount of LT and HT coke based on the proportion of the area of the peaks and the results are reported in Table 6.13. Looking at the results it is evident an increase in the relative contribution of HT coke from MCM22-20 (68%) to ITQ2-18 (74%), indicating that incomplete delamination has compromised the stability of the ITQ2-18 zeolite.

However, the zeolites MFI27 and MFI17M had the least amount of coke on its acid sites, if the ratio between the intensity of the peaks is taken into account. This was in line with the fact that it was the most stable during the 27-hour CO_2 hydrogenation reaction (Figure 6. 13, Figure 6. 15). These results, which were supported by TG and elemental analysis tests, showed that MFI zeolite are more resistant to coke formation rather than other zeolite structures.

The shape selectivity of zeolites not only influences product distribution, but also affects the quantity and nature of coke deposition. Coke formation in zeolites is a complex, shape-selective catalytic process that occurs on acid sites, with pore structure playing a significant role. According to the results of the characterization, coke starts to form inside micropores or on the outside surfaces during CO_2 hydrogenation. It then stops reactants from getting to the active sites, which turns off the zeolite [213].

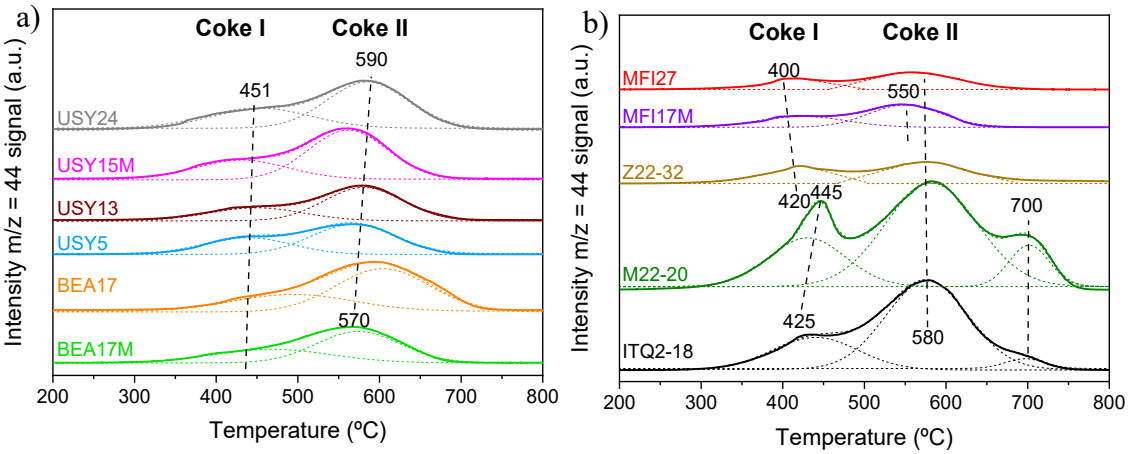


Figure 6. 19. TPO-MS profiles (CO_2 signal, m/z=44) for a) spent large pore (12-ring) and b) medium pore (10-ring) zeolites.

Table 6.13. Type of coke deposits in spent zeolites determined by temperature-programmed oxidation (TPO).

Sample	TPO			
	LT		HT	
	T_{max} (°C)	Area (%)	T_{max} (°C)	Area (%)
USY24	451	36	586	64
USY15M	430	31	562	69
USY13	448	24	561	76
USY5	440	36	567	64
BEA17	494	33	604	67
BEA17M	468	38	573	62
MFI27	416	32	558	68
MFI17M	425	37	550	63
Z22-32	421	36	579	64
M22-20	430	32	582	68
ITQ2-18	440	26	577	74

6.4. Conclusion

Dual bed tests, including 1NaFe CO_2-FTS component and large-pore zeolite (USY24, USY15M, USY13, USY5, BEA17, BEA17M) or medium-pore zeolite (MFI27, MFI7M, Z22-32, M22-20 and ITQ2-18) were shown to enhance both the selectivity and the quality of the gasoline produced directly from CO_2. All the tests were conduct under the following conditions: 340 °C, 2.0 MPa, H_2/CO_2 = 3, for 27-hour on steam. In the initial phase of the study, it was examined the effect of large-pore zeolites. Focusing the attention on the results obtained after 1.5 hours of testing, no significant variations in the acidity levels among FAU-type zeolites (USY24, USY13, and USY5). However, through dealumination of zeolite USY24, subsequently referred to as USY15M, it was observed improvements in both gasoline selectivity and iso-paraffin selectivity. Despite these enhancements, the dealumination process proved insufficient to mitigate the deactivation of FAU-type zeolites over time. Similar behavior was noted in other large-pore zeolites, such as BEA17 and its dealuminated derivative (BEA17M), mirroring the patterns observed in USY24 and USY15E. Transitioning to the subsequent phase of the investigation, which involved medium-pore zeolites, it was found that MFI-type zeolites demonstrated the highest stability over time. Even with the introduction of mesoporosity, no significant improvements were noted. Remarkably, M22-20 zeolites and their delaminated counterpart, ITQ2-18, displayed notable isomerization capabilities. In particular for the ITQ2-18 the iso-$C_5/\sum C_5$ ratio was of 0.82, surpassing not only the isomerization capability of M22-20 (0.64), but also those of MFI-type zeolites. In fact, MFI27 and MFI17M showed a iso-$C_5/\sum C_5$ ratio respectively of 0.79 and 0.78. However, these results are true for the first stage of the reaction (ca 1.5 h). Moreover the incomplete delamination of ITQ2-18 restricted its advantages compared to M22-20 overtime. Conversely, Z22-32 zeolite showed a really low capability of isomerization (the iso-$C_5/\sum C_5$ ratio was of 0.34), despite its medium pore size. Furthermore, it exhibited negligible differences compared to 1NaFe, even during the initial stages of catalytic testing. This observation is likely attributed to the presence of one-dimensional channels. In this scenario, although coke formation within the channels is reduced compared to 2D structures, as determined by elemental and TG analysis, this low amount remains sufficient to induce deactivation.

Chapter 7

7. Conclusion

The main objective of this thesis was to study the thermochemical conversion of CO_2 into valuable added products in order to reduce the increasing amount of CO_2 emissions in the atmosphere. This doctoral thesis was mostly about changing the structure of some zeolites and making iron-based (Fe) materials impregnated with sodium (Na) so that CO_2 can be turned into hydrocarbons. The goal was to make a positive contribution to the current climate challenge. The idea to involve the zeolite was based on the fact that the zeolite, thanks to the presence of acid-base sites, is capable of modulating the final product by isomerizing, aromatizing, and oligomerizing the olefin intermediates.

The work began with *Chapter 1*, which outlined the causes of global warming and some possible solutions, identifying CO_2 as the most abundant species among greenhouse gases. Regarding CO_2 conversion technologies, the thermochemical process was shown to be beneficial for its possible application in utilising surplus renewable energy to produce high-value-added products.

In *Chapter 2* were reported and described all the synthesis of the materials and all the characterization and testing methods applied in the experimental work of this thesis.

The first experimental results were reported in *Chapter 3*. Initially, the study focus on the comparison of iron-based catalysts synthesized in two different ways: via impregnation and via coprecipitation, both containing the same sodium content. The preliminary results showed no significant differences in performance between the two methods. However, from an energy efficiency perspective, the coprecipitation method emerged as the easier and more economical option. This method seems to be advantageous thanks to the single-step synthesis of the sample, eliminating the need of calcination of the material before its use, which simplifies its preparation and reduces water consumption. Therefore, adopting coprecipitation can lead to significant energy and resource savings, making it a preferred choice for industrial applications. Catalyst performance was further

improved by using a physical mixture of Na-promoted Fe-based metallic phases and acid zeolites. This combination achieved higher conversion rates and increased selectivity for heavier hydrocarbons, mainly due to the oligomerization and aromatization processes facilitated by the acid zeolites. The introduction of hierarchical zeolites, thanks to the presence of mesopores, proved to be a valuable strategy for increasing product yields within the gasoline range. Mesopores facilitate product release compared to conventional zeolites. This result underscores the importance of zeolite structural properties in optimizing catalytic performance. However, the study reported in Chapter 3 also highlighted that sodium migration from iron catalytic sites to zeolite acid sites is a significant challenge capable of compromising catalyst effectiveness. This crucial finding was the starting point for the development of the study reported in *Chapter 4*.

Chapter 4 was based on effective iron and sodium confinement strategies to mitigate sodium migration when a zeolite is involved. The study demonstrated that confining iron and sodium inside carbon nanotubes (CNTs), plays a fundamental role in reducing alkali metal migration. In particular, the CNT-S-10FeNa sample showed minimal variations in different contact modes with the zeolite, confirming the efficacy of the carbonaceous barrier in separating iron from zeolite acid sites. In fact, this barrier proved essential for preventing the loss of alkali metal promotion and preserving zeolite acidity, crucial for maintaining overall catalyst performance.

Chapter 5, instead, aimed to avoid alkali metal migration from sodium to zeolite acid sites by focusing on the morphological properties of MFI-type zeolites to understand their impact on sodium migration and catalytic performance. It was observed that coating the zeolite with an amorphous SiO_2 layer on the external surface of commercial MFI27 zeolite was effective, although not a completely resolving method for inhibiting sodium migration. While the reduction of the external surface area (μMFI35) of the zeolite was found to greatly limit sodium migration. These results provide valuable insights for the design of high-performance zeolites resistant to sodium ion exchange, essential for maintaining catalyst stability and efficiency over time.

Chapter 6, on the other hand, aimed to assess the products obtained through dual-bed systems, combining 1NaFe CO_2-FTS components with various large and medium-pore zeolites. These systems improved both the selectivity and quality of gasoline produced directly from CO_2. In the initial phase of the study, large-pore zeolites were examined, revealing no significant variations in acidity levels among

FAU-type zeolites. However, dealumination of zeolite USY24, resulting in USY15M, improved gasoline selectivity and iso-paraffin selectivity. Despite these improvements, dealumination alone was insufficient to mitigate the deactivation of FAU-type zeolites. Similar behavior was observed in other large-pore zeolites such as BEA17 and its dealuminated derivative BEA17M. The transition to medium-pore zeolites revealed that MFI-type zeolites demonstrated the highest stability over time. The introduction of mesoporosity did not significantly improve performance. Furthermore, zeolites like M22-20 and its delaminated counterpart, ITQ2-18, showed remarkable isomerization capabilities in the first stage of the catalytic test. In particular, ITQ2-18 exhibited a high iso-$C_5/\sum C_5$ ratio, surpassing that of M22-20 and MFI27 zeolites. However, incomplete delamination of ITQ2-18 limited its advantages over time. In contrast, zeolite Z22-32 showed low isomerization capability and significant deactivation due to coke formation in its one-dimensional channels, as demonstrated by TPO and TG analysis.

In conclusion, this doctoral study provided a solid foundation for the synthesis and optimization of multifunctional catalysts for hydrocarbon production via CO_2 hydrogenation. The results highlight the importance of synthesis methods, effective control of sodium migration, and zeolite structural properties in developing efficient and stable catalysts and in modulating the final products.

Future research should focus on in situ characterizations to further improve the performance of the catalysts involved. These insights are indispensable for more sustainable and efficient CO_2-FTS process, contributing to the advancement of clean energy technologies.

References

[1] E. Corrao *et al.*, "CO 2 conversion into hydrocarbons via modified Fischer-Tropsch synthesis by using bulk iron catalysts combined with zeolites," 2023, doi: 10.1016/j.cherd.2023.07.052.

[2] S. Mohammed *et al.*, "An overview of greenhouse gases emissions in Hungary," *J Clean Prod*, vol. 314, p. 127865, Sep. 2021, doi: 10.1016/j.jclepro.2021.127865.

[3] T. Matthews, "Humid heat and climate change," *Progress in Physical Geography: Earth and Environment*, vol. 42, no. 3, pp. 391–405, Jun. 2018, doi: 10.1177/0309133318776490.

[4] V. Mendoza, M. Pazos, R. Garduño, and B. Mendoza, "Thermodynamics of climate change between cloud cover, atmospheric temperature and humidity," *Sci Rep*, vol. 11, no. 1, p. 21244, Oct. 2021, doi: 10.1038/s41598-021-00555-5.

[5] B. M. Smirnov, "Infrared Radiation in the Energetics of the Atmosphere," *High Temperature*, vol. 57, no. 4, pp. 573–595, Jul. 2019, doi: 10.1134/S0018151X19040199.

[6] P. Forster *et al.*, "The Earth's Energy Budget, Climate Feedbacks and Climate Sensitivity," pp. 923–1054, 2021, doi: 10.1017/9781009157896.009.

[7] M. Wild *et al.*, "The energy balance over land and oceans: an assessment based on direct observations and CMIP5 climate models," *Clim Dyn*, vol. 44, no. 11, pp. 3393–3429, 2015, doi: 10.1007/s00382-014-2430-z.

[8] M. Wild *et al.*, "The cloud-free global energy balance and inferred cloud radiative effects: an assessment based on direct observations and climate models," vol. 52, pp. 4787–4812, 2019, doi: 10.1007/s00382-018-4413-y.

[9] Intergovernmental Panel on Climate Change, *Climate Change 2007: Mitigation. Contribution of Working Group III to the Fourth Assessment Report of the Intergovernmental Panel on Climate Change*. Cambridge

University Press, Cambridge, United Kingdom and New York, NY, USA, 2007.

[10] C. Korner, "Biosphere Responses to CO 2 Enrichment," *Ecological Applications*, vol. 10, no. 6, p. 1590, Dec. 2000, doi: 10.2307/2641226.

[11] J. Blunden and D. S. Arndt, "State of the Climate in 2019," *Bull Am Meteorol Soc*, vol. 101, no. 8, pp. S1–S429, Aug. 2020, doi: 10.1175/2020BAMSStateoftheClimate.1.

[12] Unfccc, "ADOPTION OF THE PARIS AGREEMENT - Paris Agreement text English," 2015.

[13] S. C. Peter, "Reduction of CO $_2$ to Chemicals and Fuels: A Solution to Global Warming and Energy Crisis," *ACS Energy Lett*, vol. 3, no. 7, pp. 1557–1561, Jul. 2018, doi: 10.1021/acsenergylett.8b00878.

[14] W. J. Ripple *et al.*, "The 2023 state of the climate report: Entering uncharted territory," *Bioscience*, vol. 0, pp. 1–10, 2023, doi: 10.1093/biosci/biad080.

[15] I. Energy Agency, "Net Zero by 2050 - A Roadmap for the Global Energy Sector," 2050. [Online]. Available: www.iea.org/t&c/

[16] T. Lin *et al.*, "Advances in Selectivity Control for Fischer–Tropsch Synthesis to Fuels and Chemicals with High Carbon Efficiency," *ACS Catal*, pp. 12092–12112, 2022, doi: 10.1021/acscatal.2c03404.

[17] Intergovernmental Panel on Climate Change (IPCC), *Climate Change 2022 – Impacts, Adaptation and Vulnerability*. Cambridge University Press, 2023. doi: 10.1017/9781009325844.

[18] I. Energy Agency, "Global Energy Review: CO2 Emissions in 2021 Global emissions rebound sharply to highest ever level," 2021, Accessed: Oct. 01, 2022. [Online]. Available: www.iea.org/t&c/

[19] Q. Yang *et al.*, "Identifying Performance Descriptors in CO2 Hydrogenation over Iron-Based Catalysts Promoted with Alkali Metals," *Angewandte Chemie - International Edition*, 2022, doi: 10.1002/ANIE.202116517.

[20] National Oceanic and Atmospheric Administration, "Greenhouse gases continued to increase rapidly in 2022 | National Oceanic and Atmospheric Administration." Accessed: Oct. 25, 2023. [Online]. Available: https://www.noaa.gov/news-release/greenhouse-gases-continued-to-increase-rapidly-in-2022

[21] The World Bank, "Carbon Pricing Dashboard | Up-to-date overview of carbon pricing initiatives." Accessed: Oct. 25, 2023. [Online]. Available: https://carbonpricingdashboard.worldbank.org/map_data

[22] "H.R.5376 - Inflation Reduction Act," pp. 117–169, 2022.

[23] A. H. Alami *et al.*, "Materials and logistics for carbon dioxide capture, storage and utilization," *Science of The Total Environment*, vol. 717, p. 137221, May 2020, doi: 10.1016/j.scitotenv.2020.137221.

[24] "Olefins Market Opportunities, Drivers, Challenges, Scope, Share, & Forecast Analysis By 2029." Accessed: Oct. 25, 2023. [Online]. Available: https://www.databridgemarketresearch.com/reports/global-olefins-market

[25] "Sustainable Aviation Fuel Market Size by Technology, Platform, Fuel Type, Biofuel Blending Capacity, Regions, Global Industry Analysis, Share, Growth, Trends, and Forecast 2022 to 2030 | The Brainy Insights." Accessed: Oct. 25, 2023. [Online]. Available: https://www.thebrainyinsights.com/report/sustainable-aviation-fuel-market-12818

[26] K. GAO and Y. ZHENG, "Combined effects of ocean acidification and solar UV radiation on photosynthesis, growth, pigmentation and calcification of the coralline alga *Corallina sessilis* (Rhodophyta)," *Glob Chang Biol*, vol. 16, no. 8, pp. 2388–2398, Aug. 2010, doi: 10.1111/j.1365-2486.2009.02113.x.

[27] C.-H. Huang and C.-S. Tan, "A Review: CO2 Utilization," *Aerosol Air Qual Res*, vol. 14, no. 2, pp. 480–499, 2014, doi: 10.4209/aaqr.2013.10.0326.

[28] S. Roy, A. Cherevotan, and S. C. Peter, "Thermochemical CO_2 Hydrogenation to Single Carbon Products: Scientific and Technological

Challenges," *ACS Energy Lett*, vol. 3, no. 8, pp. 1938–1966, Aug. 2018, doi: 10.1021/acsenergylett.8b00740.

[29] Q. Deng, X. Ling, K. Zhang, L. Tan, G. Qi, and J. Zhang, "CCS and CCUS Technologies: Giving the Oil and Gas Industry a Green Future," *Front Energy Res*, vol. 10, Jun. 2022, doi: 10.3389/fenrg.2022.919330.

[30] K. D. Ramachandriya, D. K. Kundiyana, M. R. Wilkins, J. B. Terrill, H. K. Atiyeh, and R. L. Huhnke, "Carbon dioxide conversion to fuels and chemicals using a hybrid green process," *Appl Energy*, vol. 112, pp. 289–299, Dec. 2013, doi: 10.1016/j.apenergy.2013.06.017.

[31] C. Song, "Global challenges and strategies for control, conversion and utilization of CO2 for sustainable development involving energy, catalysis, adsorption and chemical processing," *Catal Today*, vol. 115, no. 1–4, pp. 2–32, Jun. 2006, doi: 10.1016/j.cattod.2006.02.029.

[32] M. Aresta and A. Dibenedetto, "Utilisation of CO2 as a chemical feedstock: opportunities and challenges," *Dalton Transactions*, no. 28, p. 2975, 2007, doi: 10.1039/b700658f.

[33] L. Fu *et al.*, "Research progress on CO2 capture and utilization technology," *Journal of CO2 Utilization*, vol. 66, pp. 2212–9820, 2022, doi: 10.1016/j.jcou.2022.102260.

[34] Rodney Allam *et al.*, *Chapter 3: Capture of CO2*. Cambridge, United Kingdom and New York, NY, USA : Cambridge University Press, 2005.

[35] T. M. Gür, "Carbon Dioxide Emissions, Capture, Storage and Utilization: Review of Materials, Processes and Technologies," *Prog Energy Combust Sci*, vol. 89, p. 100965, Mar. 2022, doi: 10.1016/j.pecs.2021.100965.

[36] X. Wang, F. Zhang, L. Li, H. Zhang, and S. Deng, "Carbon dioxide capture," 2021, pp. 297–348. doi: 10.1016/bs.ache.2021.10.005.

[37] B. Dziejarski, J. Serafin, K. Andersson, and R. Krzyżyńska, "CO2 capture materials: a review of current trends and future challenges," *Materials Today Sustainability*, vol. 24, p. 100483, Dec. 2023, doi: 10.1016/j.mtsust.2023.100483.

[38] International Energy Agency, "Direct Air Capture: A key technology for net zero", Accessed: Nov. 28, 2023. [Online]. Available: www.iea.org/t&c/

[39] M. Aghaie, N. Rezaei, and S. Zendehboudi, "A systematic review on CO2 capture with ionic liquids: Current status and future prospects," *Renewable and Sustainable Energy Reviews*, vol. 96, pp. 502–525, Nov. 2018, doi: 10.1016/j.rser.2018.07.004.

[40] M. Takht Ravanchi and S. Sahebdelfar, "Carbon dioxide capture and utilization in petrochemical industry: potentials and challenges," *Appl Petrochem Res*, vol. 4, no. 1, pp. 63–77, May 2014, doi: 10.1007/s13203-014-0050-5.

[41] A. Al-Mamoori, A. Krishnamurthy, A. A. Rownaghi, and F. Rezaei, "Carbon Capture and Utilization Update," *Energy Technology*, vol. 5, no. 6, pp. 834–849, Jun. 2017, doi: 10.1002/ente.201600747.

[42] A. Gulzar, A. Gulzar, M. B. Ansari, F. He, S. Gai, and P. Yang, "Carbon dioxide utilization: A paradigm shift with CO2 economy," *Chemical Engineering Journal Advances*, vol. 3, p. 100013, Nov. 2020, doi: 10.1016/j.ceja.2020.100013.

[43] C. H. Vo, C. Mondelli, H. Hamedi, J. Pérez-Ramírez, S. Farooq, and I. A. Karimi, "Sustainability Assessment of Thermocatalytic Conversion of CO $_2$ to Transportation Fuels, Methanol, and 1-Propanol," *ACS Sustain Chem Eng*, vol. 9, no. 31, pp. 10591–10600, Aug. 2021, doi: 10.1021/acssuschemeng.1c02805.

[44] D. S. A. Simakov, "Thermocatalytic Conversion of CO2," 2017, pp. 1–25. doi: 10.1007/978-3-319-61112-9_1.

[45] D. S. A. Simakov and Y. Román-Leshkov, "Highly efficient methane reforming over a low-loading Ru/γ-Al2O3 catalyst in a Pd-Ag membrane reactor," *AIChE Journal*, vol. 64, no. 8, pp. 3101–3108, Aug. 2018, doi: 10.1002/aic.16094.

[46] A. Wolf, A. Jess, and C. Kern, "Syngas Production via Reverse Water-Gas Shift Reaction over a Ni-Al $_2$ O $_3$ Catalyst: Catalyst Stability, Reaction Kinetics, and Modeling," *Chem Eng Technol*, vol. 39, no. 6, pp. 1040–1048, Jun. 2016, doi: 10.1002/ceat.201500548.

[47] P. Häussinger, R. Lohmüller, and A. M. Watson, "Hydrogen," in *Ullmann's Encyclopedia of Industrial Chemistry*, Weinheim, Germany: Wiley-VCH Verlag GmbH & Co. KGaA, 2000. doi: 10.1002/14356007.a13_297.

[48] N. Armaroli and V. Balzani, "The Hydrogen Issue," *ChemSusChem*, vol. 4, no. 1, pp. 21–36, Jan. 2011, doi: 10.1002/cssc.201000182.

[49] International Energy Agency, "The Future of Hydrogen." Accessed: Nov. 28, 2023. [Online]. Available: https://www.iea.org/reports/the-future-of-hydrogen

[50] M. Kayfeci, A. Keçebaş, and M. Bayat, "Hydrogen production," in *Solar Hydrogen Production*, Elsevier, 2019, pp. 45–83. doi: 10.1016/B978-0-12-814853-2.00003-5.

[51] J. Chi and H. Yu, "Water electrolysis based on renewable energy for hydrogen production," *Chinese Journal of Catalysis*, vol. 39, no. 3, pp. 390–394, Mar. 2018, doi: 10.1016/S1872-2067(17)62949-8.

[52] A. Buttler and H. Spliethoff, "Current status of water electrolysis for energy storage, grid balancing and sector coupling via power-to-gas and power-to-liquids: A review," *Renewable and Sustainable Energy Reviews*, vol. 82, pp. 2440–2454, Feb. 2018, doi: 10.1016/j.rser.2017.09.003.

[53] A. Hauch *et al.*, "Recent advances in solid oxide cell technology for electrolysis," *Science (1979)*, vol. 370, no. 6513, Oct. 2020, doi: 10.1126/science.aba6118.

[54] A. Velty and A. Corma, "Advanced zeolite and ordered mesoporous silica-based catalysts for the conversion of CO_2 to chemicals and fuels," *Chem Soc Rev*, vol. 52, no. 5, pp. 1773–1946, 2023, doi: 10.1039/D2CS00456A.

[55] V. Uusitalo, S. Väisänen, E. Inkeri, and R. Soukka, "Potential for greenhouse gas emission reductions using surplus electricity in hydrogen, methane and methanol production via electrolysis," *Energy Convers Manag*, vol. 134, pp. 125–134, Feb. 2017, doi: 10.1016/j.enconman.2016.12.031.

[56] E. Giglio, R. Pirone, and S. Bensaid, "Dynamic modelling of methanation reactors during start-up and regulation in intermittent power-to-gas

applications," *Renew Energy*, vol. 170, pp. 1040–1051, Jun. 2021, doi: 10.1016/J.RENENE.2021.01.153.

[57] E. Giglio, G. Vitale, A. Lanzini, and M. Santarelli, "Integration between biomass gasification and high-temperature electrolysis for synthetic methane production," *Biomass Bioenergy*, vol. 148, May 2021, doi: 10.1016/J.BIOMBIOE.2021.106017.

[58] D. Parigi, E. Giglio, A. Soto, and M. Santarelli, "Power-to-fuels through carbon dioxide Re-Utilization and high-temperature electrolysis: A technical and economical comparison between synthetic methanol and methane," *J Clean Prod*, vol. 226, pp. 679–691, Jul. 2019, doi: 10.1016/J.JCLEPRO.2019.04.087.

[59] F. Salomone, E. Giglio, D. Ferrero, M. Santarelli, R. Pirone, and S. Bensaid, "Techno-economic modelling of a Power-to-Gas system based on SOEC electrolysis and CO2 methanation in a RES-based electric grid," *Chemical Engineering Journal*, vol. 377, p. 120233, Dec. 2019, doi: 10.1016/J.CEJ.2018.10.170.

[60] A. Mazza, F. Salomone, F. Arrigo, S. Bensaid, E. Bompard, and G. Chicco, "Impact of Power-to-Gas on distribution systems with large renewable energy penetration," *Energy Conversion and Management: X*, vol. 7, p. 100053, Sep. 2020, doi: 10.1016/J.ECMX.2020.100053.

[61] H. Guzmán *et al.*, "How to make sustainable CO2 conversion to Methanol: Thermocatalytic versus electrocatalytic technology," *Chemical Engineering Journal*, vol. 417, p. 127973, Aug. 2021, doi: 10.1016/J.CEJ.2020.127973.

[62] H. Guzmán, F. Salomone, S. Bensaid, M. Castellino, N. Russo, and S. Hernández, "CO2Conversion to Alcohols over Cu/ZnO Catalysts: Prospective Synergies between Electrocatalytic and Thermocatalytic Routes," *ACS Appl Mater Interfaces*, vol. 14, no. 1, pp. 517–530, Jan. 2022, doi: https://doi.org/10.1021/acsami.1c15871.

[63] F. Salomone *et al.*, "CO2 hydrogenation to methanol over Zr- and Ce-doped indium oxide," *Catal Today*, Feb. 2023, doi: 10.1016/J.CATTOD.2023.01.030.

[64] F. Salomone *et al.*, "Physico-Chemical Modifications Affecting the Activity and Stability of Cu-Based Hybrid Catalysts during the Direct Hydrogenation of Carbon Dioxide into Dimethyl-Ether," *Materials*, vol. 15, no. 21, p. 7774, Nov. 2022, doi: 10.3390/MA15217774/S1.

[65] V. Dieterich, A. Buttler, A. Hanel, H. Spliethoff, and S. Fendt, "Power-to-liquid via synthesis of methanol, DME or Fischer–Tropsch-fuels: a review," *Energy Environ Sci*, vol. 13, no. 10, pp. 3207–3252, 2020, doi: 10.1039/d0ee01187h.

[66] T. Numpilai, C. K. Cheng, J. Limtrakul, and T. Witoon, "Recent advances in light olefins production from catalytic hydrogenation of carbon dioxide," *Process Safety and Environmental Protection*, vol. 151, pp. 401–427, Jul. 2021, doi: 10.1016/J.PSEP.2021.05.025.

[67] Y. Wang *et al.*, "Rationally Designing Bifunctional Catalysts as an Efficient Strategy to Boost CO 2 Hydrogenation Producing Value-Added Aromatics," *ACS Catal*, vol. 9, no. 2, pp. 895–901, 2019, doi: 10.1021/acscatal.8b01344.

[68] O. A. Ojelade and S. F. Zaman, "A review on CO2 hydrogenation to lower olefins: Understanding the structure-property relationships in heterogeneous catalytic systems," *Journal of CO2 Utilization*, vol. 47, p. 101506, May 2021, doi: 10.1016/J.JCOU.2021.101506.

[69] Y. Gambo, S. Adamu, R. A. Lucky, M. S. Ba-Shammakh, and M. M. Hossain, "Tandem catalysis: A sustainable alternative for direct hydrogenation of CO2 to light olefins," *Appl Catal A Gen*, vol. 641, p. 118658, Jul. 2022, doi: 10.1016/J.APCATA.2022.118658.

[70] C. Panzone, R. Philippe, A. Chappaz, P. Fongarland, and A. Bengaouer, "Power-to-Liquid catalytic CO2 valorization into fuels and chemicals: Focus on the Fischer-Tropsch route," *Journal of CO2 Utilization*, vol. 38, no. February, pp. 314–347, 2020, doi: 10.1016/j.jcou.2020.02.009.

[71] F. Salomone *et al.*, "Process simulation and energy analysis of synthetic natural gas production from water electrolysis and CO 2 capture in a waste incinerator," 2023, doi: 10.1016/j.apenergy.2023.121200.

[72] Z. Zhang *et al.*, "Recent advances in carbon dioxide utilization," *Renewable and Sustainable Energy Reviews*, vol. 125, p. 109799, Jun. 2020, doi: 10.1016/j.rser.2020.109799.

[73] I. Ganesh, "Conversion of carbon dioxide into methanol – a potential liquid fuel: Fundamental challenges and opportunities (a review)," *Renewable and Sustainable Energy Reviews*, vol. 31, pp. 221–257, Mar. 2014, doi: 10.1016/j.rser.2013.11.045.

[74] M. North, "What is CO2? Thermodynamics, Basic Reactions and Physical Chemistry," in *Carbon Dioxide Utilisation*, Elsevier, 2015, pp. 3–17. doi: 10.1016/B978-0-444-62746-9.00001-3.

[75] P. Gao *et al.*, "Direct Production of Lower Olefins from CO2 Conversion via Bifunctional Catalysis," *ACS Catal*, vol. 8, no. 1, pp. 571–578, 2018, doi: 10.1021/acscatal.7b02649.

[76] M. D. Garba *et al.*, "CO2 towards fuels: A review of catalytic conversion of carbon dioxide to hydrocarbons," *J Environ Chem Eng*, vol. 9, no. 2, p. 104756, Apr. 2021, doi: 10.1016/j.jece.2020.104756.

[77] C. Perego, R. Bortolo, and R. Zennaro, "Gas to liquids technologies for natural gas reserves valorization: The Eni experience," *Catal Today*, vol. 142, no. 1–2, pp. 9–16, Apr. 2009, doi: 10.1016/J.CATTOD.2009.01.006.

[78] P. Sharma, J. Sebastian, S. Ghosh, D. Creaser, and L. Olsson, "Recent advances in hydrogenation of CO2into hydrocarbonsviamethanol intermediate over heterogeneous catalysts," *Catal Sci Technol*, vol. 11, no. 5, pp. 1665–1697, 2021, doi: 10.1039/d0cy01913e.

[79] P. Marocco *et al.*, "CO2 methanation over Ni/Al hydrotalcite-derived catalyst: Experimental characterization and kinetic study," *Fuel*, vol. 225, pp. 230–242, Aug. 2018, doi: 10.1016/J.FUEL.2018.03.137.

[80] A. Porta, L. Falbo, C. G. Visconti, L. Lietti, C. Bassano, and P. Deiana, "Synthesis of Ru-based catalysts for CO2 methanation and experimental assessment of intraporous transport limitations," *Catal Today*, vol. 343, pp. 38–47, Mar. 2020, doi: 10.1016/J.CATTOD.2019.01.042.

[81] J. Artz *et al.*, "Sustainable Conversion of Carbon Dioxide: An Integrated Review of Catalysis and Life Cycle Assessment," *Chem Rev*, vol. 118, no. 2, pp. 434–504, Jan. 2018, doi: 10.1021/acs.chemrev.7b00435.

[82] T. Hos, M. V. Landau, and M. Herskowitz, "Hydrogenation of CO_2 on Fe-Based Catalysts: Preferred Route to Renewable Liquid Fuels," *Ind Eng Chem Res*, vol. 61, no. 29, pp. 10387–10399, Jul. 2022, doi: 10.1021/acs.iecr.1c04254.

[83] B. Liang *et al.*, "Mn decorated Na/Fe catalysts for CO 2 hydrogenation to light olefins," *Catal Sci Technol*, vol. 9, no. 2, pp. 456–464, 2019, doi: 10.1039/c8cy02275e.

[84] A. De Klerk, "Transport Fuel: Biomass-, Coal-, Gas- and Waste-to-Liquids Processes," *Future Energy: Improved, Sustainable and Clean Options for our Planet*, pp. 245–270, Jan. 2014, doi: 10.1016/B978-0-08-099424-6.00012-0.

[85] Y. Jiang *et al.*, "Recent advances in thermocatalytic hydrogenation of carbon dioxide to light olefins and liquid fuels via modified Fischer-Tropsch pathway," *Journal of CO2 Utilization*, vol. 67, Jan. 2023, doi: 10.1016/J.JCOU.2022.102321.

[86] C. WANG, J. ZHANG, X. GAO, and T. ZHAO, "Research progress on iron-based catalysts for CO2 hydrogenation to long-chain linear α-olefins," *Journal of Fuel Chemistry and Technology*, vol. 51, no. 1, pp. 67–85, Jan. 2023, doi: 10.1016/S1872-5813(22)60058-6.

[87] J. Liu *et al.*, "Direct Transformation of Carbon Dioxide to Value-Added Hydrocarbons by Physical Mixtures of Fe5C2 and K-Modified Al2O3," *Ind Eng Chem Res*, vol. 57, no. 28, pp. 9120–9126, 2018, doi: 10.1021/acs.iecr.8b02017.

[88] D. Heskett, "The interaction range in alkali metal-promoted systems," *Surf Sci*, vol. 199, no. 1–2, pp. 67–86, Jan. 1988, doi: 10.1016/0039-6028(88)90397-4.

[89] J. Li *et al.*, "Effect of alkalis on iron-based Fischer-Tropsch synthesis catalysts: Alkali-FeOx interaction, reduction, and catalytic performance,"

Appl Catal A Gen, vol. 528, pp. 131–141, Nov. 2016, doi: 10.1016/j.apcata.2016.10.006.

[90] J. Li *et al.*, "Alkalis in iron-based Fischer–Tropsch synthesis catalysts: distribution, migration and promotion," *Journal of Chemical Technology & Biotechnology*, vol. 92, no. 6, pp. 1472–1480, Jun. 2017, doi: 10.1002/jctb.5152.

[91] C. Wei *et al.*, "The evolutions of carbon and iron species modified by Na and their tuning effect on the hydrogenation of CO2 to olefins," *Appl Surf Sci*, vol. 525, p. 146622, Sep. 2020, doi: 10.1016/j.apsusc.2020.146622.

[92] J.-Y. Jia, Y.-L. Shan, Y.-X. Tuo, H. Yan, X. Feng, and D. Chen, "Review of Iron-Based Catalysts for Carbon Dioxide Fischer–Tropsch Synthesis," *Transactions of Tianjin University*, vol. 30, no. 2, pp. 178–197, Apr. 2024, doi: 10.1007/s12209-024-00392-3.

[93] P. Zhai *et al.*, "Highly Tunable Selectivity for Syngas-Derived Alkenes over Zinc and Sodium-Modulated Fe $_5$ C $_2$ Catalyst," *Angewandte Chemie International Edition*, vol. 55, no. 34, pp. 9902–9907, Aug. 2016, doi: 10.1002/anie.201603556.

[94] P. Tian, M. Gu, R. Qiu, Z. Yang, F. Xuan, and M. Zhu, "Tunable Carbon Dioxide Activation Pathway over Iron Oxide Catalysts: Effects of Potassium," *Ind Eng Chem Res*, vol. 60, no. 24, pp. 8705–8713, Jun. 2021, doi: 10.1021/acs.iecr.1c01592.

[95] Y. Liu *et al.*, "CO2 hydrogenation to olefins on supported iron catalysts: Effects of support properties on carbon-containing species and product distribution," *Fuel*, vol. 324, p. 124649, Sep. 2022, doi: 10.1016/j.fuel.2022.124649.

[96] F. Ding *et al.*, "CO $_2$ Hydrogenation to Hydrocarbons over Iron-based Catalyst: Effects of Physicochemical Properties of Al $_2$ O $_3$ Supports," *Ind Eng Chem Res*, vol. 53, no. 45, pp. 17563–17569, Nov. 2014, doi: 10.1021/ie5031166.

[97] J. Wei *et al.*, "Directly converting CO2 into a gasoline fuel," *Nat Commun*, vol. 8, no. May, pp. 1–8, 2017, doi: 10.1038/ncomms15174.

[98] J. L. Weber, I. Dugulan, P. E. de Jongh, and K. P. de Jong, "Bifunctional Catalysis for the Conversion of Synthesis Gas to Olefins and Aromatics," *ChemCatChem*, vol. 10, no. 5, pp. 1107–1112, 2018, doi: 10.1002/cctc.201701667.

[99] X. Cui *et al.*, "Selective Production of Aromatics Directly from Carbon Dioxide Hydrogenation," *ACS Catal*, vol. 9, no. 5, pp. 3866–3876, May 2019, doi: 10.1021/acscatal.9b00640.

[100] F. Song *et al.*, "FeMn@HZSM-5 capsule catalyst for light olefins direct synthesis via Fischer-Tropsch synthesis: Studies on depressing the CO2 formation," *Appl Catal B*, vol. 300, no. June 2021, p. 120713, 2022, doi: 10.1016/j.apcatb.2021.120713.

[101] J. Fuhse and F. Bandermann, "Conversion of organic oxygen compounds and their mixtures on H-ZSM-5," *Chem Eng Technol*, vol. 10, no. 1, pp. 323–329, Jan. 1987, doi: 10.1002/CEAT.270100139.

[102] J. Wei *et al.*, "Directly converting CO2 into a gasoline fuel," *Nat Commun*, vol. 8, no. 1, p. 15174, May 2017, doi: 10.1038/ncomms15174.

[103] J. Wei *et al.*, "Precisely regulating Brønsted acid sites to promote the synthesis of light aromatics via CO2 hydrogenation," *Appl Catal B*, vol. 283, p. 119648, Apr. 2021, doi: 10.1016/J.APCATB.2020.119648.

[104] J. L. Weber *et al.*, "Effect of proximity and support material on deactivation of bifunctional catalysts for the conversion of synthesis gas to olefins and aromatics," *Catal Today*, vol. 342, no. August 2018, pp. 161–166, 2020, doi: 10.1016/j.cattod.2019.02.002.

[105] M. Li, M. A. Nawaz, G. Song, W. Q. Zaman, and D. Liu, "Influential Role of Elemental Migration in a Composite Iron − Zeolite Catalyst for the Synthesis of Aromatics from Syngas," 2020, doi: 10.1021/acs.iecr.0c01282.

[106] Y. Wang *et al.*, "Visualizing Element Migration over Bifunctional Metal-Zeolite Catalysts and its Impact on Catalysis," *Angewandte Chemie - International Edition*, vol. 60, no. 32, pp. 17735–17743, 2021, doi: 10.1002/anie.202107264.

[107] T. Wang *et al.*, "Sodium-Mediated Bimetallic Fe–Ni Catalyst Boosts Stable and Selective Production of Light Aromatics over HZSM-5 Zeolite," *ACS Catal*, vol. 11, no. 6, pp. 3553–3574, Mar. 2021, doi: 10.1021/acscatal.1c00169.

[108] R. Wang *et al.*, "Critical role of sodium migration in iron-based FT- zeolite tandem catalyst system for syngas hydrogenation to gasoline," *Appl Catal B*, vol. 322, no. September 2022, p. 122132, 2023, doi: 10.1016/j.apcatb.2022.122132.

[109] Y. Zhong *et al.*, "Fabrication of Magnetic Pd/MOF Hollow Nanospheres with Double-Shell Structure: Toward Highly Efficient and Recyclable Nanocatalysts for Hydrogenation Reaction," *ACS Appl Mater Interfaces*, vol. 11, no. 35, pp. 32251–32260, Sep. 2019, doi: https://doi.org/10.1021/acsami.9b07864.

[110] C. Wen *et al.*, "Single-Step Selective Conversion of Carbon Dioxide to Aromatics over Na-Fe3O4/Hierarchical HZSM-5 Zeolite Catalyst," *Energy and Fuels*, vol. 34, no. 9, pp. 11282–11289, 2020, doi: 10.1021/acs.energyfuels.0c02120.

[111] W. Chen, Z. Fan, X. Pan, and X. Bao, "Effect of confinement in carbon nanotubes on the activity of Fischer-Tropsch iron catalyst," *J Am Chem Soc*, vol. 130, no. 29, pp. 9414–9419, 2008, doi: 10.1021/ja8008192.

[112] B. Gu *et al.*, "Synergy of nanoconfinement and promotion in the design of efficient supported iron catalysts for direct olefin synthesis from syngas," *J Catal*, vol. 376, pp. 1–16, 2019, doi: 10.1016/j.jcat.2019.06.035.

[113] A. Bressel, T. Donauer, S. Sealy, and Y. Traa, "Influence of aluminum content, crystallinity and crystallite size of zeolite Pd/H-ZSM-5 on the catalytic performance in the dehydroalkylation of toluene with ethane," *Microporous and Mesoporous Materials*, vol. 109, no. 1–3, pp. 278–286, Mar. 2008, doi: 10.1016/j.micromeso.2007.05.002.

[114] K. A. Tarach, K. Góra-Marek, J. Martinez-Triguero, and I. Melián-Cabrera, "Acidity and accessibility studies of desilicated ZSM-5 zeolites in terms of their effectiveness as catalysts in acid-catalyzed cracking processes," *Catal Sci Technol*, vol. 7, no. 4, pp. 858–873, 2017, doi: 10.1039/C6CY02609E.

[115] R. Murciano, J. M. Serra, and A. Martínez, "Direct hydrogenation of CO2 to aromatics via Fischer-Tropsch route over tandem K-Fe/Al2O3+H-ZSM-5 catalysts: Influence of zeolite properties," *Catal Today*, vol. 427, p. 114404, Feb. 2024, doi: 10.1016/j.cattod.2023.114404.

[116] S. Al-Khattaf, S. A. Ali, A. M. Aitani, N. Žilková, D. Kubička, and J. Čejka, "Recent Advances in Reactions of Alkylbenzenes Over Novel Zeolites: The Effects of Zeolite Structure and Morphology," *Catalysis Reviews*, vol. 56, no. 4, pp. 333–402, Oct. 2014, doi: 10.1080/01614940.2014.946846.

[117] R. W. Weber, K. P. Möller, and C. T. O'Connor, "The chemical vapour and liquid deposition of tetraethoxysilane on ZSM-5, mordenite and beta," *Microporous and Mesoporous Materials*, vol. 35–36, pp. 533–543, Apr. 2000, doi: 10.1016/S1387-1811(99)00248-6.

[118] S. Zheng, H. R. Heydenrych, A. Jentys, and J. A. Lercher, "Influence of Surface Modification on the Acid Site Distribution of HZSM-5," *J Phys Chem B*, vol. 106, no. 37, pp. 9552–9558, Sep. 2002, doi: 10.1021/jp014091d.

[119] J. Wei, J. Sun, Z. Wen, C. Fang, Q. Ge, and H. Xu, "New insights into the effect of sodium on Fe3O4- based nanocatalysts for CO2 hydrogenation to light olefins," *Catal Sci Technol*, vol. 6, no. 13, pp. 4786–4793, 2016, doi: 10.1039/c6cy00160b.

[120] G. Tyler and J. Yvon, "ICP-OES, ICP-MS and AAS Techniques Compared".

[121] "XRF Theory 1 - Overview of XRF - THEORY OF XRF Getting acquainted with the principles Peter Brouwer - Studocu." Accessed: Nov. 21, 2023. [Online]. Available: https://www.studocu.com/row/document/ghulam-ishaq-khan-institute-of-engineering-sciences-and-technology/characterization-of-nanomaterials/xrf-theory-1-overview-of-xrf/11301618

[122] M. Naderi, "Surface Area," in *Progress in Filtration and Separation*, Elsevier, 2015, pp. 585–608. doi: 10.1016/B978-0-12-384746-1.00014-8.

[123] S. Brunauer, P. H. Emmett, and E. Teller, "Adsorption of Gases in Multimolecular Layers," *J Am Chem Soc*, vol. 60, no. 2, pp. 309–319, Feb. 1938, doi: 10.1021/ja01269a023.

[124] W. D. Harkins and G. Jura, "Surfaces of Solids. XIII. A Vapor Adsorption Method for the Determination of the Area of a Solid without the Assumption of a Molecular Area, and the Areas Occupied by Nitrogen and Other Molecules on the Surface of a Solid," *J Am Chem Soc*, vol. 66, no. 8, pp. 1366–1373, Aug. 1944, doi: 10.1021/ja01236a048.

[125] E. P. Barrett, L. G. Joyner, and P. P. Halenda, "The Determination of Pore Volume and Area Distributions in Porous Substances. I. Computations from Nitrogen Isotherms," *J Am Chem Soc*, vol. 73, no. 1, pp. 373–380, Jan. 1951, doi: 10.1021/JA01145A126/ASSET/JA01145A126.FP.PNG_V03.

[126] A. A. Bunaciu, E. gabriela Udriştioiu, and H. Y. Aboul-Enein, "X-Ray Diffraction: Instrumentation and Applications," *Crit Rev Anal Chem*, vol. 45, no. 4, pp. 289–299, Oct. 2015, doi: 10.1080/10408347.2014.949616.

[127] B. D. (Bernard D. Cullity, *Elements of x-ray diffraction*. Addison-Wesley Publishing Company, Inc, 1978.

[128] J.-W. Lee, W. B. Park, J. H. Lee, S. P. Singh, and K.-S. Sohn, "A deep-learning technique for phase identification in multiphase inorganic compounds using synthetic XRD powder patterns," *Nat Commun*, vol. 11, no. 1, p. 86, Jan. 2020, doi: 10.1038/s41467-019-13749-3.

[129] V. Uvarov and I. Popov, "Metrological characterization of X-ray diffraction methods for determination of crystallite size in nano-scale materials," *Mater Charact*, vol. 58, no. 10, pp. 883–891, Oct. 2007, doi: 10.1016/j.matchar.2006.09.002.

[130] V. Jorik, "Semiempirical approach to determinationof framework aluminum content in faujasite-type zeolites by X-ray powder diffraction," *Zeolites*, vol. 13, no. 3, pp. 187–191, Mar. 1993, doi: 10.1016/S0144-2449(05)80276-3.

[131] S. Bonnamy and A. Oberlin, "Transmission Electron Microscopy," in *Materials Science and Engineering of Carbon*, Elsevier, 2016, pp. 45–70. doi: 10.1016/B978-0-12-805256-3.00004-0.

[132] Z. L. Wang, "Transmission Electron Microscopy of Shape-Controlled Nanocrystals and Their Assemblies," *J Phys Chem B*, vol. 104, no. 6, pp. 1153–1175, Feb. 2000, doi: 10.1021/jp993593c.

[133] F. Huber *et al.*, "Remarks on the passivation of reduced Cu-, Ni-, Fe-, Co-based catalysts," *Catal Letters*, vol. 110, no. 3–4, pp. 211–220, Sep. 2006, doi: 10.1007/s10562-006-0111-1.

[134] M. Abd Mutalib, M. A. Rahman, M. H. D. Othman, A. F. Ismail, and J. Jaafar, "Scanning Electron Microscopy (SEM) and Energy-Dispersive X-Ray (EDX) Spectroscopy," in *Membrane Characterization*, Elsevier, 2017, pp. 161–179. doi: 10.1016/B978-0-444-63776-5.00009-7.

[135] M. Scimeca, S. Bischetti, H. K. Lamsira, R. Bonfiglio, and E. Bonanno, "Energy Dispersive X-ray (EDX) microanalysis: A powerful tool in biomedical research and diagnosis," *European Journal of Histochemistry*, Mar. 2018, doi: 10.4081/ejh.2018.2841.

[136] V. Hodoroaba, S. Rades, and W. E. S. Unger, "Inspection of morphology and elemental imaging of single nanoparticles by high-resolution SEM/EDX in transmission mode," *Surface and Interface Analysis*, vol. 46, no. 10–11, pp. 945–948, Oct. 2014, doi: 10.1002/sia.5426.

[137] J. T. Scanlon and D. E. Willis, "Calculation of flame ionization detector relative response factors using the effective carbon number concept," *J Chromatogr Sci*, vol. 23, no. 8, pp. 333–340, 1985, doi: 10.1093/chromsci/23.8.333.

[138] C. López Cruz, "Materiales mesoporosos y zeolitas deslaminadas como soportes para catalizadores de Fischer-Tropsch basados en Cobalto.," Universitat Politècnica de València, Valencia (Spain), 2004. doi: 10.4995/Thesis/10251/131736.

[139] W. A. Dietz, "Response Factors for Gas Chromatographic Analyses," *J Chromatogr Sci*, vol. 5, no. 2, pp. 68–71, Feb. 1967, doi: 10.1093/chromsci/5.2.68.

[140] G. Ma *et al.*, "An Na-modified Fe@C core-shell catalyst for the enhanced production of gasoline-range hydrocarbons via Fischer-Tropsch synthesis †," 2020, doi: 10.1039/d0ra01036g.

[141] J. M. Cho, M. H. Jeong, • Jong, and W. Bae, "Fischer-Tropsch synthesis on potassium-modified Fe 3 O 4 nanoparticles," *Research on Chemical Intermediates*, vol. 42, pp. 335–350, 2016, doi: 10.1007/s11164-015-2360-3.

[142] D. P. Serrano, J. Aguado, J. M. Escola, J. M. Rodriguez, and A. Peral, "Effect of the organic moiety nature on the synthesis of hierarchical ZSM-5 from silanized protozeolitic units," *J Mater Chem*, vol. 18, no. 35, pp. 4210–4218, 2008, doi: 10.1039/b805502e.

[143] Y. Xu *et al.*, "Selective production of aromatics from CO 2," *Catal Sci Technol*, vol. 9, no. 3, pp. 593–610, 2019, doi: 10.1039/c8cy02024h.

[144] J. Wei *et al.*, "Catalytic Hydrogenation of CO 2 to Isoparaffins over Fe-Based Multifunctional Catalysts," 2018, doi: 10.1021/acscatal.8b02267.

[145] Z. Zhang *et al.*, "Effects of the reducing gas atmosphere on performance of FeCeNa catalyst for the hydrogenation of CO 2 to olefins," *Chemical Engineering Journal*, vol. 428, pp. 1385–8947, 2022, doi: 10.1016/j.cej.2021.131388.

[146] E. De Smit *et al.*, "Stability and reactivity of ε-X-θ iron carbide catalyst phases in fischer-tropsch synthesis: Controlling μc," *J Am Chem Soc*, vol. 132, no. 42, pp. 14928–14941, Oct. 2010, doi: 10.1021/JA105853Q/SUPPL_FILE/JA105853Q_SI_001.PDF.

[147] T. Riedel, H. Schulz, G. Schaub, K.-W. Jun, J.-S. Hwang, and K.-W. Lee, "Fischer–Tropsch on Iron with H $_2$ /CO and H $_2$ /CO $_2$ as Synthesis Gases: The Episodes of Formation of the Fischer–Tropsch Regime and Construction of the Catalyst," *Top Catal*, vol. 26, no. 1–4, pp. 41–54, Dec. 2003, doi: 10.1023/B:TOCA.0000012986.46680.28.

[148] G. Bian, A. Oonuki, N. Koizumi, H. Nomoto, and M. Yamada, "Studies with a precipitated iron Fischer-Tropsch catalyst reduced by H 2 or CO," *J Mol Catal A Chem*, vol. 186, pp. 203–213, 2002.

[149] H. Jin Chae *et al.*, "Catalytic Technologies for CO Hydrogenation for the Production of Light Hydrocarbons and Middle Distillates," *Catalysts*, 2020, doi: 10.3390/catal10010099.

[150] R. M. M. Abbaslou, A. Tavassoli, J. Soltan, and A. K. Dalai, "Iron catalysts supported on carbon nanotubes for Fischer-Tropsch synthesis: Effect of catalytic site position," *Appl Catal A Gen*, vol. 367, no. 1–2, pp. 47–52, 2009, doi: 10.1016/j.apcata.2009.07.025.

[151] Y. Xu, T. Wang, C. Shi, B. Liu, F. Jiang, and X. Liu, "Experimental Investigation on the Two-Sided Effect of Acidic HZSM-5 on the Catalytic Performance of Composite Fe-Based Fischer-Tropsch Catalysts and HZSM-5 Zeolite in the Production of Aromatics from CO2/H2," *Ind Eng Chem Res*, vol. 59, no. 18, pp. 8581–8591, 2020, doi: 10.1021/acs.iecr.0c00992.

[152] Q. Yang, A. Skrypnik, A. Matvienko, H. Lund, M. Holena, and E. V. Kondratenko, "Revealing property-performance relationships for efficient CO2 hydrogenation to higher hydrocarbons over Fe-based catalysts: Statistical analysis of literature data and its experimental validation," *Appl Catal B*, vol. 282, no. September 2020, p. 119554, 2021, doi: 10.1016/j.apcatb.2020.119554.

[153] J. Chai, R. Pestman, F.-K. Chiang, Z. Men, P. Wang, and E. J. M. Hensen, "Influence of carbon deposits on Fe-carbide for the Fischer-Tropsch reaction," *Journal of Catalysis* , vol. 416, pp. 289–300, 2022, doi: 10.1016/j.jcat.2022.11.002.

[154] C.D. Wagner et al., "NIST X-ray Photoelectron Spectroscopy (XPS) Database 20, Version 3.4," web version. Accessed: May 27, 2023. [Online]. Available: https://srdata.nist.gov/xps/

[155] A. P. Grosvenor, B. A. Kobe, M. C. Biesinger, and N. S. McIntyre, "Investigation of multiplet splitting of Fe 2p XPS spectra and bonding in iron compounds," *Surface and Interface Analysis*, vol. 36, no. 12, pp. 1564–1574, Dec. 2004, doi: 10.1002/SIA.1984.

[156] L. Guo *et al.*, "Directly converting carbon dioxide to linear α-olefins on bio-promoted catalysts," *Commun Chem*, 2018, doi: 10.1038/s42004-018-0012-4.

[157] A. Furlan, U. Jansson, J. Lu, L. Hultman, and M. Magnuson, "Structure and bonding in amorphous iron carbide thin films," *Journal of Physics: Condensed Matter*, vol. 27, p. 045002, 2015, doi: 10.1088/0953-8984/27/4/045002.

[158] J. B. Li, H. F. Ma, H. T. Zhang, Q. W. Sun, W. Y. Ying, and D. Y. Fang, "Sodium promoter on iron-based catalyst for direct catalytic synthesis of light alkenes from syngas," *Fuel Processing Technology*, vol. 125, pp. 119–124, 2014, doi: 10.1016/j.fuproc.2014.03.017.

[159] A. V. Karre, A. Kababji, E. L. Kugler, and D. B. Dadyburjor, "Effect of addition of zeolite to iron-based activated-carbon-supported catalyst for Fischer-Tropsch synthesis in separate beds and mixed beds," *Catal Today*, vol. 198, no. 1, pp. 280–288, 2012, doi: 10.1016/j.cattod.2012.04.068.

[160] H. M. Torres Galvis, J. H. Bitter, C. B. Khare, M. Ruitenbeek, A. I. Dugulan, and K. P. de Jong, "Supported Iron Nanoparticles as Catalysts for Sustainable Production of Lower Olefins," *Science (1979)*, vol. 335, no. 6070, pp. 835–838, Feb. 2012, doi: 10.1126/science.1215614.

[161] R. A. Friedel and R. B. Anderson, "Composition of Synthetic Liquid Fuels. I. Product Distribution and Analysis of C_5 —C_8 Paraffin Isomers from Cobalt Catalyst [1]," *J Am Chem Soc*, vol. 72, no. 3, pp. 1212–1215, Mar. 1950, doi: 10.1021/ja01159a039.

[162] R. L. Varma, N. N. Bakhshi, J. F. Mathews, and S. H. Ng, "Performance of dual-reactor system for conversion of syngas to aromatic-containing hydrocarbons," *Ind Eng Chem Res*, vol. 26, no. 2, pp. 183–188, Feb. 1987, doi: 10.1021/ie00062a001.

[163] A. K. Fellenberg *et al.*, "Iron and copper nanoparticles inside and outside carbon nanotubes: Nanoconfinement, migration, interaction and catalytic performance in Fischer-Tropsch synthesis," *J Catal*, vol. 404, pp. 306–323, 2021, doi: 10.1016/j.jcat.2021.09.034.

[164] Q. Xu, D. He, M. Fujiwara, M. Tanaka, Y. Souma, and H. Yamanaka, "Hydrogenation of carbon dioxide over Fe-Cu-Narzeolite composite catalysts: Na migration via solid-solid reaction and its effects on the catalytic activity," 1998.

[165] R. M. M. Abbaslou, A. Tavassoli, J. Soltan, and A. K. Dalai, "Iron catalysts supported on carbon nanotubes for Fischer-Tropsch synthesis: Effect of catalytic site position," *Appl Catal A Gen*, vol. 367, no. 1–2, pp. 47–52, 2009, doi: 10.1016/j.apcata.2009.07.025.

[166] Y. Yan *et al.*, "Carbon nanotube catalysts: recent advances in synthesis, characterization and applications," *Chem Soc Rev*, vol. 44, no. 10, pp. 3295–3346, 2015, doi: 10.1039/C4CS00492B.

[167] R. Liu, Y. Xu, Z. Li, and X. Ma, "A Facile and Efficient Modification of CNTs for Improved Fischer–Tropsch Performance on Iron Catalyst: Alkali Modification," *ChemCatChem*, vol. 8, no. 8, pp. 1454–1458, Apr. 2016, doi: 10.1002/cctc.201501219.

[168] D. R. Minett *et al.*, "Fe@CNT-monoliths for the conversion of carbon dioxide to hydrocarbons: structural characterisation and Fischer–Tropsch reactivity investigations," *Catal. Sci. Technol.*, vol. 4, no. 9, pp. 3351–3358, 2014, doi: 10.1039/C4CY00616J.

[169] R. M. M. Abbaslou, J. Soltan, and A. K. Dalai, "Effects of nanotubes pore size on the catalytic performances of iron catalysts supported on carbon nanotubes for Fischer-Tropsch synthesis," *Appl Catal A Gen*, vol. 379, no. 1–2, pp. 129–134, May 2010, doi: 10.1016/j.apcata.2010.03.006.

[170] Y. Chen, J. Wei, M. S. Duyar, V. V. Ordomsky, A. Y. Khodakov, and J. Liu, "Carbon-based catalysts for Fischer–Tropsch synthesis," *Chem Soc Rev*, vol. 50, no. 4, pp. 2337–2366, Mar. 2021, doi: 10.1039/D0CS00905A.

[171] W. Chen, Z. Fan, X. Pan, and X. Bao, "Effect of confinement in carbon nanotubes on the activity of Fischer-Tropsch iron catalyst," *J Am Chem Soc*, vol. 130, no. 29, pp. 9414–9419, 2008, doi: 10.1021/ja8008192.

[172] H. Xiong, M. A. M. Motchelaho, M. Moyo, L. L. Jewell, and N. J. Coville, "Correlating the preparation and performance of cobalt catalysts supported on carbon nanotubes and carbon spheres in the Fischer-Tropsch synthesis," *J Catal*, vol. 278, no. 1, pp. 26–40, 2011, doi: 10.1016/j.jcat.2010.11.010.

[173] H. Xiong, M. A. Motchelaho, M. Moyo, L. L. Jewell, and N. J. Coville, "Fischer-Tropsch synthesis: Iron-based catalysts supported on nitrogen-doped carbon nanotubes synthesized by post-doping," *Appl Catal A Gen*,

vol. 482, no. November 2018, pp. 377–386, 2014, doi: 10.1016/j.apcata.2014.06.019.

[174] A. Corma, "Inorganic Solid Acids and Their Use in Acid-Catalyzed Hydrocarbon Reactions," *Chem Rev*, vol. 95, no. 3, pp. 559–614, May 1995, doi: 10.1021/cr00035a006.

[175] T. Armaroli *et al.*, "Effects of crystal size and Si/Al ratio on the surface properties of H-ZSM-5 zeolites," *Appl Catal A Gen*, vol. 306, pp. 78–84, Jun. 2006, doi: 10.1016/j.apcata.2006.03.030.

[176] F. Yi *et al.*, "Correlation of Brønsted acid sites and Al distribution in ZSM-5 zeolites and their effects on butenes conversion," *Fuel*, vol. 320, p. 123729, Jul. 2022, doi: 10.1016/j.fuel.2022.123729.

[177] J. Yang *et al.*, "Enhanced aromatic selectivity by the sheet-like ZSM-5 in syngas conversion," *Journal of Energy Chemistry*, vol. 35, pp. 44–48, Aug. 2019, doi: 10.1016/j.jechem.2018.10.008.

[178] P. Morales-Pacheco, F. Alvarez-Ramirez, P. Del Angel, L. Bucio, and J. M. Domínguez, "Synthesis and Structural Properties of Zeolytic Nanocrystals I. MFI Type Zeolites," *The Journal of Physical Chemistry C*, vol. 111, no. 6, pp. 2368–2378, Feb. 2007, doi: 10.1021/jp064780v.

[179] C. T. Nimlos *et al.*, "Experimental and Theoretical Assessments of Aluminum Proximity in MFI Zeolites and Its Alteration by Organic and Inorganic Structure-Directing Agents," *Chemistry of Materials*, vol. 32, no. 21, pp. 9277–9298, Nov. 2020, doi: 10.1021/acs.chemmater.0c03154.

[180] P. He *et al.*, "Impact of Al sites on the methane co-aromatization with alkanes over Zn/HZSM-5," *Catal Today*, vol. 323, pp. 94–104, Feb. 2019, doi: 10.1016/j.cattod.2018.05.051.

[181] T. N. Pham, V. Nguyen, H. Nguyen-Phu, B. Wang, and S. Crossley, "Influence of Brønsted Acid Site Proximity on Alkane Cracking in MFI Zeolites," *ACS Catal*, vol. 13, no. 2, pp. 1359–1370, Jan. 2023, doi: 10.1021/acscatal.2c05291.

[182] Y. Zhang *et al.*, "Promotion of protolytic pentane conversion on H-MFI zeolite by proximity of extra-framework aluminum oxide and Brønsted

acid sites," *J Catal*, vol. 370, pp. 424–433, Feb. 2019, doi: 10.1016/j.jcat.2019.01.006.

[183] E. BRUNNER, "Magic-angle-spinning NMR studies of acid sites in zeolite H-ZSM-5," *J Catal*, vol. 127, no. 1, pp. 34–41, Jan. 1991, doi: 10.1016/0021-9517(91)90206-J.

[184] G. L. Woolery, G. H. Kuehl, H. C. Timken, A. W. Chester, and J. C. Vartuli, "On the nature of framework Brønsted and Lewis acid sites in ZSM-5," *Zeolites*, vol. 19, no. 4, pp. 288–296, Oct. 1997, doi: 10.1016/S0144-2449(97)00086-9.

[185] J.-P. Gilson *et al.*, "Penta-co-ordinated aluminium in zeolites and aluminosilicates," *J Chem Soc Chem Commun*, no. 2, p. 91, 1987, doi: 10.1039/c39870000091.

[186] J. KANELLOPOULOS, A. UNGER, W. SCHWIEGER, and D. FREUDE, "Catalytic and multinuclear MAS NMR studies of a thermally treated zeolite ZSM-5," *J Catal*, vol. 237, no. 2, pp. 416–425, Jan. 2006, doi: 10.1016/j.jcat.2005.11.030.

[187] K.-Y. Lee, S.-W. Lee, and S.-K. Ihm, "Acid Strength Control in MFI Zeolite for the Methanol-to-Hydrocarbons (MTH) Reaction," *Ind Eng Chem Res*, vol. 53, no. 24, pp. 10072–10079, Jun. 2014, doi: 10.1021/ie5009037.

[188] G. Busca, "The surface acidity of solid oxides and its characterization by IR spectroscopic methods. An attempt at systematization," *Physical Chemistry Chemical Physics*, vol. 1, no. 5, pp. 723–736, 1999, doi: 10.1039/a808366e.

[189] R. Murciano, J. M. Serra, and A. Martínez, "Direct hydrogenation of CO2 to aromatics via Fischer-Tropsch route over tandem K-Fe/Al2O3+H-ZSM-5 catalysts: Influence of zeolite properties," *Catal Today*, vol. 427, p. 114404, Feb. 2024, doi: 10.1016/j.cattod.2023.114404.

[190] J. Zhang *et al.*, "Integrating HZSM-5 nanosheets with Fe-Co bimetallic catalyst toward efficient CO2-to-gasoline fuel conversion," *Fuel*, vol. 357, p. 129904, Feb. 2024, doi: 10.1016/j.fuel.2023.129904.

[191] Q. Jiang *et al.*, "Selective Hydrogenation of CO_2 to Aromatics over Composite Catalyst Comprising NaZnFe and Polyethylene Glycol-Modified HZSM-5 with Intra- and Intercrystalline Mesoporous Structure," *Ind Eng Chem Res*, vol. 62, no. 23, pp. 9188–9200, Jun. 2023, doi: 10.1021/acs.iecr.3c00915.

[192] G. Singh *et al.*, "Emerging trends in porous materials for CO_2 capture and conversion," *Chem Soc Rev*, vol. 49, no. 13, pp. 4360–4404, 2020, doi: 10.1039/D0CS00075B.

[193] A. Ramirez *et al.*, "Selectivity descriptors for the direct hydrogenation of CO2 to hydrocarbons during zeolite-mediated bifunctional catalysis," *Nat Commun*, vol. 12, no. 1, p. 5914, Oct. 2021, doi: 10.1038/s41467-021-26090-5.

[194] Y. Ou *et al.*, "Deep mitigation of CO2 and non-CO2 greenhouse gases toward 1.5 °C and 2 °C futures," *Nat Commun*, vol. 12, no. 1, p. 6245, Oct. 2021, doi: 10.1038/s41467-021-26509-z.

[195] S.-K. Kim *et al.*, "Widespread irreversible changes in surface temperature and precipitation in response to CO2 forcing," *Nat Clim Chang*, vol. 12, no. 9, pp. 834–840, Sep. 2022, doi: 10.1038/s41558-022-01452-z.

[196] Y. Li *et al.*, "Direct conversion of carbon dioxide into liquid fuels and chemicals by coupling green hydrogen at high temperature," *Appl Catal B*, vol. 324, p. 122299, May 2023, doi: 10.1016/j.apcatb.2022.122299.

[197] P. Yan, H. Peng, J. Vogrin, H. Rabiee, and Z. Zhu, "Selective CO_2 hydrogenation over zeolite-based catalysts for targeted high-value products," *J Mater Chem A Mater*, vol. 11, no. 34, pp. 17938–17960, 2023, doi: 10.1039/D3TA03150K.

[198] Q. Ji *et al.*, "Direct synthesis of iso-olefins from carbon dioxide hydrogenation via tandem catalysis," *Cell Rep Phys Sci*, vol. 5, no. 2, p. 101826, Feb. 2024, doi: 10.1016/j.xcrp.2024.101826.

[199] C. C. Amoo, J. I. Orege, Q. Ge, and J. Sun, "Translating clean liquid fuels synthesis with low aromatics over NaFe@C/HZSM-22 directly in CO2 hydrogenation," *Appl Catal B*, vol. 340, p. 123193, Jan. 2024, doi: 10.1016/j.apcatb.2023.123193.

[200] C. Xing *et al.*, "Syngas to isoparaffins: Rationalizing selectivity over zeolites assisted by a predictive isomerization model," *Fuel*, vol. 285, p. 119233, Feb. 2021, doi: 10.1016/j.fuel.2020.119233.

[201] A. Ramirez *et al.*, "Selectivity descriptors for the direct hydrogenation of CO2 to hydrocarbons during zeolite-mediated bifunctional catalysis," *Nat Commun*, vol. 12, no. 1, p. 5914, Oct. 2021, doi: 10.1038/s41467-021-26090-5.

[202] C. C. Amoo, C. Xing, N. Tsubaki, and J. Sun, "Tandem Reactions over Zeolite-Based Catalysts in Syngas Conversion," *ACS Cent Sci*, vol. 8, no. 8, pp. 1047–1062, Aug. 2022, doi: 10.1021/acscentsci.2c00434.

[203] S. Jeong, K.-J. Jeon, Y.-K. Park, B.-J. Kim, K.-H. Chung, and S.-C. Jung, "Catalytic Properties of Microporous Zeolite Catalysts in Synthesis of Isosorbide from Sorbitol by Dehydration," *Catalysts*, vol. 10, no. 2, p. 148, Jan. 2020, doi: 10.3390/catal10020148.

[204] M.K. Rubin and P. Chu, "Composition of synthetic porous crystalline material, its synthesis and use," US Patent 4,954,325, 1990

[205] C. Delitala *et al.*, "Synthesis of MCM-22 zeolites of different Si/Al ratio and their structural, morphological and textural characterisation," *Microporous and Mesoporous Materials*, vol. 118, no. 1–3, pp. 1–10, Feb. 2009, doi: 10.1016/j.micromeso.2008.07.047.

[206] F. Rosso *et al.*, "Insight on MWW siliceous zeolites: From 2D precursors toward 3D structure," *Microporous and Mesoporous Materials*, vol. 366, p. 112924, Feb. 2024, doi: 10.1016/j.micromeso.2023.112924.

[207] M. E. Leonowicz, J. A. Lawton, S. L. Lawton, and M. K. Rubin, "MCM-22: A Molecular Sieve with Two Independent Multidimensional Channel Systems," *Science (1979)*, vol. 264, no. 5167, pp. 1910–1913, Jun. 1994, doi: 10.1126/science.264.5167.1910.

[208] A. Ahmad, S. R. Naqvi, M. Rafique, H. Nasir, and A. Sarosh, "Synthesis, characterization and catalytic testing of MCM-22 derived catalysts for n-hexane cracking," *Sci Rep*, vol. 10, no. 1, p. 21786, Dec. 2020, doi: 10.1038/s41598-020-78746-9.

[209] M. Rutkowska *et al.*, "Modification of MCM-22 Zeolite and Its Derivatives with Iron for the Application in N2O Decomposition," *Catalysts*, vol. 10, no. 10, p. 1139, Oct. 2020, doi: 10.3390/catal10101139.

[210] A. Corma, V. Fornes, S. B. Pergher, Th. L. M. Maesen, and J. G. Buglass, "Delaminated zeolite precursors as selective acidic catalysts," *Nature*, vol. 396, no. 6709, pp. 353–356, Nov. 1998, doi: 10.1038/24592.

[211] P. Frontera, F. Testa, R. Aiello, and J. B. Nagy, "The behaviour of the framework aluminium during ITQ-2 formation from MCM-22(P)," 2005, pp. 271–278. doi: 10.1016/S0167-2991(05)80349-0.

[212] E. García-Hurtado, A. Rodríguez-Fernández, M. Moliner, and C. Martínez, "CO $_2$ hydrogenation using bifunctional catalysts based on K-promoted iron oxide and zeolite: influence of the zeolite structure and crystal size," *Catal Sci Technol*, vol. 10, no. 16, pp. 5648–5658, 2020, doi: 10.1039/D0CY00712A.

[213] J. Wei *et al.*, "Catalytic Hydrogenation of CO2 to Isoparaffins over Fe-Based Multifunctional Catalysts," *ACS Catal*, vol. 8, no. 11, pp. 9958–9967, 2018, doi: 10.1021/acscatal.8b02267.

[214] H. Tian *et al.*, "Tandem catalysts composed of different morphology HZSM-5 and metal oxides for CO2 hydrogenation to aromatics," *Fuel*, vol. 314, p. 123119, Apr. 2022, doi: 10.1016/j.fuel.2021.123119.

[215] A. Martínez, E. Peris, and G. Sastre, "Dehydroaromatization of methane under non-oxidative conditions over bifunctional Mo/ITQ-2 catalysts," *Catal Today*, vol. 107–108, pp. 676–684, Oct. 2005, doi: 10.1016/j.cattod.2005.07.051.

[216] Q. Zhang, J. Yu, and A. Corma, "Applications of Zeolites to C1 Chemistry: Recent Advances, Challenges, and Opportunities," *Advanced Materials*, vol. 32, no. 44, Nov. 2020, doi: 10.1002/adma.202002927.

[217] X. Peng *et al.*, "Impact of Hydrogenolysis on the Selectivity of the Fischer–Tropsch Synthesis: Diesel Fuel Production over Mesoporous Zeolite-Y-Supported Cobalt Nanoparticles," *Angewandte Chemie International Edition*, vol. 54, no. 15, pp. 4553–4556, Apr. 2015, doi: 10.1002/anie.201411708.

[218] J. Chen *et al.*, "Regulation of Framework Aluminum Siting and Acid Distribution in H-MCM-22 by Boron Incorporation and Its Effect on the Catalytic Performance in Methanol to Hydrocarbons," *ACS Catal*, vol. 6, no. 4, pp. 2299–2313, Apr. 2016, doi: 10.1021/acscatal.5b02862.

[219] A. Martínez, S. Valencia, R. Murciano, H. S. Cerqueira, A. F. Costa, and E. F. S.-Aguiar, "Catalytic behavior of hybrid Co/SiO2-(medium-pore) zeolite catalysts during the one-stage conversion of syngas to gasoline," *Appl Catal A Gen*, vol. 346, no. 1–2, pp. 117–125, Aug. 2008, doi: 10.1016/j.apcata.2008.05.015.

[220] A. Martínez and E. Peris, "Non-oxidative methane dehydroaromatization on Mo/HZSM-5 catalysts: Tuning the acidic and catalytic properties through partial exchange of zeolite protons with alkali and alkaline-earth cations," *Appl Catal A Gen*, vol. 515, pp. 32–44, Apr. 2016, doi: 10.1016/j.apcata.2016.01.044.

Appendix 1

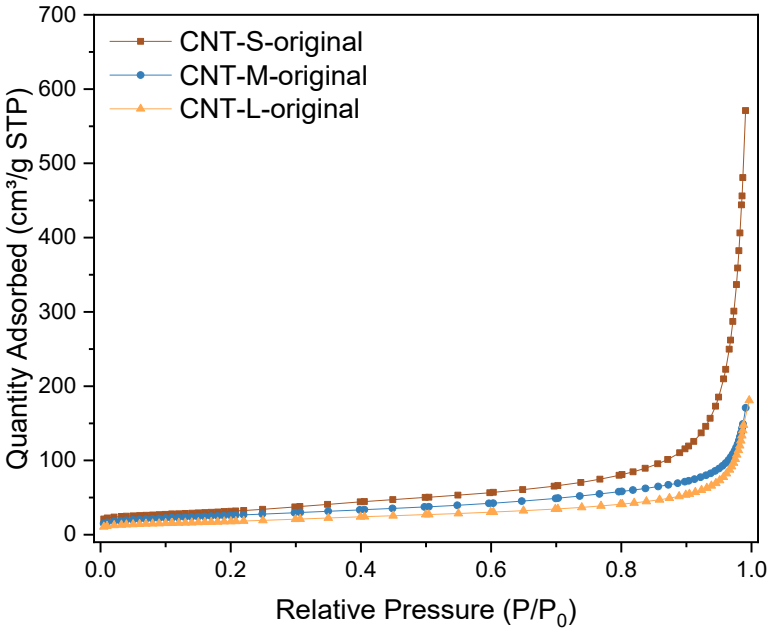


Figure A1. 1. N_2 adsorption of original CNT, without any treatment.

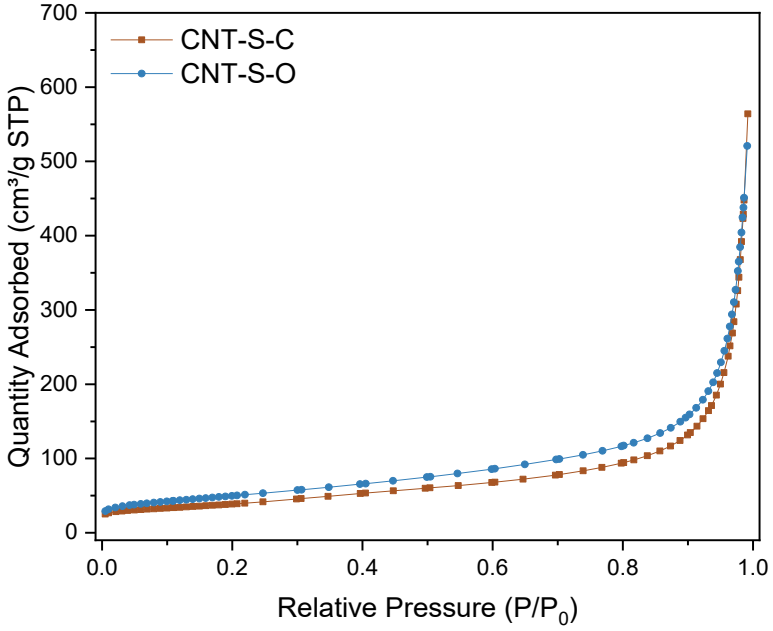


Figure A1. 2. N_2 adsorption of small CNT (CNT-S-original), subjected to mild acid treatment (MAT) and strong acid treatment (SAT).

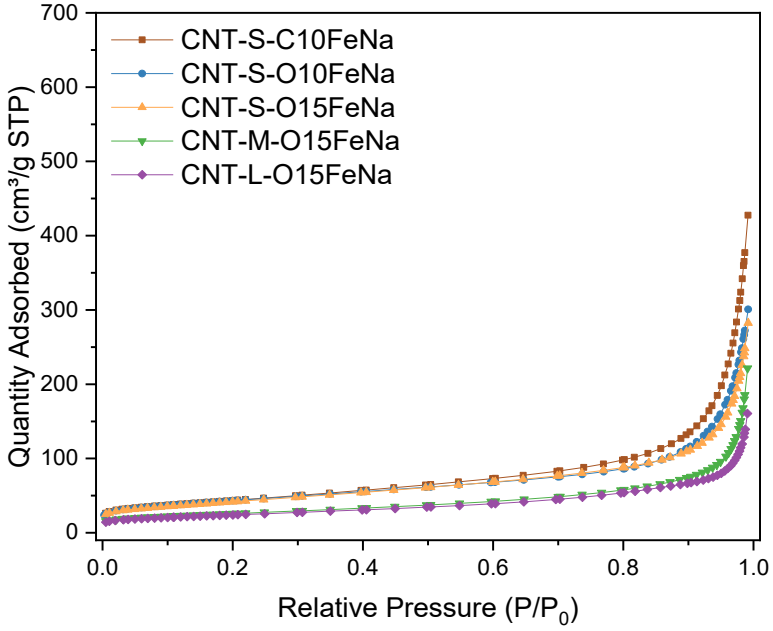
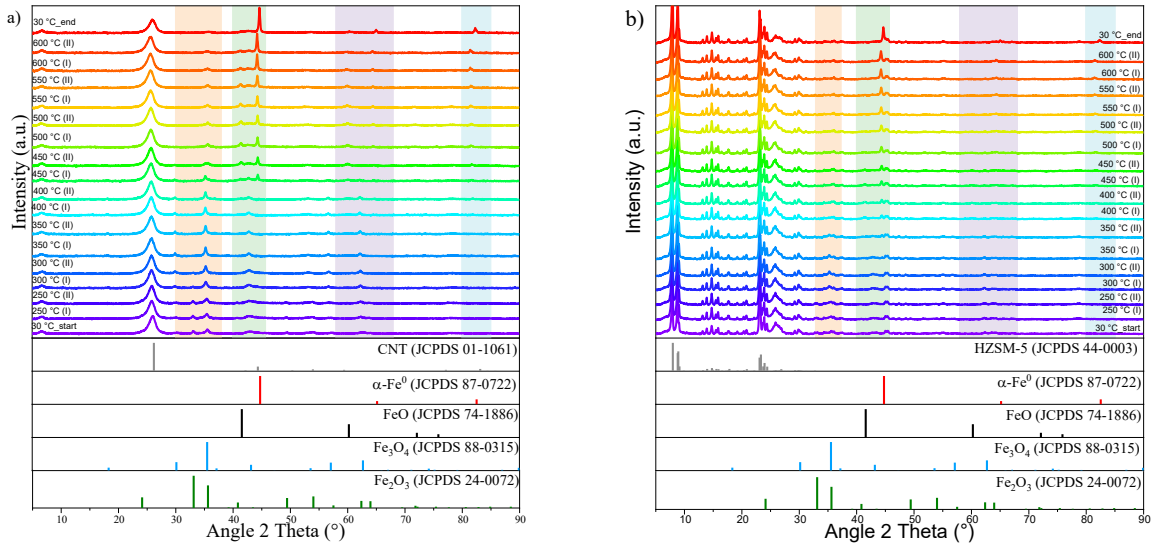


Figure A1. 3. N_2 adsorption of CNTs with Fe and Na inside and/or outside the CNT.



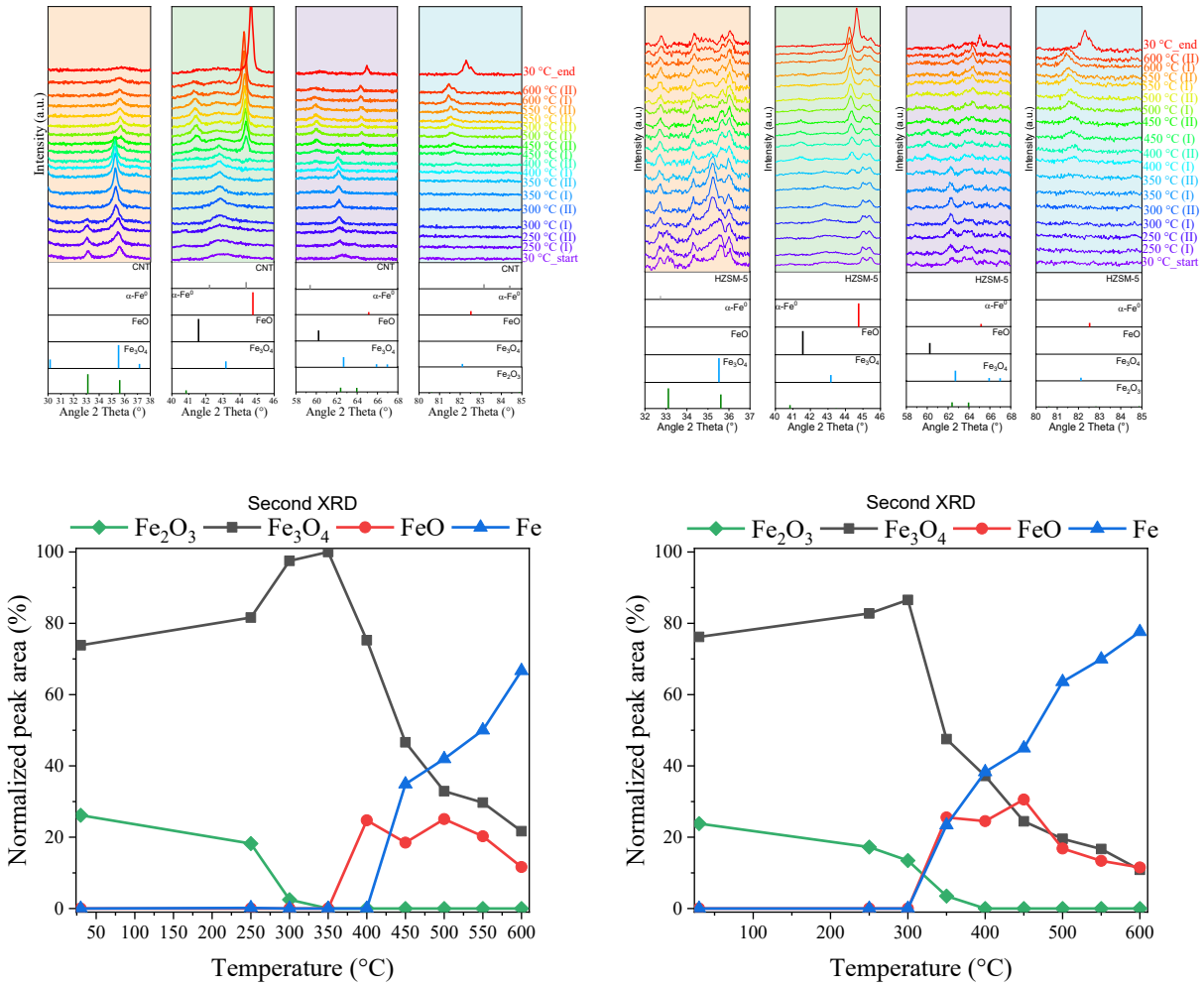


Figure A1. 4. Temperature-resolved X-ray diffractograms were obtained for the following catalysts: a) CNT-S-C10FeNa, b) CNT-S-C10FeNa+MFI27 (PM), during in situ reduction treatment in a flowing 10% H2/N2 atmosphere. Additionally, the corresponding temperature-resolved evolution of the normalized area for the most intense diffraction line of detected crystalline species was examined. These species include: Fe2O3 (1 0 4), JCPDS24-0072; Fe3O4 (3 1 1), JCPDS 88-0315; FeO (2 0 0), JCPDS 74-1886 and Fe0 (1 1 0), JCPDS 87-0722.

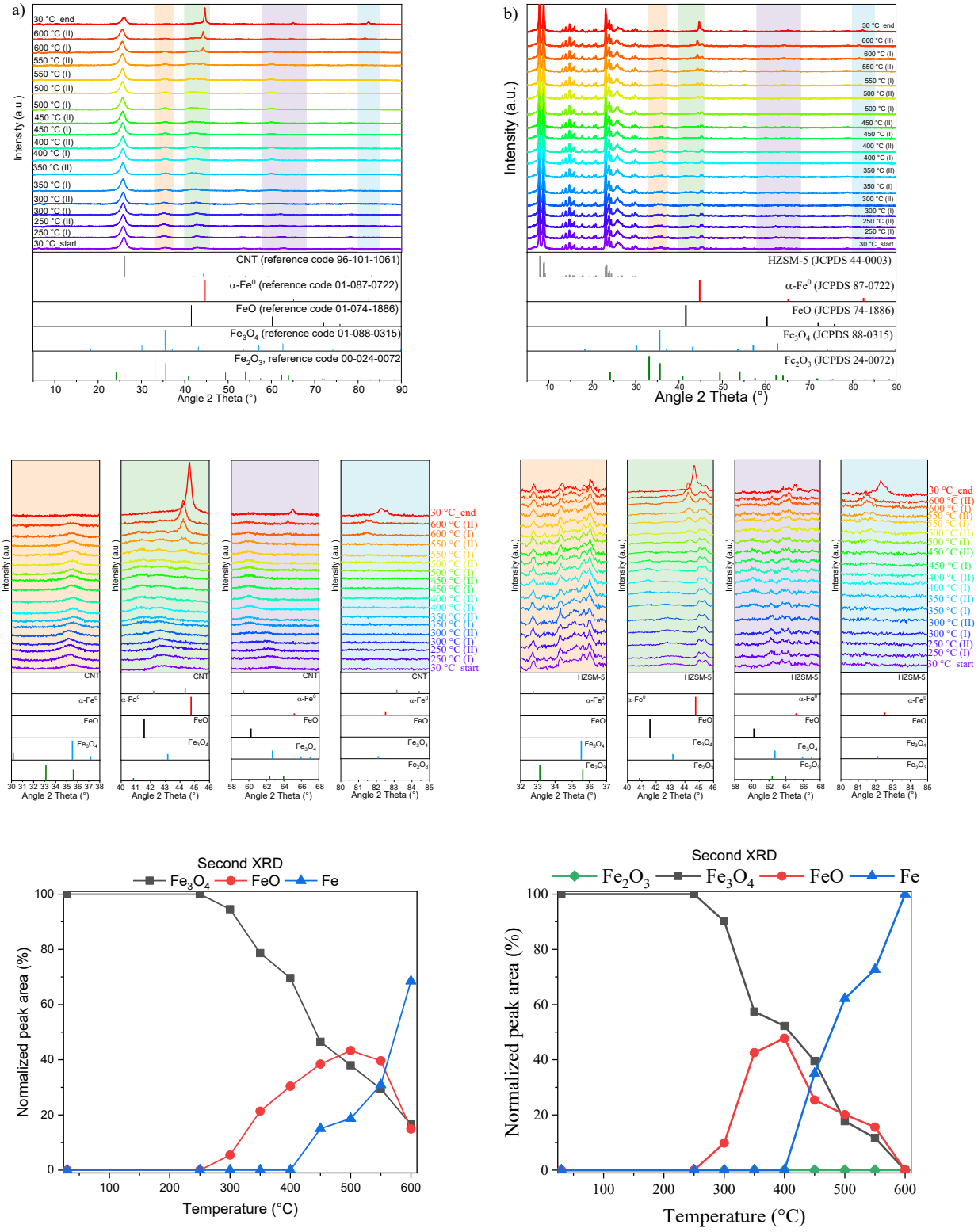
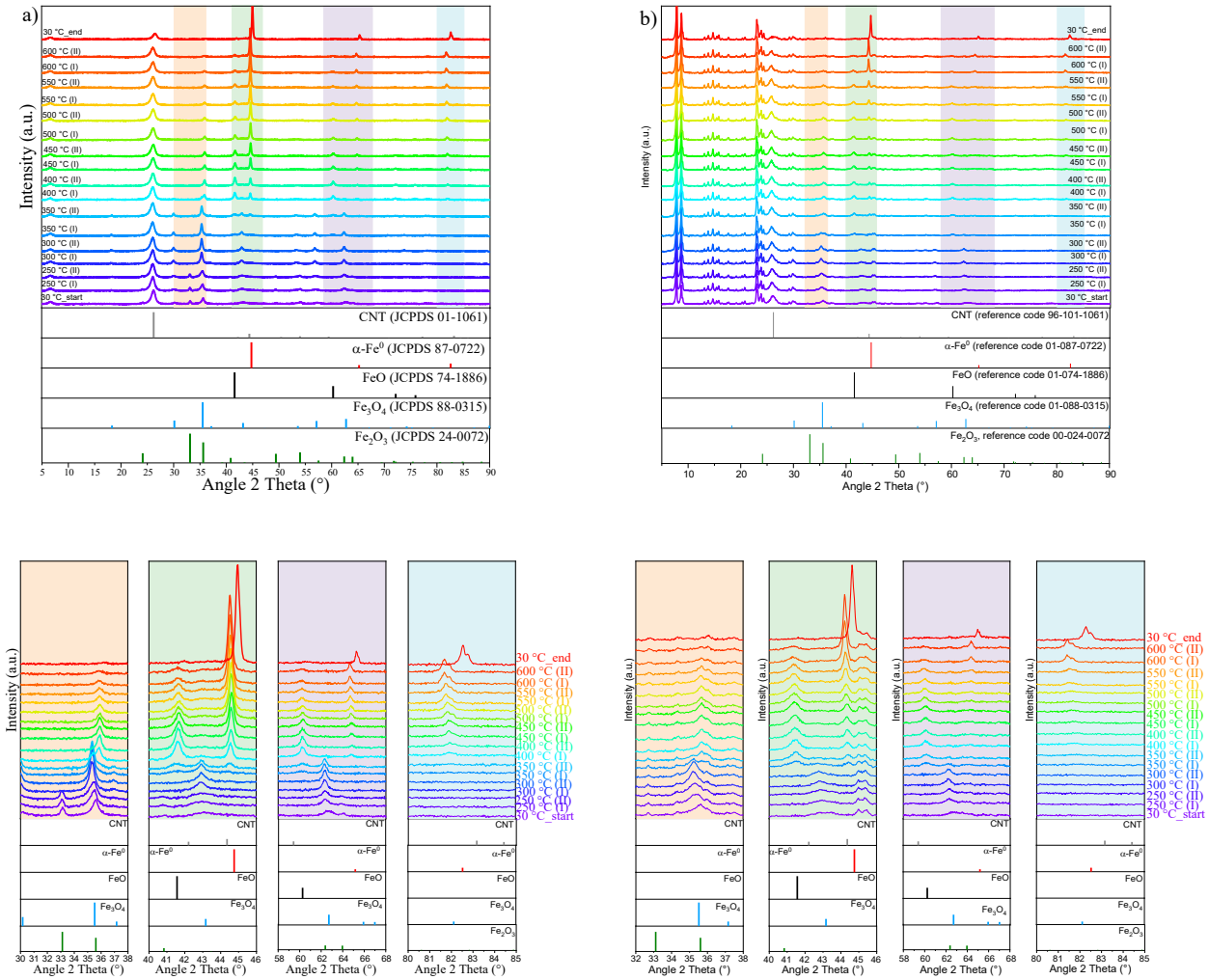

a)
b)
Intensity (a.u.)
Angle 2 Theta (°)
30 °C_end
600 °C (II)
600 °C (I)
550 °C (II)
550 °C (I)
500 °C (II)
500 °C (I)
450 °C (II)
450 °C (I)
400 °C (II)
400 °C (I)
350 °C (II)
350 °C (I)
300 °C (II)
300 °C (I)
250 °C (II)
250 °C (I)
30 °C_start
CNT (reference code 96-101-1061)
α-Fe0 (reference code 01-087-0722)
FeO (reference code 01-074-1886)
Fe3O4 (reference code 01-088-0315)
Fe2O3, reference code 00-024-0072
HZSM-5 (JCPDS 44-0003)
α-Fe0 (JCPDS 87-0722)
FeO (JCPDS 74-1886)
Fe3O4 (JCPDS 88-0315)
Fe2O3 (JCPDS 24-0072)
CNT
HZSM-5
α-Fe0
FeO
Fe3O4
Fe2O3
Second XRD
Fe3O4
FeO
Fe
Fe2O3
Normalized peak area (%)
Temperature (°C)

Figure A1. 5. Temperature-resolved X-ray diffractograms were obtained for the following catalysts: a) CNT-S-O10FeNa, b) CNT-S-O10FeNa+MFI27 (PM), during in situ reduction treatment in a flowing 10% H2/N2 atmosphere. Additionally, the corresponding temperature-resolved evolution of the normalized area for the most intense diffraction line of detected crystalline species was examined. These species include: Fe2O3 (1 0 4), JCPDS24-0072; Fe3O4 (3 1 1), JCPDS 88-0315; FeO (2 0 0), JCPDS 74-1886 and Fe0 (1 1 0), JCPDS 87-0722.



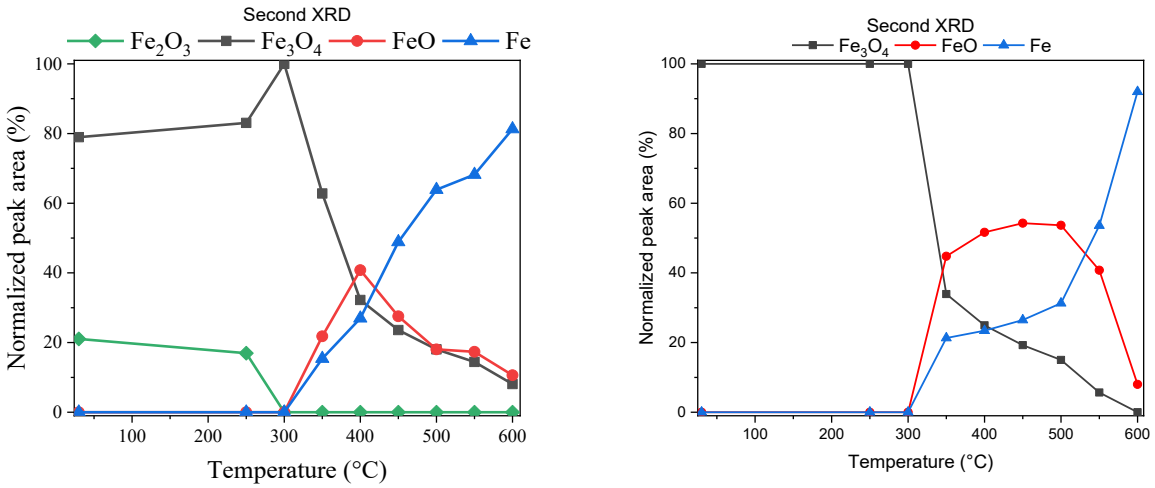


Figure A1. 6. Temperature-resolved X-ray diffractograms were obtained for the following catalysts: a) CNT-M-O15FeNa, b) CNT-M-O15FeNa+MFI27 (PM), during in situ reduction treatment in a flowing 10% H2/N2 atmosphere. Additionally, the corresponding temperature-resolved evolution of the normalized area for the most intense diffraction line of detected crystalline species was examined. These species include: Fe2O3 (1 0 4), JCPDS24-0072; Fe3O4 (3 1 1), JCPDS 88-0315; FeO (2 0 0), JCPDS 74-1886 and Fe0 (1 1 0), JCPDS 87-0722.

Appendix 2

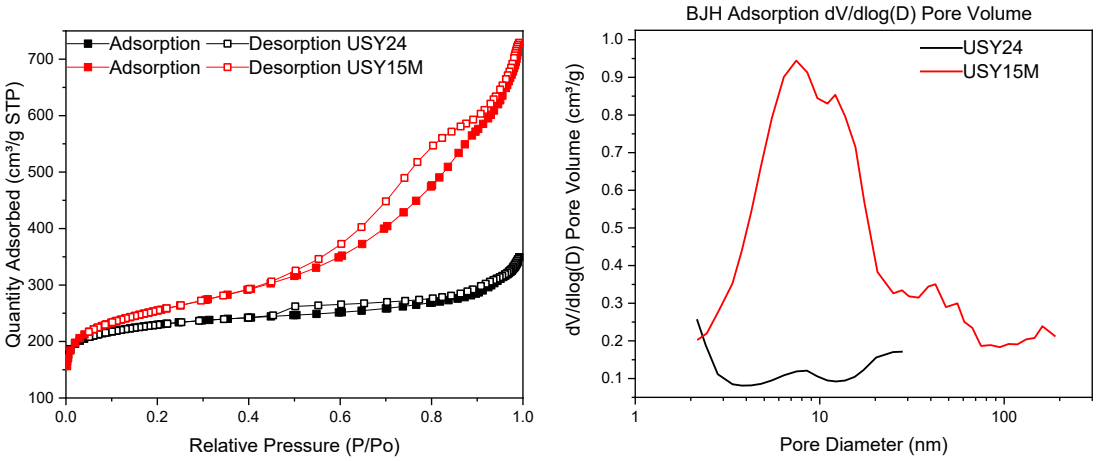


Figure A2. 1. Nitrogen adsorption-desorption isotherms and pore distribution of commercial USY24 and mesoporous USY15M.

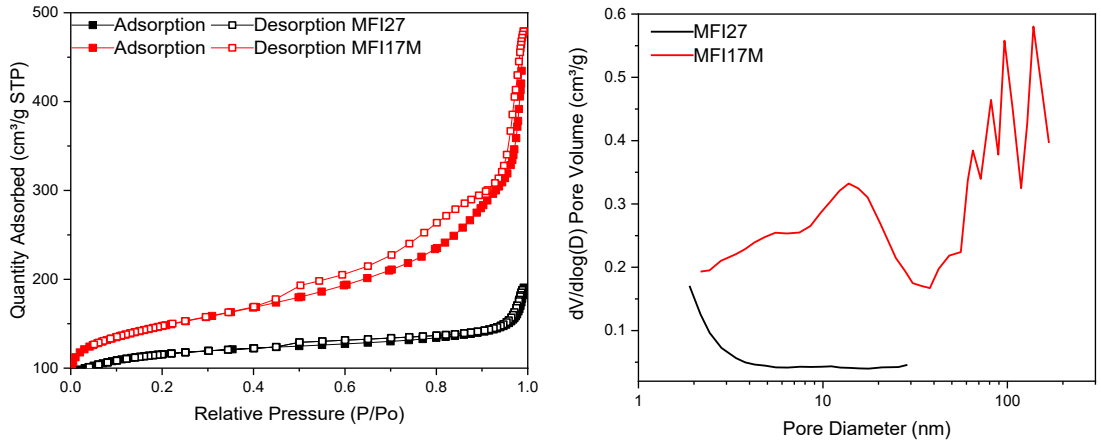


Figure A2. 2. Nitrogen adsorption-desorption isotherms and pore distribution of MFI27 and mesoporous MFI17M.

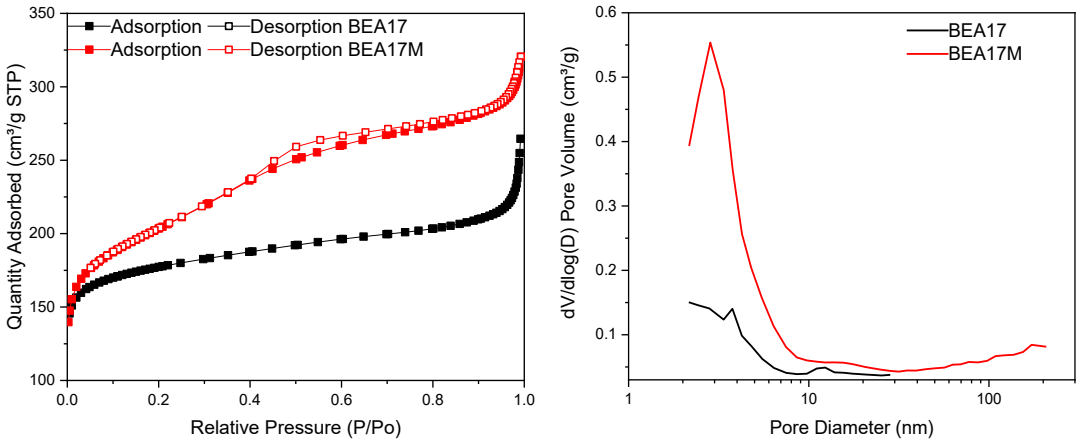


Figure A2. 3. Nitrogen adsorption-desorption isotherms and pore distribution of BEA17 and mesoporous BEA17M.

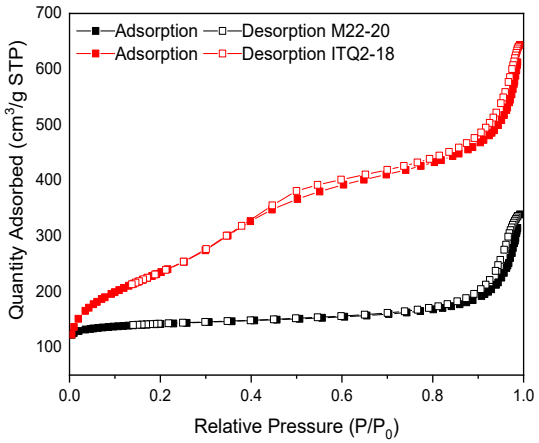


Figure A2. 4. Nitrogen adsorption-desorption isotherms and pore distribution of M22-20 and delaminated ITQ2-18 zeolites.

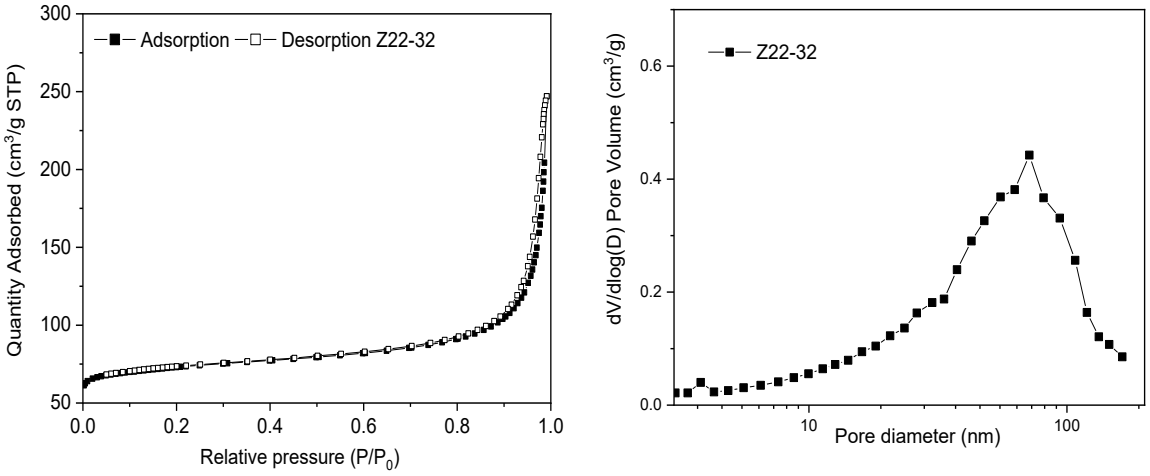
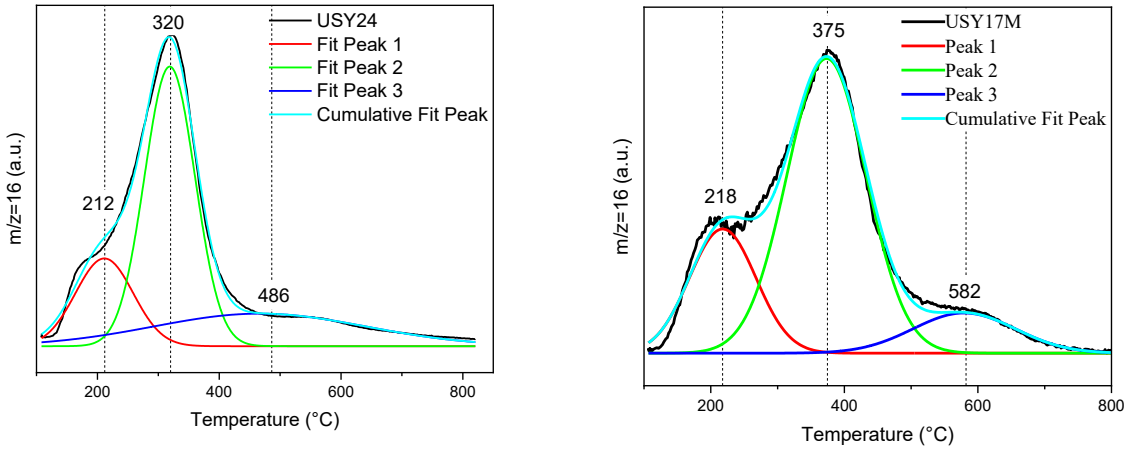
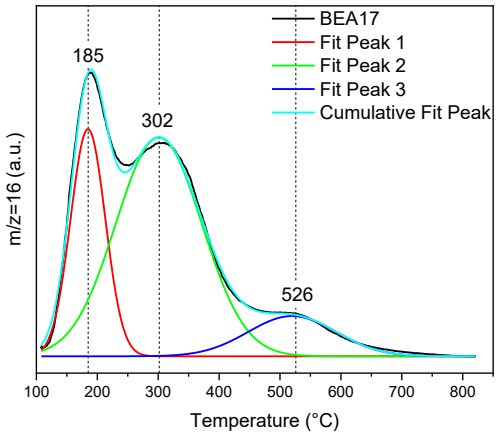
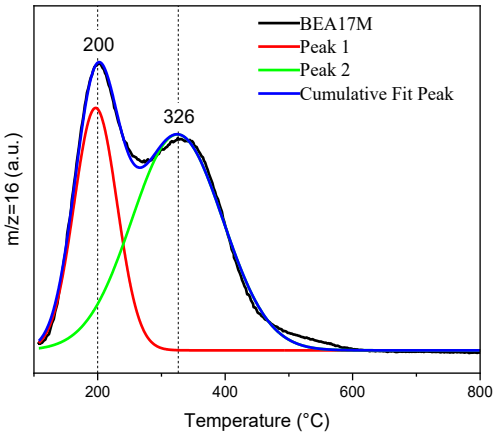
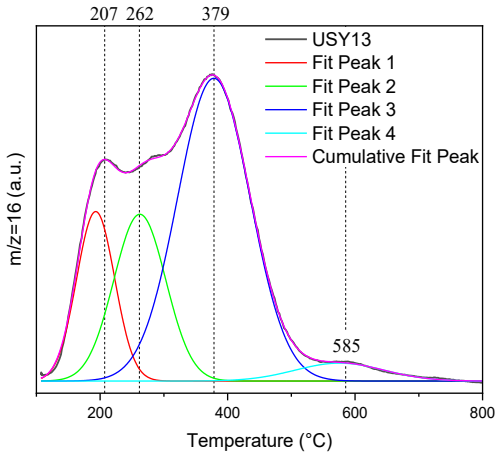


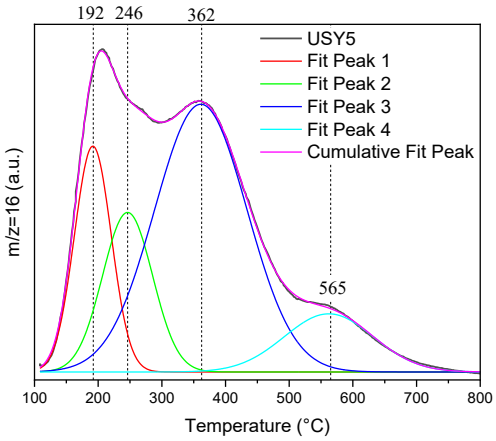
Figure A2. 5. Nitrogen adsorption-desorption isotherms and pore distribution of Z22-32 zeolite.

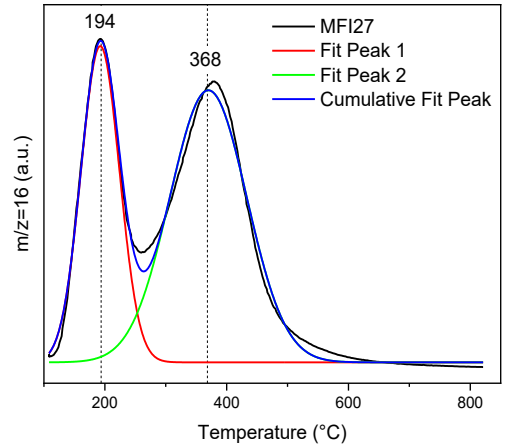


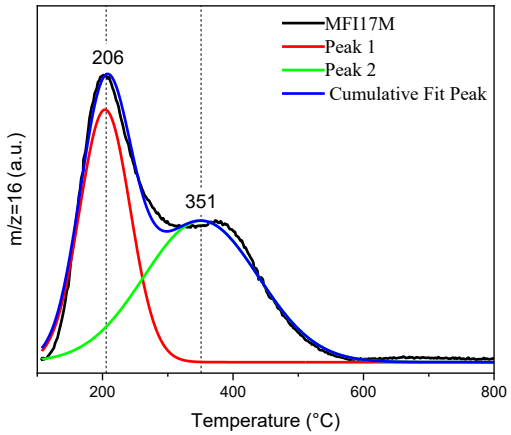

BEA17
Fit Peak 1
Fit Peak 2
Fit Peak 3
Cumulative Fit Peak
185
302
526
m/z=16 (a.u.)
100
200
300
400
500
600
700
800
Temperature (°C)

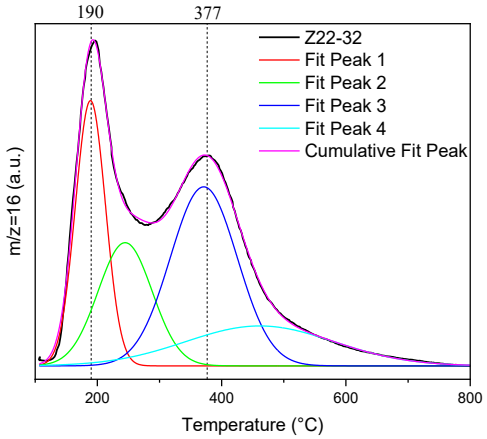

BEA17M
Peak 1
Peak 2
Cumulative Fit Peak
200
326
m/z=16 (a.u.)
200
400
600
800
Temperature (°C)

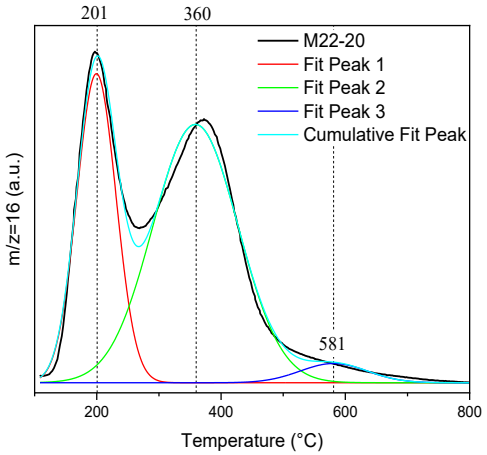

207
262
379
USY13
Fit Peak 1
Fit Peak 2
Fit Peak 3
Fit Peak 4
Cumulative Fit Peak
585
m/z=16 (a.u.)
200
400
600
800
Temperature (°C)


192
246
362
USY5
Fit Peak 1
Fit Peak 2
Fit Peak 3
Fit Peak 4
Cumulative Fit Peak
565
m/z=16 (a.u.)
100
200
300
400
500
600
700
800
Temperature (°C)


194
368
MFI27
Fit Peak 1
Fit Peak 2
Cumulative Fit Peak
m/z=16 (a.u.)
200
400
600
800
Temperature (°C)


206
351
MFI17M
Peak 1
Peak 2
Cumulative Fit Peak
m/z=16 (a.u.)
200
400
600
800
Temperature (°C)


190
377
Z22-32
Fit Peak 1
Fit Peak 2
Fit Peak 3
Fit Peak 4
Cumulative Fit Peak
m/z=16 (a.u.)
200
400
600
800
Temperature (°C)


201
360
581
M22-20
Fit Peak 1
Fit Peak 2
Fit Peak 3
Cumulative Fit Peak
m/z=16 (a.u.)
200
400
600
800
Temperature (°C)

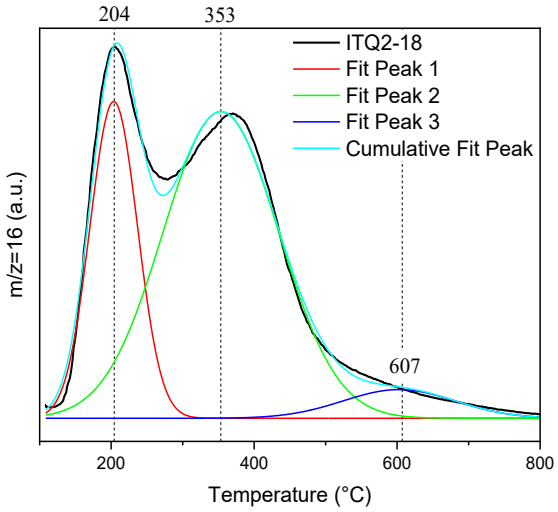


Figure A2. 6. Deconvoluted NH_3-TPD profiles of commercial BEA, USY, and MFI zeolites and their mesoporous counterparts.

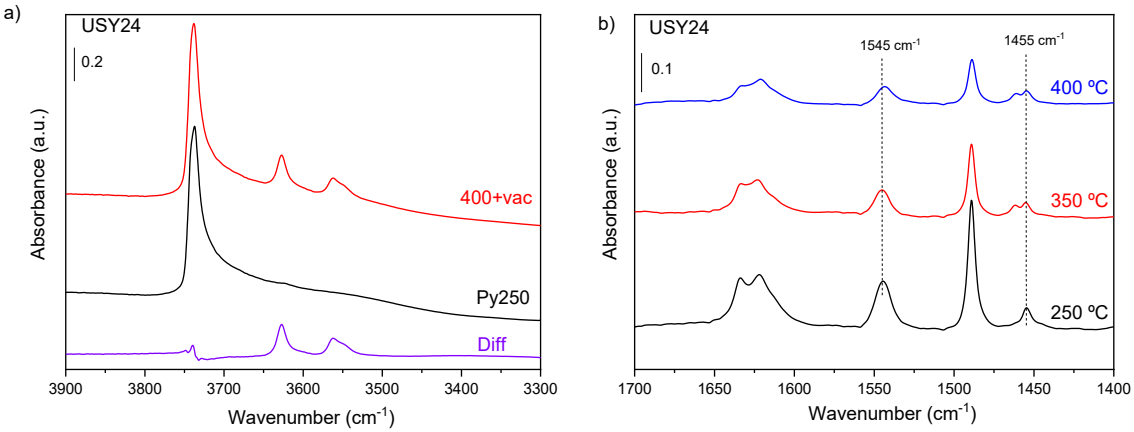


Figure A2. 7. Infrared spectra of USY24 zeolite in hydroxyl region, recorded after a) overnight activation at 400 °C under dynamic vacuum and after adsorption and desorption of pyridine at 250 °C; b) adsorption and desorption of pyridine at 250 °C, 350 °C and 400 °C.

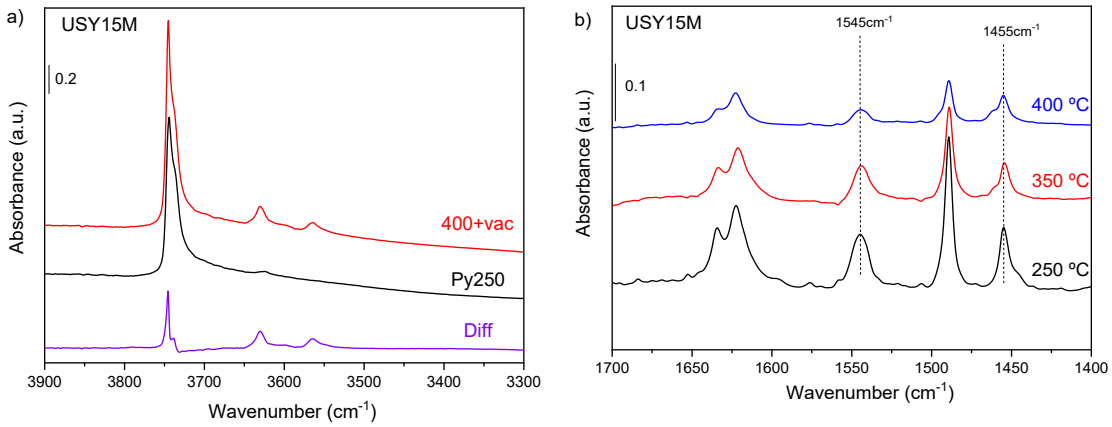


Figure A2. 8. spectra of USY15M zeolite in hydroxyl region, recorded after a) overnight activation at 400 °C under dynamic vacuum and after adsorption and desorption of pyridine at 250 °C; b) adsorption and desorption of pyridine at 250 °C, 350 °C and 400 °C.

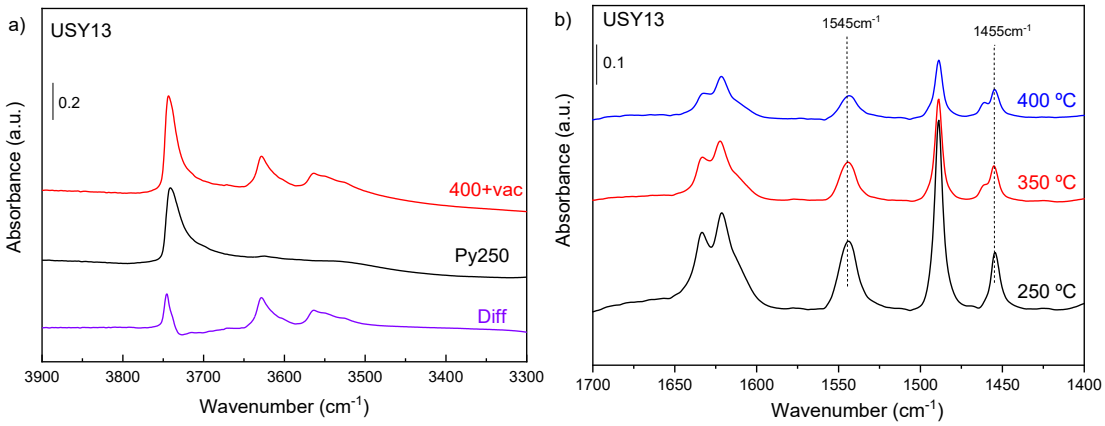


Figure A2. 9. Infrared spectra of USY13 zeolite in hydroxyl region, recorded after a) overnight activation at 400 °C under dynamic vacuum and after adsorption and desorption of pyridine at 250 °C; b) adsorption and desorption of pyridine at 250 °C, 350 °C and 400 °C.

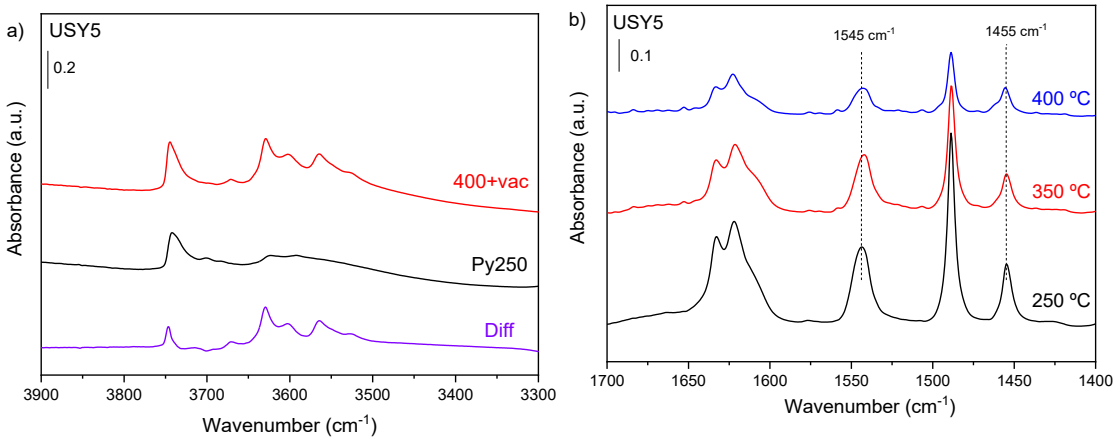


Figure A2. 10. Infrared spectra of USY5 zeolite in hydroxyl region, recorded after a) overnight activation at 400 °C under dynamic vacuum and after adsorption and desorption of pyridine at 250 °C; b) adsorption and desorption of pyridine at 250 °C, 350 °C and 400 °C.

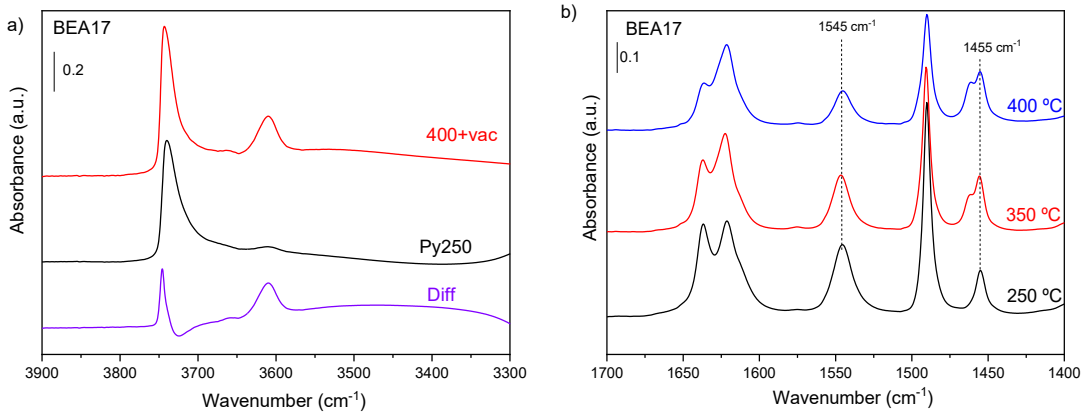


Figure A2. 11. Infrared spectra of BEA17 zeolite in hydroxyl region, recorded after a) overnight activation at 400 °C under dynamic vacuum and after adsorption and desorption of pyridine at 250 °C; b) adsorption and desorption of pyridine at 250 °C, 350 °C and 400 °C.

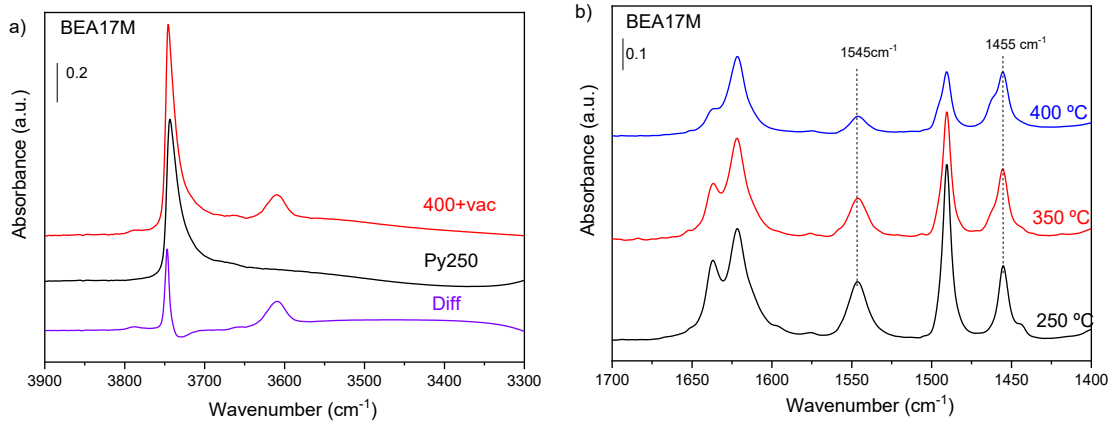


Figure A2. 12. Infrared spectra of BEA17M zeolite in hydroxyl region, recorded after a) overnight activation at 400 °C under dynamic vacuum and after adsorption and desorption of pyridine at 250 °C; b) adsorption and desorption of pyridine at 250 °C, 350 °C and 400 °C.

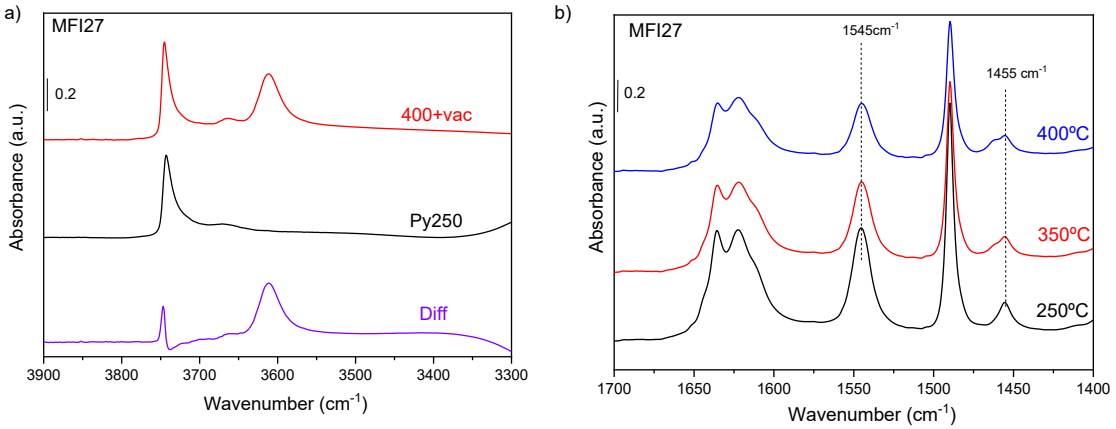


Figure A2. 13. Infrared spectra of MFI27 zeolite in hydroxyl region, recorded after a) overnight activation at 400 °C under dynamic vacuum and after adsorption and desorption of pyridine at 250 °C; b) adsorption and desorption of pyridine at 250 °C, 350 °C and 400 °C.

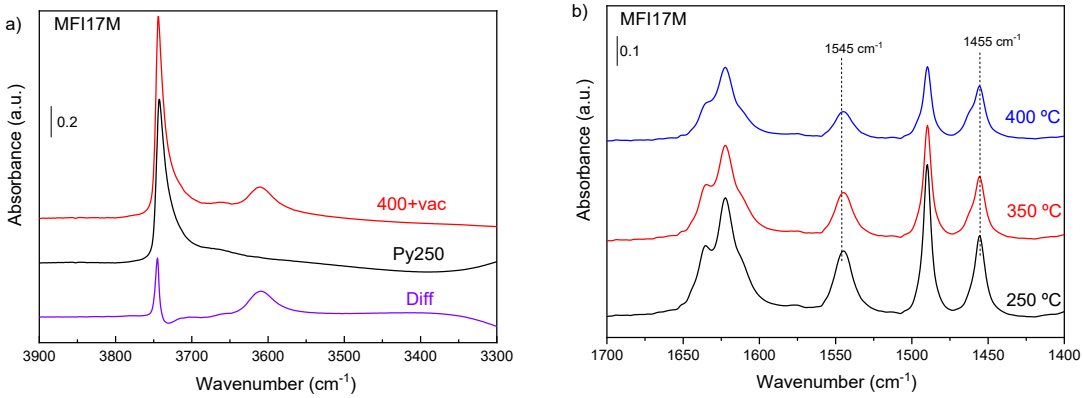


Figure A2. 14. Infrared spectra of MFI17M zeolite in hydroxyl region, recorded after a) overnight activation at 400 °C under dynamic vacuum and after adsorption and desorption of pyridine at 250 °C; b) adsorption and desorption of pyridine at 250 °C, 350 °C and 400 °C.

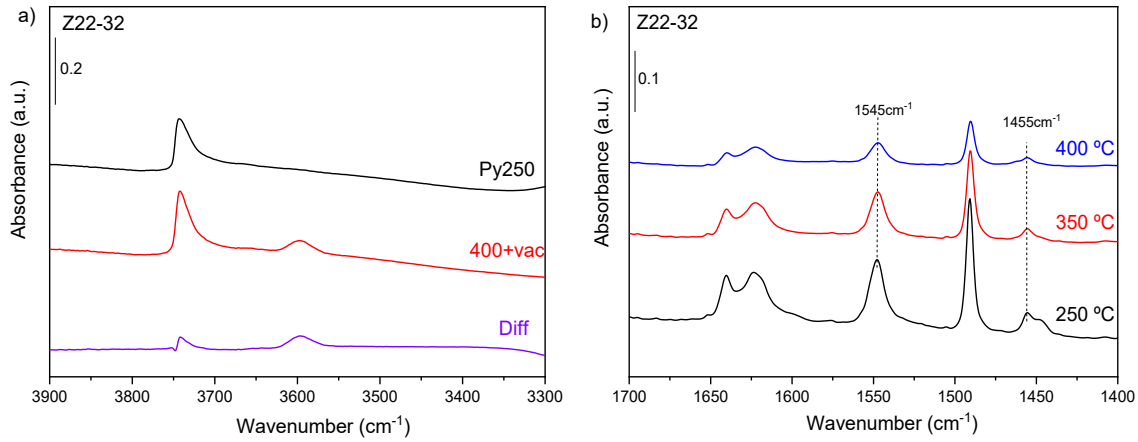


Figure A2. 15. Infrared spectra of Z22-32 zeolite in hydroxyl region, recorded after a) overnight activation at 400 °C under dynamic vacuum and after adsorption and desorption of pyridine at 250 °C; b) adsorption and desorption of pyridine at 250 °C, 350 °C and 400 °C.

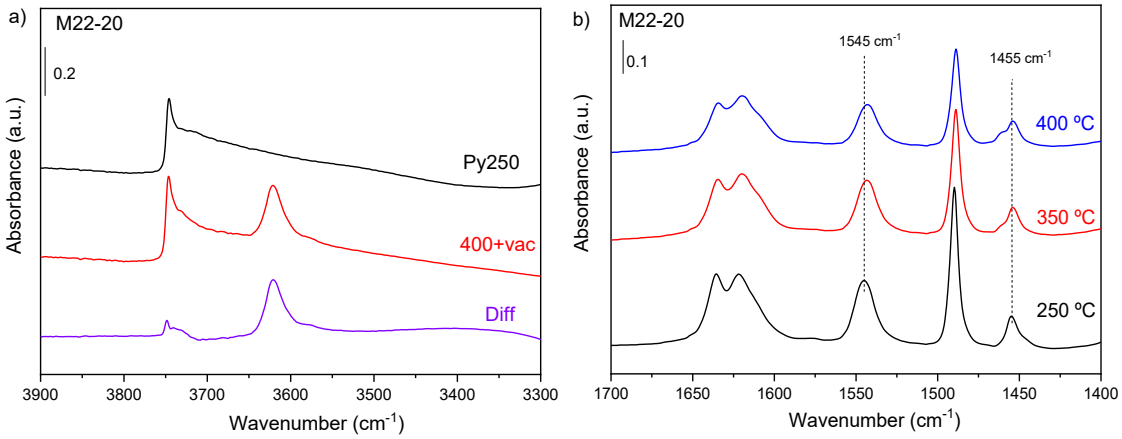


Figure A2. 16. Infrared spectra of M22-20 zeolite in hydroxyl region, recorded after a) overnight activation at 400 °C under dynamic vacuum and after adsorption and desorption of pyridine at 250 °C; b) adsorption and desorption of pyridine at 250 °C, 350 °C and 400 °C.

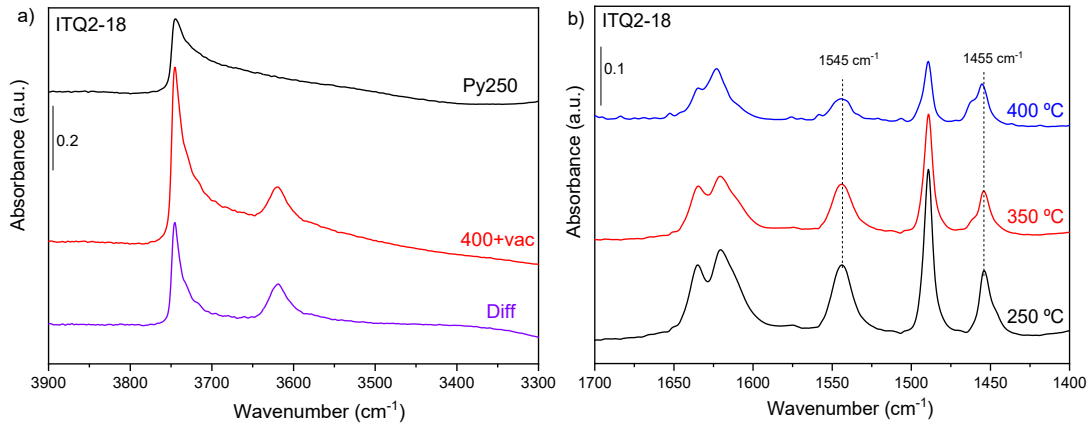


Figure A2. 17. Infrared spectra of ITQ2-18 zeolite in hydroxyl region, recorded after a) overnight activation at 400 °C under dynamic vacuum and after adsorption and desorption of pyridine at 250 °C; b) adsorption and desorption of pyridine at 250 °C, 350 °C and 400 °C.

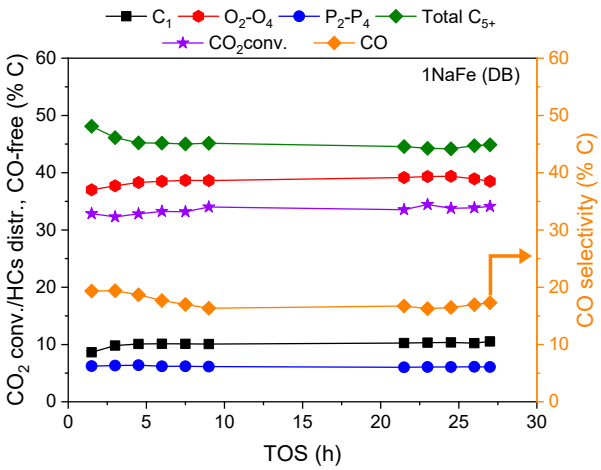


Figure A2. 18. Catalysts activity and products distribution over 1NaFe tested in dual bed mode without zeolite.